Polarization and Structure of Broad Absorption Line Quasi-Stellar Objects

Thesis by

Patrick M. Ogle

In Partial Fulfillment of the Requirements

for the Degree of

Doctor of Philosophy

California Institute of Technology

Pasadena, California

1998

(Submitted May 18, 1998)

Acknowledgements

This thesis is partly based on observations taken at the W.M. Keck Observatory in collaboration with Marshall Cohen, Hien Tran, Joseph Miller, Bob Goodrich, and Andre Martel. Special thanks to Judy Cohen and Bev Oke for building LRIS, a wonderful instrument with high efficiency and great optics. Thanks to instrument specialists Tom Bida, Randy Campbell, and Bob Goodrich and to observing assistants Barbara Schaefer, Ron Quick, and Teresa Chelminiak for their invaluable assistance at Keck. The W.M. Keck Observatory is operated as a scientific partnership among the California Institute of Technology, the University of California and the National Aeronautics and Space Administration. The Observatory was made possible by the generous financial support of the W.M. Keck Foundation.

I would like to thank Marshall Cohen, Angela Putney, John Gizis, Bradford Behr, Greg Harper, and Patrick Shopbell for assisting in the observations at Palomar Observatory. I received invaluable help from Juan Carrasco and Skip Staples, the night assistants at the "Big Eye." The Double Spectrograph, built by Bev Oke, was a trusty, easy-to-use instrument. The dual-beam polarimeters at Palomar and Keck, built by Marshall Cohen, Bob Goodrich, and Angela Putney, were the heart of my polarimetry observations, detecting polarized light at fractions of a percent in quasars at the distant reaches of the universe.

This research has made use of the NASA/IPAC Extragalactic Database (NED) which is operated by the Jet Propulsion Laboratory, California Institute of Technology, under contract with the National Aeronautics and Space Administration.

Thanks to the Palomar and Keck time allocation committees for more than generous allocations of dark time, and understanding when a large fraction of my Palomar nights were cloudy. Jim Westphal, Bob Brucato, Petra de la Paz, and Jo Ann Viengkou always made sure things were running smoothly at Palomar Observatory. Thanks to executive officers Shri Kulkarni and Roger Blandford for useful academic advice. Many thanks also to Chris Holmes for academic advisement.

Additional thanks goes to my thesis committee–Marshall Cohen, Ray Weymann, Nick Scoville, B. Tom Soifer, and Roger Blandford. I am indebted to Marshall Cohen, Nahum

Arav, Tom Barlow, and Roger Blandford for many stimulating discussions about BAL QSO. I was lucky to have such a vast resource of knowledge to draw from.

Thanks to my ever-present office mates Angela Putney, Mike Pahre, Andrew Baker, Celeste Sleeper, Rudy Danner, and Mindy Kellogg for help and advice. I am indebted to Angela Putney and Hien Tran for teaching me how to reduce spectropolarimetric data. Special thanks goes to Mike Pahre for LATEX help and suggestions. John Yamasaki is the best barbecuer in the West! Thanks to Cyndy Carlson for email and cookies. Thanks to Sah Bum Nim Erik Severin, and Boo Kyo Sah Nims William Glenn, Ricardo Hassan, Adrian Hightower, and Steve Padilla. Tang Soo!

I give extra special thanks to my good friends Peter Pich, Michael Manley, and Ann Lee for their encouragement and advice. The many adventures and good times we had together made my stay at Caltech a wonderful experience.

I could not have succeeded without the constant support of my parents Michael and Kathleen, my sister Wendy Middleton, my brother Collin, and my grandparents Bill and Bette Nickloff. My father inspired in me the love of astronomy and the dream to become an astronomer. My mother taught me the meaning of hard work and persistence. This thesis is dedicated, with love, to my family.

Abstract

This thesis is a spectropolarimetric survey of broad absorption line quasi-stellar objects (BAL QSO). We observed 36 BAL QSO at low resolution with the 5 m Hale Telescope at Palomar Observatory and the 10 m Keck Telescopes at the W. M. Keck Observatory.

The continuum, absorption trough, and emission line polarization of BAL QSO were studied in detail, yielding clues about the geometrical structure of gas in the inner regions of quasars. BAL QSO have, on average, higher polarization than other quasars, reinforcing the view that they are normal quasars viewed from a more equatorial aspect. However, there is a wide distribution of polarization values, which may be due to intrinsic differences in the geometry or optical depth to scattering. No correlations are found among emission line or broad absorption line properties and continuum polarization, suggesting that these properties are regulated by internal differences unrelated to viewing angle. The continuum polarization of BAL QSO is weakly wavelength dependent after correction for emission line dilution. In most objects, the polarization rises to the blue, suggesting that dust scattering or absorption may be important.

Broad emission line photons are polarized less than the continuum; and the position angle of the electric vector is rotated with respect to the continuum. The semi-forbidden C III] emission line is polarized differently than the C IV emission line in some cases, suggesting resonance scattering in the C III] emission line region. Resonantly scattered photons from the broad absorption line region are detected at high velocities red-ward and blue-ward of the C IV line center in the spectra of some objects. These photons are negatively polarized with respect to the continuum photons, showing that the broad absorption line region and the continuum scattering region are oriented perpendicular to each other.

The polarization increases in the BAL troughs, due mainly to partial coverage of the central source by the broad absorption line region. Partial coverage of the continuum and broad emission line clouds leads to difficulties in determining the true optical depth of the BAL outflow. The geometry of the intervening BAL clouds is skewed with respect to the continuum scattering region, which results in position angle rotations in the BAL. The variation of polarization with velocity in the BAL is consistent with a non-radial,

accelerating outflow of ionized gas. Our polarimetry observations are consistent with a model which unifies BAL QSO and non-BAL QSO. The BAL wind appears to occupy a narrow range of equatorial latitudes. When we view a QSO through this outflow, we see the characteristic troughs in BAL QSO.

Contents

List of Figures

List of Tables

Chapter 1 Introduction

Many galaxies contain active galactic nuclei (AGN), which appear to be powered by accretion onto a super-massive ($M \simeq 10^8 M_\odot$) black hole. The most powerful AGN are the quasi-stellar objects (QSO), which have luminosities in the range $10^{44} - 10^{48}$ erg/s. They out-shine their host galaxies by factors of up to 10^4. It is important to understand the workings of these most luminous objects in the universe because they provide a laboratory to study high-energy physics and also because they may play a crucial role in the formation and evolution of galaxies.

Spectroscopy has yielded advances in our understanding of QSO, but it is often difficult to separate the various spectral components. The spectrally distinct components in the UV-optical spectra of QSO include the blue featureless continuum (FC), the broad emission lines (BEL), the broad absorption lines (BAL), and sometimes narrow absorption lines (NAL). However, the broad nature of many features makes it difficult to measure them accurately. There are many overlapping broad lines which makes identifying and measuring individual lines difficult. These blends, especially of Fe II emission, are extensive in the UV part of the spectrum and make it very difficult to define a continuum level. Spectropolarimetry provides a way of disentangling spectral components which have distinct polarization.

The study of QSO is hampered by the small angular sizes of the central optical and ultraviolet emitting regions. Recently, reverberation mapping has yielded a rough estimate of the size of the BEL region (BELR), which is about 0.1 pc (3×10^{17} cm) across (Kaspi et al., 1996). It is at present impossible to resolve these regions directly; it would require space-based interferometry with a resolution of less than 10^{-4} arcseconds. The size of the continuum emitting region is much smaller, of order the Schwarzschild radius of $R_S \simeq 10^{-5}$ pc.

The reverberation mapping technique measures the delay between broad line and continuum variations, using it to determine a characteristic distance between the continuum source and broad line clouds. In principle, the response curve (transfer function) of the BEL can tell us about the shape of the BELR (Peterson, 1993), but the promise of this technique has not yet been fully realized. Spectropolarimetry is a complimentary technique to

reverberation mapping. In reverberation mapping, the transfer function is symmetric with respect to rotations around the line of sight, so it is not possible to determine the position angle between a BEL cloud and the central source. The polarization transfer function is sensitive to the scattering angle, but not to distance from the central source.

In principle, it would be possible to map the position of a scattering electron to within a 4 point degeneracy using the combined techniques of reverberation and spectropolarimetry. If a pulse came from the central source and was scattered into the line of sight by an electron, the time delay between the direct and scattered signal would confine the location of the electron to a paraboloid with the source at its focus. The polarization level of the scattered light would define a cone with the source at its apex, and the position angle of the polarization would determine the scattering plane. The intersection of these three surfaces would give four possible points for the location of the electron.

The remaining degeneracies are due to the symmetry between left and right scattering and between front and back scattering. The degeneracy between front and back scattering is broken if the scatterers are dust grains instead of electrons. If the pulse is monochromatic, it would also be possible to determine the line of sight motion of the scattering particle relative to the central source. This is equivalent to the technique of Doppler radar tomography, which is used to map the surfaces of planets.

Spectropolarimetry by itself only gives limited information on the spatial distribution of plasma in quasars. We can determine the symmetry axis of the distribution in the plane of the sky from the electric vector position angle. We can also use the polarization level to make a rough estimate of the departure from circular symmetry. The polarization of the scattered light is generally diluted by an unknown amount of direct light, which depends on the optical depth of the scattering material and obscuration by intervening material. This makes it difficult to separate geometrical and optical depth effects on the polarization. The wavelength dependence of the continuum polarization can give us clues about the amount of obscuration and also the nature of the scattering particles.

We can learn about the radial distribution of the BELR and BALR by comparing the emission and absorption line polarization to the continuum polarization. If the emission line and continuum polarization are the same, it suggests that the sources of radiation are unresolved relative to the scattering region. However, if the line polarization is lower than the continuum polarization, it suggests that the BELR is larger than the scattering region.

Similarly, polarization variations across the BAL indicate that the BALR has a similar size scale to the to the scattering region.

While spectropolarimetry yields new information on the spatial distribution of material in QSO, it can not provide a full 2-D map in the plane of the sky. The polarization and mean electric vector direction are spatially integrated quantities and do not yield a unique distribution of scatterers. We have studied a moderately large sample of BAL QSO, which are presumably viewed from a variety of perspectives, to gain a more complete understanding of the 3-D distribution of matter in QSO. However, our sample of 36 objects is still not enough to separate object to object differences from viewing angle effects.

1.1 Unification

AGN are classified by their characteristics in various wave-bands. The primary distinction is between radio-loud and radio-quiet objects. Another important distinction is between objects with broad emission lines (type 1), and those without (type 2). There has been much success recently in unifying various types of AGN by considering orientation effects (Antonucci, 1993; Urry & Padovani, 1995). The radiation pattern from the nucleus is highly anisotropic and wavelength dependent–very strong along a polar axis and weak along the equator. Hence the classification of AGN is highly aspect-dependent.

In type 2 objects, the equatorial view of the nucleus is obscured by dusty molecular clouds arranged in a disk or torus. The resultant anisotropy in the ultraviolet continuum is seen in the ionization cones of Seyfert galaxies (e.g., Pogge, 1988; Wilson et al., 1993) and radio galaxies (e.g., Jackson et al., 1996). The nucleus can also be viewed indirectly in light reflected by electrons and dust along the disk axis. Galaxy-size reflection nebulae coinciding with the ionization cones have been seen in a number of radio galaxies (e.g., Ogle et al., 1997). Scattered broad lines have been detected in Seyfert 2s (Antonucci & Miller, 1985; Tran, 1995), ultra-luminous infrared galaxies (ULIG, Hines et al., 1995; Goodrich et al., 1996), and narrow-line radio galaxies (NLRG Ogle et al., 1997; Tran et al., 1998). Type 1 objects (Seyfert 1s, BLRG, and QSO) have directly visible BEL and are presumably viewed through an opening in the center of the disk.

While many type 2 AGN contain hidden type 1 AGN, it is not known if all type 1 objects have equatorial obscuration. It is very difficult to identify type 2 counterparts to

radio-quiet QSO because of their radio silence and heavy obscuration; only a few examples are known. The best hope for detecting these objects is in the far infrared or hard X-rays. Perhaps the ULIG are examples of the most luminous QSO viewed in the equatorial plane.

About 12% (Weymann et al., 1991) of all radio-quiet QSO (RQQ) have broad absorption lines (BAL) in their spectra indicating a fast (up to 0.1 c or greater) outflow. These are the broad absorption line quasi-stellar objects (BAL QSO). Sowinski et al. (1997) list 304 QSO (plus 133 candidates) with associated absorption lines or BAL. The BAL phenomenon appears to be confined to luminous radio-quiet objects and does not appear in Seyfert galaxies or radio-loud QSO. However, low-velocity intrinsic absorption systems are commonly seen in all subtypes of type 1 AGN.

The question of whether or not BAL QSO can be unified with other types of QSO has important implications for the structure and physics of AGN. It has been suggested that BAL QSO are viewed at an intermediate angle which skims the accretion disk or torus. This transition region is likely to be heavily affected by obscuration. It is also interesting as a transition zone between regions of inflow and outflow.

At this point, we define some terminology which is used to describe the geometry of the broad absorption line region. The global covering fraction f is the fraction of solid angle covered by the BALR as seen from the central continuum source. This parameter is important for understanding the global geometry of the BALR, and for QSO unification. The local covering fraction f_l is the fraction of direct sight-lines to the observer from the emission source which are covered by BAL clouds. When the local covering fraction is less than one, we speak of partial coverage of the continuum, BEL, or scattering region. The local covering fraction depends on both the patchiness of the BALR and the viewing angle.

The following sections examine the many clues that have been gathered on the geometry and other physical parameters of BAL QSO. The evidence suggests that BAL QSO are normal radio-quiet QSO viewed from a special angle. Despite this general agreement on the nature of BAL QSO, a number of fundamental parameters remain undetermined. The geometry of the BAL region is not well constrained by observations, and estimates of its distance from the central continuum source range from 0.1-500 pc (e.g., Turnshek et al., 1988).

1.2 Ultraviolet Spectra

BAL QSO typically show high ionization BAL from the Lyman series H I λ1216, 1026; the lithium-like ions C IV λ1549, N V λ1240, and O VI λ1034; and the sodium-like ions Si IV λ1397 and S VI λ939. The strength of these lines is determined by the elemental abundances and ionization state of the gas. Many other transitions from a range of ionization states have been identified with the Hubble Space Telescope (HST), including those of C III, N III, N IV, N V, O III, O IV, and O V (Korista & Arav, 1997).

The BAL ions are presumably photoionized by far-ultraviolet and soft X-ray flux from the central continuum source. Unfortunately, the shape of the ionizing continuum is not well observed, and may be heavily modified by its passage through the BALR. For high redshift objects, the continuum blue-ward of Lyα is also heavily absorbed by intervening absorption systems. Ultraviolet spectra of a few objects have been taken down to 550 Å (22.5 eV) with HST (Korista et al., 1992; Korista & Arav, 1997) and demonstrate that the continuum is still strong at this short wavelength. As discussed below, BAL QSO are relatively weak in soft X-rays (0.1-1 keV). It is likely that this is due to a high intrinsic column density along the line of sight.

Hamman et al. (1993) show that the BAL trough shapes are insensitive to the geometry of the BALR outflow, so it is difficult to distinguish between polar and disk configurations using the absorption line profiles. They also use the ratio of C IV emission to absorption equivalent widths, along with detailed modeling of scattered light from BAL outflows, to derive a conservative 20% upper limit to the global covering factor of the BAL region (Hamman et al., 1993). A low global covering fraction keeps the BAL from filling in with resonantly scattered photons. This suggests that BAL QSO appear as non-BAL QSO from most directions. However, there are ways to avoid this conclusion if the scattered photons are preferentially absorbed in some directions.

Weymann et al. (1991) find that the emission line properties of BAL QSO are quite similar to those of non-BAL QSO, and suggest that all radio quiet QSO contain a BAL outflow. However, they find small differences between BAL and non-BAL QSO emission lines which this does not explain. There is a 25% enhancement of N V emission relative to non-BAL QSO and a correlation between Fe II emission strength and BAL equivalent width. Hamman et al. (1993) suggest that the profile of the N V excess is too narrow to be

accounted for by resonance scattering in the BALR, and that the excess is due instead to anisotropic emission from the NV BEL clouds. The variation in line emission with viewing geometry might be caused by shadowing or limb-brightening effects.

The similarity of BAL QSO spectra to non-BAL QSO spectra is consistent with the hypothesis that most QSO have outflows and would show BAL if viewed along a line of sight intersecting the BALR. If this is true, then the mean global covering fraction of the BAL region must be about 10%, equal to the fraction of QSO that show broad absorption lines (Weymann et al., 1991). Selection effects could exclude or reduce the number of objects viewed from a given perspective and lead to an overestimate of the BALR covering fraction. This would occur if there was an obscuring torus blocking equatorial views or if dust or electrons in the BALR caused attenuation of the central source (Goodrich, 1997).

The relative position of the BELR and BALR along the line of sight can be inferred from the absorption of the BEL by the BAL. The N V λ1240 BAL usually cuts into the Lyα λ1216 BEL, and the C IV BEL is sometimes cut on the blue side by the C IV BAL. In troughs where the residual flux at the emission line location is reduced below the flux of the unabsorbed red side of the BEL, the blue wing of the BEL must be absorbed. This means that the BALR is at least partly external to or co-spatial with the BELR (Turnshek et al., 1988). In some cases, residual line emission is seen in troughs which are otherwise saturated (e.g., PHL 5200). This is due to incomplete coverage of the BELR by the BALR. Unless there is a fortuitous alignment, the size of the BELR must be larger than the size of an individual BAL cloud.

Some BAL velocity profiles provide strong evidence that radiative acceleration is important to the dynamics of BAL outflows. Radiative acceleration explains the "ghost of Lyα" seen in some C IV troughs (Arav et al., 1994) and perhaps the double trough phenomenon (Turnshek et al., 1988; Weymann et al., 1991). The Lyα emission line must provide a significant fraction of the radiation pressure to leave its imprint on the dynamics of the BAL outflow. Clouds which are in resonance with Lyα receive an extra push and are accelerated to higher velocities, leaving a dip in the optical depth profile. Another example of line-locking is seen among Si IV absorption systems in BAL QSO 1303+308 (Foltz et al., 1987). However, it seems unlikely that the low equivalent width Si IV BAL has an important influence on the dynamics of the flow.

Weymann et al. (1991) quantify the differences in BAL QSO troughs in terms of

their "balnicity" (trough equivalent width) and detachment (between emission line and absorption trough) indices. Troughs are also characterized by their multiplicity (number of sub-troughs per BAL) and velocity width. The variety of trough morphologies could either be due to intrinsic differences or differences in viewing angle and line-of-sight.

Multiple and detached troughs may indicate non-radial multiple BAL outflow components (Arav, 1996). It is difficult to understand these features in terms of a radial outflow, especially since the trough components do not appear to accelerate. The multiple components have been explained in terms of streamers which rise perpendicular to the accretion disk then are swept into a radial direction by radiation or ram pressure. It is also possible that there is some tangential deflection due to the centrifugal force of a rotating disk. In this model, a BAL QSO with troughs that start at zero velocity must be viewed on a near-equatorial line of sight which passes close to the foot points of the streamers.

1.3 BAL Trough Saturation

Determinations of BAL column densities usually assume that trough depth gives a direct measurement of BAL optical depth, but this is likely to be incorrect. Korista et al. (1992) find residual intensity in the Si IV trough of 0226-1024, even though a doublet ratio of unity indicates that the trough is optically thick. Arav (1997) also points out that the optical depths of the C IV, N V, and O VI troughs are identical within uncertainties. This coincidence is unlikely given the possible range of abundances of these ions. A number of objects (e.g., 0105-265) have smooth-bottomed, saturated troughs with a residual flux of about 10%. Keck HIRES observations of BAL QSO (e.g., 0226-1024, Barlow, 1994) have shown that the troughs are smooth and do not break up into narrower lines, so the residual intensity in saturated troughs is not a resolution effect.

What is the source of the residual flux in the troughs? Spectropolarimetry of 0105-265 and PHL 5200 by Cohen et al. (1995) shows that the residual flux is highly polarized, indicating a scattering origin. They suggest this could be light scattered by electrons or resonantly scattered in the BALR. It is often pointed out that the residual flux in the troughs is about 10%, which would be expected if the BALR has a 10% global covering fraction. In addition to scattered light, there may be direct contributions from the partially covered central continuum source and BELR. A similar effect is seen in associated absorption

systems (e.g., Barlow & Sargent, 1997).

Saturated BAL are useless for determining the column densities, ionization and abundances of the BALR. There is some hope of using the unsaturated portions of the troughs to perform this type of analysis (Arav, 1997). Great care must be taken because the local covering fraction of the continuum and BEL by the BALR is probably velocity dependent. Changes in optical depth can be mimicked by changes in local covering fraction. Past studies of BALR ionic abundances have ignored these effects, and typically give incredibly high metalicities (up to 200 times solar, Turnshek (1997)). Hamman (1998) suggests that the strength of the P V BAL in PG 1254+047 is due to high column densities instead of high metal abundance, and that the C IV trough must therefore be saturated.

Traditional limits on the column density, electron density and radial extent of the BALR argue for a small volume filling factor ($< 10^{-5}$) for BAL clouds (Weymann et al., 1985; Barlow, 1993). Such a small filling factor would require a confining wind or magnetic field to keep the BAL clouds from dispersing. The column density and electron density used in these estimates depend on the optical depths measured from saturated BAL. The estimated electron density also depends on the shape of the photoionizing continuum and distance from the central source, which are not well known. In addition, the radial extent of the BALR is not well constrained.

1.4 Continuum and Trough Variability

Variability has been detected in the troughs of several BAL QSO (Foltz et al., 1987; Turnshek et al., 1988; Barlow et al., 1989, 1992; Barlow, 1993). The trough depth can change by 10% on a time scale of one month in the QSO rest frame. Barlow (1993) monitored 23 objects over a period of 3 years (1 year, rest frame), and 15 of these showed significant variation in the BAL. Since most of these objects were only observed at two epochs, it is probable that all BAL troughs are variable.

Barlow et al. (1989) suggest that trough depth variations are due to changing ionization in response to continuum intensity variations. Because of the short recombination time, and the light travel time across the BALR, the continuum and trough variations in the line of sight appear to be nearly simultaneous. In most objects, the C IV trough depth decreases in response to an increase in the UV continuum (Barlow, 1993). This implies that the

C IV abundance falls in response to a high, increasing ionization parameter. However, the variation observed in the UV continuum is not nearly enough to account for the large changes in ionization parameter inferred from trough variability. The far UV continuum must be changing more than the continuum at 1000 Å.

While variability has been seen in BAL optical depth, variability has not been detected in the velocities of distinct trough components. Instead, all objects have preserved their unique trough velocity structures. The radial acceleration time scale of these features must be longer than 10 years (30 years in the observed frame). The lack of acceleration suggests that the main velocity components are from standing features in the BALR flow instead of discrete clouds. This is consistent with a non-radial outflow picture, where BAL flux tubes cross the line of sight. The time scale for variation in the velocity structure is then the time for the flow tubes to move across the line of sight. In this case, we would expect to see old components disappear completely and new ones appear at a different velocity.

There are cases where there is no apparent correlation between the trough and continuum variability. We suggest that in these cases, the trough variation is due to a variation in the BAL density, not in the photon flux from the central source. When blobs (density enhancements) of material flowing through a BAL flow tube cross the line of sight, the corresponding BAL sub-trough deepens. This idea can be tested by watching for the effect to propagate across a sub-trough. If the blob angular sizes are larger than the angular size of the central continuum source, then there will be a uniform dimming for most of the duration of the eclipse event. A much better sampling of BAL trough variation will be necessary to test this hypothesis.

Trough variability gives additional evidence for partial coverage of the central source. The deep portions of the C IV trough of CSO 203 must be saturated since they do not vary at all when the Si IV trough and the shallow portions of the C IV trough vary (Barlow et al., 1992). The residual flux at the bottom of the C IV trough is about 15%, indicating a local covering fraction of 85%.

1.5 Polarization

A survey of 142 bright QSO (Stockman et al., 1984) shows that the great majority (99%) have low polarization (LPQ, $P < 3\%$). While there are no large polarimetric surveys

of high-redshift QSO, the small number which have been observed appear to be LPQ as well (e.g., Antonucci et al., 1996; Impey et al., 1995). The small fraction of QSO with high polarization (HPQ, $P > 3\%$) are mostly blazars, which emit optical synchrotron light boosted by relativistic motion in a jet pointed close to the line of sight. There is one peculiar object, OI 287, a radio-loud quasar which shows high, steady polarization at a level of 7%. This object may be polarized by scattering in a thin accretion disk (Goodrich & Miller, 1988; Rudy & Schmidt, 1988). BAL QSO make up the remainder of the HPQ class, but not all BAL QSO are highly polarized. The source of BAL QSO polarization is the main concern of this thesis.

The source of polarization in LPQ is a subject of current debate (e.g., Webb et al., 1993). UV-optical emission from QSO (the big blue bump) is commonly thought to be dominated by thermal emission from an accretion disk (e.g., Sun & Malkan, 1989). It was originally predicted that emission from an accretion disk should be highly polarized (up to 12%) due to scattering (Lightman & Shapiro, 1975; Chandrasekhar, 1960). The polarization should also be perpendicular to the disk axis for an optically thick disk. When observations showed that the polarization of QSO is low and sometimes parallel to the radio axis, this weighed heavily against the standard accretion disk model.

Another prediction of the accretion disk model is that the Lyman edge (912 Å) should be seen in absorption in total and polarized flux. The absorption edge should be accompanied by a drop in polarization (e.g., Laor et al., 1990) since scattered rays should be more heavily absorbed than direct rays. Recent HST observations of QSO with partial Lyman edges do not show the expected effect. Instead, the UV polarization of some QSO rises steeply blue-ward of 800 Å (Koratkar et al., 1995).

Various de-polarizing mechanisms have been suggested, including Faraday rotation in a strong magnetic field, hydrogen absorption opacity, and gravitational lensing effects (Laor et al., 1990; Blaes & Agol, 1996). Antonucci et al. (1996) give a concise review of these and other schemes to reduce the UV polarization while maintaining the geometrically thin, optically thick accretion disk model. However, none seem to reproduce the observations. It has recently been suggested that there is no big blue bump (Mushotzky, 1997). UV observations by HST along with ROSAT soft X-ray observations show that the continuum may be better parameterized by a power law short-ward of 1000 Å (Laor et al., 1997).

It is likely that the UV emission from QSO is not emitted from a geometrically thin

accretion disk, since it lacks the predicted polarization. One possible alternative is emission from a puffed up ion torus. Such a source would be nearly spherically symmetric and have low polarization. The polarization we do see could come from scattering by material far from the central source, such as the BEL clouds.

It is useful to compare the polarization of quasars to that of radio galaxies. Antonucci (1984) finds that radio galaxies can be split into two classes based on their polarization properties. The first class consists of narrow-line radio galaxies (NLRG) with high polarization perpendicular to the radio axis. In these objects the central continuum source is obscured and the nuclear spectrum is seen in highly polarized scattered light. The second class consists of broad-line radio galaxies (BLRG) with low polarization. It has been claimed that the polarization is parallel to the radio axis (as expected from scattering in an optically thin accretion disk) in these objects, but recent high-quality spectropolarimetry (Cohen et al., 1998) casts doubt on this. The source of the low polarization in BLRG is not understood but is probably similar to the source of polarization in LPQ. The polarization of the broad emission lines is different from the polarization of the continuum in both LPQ and BLRG, suggesting that the scattering regions are close to the center in the low-polarization, type 1 objects, perhaps associated with the BELR.

It has been suggested that BAL QSO are more highly polarized than other QSO because they are viewed from the equatorial plane. This is based on a few highly polarized objects, and has not been rigorously tested. It is necessary to make a polarimetric survey of BAL QSO and non-BAL QSO at the same redshift to test this claim. Most polarimetric surveys of QSO are skewed to bright, low redshift objects, while BAL QSO are readily identified at redshifts $z \geq 1.6$, where the C IV BAL comes into the optical range. Our survey of BAL QSO improves the statistics of the BAL QSO polarization distribution, and we test the contention that high polarization is due to viewing angle in Chapter 4.

Spectropolarimetry has been published for a small number of BAL QSO (e.g., Stockman et al., 1981; Glenn et al., 1994; Goodrich & Miller, 1995; Cohen et al., 1995; Schmidt et al., 1997). These studies reveal that the BEL have lower polarization than the continuum. The continuum polarizations of BAL QSO rise slightly to the blue, and the polarized continuum flux can be represented by a smooth curve (e.g., Cohen et al., 1995). This thesis extends these results to a much larger sample of objects, and looks for systematics in the polarization properties of BAL QSO.

While scattering by electrons or dust is the most likely cause of polarization in BAL QSO, other sources are not completely ruled out. The other candidates are synchrotron emission and selective absorption by aligned dust grains. The synchrotron source would have to be steady, unlike the highly variable sources observed in blazars. Polarization by dust transmission is unlikely since it is typically accompanied by a large degree of reddening, which is not seen in most QSO.

1.6 Low-Ionization BAL QSO

A small subset of BAL QSO (10%) have (in addition to their high-ionization BAL) large equivalent width low ionization BAL such as those from the sodium-like ions Na I λ5894, Mg II λ2798, and Al III λ1858. These low-ionization BAL are also weakly present in most objects which are classified as high-ionization BAL QSO (e.g., Mg II absorption in PHL 5200). The distinction between low and high-ionization BAL QSO is therefore ill-defined.

The deep low-ionization troughs may simply be due to high column density instead of a low ionization parameter. Objects with high column density BAL show saturated Si IV and C IV troughs and moderately deep Al III absorption. There need not be any physical separation between the low and high ionization gas. Even in objects such as 0059-2735, where there appears to be a definite velocity difference between the low-velocity, low-ionization BAL systems and high-velocity, high-ionization BAL systems (Wampler et al., 1995), this could simply be due to saturation of the lines at low velocity. At velocities where C IV is unsaturated, absorption from the less abundant low-ionization species disappears.

While the distinction between high and low-ionization BAL QSO has been exaggerated, the difference in column densities may be connected to other observables. There appears to be a correlation between strong low-ionization emission and strong low-ionization absorption (Weymann et al., 1991). This suggests a physical association between the low-ionization BALR and BELR, but may also be due to a secondary correlation with viewing angle. Boroson & Meyers (1992) find the low-ionization BAL QSO in their sample to be unusually weak [O III] emitters. It is unknown if this is true of BAL QSO in general or just low-ionization BAL QSO. This does not necessarily rule out QSO unification scenarios since a large portion of the [O III] emission may be emitted anisotropically. The amount of reddening associated with the BALR is quite low, even in objects with strong low-ionization

BAL. However, there appears to be an excess of low-ionization BAL QSO among warm IR-selected QSO (Boroson & Meyers, 1992). This runs contrary to the unification hypothesis if the IR emission at 25 μm is emitted isotropically.

The differences between low and high column density BAL QSO could simply be due to viewing geometry. There are likely to be both random and systematic differences in BAL depth which depend on the line of sight through the BALR. This is hinted at in the complicated velocity structure of the BAL troughs in individual objects. We would expect the optical depth to increase towards the equator in models where the BAL is ablated off an accretion disk. On the other hand, there may be object-to-object intrinsic differences in the BALR optical depth. Perhaps these differences are related to the age of the QSO. Young objects might be in the process of expelling a dense cocoon of gas, while older objects have cleared this material away through radiation pressure. Distinguishing between the the intrinsic and geometric scenarios would require a comparison of the isotropic properties of large samples of high and low column density BAL QSO.

An even smaller fraction (1%) of BAL QSO show associated narrow absorption lines (NAL) from a variety of low-ionization species, including transitions from meta-stable states. These objects are sometimes referred to as Fe II Lo-BAL (Becker et al., 1997) because of the large number of Fe II NAL. The continuum emission in these objects is quite red, perhaps from extinction by dust (Sprayberry & Foltz, 1992). A large fraction of these objects have been discovered via the FIRST radio survey, which suggests that there is an observational bias against them in optical QSO surveys. This may be due to extinction and reddening.

Brotherton et al. (1997) present spectropolarimetry of two Fe II Lo-BAL objects (FIRST 0840+3633 and FIRST 1556+3517). The polarization of FIRST 0840+3633 is quite similar to that of high-ionization BAL QSO, dropping in the BEL and rising in the BAL. The polarization of FIRST 1556+3517 (the only known radio-loud BAL QSO) is extremely high (15% at 1800 Å). Unlike other BAL QSO, the emission lines are polarized and the polarization drops in the absorption troughs (see Chapter 4). This object is quite extreme in its properties, and its connection to other types of BAL QSO is unknown.

1.7 Radio Properties

About 10% of optically selected, high redshift QSO are radio-loud (Stocke et al., 1992). The distribution of the ratio of radio to optical flux (R) is bimodal, though there is some overlap between radio-loud and radio-quiet quasars (Kellermann et al., 1989) at the $\log R = 1$ dividing line. The physical mechanism which causes the dichotomy between radio-loud and radio-quiet quasars is currently unknown. Blandford & Znajek (1977) hypothesize that radio jets are powered by extraction of spin energy from a super-massive black hole. This mechanism requires a spinning black hole and a magnetized accretion disk. Wilson & Colbert (1995) suggest that only rapidly spinning holes formed by the merger of binary black holes have enough angular momentum to produce a highly collimated radio jet. This merger hypothesis could also explain why radio-loud quasars are only found in disturbed elliptical hosts. Radio-quiet quasars could be produced by less dramatic merger and accretion events which leave a slowly spinning black hole.

Stocke et al. (1992) find that optically-selected, high-ionization BAL QSO are exclusively radio-quiet, with radio/optical flux ratios $\log R < 1.0$. Conversely, there are no radio-loud objects with broad absorption lines (except for FIRST 1556+3517, a Fe II Lo-BAL). Objects with powerful radio jets do not contain BAL outflows, and vice versa. Because BAL QSO radio emission is so weak, there is little information on its spatial distribution. This makes it difficult to determine a fundamental symmetry axis for these AGN.

While there are no radio-loud BAL QSO, a large fraction (4/6) of radio-moderate ($0.2 < \log R < 1.0$) QSO in the sample of Francis et al. (1993) are BAL QSO. Note that neither the radio emission nor optical emission from QSO is isotropic and aspect-independent. Obscuration and beaming of the optical emission and beaming of the radio emission could all contribute to the excess number of radio-moderate BAL QSO, and may do so in concert. Goodrich (1997) suggests that the optical flux is suppressed in BAL QSO by scattering in the BALR. The opposite contention is that the radio flux is more highly beamed in BAL QSO than in other radio-quiet QSO. However, a simple beaming model over-predicts the number of radio-moderate QSO (Francis et al., 1993). If excess radio emission is an intrinsic property of some BAL QSO, then the BALR must have a large covering fraction in such objects.

1.8 X-ray Properties

The 0.2-2 keV X-ray spectra of bright, low-redshift QSO (BQS Survey) are well represented by a power law with $\alpha_x = 0.9 - 2.0$ (Laor et al., 1997). Laor et al. (1997) also find no evidence for a spectral break or soft X-ray excess. As discussed above, this runs contrary to the standard model of a thermal big blue bump powered by viscous dissipation in an optically thick accretion disk.

While about 50% of Seyfert galaxies show absorption features due to ionized warm absorbers, only $\sim 5\%$ of QSO show such features (Laor et al., 1997). For a larger sample of QSO with detected X-ray flux, Green et al. (1995) measure optical to X-ray indices in the range $\alpha_{ox} = 1.3 - 1.7$. There is a tendency for α_{ox} to increase with QSO luminosity. This may be due to enhanced absorption in the more luminous objects (Green, 1997b). BAL QSO are under-luminous in soft X-rays relative to non-BAL QSO, and most have lower limits of $\alpha_{ox} > 1.8$ (Green & Mathur, 1996; Green, 1997a). So if BAL QSO/non-BAL QSO unification is correct, then a large column of gas must hide the central X-ray source in BAL QSO. Green & Mathur (1996) suggest that the intrinsic (unabsorbed) X-ray spectra of BAL QSO and non-BAL QSO are similar since their UV emission line spectra are similar.

Only two BAL QSO have actually been detected in X-rays (both are in our polarization survey). PHL 5200 is bright enough for spectral observations with ASCA. Mathur et al. (1995) find a column density of $N_H = 1.3 \times 10^{23}\mathrm{cm}^{-2}$ in PHL 5200, with $\alpha_{ox} = 1.5$. Green & Mathur (1996) similarly derive a column of $N_H = 1.2 \times 10^{23}\mathrm{cm}^{-2}$ and $\alpha_{ox} = 1.98$ in 1246-0542 from the total hard X-ray counts, assuming an intrinsic $\alpha_x = 1.5$. These estimates of the column density also assume absorption by neutral gas with solar abundances, and should be increased if the gas is highly ionized. In contrast, typical estimates of the column density from the UV BAL are of order $N_H = 10^{20}\mathrm{cm}^{-2}$, for an ionization parameter $\log U = -1$ (Hamman et al., 1993).

The large discrepancy between the UV and X-ray determinations of N_H can be reconciled if the BAL gas is highly ionized and the UV BAL are saturated (e.g., Hamman, 1998). However, it is also possible that the UV and X-ray absorbers lie in separate zones and are only indirectly related. For example, the X-ray absorber could correspond to BEL clouds which shield the UV-absorbing BALR. It is important to establish the connection between the UV and X-ray absorbers. If the UV and X-ray absorption is caused by the same gas,

then X-ray measurements will give powerful diagnostics of the physical conditions in the BALR, including column density and ionization state (e.g., Mathur, 1994).

One way to test for the equivalence of the UV and X-ray absorbers is to search for a scattered soft X-ray component. If the absorbers are the same, we expect to see a 10% residual scattered flux at the saturated X-ray absorption edges, similar to the residual flux at the bottom of the BAL troughs. This will require much more collecting area than is available in current telescopes. An even more ambitious project would be to measure the polarization at the photoionization edges. This would help to distinguish between the electron scattering and resonance scattering models for the BAL trough polarization. The resonance scattering model predicts that the edges should be unpolarized, while the electron scattering model predicts that they should be polarized like the BAL troughs. X-ray polarimetry may also allow a distinction between electron and dust scattering.

1.9 Physical Models

The standard model that has emerged is that BAL QSO are normal radio-quiet QSO observed through an out-flowing disk wind. The most contentious aspect of this model is the filling factor and ionization of the wind. The two competing models are the clumpy and the smooth wind models. In the clumpy model, a spray of BAL cloudlets is ablated off the accretion disk and flows outward along and is confined by magnetic field lines. In the smooth model, a continuous wind of much higher column density and ionization flows from the disk. The smooth wind models are favored by recent X-ray observations and also are appealing because there is less of a problem with pressure confinement of the BAL clouds. While disk wind models are popular, there is still room for consideration of alternate geometries.

An accretion disk or torus of molecular gas provides a natural source for the BAL wind. However, the disk must be warped or flared so that its surface is exposed to the central continuum source. The BAL gas could then be ablated from the disk by UV radiation. A similar physical process has been observed in the Orion (Johnstone et al., 1996) and Helix nebulae, where a central FUV source evaporates gas from molecular gas condensations such as protoplanetary disks (proplyds). Similar processes are also seen in comets. The evaporated gas flows out from the reservoir at the sound speed and is ionized at an ionization front. Subsequently, radiation pressure (on ions and/or dust) drives the ionized gas away

from the central source, giving rise to cometary tails.

The continuous disk wind model proposed by Murray et al. (1995) is physically well motivated. However, it invokes a somewhat ad-hoc "hitchhiking" gas component to shield the outflow from soft X-rays. The hitchhiking gas is supposedly entrained by the outflow. However, it seems that the shield needs to be in place before the BAL plasma can be radiatively accelerated. It is possible that protrusions from the molecular disk could serve as shields and foot points of BAL streamers. Alternatively, dense stellar blobs would be naturally self-shielding. If the radiative acceleration is due mainly to dust (Scoville & Norman, 1995) instead of ions, then the ionization parameter is not as relevant to the dynamics.

The nature of the gas reservoir supplying the BALR outflow is unknown. Does it consist of many discrete sources such as proplyds, planets (Dar, 1997), AGB winds (Scoville & Norman, 1995), or novae (Shields, 1996) (stellar hypothesis); or is the reservoir the accretion disk or an obscuring torus? In the stellar hypothesis, we expect the sources (stars) to be distributed more or less isotropically around the central continuum source. In the disk/torus wind hypothesis, the outflow should be confined to the equatorial plane in the case of a thin disk or to some intermediate range of inclination for a torus. In all cases, the global covering factor must be $< 10\%$. Polarization can potentially be used to discriminate between the different viewing geometries since it depends on inclination angle. The BELR and BALR may derive from the same source so their properties may be intimately connected (e.g., Murray et al., 1995).

1.10 Organization of Thesis

This thesis addresses a number of questions about the structure and physics of BAL QSO. The primary observational goal is to determine the source of polarization. A large sample of objects is studied to address the distribution and wavelength dependence of BAL QSO continuum polarization as a function of spectral properties and determine if there is a common polarizing mechanism.

High S/N Keck observations are used to investigate the details of the polarization spectra and to study the structure and gas dynamics in BAL QSO. Multiple sources of polarized light in the spectra of active galactic nuclei (AGN) probe the structure along multiple lines

of sight. This makes it possible to constrain the spatial distribution of various components, including the central continuum source, broad emission line region (BELR), and broad absorption line region (BALR). The polarization variation across the BAL is used to study the geometry of the BALR as a function of velocity, giving clues to the dynamics of the outflow. The geometries of the scattering and broad absorption line regions are studied to discriminate between polar and equatorial outflows.

Spectropolarimetry of 20 BAL QSO with the W. M. Keck Telescope is presented in Chapter 2. The observational techniques are described in detail, and a brief description of the individual objects is given. In addition, the continuum polarization and equivalent widths of spectral features are tabulated.

Spectropolarimetry of 24 BAL QSO with the Hale Telescope is presented in Chapter 3. The observations and calibrations are discussed and continuum polarizations are tabulated. Individual objects are briefly discussed.

In Chapter 4 we investigate the continuum polarization properties of BAL QSO. We study the polarization distribution, and compare it to the polarization distribution of non-BAL QSO. A simple unification model and axisymmetric scattering geometry are used to explore the connection between BAL QSO and non-BAL QSO. We study the effects of dilution by broad Fe II emission on the wavelength dependence of the polarization and derive spectra of the unpolarized emission line components. We compare the wavelength dependence of the polarization with predictions for electron and dust scattering. The effects of opacity sources in the scattering medium are also considered. Finally, we tabulate the BEL and BAL equivalent widths in total flux and look for correlations with the continuum polarization.

In Chapter 5 we examine the polarization of the broad absorption lines and broad emission lines. We present polarization and equivalent width measurements for the BEL and BAL. We find and discuss evidence for resonance scattering and partial continuum coverage in a number of individual objects with high S/N. The amount of resonantly scattered polarized light is measured and used to estimate the global covering fraction of the BALR. The implications of our polarimetry for the structure of the BELR, BALR, and scattering regions are explored. The dynamics of the BALR are also studied using the velocity dependence of the polarization in the BAL troughs.

Chapter 6 summarizes the results of this thesis, and puts them in the context of models

of the structure of the BELR and BALR. Finally, we suggest further experiments which would increase our knowledge of the structure and physics of QSO.

Chapter 2 Keck Spectropolarimetry

We observed 20 BAL QSO with the W. M. Keck 10 m telescopes. The objects were selected primarily (15/20) from the sample of Weymann et al. (1991). Our Palomar BAL QSO survey was used to select objects with detectable polarization for re-observation at higher S/N with Keck. However, the Palomar survey was not finished until after the Keck survey, which means that a few polarized objects were omitted from the Keck sample. Other objects not in the Palomar survey were selected for observation at Keck because they are bright or have high polarization.

A summary of the observations is given in Table 2.1, including IAU and alternate designation, redshift, visual magnitude, UT date, exposure time, and spectrograph slit position angle. Total exposure times range from 1 to 6 hr, for an average of 2.2 hr per object. Results for 0105-265 and PHL 5200 are presented by Cohen et al. (1995), but are discussed in additional detail in this thesis.

2.1 Spectroscopy

Spectropolarimetry was taken with the Low Resolution Imaging Spectrograph (LRIS, Oke et al., 1995) and polarimeter combination. A 300 groove/mm grating with a dispersion of 2.49 Å per pixel gave a resolution of 10 Å. This translates into a velocity resolution of 600 km/s in the C IV λ1549 BAL for a QSO at redshift $z = 2.2$. Hence the C IV doublet separation of 500 km/s is unresolved in our spectra. This resolution is sufficient for studying the polarization of the broad emission lines and troughs in BAL QSO, which typically span 10,000-30,000 km/s. Higher resolution spectropolarimetry is only useful for the brightest QSO ($V < 17.0$) since it requires a S/N per spectral bin of at least 100 to detect polarization at the level of 1%.

The detector is a 2048×2048 pixel charge coupled device (CCD) manufactured by Tektronix. It has an inverse gain of 2 electrons per data number and a read noise of approximately 6 electrons. The maximum efficiency of the spectrograph plus CCD combination is approximately 40% at the blaze angle of the grating.

IAU	Name	z	Mag	UT date	t(sec)	PA	
0019+0107	UM 232	2.123	17.7	07 29 95	6240	315	
				12 15 95	6000	35.4	
0043+0048	UM 275	2.146	18.4	10 29 94	10800	305	np
0059−2735		1.593	18.0	12 30 94	6240	20	
				07 28 95	6240	0	
0105−265		3.488	17.3	08 03 94	3600	0	
				10 28 94	3600	0	
				11 06 94	3600	33.4	np
0137−0153	UM 356	2.234	17.8	12 17 95	6000	227	np
0146+0142	UM 141	2.892	17.7	11 06 94	3600	60.6	np
				12 15 95	4800	50	
0226−1024		2.256	16.9	12 31 94	6000	45	
				10 05 96	7200	181.5	
				10 06 96	7200	181.5	np
07598+6508	IRAS	0.148	14.5	01 28 95	2400	45	
0842+3431	CSO 203	2.130	17.3	11 06 94	3600	270	np
				12 17 95	6000	160	np
0856+1714		2.327	18.9	11 07 94	3600	283	np
0903+1734		2.773	17.4	04 17 96	4800	90	
0932+5006		1.911	16.9	12 15 95	6000	215	
1212+1445		1.626	17.4	05 19 96	7200	0	np
1235+0857		2.887	17.5	05 20 96	3600	50	np
1246−0542		2.226	16.4	12 30 94	7050	315	
1331−0108	UM 587	1.874	17.2	05 19 96	1680	57	np
1333+2840	RS 23	1.910	18.7	01 28 95	4800	270	
				04 17 96	6000	100	
1413+1143	Cloverleaf	2.545	16.8	05 19 96	3600	68	np
1524+5147	CSO 755	2.88	17.0	04 17 96	3600	132	
2225−0534	PHL 5200	1.980	17.9	08 03 94	3600	180	
				10 28 94	3600	35	

Table 2.1: Keck observation log. The columns are 1) IAU designation, 2) Name, 3) redshift, 4) visual magnitude, 5) date, 6) exposure time, and 7) spectrograph slit PA. Non-photometric nights are marked "np," indicating clouds or fog. Data for columns 3 and 4 are primarily from the NASA Extragalactic Database (NED).

The spectra cover the observed wavelength range of 3800-8900 Å. This corresponds to the rest wavelength range between Lyα and Mg II λ2798 for a $z = 2.2$ QSO. The C IV λ1549 line is the most useful for our study because the BAL is typically deep enough to show a large polarization signature and it is well isolated from other emission and absorption lines, including intervening Lyα absorption systems. There is some possibility of confusion from intervening Mg II and Fe II metal line absorption systems, which are apparent in at least ten of our sample objects; but these always have equivalent widths which are much smaller than the BAL equivalent width. The C IV BAL is visible in all but two of our objects, which are at redshifts $z < 1.6$ and display absorption from low-ionization species.

Slit widths of 1 and 1.5 arc seconds were used to match the atmospheric seeing, and the pixel scale was 0.2 arcsec/pixel. The useful slit length is only 30 arcsec in LRIS polarimetry mode because of vignetting by the beam splitter. We expect that the contribution of extended emission from the narrow line region and starlight from the host galaxy within the slit aperture is negligible. There are a few cases where foreground galaxies serendipitously fell in the slit, but they were never close enough to the BAL QSO to contaminate its spectrum (except for the galaxy which lenses 1413+1143). Indeed, there is no evidence for narrow emission lines or stellar photospheric lines in any of our spectra. The relatively narrow slit widths along with variable seeing conditions yield large uncertainties in the absolute photometry, however we are only interested in relative fluxes.

The spectrograph slit was set at the mean parallactic angle for most observations. This resulted in a minimum loss of light from differential atmospheric refraction. However, the differential slit losses were still significant–up to 20% between the blue and red ends of the spectra. This is seen in the ratio of spectra taken at different epochs. Without large aperture photometric data, we can not correct for differential refraction in our spectra. It is important to consider this uncertainty when analyzing the color of the flux spectra, but it does not affect the polarization.

The slit orientation on the sky was held constant during each set of observations to avoid mixing the Stokes parameters. Because the Keck Telescope has an altitude-azimuth mount, this was accomplished by rotating the spectrograph. Observations were scheduled to avoid close passage to the zenith, where the telescope has difficulty tracking reliably. When multiple observations were taken over the span of several hours, the slit PA was set to the parallactic angle at the midpoint of the series of observations. All observations of an

object on the same night were taken at the same slit PA to allow co-addition of multiple sets. When observations from different nights were taken with different slit PA, the Stokes parameters were averaged after calibration to the sky coordinate system.

2.2 Polarimetry

The performance of the LRIS polarimeter and the robustness of the reduction techniques are discussed by Cohen et al. (1997). The polarimetry module is inserted directly below the slit mask in the spectrograph. It is a dual-beam instrument which separates and simultaneously measures two orthogonal polarization senses using a calcite beam splitter. The beam splitter is a modified Glan-Taylor prism using blocks of Ultran-30 for focus equalization in the two beams (Goodrich, 1991; Goodrich et al., 1995). The spectra of the two beams are recorded side by side on the CCD chip. Simultaneous measurement of the ordinary and extraordinary beams nearly eliminates the effects of atmospheric transparency and seeing variations on the calculated Stokes parameters.

The second active component of the polarimeter is a half-wave plate. The half-wave plate has a retardance of 180 degrees and serves to reflect the polarization vector about the fast axis. Rotating the half-wave plate 45 degrees rotates the PA of the input electric vector by 90 degrees. This swaps the ordinary and extraordinary beams, allowing a correction for the gain difference along the two optical paths and for the gain difference at two locations on the CCD chip. Rotating the half-wave plate by 22.5 degrees allows an independent determination of the Stokes parameters (Q, U). A complete set of observations is taken at four half-wave plate settings (0, 45, 22.5, and 67.5 degrees). This yields eight spectra (one per beam) which are used to compute the flux (F) and Stokes parameters.

The Stokes parameters (Q, U) completely characterize the linear polarization. The circular polarization, given by the Stokes parameter V, is negligible for QSO. If the intensities of the ordinary and extraordinary rays are X and Y, respectively, then the total flux and normalized Stokes parameters are given by

$$F = X_0 + Y_0 = X_{45} + Y_{45} = X_{22.5} + Y_{22.5} = X_{67.5} + Y_{67.5} \tag{2.1}$$

$$Q = \frac{X_0 - Y_0}{F} = \frac{Y_{45} - X_{45}}{F} \tag{2.2}$$

$$U = \frac{X_{22.5} - Y_{22.5}}{F} = \frac{Y_{67.5} - X_{67.5}}{F} \tag{2.3}$$

where the subscripts give the position angle of the half wave-plate. Note that we measure Q and U twice each, and take the average of the two measurements. However, these two measurements are not independent, since they are used to compute the gain ratios between the beams.

The above equations assume that the instrumental gains are equal for the two beams and the atmosphere doesn't vary. In practice, the fluxes X and Y are corrected for the geometric mean G of the gain ratio between the two beams and the ratio of atmospheric transparencies Ω. For the Q observations (and similarly for U),

$$G = \sqrt{\frac{X_0 X_{45}}{Y_0 Y_{45}}} \tag{2.4}$$

$$\Omega = \sqrt{\frac{X_0 Y_0}{X_{45} Y_{45}}} \tag{2.5}$$

The fractional polarization P and position angle PA of the electric vector are computed from the Stokes parameters via

$$P = \sqrt{Q^2 + U^2} \tag{2.6}$$

$$PA = \frac{1}{2} \arctan(U/Q) \tag{2.7}$$

Measurements of (Q, U) and the derivative quantities fractional polarization and position angle (P, PA) are subject to a number of biases when the number of photons is small (Clarke et al., 1983; Naghizadeh-Khouei & Clarke, 1993). P is a positive definite quantity, and therefore does not obey Gaussian statistics. Q and U do obey Gaussian statistics, except at very low S/N. It is therefore preferable to rotate (Q, U) by a fit to the continuum PA curve instead of calculating a de-biased P (Simmons & Stewart, 1985). This is only

possible when the PA is a slowly varying function of wavelength. Where there are PA rotations across the emission and absorption lines, the polarization will be underestimated by this method; then it is necessary to inspect both Q and U to determine the line polarization.

2.3 Data Reductions

Data reductions were done on a SUN Sparcstation with VISTA[1] image processing software. Cosmic ray events were eliminated interactively from the CCD frames using a 5×5 median filter. Pixels which deviated by more than 3σ were rejected and replaced by the median value. It was often necessary to iterate this procedure to eliminate cosmic rays with long tracks that covered several pixels. It was sometimes impossible to remove cosmic ray tracks which fell on the object spectra, and these are flagged in the spectra as "hits." Noise introduced by cosmic ray events is a serious problem at the Keck Observatory, perhaps due to its high altitude. To help identify and mitigate contamination from cosmic rays, the observations were typically split into two sets.

The CCD frames were de-biased using an average value from the over-scan region of the CCD image. The bias voltage level of the CCD amplifier was typically 1000 data numbers (DN). No corrections were made for dark current since the thermal noise in the liquid nitrogen cooled CCD dewar is negligible.

All object frames were divided by a flat field to remove small spatial variations in the CCD response. Flat field corrections help ensure proper sky subtraction and flux calibration. Note that in the case of negligible sky background, the flat field cancels out of the equation for the Stokes parameters, which involves the ratio of fluxes. Hence the polarization is quite insensitive to flat-fielding. However, accurate flat-fielding is necessary for accurate relative flux calibration. Series of flat fields were generated using a halogen lamp internal to the spectrograph. Though the illumination of the spectrograph by the internal lamps is slightly different from the sky illumination, this effect is small and outweighed by the convenience of internal flats. A median of several flat field exposures was taken to provide a high S/N flat devoid of cosmic-ray features. The final flat was divided by a polynomial fit along the spectral direction to remove slow variations due to the spectrum of the halogen lamp.

The object spectra were extracted using 3-6 arcsec wide windows centered along a spline

[1]VISTA was originally developed by R. J. Stover and T. R. Lauer in 1982. It is primarily used at Lick Observatory. The current version is maintained by John Holtzman (email holtz@nmsu.edu).

fit to their centroids on the CCD chip. The width of the window was chosen to include most of the flux, as judged by eye from cross-cuts of the spectra. The centroids tend to wander, probably due to spectrograph flexure, over the course of a night. Night sky spectra were extracted from windows on both sides of the object window, averaged, scaled, and subtracted from the object spectra. Noise spectra were calculated from the photon statistics of the object and sky spectra. The flux and noise spectra from the eight beams for each set of observations were used to compute the Stokes parameters and their uncertainties. The propagated noise spectra agree well with the pixel-to-pixel variance, and we are confident in their accuracy.

Spectra were wavelength calibrated and re-binned to a linear scale before computing the Stokes parameters. We used Ne, Ar and Hg+Kr internal lamps to determine the wavelength scale. We typically used a third order polynomial fit to the wavelengths of a large number of arc lines to characterize the scale. Unfortunately, there are few arc lines at the blue end of our spectral range (3800-5000 Å), so the relative uncertainty in the scale is somewhat larger (up to 0.1 Å) there. However, this is completely adequate given the low resolution of our spectra and the broad width of QSO lines. Spectra were also corrected for zero-point offsets due to spectrograph flexure using the night sky spectra.

All spectra were de-redshifted using the nominal redshift values given in Table 2.1, and the flux spectra were binned by 5 Å (rest) before calculating the Stokes parameters. Binning fluxes first reduces the biases that can be introduced by noisy data and enhances the signal-to-noise ratio S/N of the Stokes parameters. The total flux spectra are presented un-binned to show maximum spectral resolution.

2.4 Flux Calibrations

Flux spectra were corrected for extinction using the prescription of Hayes (1970). We used an average extinction curve for Mauna Kea, measured at UKIRT (Beland et al., 1988). There were often variable cirrus clouds, so the absolute flux calibration of the spectra are generally only good to within 50%.

Flux calibrations were made using spectrophotometric standards (Oke, 1990). The standards are hot stars with substantial flux at 3800 Å and weak photospheric absorption lines. The standards had to be dim enough not to saturate the CCD in a 1 second exposure

time. We interpolated over stellar and atmospheric absorption features in the standard and observed flux curves then took the ratio to get the flux calibration curve. The final curves were smoothed by 20 wavelength bins to increase the S/N.

BAL QSO observations were taken without an order-blocking filter, and there may be contamination by second-order blue light red-ward of 7000 Å. The magnitude of this effect (Putney & Cohen, 1996) is less than 1.8% of the flux at the blue end of the spectrum (3500-4500 Å). All flux standards were observed both with and without a GG-495 order-blocking filter to avoid contamination by second-order light in the flux calibration curve. This was necessary because the contamination can be large in the hot, blue flux standards.

Contamination due to second order light in the BAL QSO is minimal. The continua are not nearly as blue as in the flux standards, rising less than a factor of 3 over the observed wavelength range. This translates to an error of 5% in flux at the red end of the spectrum of the bluest object. Since the polarization in BAL QSO rises to the blue (Chapter 4), this could lead to a polarization error of 0.082%. There is a potentially larger effect from the Lyα emission line showing up in second order at 2432 Å. This falls in a fairly uninteresting region of the spectrum, away from major emission and absorption lines.

Flux spectra were corrected for atmospheric absorption in the telluric bands (O_2 A, B, and γ; and H_2O), using templates derived from the flux standards. The absorption templates were scaled and smoothed to give the best correction. Scaling in the range 0.9-1.1 was typical and served as an adjustment for changing atmospheric conditions.

2.5 Polarization Calibrations

UV and IR polarizers were used to determine and correct for the position angle (PA) rotation of the half-wave plate fast axis with wavelength. This required observations of a bright star through the polarizers, which induced nearly 100% linear polarization at a constant PA. The half-wave plate is super-achromatic (Goodrich, 1991), designed to give a retardance close to 180 degrees over a large wavelength range. However, this design introduces a wavelength-dependent rotation into the instrumental PA curves with amplitude ± 4.8 degrees. The PA correction curve (Figure 2.1) was measured on several occasions and averaged to obtain a curve with relative uncertainty of < 0.2 degrees at all wavelengths. All observations were corrected by a spline fit to this average curve.

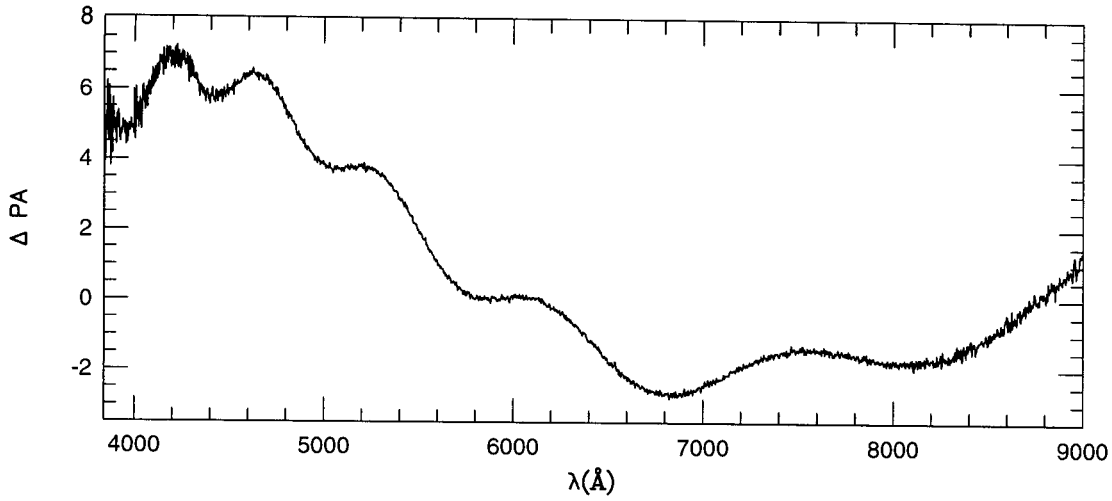

Figure 2.1: Keck PA calibration curve, showing rotation of the half-wave plate fast axis with wavelength.

The PA of the electric vector is measured from north to east. The PA offset between the half-wave plate coordinate system and the sky coordinate system was determined for each run using polarized standard stars. We used HST standards from the list of Schmidt et al. (1992), who use scattered moonlight as their primary PA standard. B and V-band polarizations of the standards were measured by averaging over the bands 3950-4900 Å and 5050-5950 Å, respectively. Some of the standards show curvature in their PA spectra, amounting to 1-2 degrees over the range 3800-8900 Å. The PA variation within the B or V band is less than 0.5 degrees, and the error introduced by not considering the shape of the Johnson filter curves is less than 0.2 degrees. In principle, the B and V band PA could be computed more accurately if we had the instrumental response curves for the Schmidt et al. (1992) observations.

It was necessary to establish a set of secondary and tertiary standards which were dim enough to view with the Keck Telescope and covered the sky. We have listed our polarized standard stars in Table 2.2. The PA values of the tertiary standards were set by minimizing the difference between PA offsets determined from all secondary standards over a number of observing runs. The absolute PA calibration is internally consistent to ± 0.6 degrees. This is commensurate to random uncertainties as large as 0.4 degrees published for the secondary standards. All of our standards have polarization curves approximated by a Serkowski et al. (1975) function, indicating an interstellar and not an intrinsic origin

Star	Band	$P\%$	σ	PA	σ
HD 155528	V	5.00	0.17	92.61	0.37
HD 245310	B	4.38	0.004	145.97	0.40
VI Cyg 12	V	9.16	0.06	116.41	0.13
Hiltner 102	V	5.18	0.10	73.20	0.80
HD 251204	V	4.98	0.05	151.60	....

Table 2.2: Polarized standard stars. The mean Keck polarization and PA measurements of standard stars are given in columns 3 and 4. No PA uncertainty is listed for HD 251204, because it was observed on only one occasion.

Star	Date	$Q\%$	$U\%$
G191B2B	12 94	0.052	0.009
	12 95	-0.050	-0.045
	10 96	0.002	0.037
BD +28 4211	7 95	-0.069	-0.079
	10 96	0.033	-0.111
BD +32 3739	7 95	0.057	-0.096
mean		0.004	-0.048
σ		0.05	0.06

Table 2.3: Null polarization standard stars. Three null standards were observed on a number of observing runs. We list the Stokes Q and U parameters, which are typically $< 0.1\%$.

for their polarization. Interstellar polarization is unlikely to be variable since it is the integrated effect of a long column of Galactic dust. We excluded standards which appear to show polarization variability from our calibration set. Another potential source of error is precession of the celestial coordinate system, which can amount to 1 degree in 100 years (Hsu & Breger, 1982).

Null polarization standards (Schmidt et al., 1992) were observed on several occasions (Table 2.3), and were always found to be null to within 0.1% (4000-7000 Å). The standard deviation of all null observations was (σ_Q, σ_U)= (0.05%, 0.06%). There was no evidence for systematic instrumental polarization effects, so no instrumental polarization correction was required. The lack of instrumental polarization indicates near-perfect alignment and uniform reflectivity of the primary and secondary telescope mirrors.

A prevalent concern in polarimetry is contamination of the Stokes parameters by foreground and intervening dust. Polarization can be induced by selective absorption by mag-

netically aligned dust grains. Interstellar dust polarization in the Galaxy should have only a small effect on the Stokes parameters since all objects have a Galactic latitude of $b > 30$ degrees. Table 2.4 gives the Galactic latitude for each object in the Keck and Palomar samples. The maximum interstellar polarization P_{max} was estimated using the prescription of Serkowski et al. (1975) and the extinction values of Burstein & Heiles (1984), which are listed in NED[2]. We used the formula $P_{max} = 9E(B-V) = (9/4)A_B$ to convert from extinction values to polarization. The maximum expected interstellar polarization is typically less than 0.2%.

We also list the polarization P_s, position angle PA_s, distance d, and separation $d\theta$ of the closest field star within 5 degrees of each QSO from Matthewson & Ford (1970). This is at best a crude estimate of the interstellar polarization in the direction of the QSO. Some of these stars are too close to the observer to sample the total dust column in the Galactic disk. Ideally, we would like to take spectropolarimetry of several stars within a few arc minutes of the QSO which have large spectroscopic distances (> 0.5 kpc). Then it would be possible to make a reliable correction for the interstellar polarization. The number of observations required for this would be prohibitively large and impractical for this thesis. We consider any measured QSO polarization greater than 0.2% to be intrinsic to the QSO. However, we also investigate the possibility of interstellar contamination in objects which show rotation of the electric vector PA with wavelength (Chapter 4).

Another possible source of dust polarization is the interstellar medium of intervening galaxies. Many of the BAL QSO in our sample show intervening metal absorption line systems. Typically, the impact parameter of these systems is large, so we don't expect a large amount of extinction and associated dust polarization. QSO with damped Lyα absorbers at small impact parameters typically have an extinction at 1500 Å of $A < 0.1$ magnitudes (Pettini et al., 1997). We expect even less extinction and negligible interstellar polarization from the lower column density metal absorption line systems. However, 1413+1143 is lensed by a foreground galaxy, so dust absorption by the lensing galaxy may be a consideration.

[2]NED is the NASA Extragalactic Database, operated by IPAC.

IAU	Name	b	$P_{max}\%$	$P_s\%$	PA_s	d(kpc)	$d\theta$
0019+0107	UM 232	-60.6	0.11	0.11	96.6	0.100	0.97
0021−0213		-64.0	0.18	0.25	113.6	0.087	0.22
0025−0151		-63.8	0.18	0.25	113.6	0.087	0.96
0043+0048	UM 275	-61.8	0.02	0.29	78.4	0.229	3.02
0059−2735		-87.6	0.18	0.10	133.3	0.115	2.26
0105−265		-86.2	0.05	0.10	133.3	0.115	3.90
0119+0310		-58.6	0.09	0.08	156.6	0.229	0.67
0137−0153	UM 356	-61.9	0.11	0.08	128.5	0.182	1.52
0145+0416	UM 139	-55.5	0.25	0.30	128.4	0.316	1.60
0146+0142	UM 141	-57.7	0.00	0.30	128.4	0.316	3.31
0226−1024		-61.6	0.02	....	.....	.....	....
07598+6508	IRAS	32.1	0.32	....	.....	.....	....
0842+3431	CSO 203	37.5	0.18	....	.....	.....	....
0846+1540		32.9	0.20	0.02	35.0	0.063	2.82
0856+1714		35.7	0.11	0.02	35.0	0.063	3.78
0903+1734		37.5	0.16	0.03	86.0	0.016	2.81
0932+5006		46.5	0.07	0.01	115.0	0.017	1.94
1011+0906		48.5	0.07	0.06	82.7	0.066	1.80
1212+1445		74.7	0.27	0.03	116.0	0.052	0.58
1231+1320		75.4	0.11	0.05	74.0	.....	2.80
1232+1325		75.5	0.14	0.05	74.0	.....	2.91
1235+0857		71.3	0.00	0.02	39.0	0.060	1.88
1235+1453		77.1	0.11	0.22	76.0	.....	2.47
1243+0121		63.9	0.00	0.22	76.0	.....	2.47
1246−0542		56.9	0.09	0.26	45.9	0.380	2.25
1331−0108	UM 587	59.7	0.11	0.04	9.0	0.029	0.81
1333+2840	RS 23	80.0	0.00	0.08	104.0	.....	1.11
1413+1143	Clover	64.8	0.00	0.10	57.0	0.105	1.41
1442−0011		51.2	0.29	0.15	91.0	0.035	2.33
1443+0141		52.5	0.27	0.05	78.0	0.036	0.44
1524+5147	CSO 755	52.1	0.07	....	.....	.....	....
1700+5153	PG	37.8	0.05	....	.....	.....	....
2154−2005		-49.6	0.09	0.09	6.5	0.229	1.42
2201−1834		-50.6	0.16	0.08	175.9	0.437	1.29
2225−0534	PHL 5200	-49.6	0.38	0.44	160.5	0.087	2.23
2350−0045A		-59.9	0.27	0.10	128.9	0.060	2.59

Table 2.4: Interstellar polarization. Columns 3 and 4 give the Galactic latitude b and upper limit to the interstellar polarization P_{max}. P_{max} is computed from the Galactic extinction as described in the main text. Columns 5 and 6 give the polarization P_s and electric vector PA_s of a nearby interstellar probe star. The probe star distance d (in kpc) from the observer and angular distance $d\theta$ (in degrees) from the BAL QSO is given in Columns 7 and 8.

2.6 Continuum and BAL Polarization Measurements

Table 2.5 lists the continuum polarizations for the Keck BAL QSO sample. We measured the continuum polarization in two narrow wavelength bands (1600-1840 Å and 1960-2200 Å, rest) and one broad wavelength band (4000-8600 Å, observed). The narrow bands are on either side of the C III] λ1909 emission line, where the contamination from Fe II and other emission lines is relatively low. The broad-band measurements in the observed frame are presented for comparison with "white light" polarization values in the literature. The polarization P was estimated by rotating the Stokes parameters by the angle $2PA$, determined from a cubic spline fit to the PA curve. (The Stokes parameters become $(Q' = P, U' = 0)$ in the rotated coordinate system.) P was then averaged over the appropriate pixels in the spectrum, which introduced negligible bias in the high S/N continuum observations. The mean broad-band PA is listed in column 9. Objects with significant PA rotations in the continuum are indicated by an "r" in the last column. Polarization values are given as percentages and PA values are given in degrees.

BAL polarization values are listed in Table 2.6. The velocity, rotated Stokes parameters, and PA rotations were determined at the point in the trough at which Q' is a maximum. For most objects, the PA in the trough agrees with the PA in the continuum to within the measurement uncertainties. Therefore the rotated Stokes parameter Q' is a good estimate of the polarization P. The listed trough polarization values and uncertainties are for 5 Å bins. Binning inevitably reduces the peak trough polarization, but provides a more reliable value because of reduced noise (see Chapter 5).

Small but significant PA rotations are seen in the BAL troughs of 0226-1024, 1246-0542, and 1524+5147. PA rotations are seen in the troughs of other objects after averaging over several bins. PA rotations in the BAL are of interest because they indicate an asymmetry in the geometry of the BALR relative to the continuum scattering region. In general, the peaks in Q' and U' can be at different trough velocities. However, since there is a tendency for the polarization to peak where the trough is the deepest, Q' and U' usually peak at similar velocities. The error made in estimating the trough polarization from Q' is less than 0.2% for most objects because the PA rotations are small. In objects where the BAL PA rotates by more than 10 degrees, both Q' and U' must be inspected for a full description of the trough polarization (e.g., 1413+1143, Chapter 5).

IAU	Name	$P_1\%$	$\pm$	$P_2\%$	$\pm$	$P_c\%$	$\pm$	PA	$\pm$	
0019+0107	UM 232	0.94	0.03	1.10	0.03	0.98	0.02	35.0	0.5	r
0043+0048	UM 275	0.05	0.04	0.11	0.04	0.11	0.06	.....	...	
0059−2735		1.58	0.10	1.62	0.06	1.49	0.02	171.2	0.3	
0105−265		1.45	0.05	....	....	2.41	0.08	134.8	1.2	
0137−0153	UM 356	1.06	0.07	0.81	0.08	1.09	0.05	56.0	1.3	
0146+0142	UM 141	1.12	0.03	1.15	0.08	1.24	0.02	133.1	0.5	
0226−1024		1.80	0.02	1.73	0.02	1.81	0.01	167.1	0.2	
07598+6508	IRAS	....	....	....	....	1.709	0.005	123.05	0.08	r
0842+3431	CSO 203	0.52	0.02	0.55	0.03	0.51	0.01	27.1	0.6	
0856+1714		0.88	0.13	0.91	0.10	1.02	0.10	165.7	2.8	
0903+1734		0.52	0.04	0.44	0.05	0.67	0.02	62.9	0.6	
0932+5006		1.20	0.02	1.19	0.03	1.11	0.02	168.7	0.5	r
1212+1445		2.05	0.06	1.88	0.06	1.49	0.03	17.3	0.6	
1235+0857		2.76	0.06	2.65	0.09	2.53	0.07	25.1	0.7	
1246−0542		1.31	0.02	1.11	0.02	1.26	0.01	132.4	0.1	
1331−0108	UM 587	1.76	0.13	1.55	0.09	1.56	0.14	33.8	2.2	
1333+2840	RS 23	5.41	0.11	5.61	0.07	4.67	0.02	161.5	0.1	
1413+1143	Clover	1.49	0.04	1.24	0.08	1.52	0.04	55.7	0.9	
1524+5147	CSO 755	3.56	0.03	3.42	0.05	3.49	0.01	98.6	0.1	
2225−0534	PHL 5200	4.98	0.05	4.63	0.06	4.26	0.02	162.0	0.2	r

Table 2.5: Keck continuum polarization measurements. P_1 and P_2 are the continuum polarization measurements in two narrow wavelength bands (1600-1840 Å and 1960-2200 Å, rest) to either side of C III] λ1909. P_c and PA are the broad-band (unfiltered) polarization and PA (4000-8600 Å, observed). Objects with significant continuum PA rotations are indicated with an "r." Uncertainties are listed as standard deviations of the mean within the given band. They are are slightly larger than the formal uncertainty from photon statistics, due to polarization variation within the wavelength bands. There is no measurement of P_1 or P_2 for 07598+6508 because of its low redshift, and no measurement of P_2 for 0105-165 because of its high redshift. UM 275 is unpolarized, so we list $P = \sqrt{Q^2 + U^2}$ instead of $P = Q'$; and the PA is highly uncertain, so we don't list it.

IAU	Name	v_{max}	$Q'\%$	$\pm$	$U'\%$	$\pm$	dPA	
0019+0107	UM 232	-9500	4.8	1.1	0.5	1.2	-3	
0059−2735		-2500	4.3	1.6	-1.5	1.7	-10	r
0105−265		-12400	10.5	3.3	-0.9	3.5	-2	r
0137−0153	UM 356	-5600	6.5	3.8	2.3	3.9	10	
0146+0142	UM 141	-16300	4.3	1.3	-1.2	1.3	-8	r
0226−1024		-10500	7.3	1.4	1.9	0.7	7(3)	r
0842+3431	CSO 203	-10500	2.9	0.7	-1.0	0.7	-9	r
0856+1714		-8500	8.0	6.5	1.3	6.4	5	
0903+1734		-12400	5.2	2.5	2.7	2.5	14	
0932+5006		-14300	2.7	1.2	-0.2	1.3	-2	
1212+1445		-11400	4.3	1.6	-2.6	1.8	-16	r
1235+0857		-4600	3.3	1.5	0.5	1.5	4	
1246−0542		-15300	6.3	0.3	-1.3	0.4	-6(2)	r
1331−0108	UM 587	-3700	9.0	11.8	-8.0	11.0	-21	
1333+2840	RS 23	-4600	8.5	1.6	1.3	1.6	4	r
1413+1143	Clover	-5600	11.5	8.5	12.3	10.4	23	r
1524+5147	CSO 755	-12400	6.0	0.4	-1.3	0.4	-6(2)	r
2225−0534	PHL 5200	-8500	10.1	1.9	-1.5	1.9	-4	r

Table 2.6: C IV BAL trough polarization. The peak trough polarization Q' is measured in the C IV trough (1400-1549 Å), except for 0059-2735 (Mg II). U' is listed for the velocity v_{max} where Q' peaks. v_{max} is measured with respect to the peak of the C IV BEL. The formal uncertainties are calculated from photon statistics. dPA is the difference (in degrees) between the trough and continuum PA, measured at the polarization peak. Significant BAL PA rotations are flagged with an "r."

2.7 Polarimetry–General Results

The polarization in BAL QSO is stronger than in non-BAL QSO, but is weak in absolute terms. Most of the 20 BAL QSO in our Keck sample have moderate (for QSO) continuum polarizations ($P_c = 1 - 3\%$). There are only 3 highly polarized QSO (HPQ, $P_c = 3 - 6\%$), 2 of which were already known to have high polarization. Four objects have very low polarization ($P_c \leq 1\%$). The polarization distribution is discussed in detail in Chapter 4, and tested against a QSO unification model.

The wavelength dependence of the continuum polarization in BAL QSO is weak. Most (14/20) show a rise in polarization to the blue. Six BAL QSO show the polarization dilution signature of broad Fe II line emission between 2260 Å and 2800 Å. This contributes to, but doesn't completely account for, the wavelength dependence of the polarization (Chapter 4). Of the remaining objects, 4 have a flat polarization spectrum, one (UM 232) has polarization rising to the red, and one object is unpolarized (UM 275). A few objects (4) show variation of continuum PA with wavelength. The largest continuum PA rotations are seen in 0019+0107 and 0932+5006. We consider the implications of the weak wavelength dependence in the continuum polarization in Chapter 4.

The polarization is greater in the BAL than in the continuum for all objects (17/17 which have measurable C IV BAL). There are also PA rotations across the BAL of 11 objects. In some objects there are additional PA rotations of the opposite sign near the BAL and in the wings of the associated BEL (Chapter 5). The polarization variations across the troughs can be attributed to polarized light scattered around the BALR. The dominant effect is from partial coverage of the continuum scattering region, but there are some cases where a small amount of resonantly scattered light from the BALR is also present. The location and nature of the scatterers will be discussed in detail in Chapters 4 and 5.

In general, the BEL are polarized at a lower level than the continuum and to first order do not show up in polarized flux. A closer look shows small rotations and residual polarized flux across some emission lines in some objects (Chapter 5). Most notably, C III] is polarized in 2225-0534 and 0019+0107. Weakly polarized C IV photons are also detected in a few objects. The line polarization is used as a diagnostic of the geometry of the BAL, BEL, and scattering regions in Chapter 5.

2.8 Individual Objects

The spectra of 20 BAL QSO are presented in Figures 2.2-2.21. The four panels show the flux F_λ, polarization Q', polarized flux $Q' \times F$, and position angle (PA) θ. When viewing polarimetry data, it is useful to think of the total flux (panel 1) as mainly due to a direct, unpolarized component plus a small fraction of scattered light. The scattered light spectrum is well represented by the polarized flux (panel 3). The scaling between the total scattered flux and the polarized flux depends on the polarizing efficiency and optical depth of scatterers. The polarization (panel 2) is just the ratio of panels 3 and 1, so does not contain any independent information. Short descriptions of the spectra are given below. Selected objects are discussed in more detail in Chapters 4 and 5.

1. 0019+0107 (UM 232). The continuum polarization drops rapidly blue-ward of 2000 Å. This is unique to UM 232 since all other objects have P flat or rising to the blue. There is a PA rotation across the continuum corresponding to the drop in polarization. This strongly suggests at least two sources of polarized light. We consider the possibility of interstellar contamination in Chapter 5. There is a characteristic rise in polarization in the C IV trough, in spite of the rapidly falling continuum polarization at the position of the line. The C III] λ1909 emission line shows up strongly in polarized flux, while the other BEL do not. This effect is also seen in PHL 5200 (see below), and may be due to resonance scattering in the BELR. The difference in line and continuum polarization supports an intrinsic explanation for the polarization.

2. 0043+0048 (UM 275). This object is remarkable for its deep double troughs. The polarization is null, with a formal 2σ upper limit of 0.2%. The BAL troughs do not show any significant polarization signature and the broad emission lines are unpolarized as well. The lack of polarization indicates a high degree of symmetry in the continuum emitting region and a low optical depth to scattering throughout the nuclear regions. The C IV troughs are unusually deep for a BAL QSO, but there still appears to be residual flux at the bottom of the troughs. There are weak Mg II and Al III BAL, which suggests that the C IV troughs are saturated. The lack of trough polarization and deep troughs may indicate a BALR with low global covering fraction which contributes little to the scattered flux. The broad emission lines have unusually narrow profiles.

3. 0059-2735. This was the first object discovered in the extremely rare class of Fe II

low-ionization BAL QSO (Hazard et al., 1987). The polarization increases in the Mg II and Al III BAL. There are possible PA rotations in these BAL but they have low significance. The similar polarization behavior in the BAL of low-ionization and high-ionization BAL QSO suggests that they share a similar geometry. As we argued in Chapter 1, it is likely that the ionic species with low and high ionization are co-spatial and the appearance of low-ionization BAL is primarily due to high optical depth. Most BEL, including Fe II and Mg II are unpolarized, which is also similar to the high-ionization BAL QSO.

In contrast to the BAL, the polarization decreases in the narrow absorption lines (NAL), including Fe II, Ni II, Co II, and Zn II. As a result, the NAL appear deeper in polarized flux than in total flux. (See Chapter 4 for more detail.) This is especially apparent in the Fe II UV 8 lines red-ward of C IV. The NAL clouds must have a significantly different geometry from the BALR. We attribute the low polarization in the NAL to dilution by unpolarized emission lines, especially Fe II. The low local covering fraction of the Fe II BELR by the NALR suggests that the NAL clouds are located close to and perhaps intermingled with the BELR. The Fe II UV 2 NAL shows a possible 10 degree rotation in PA, but the Fe II UV 1 NAL does not. This may be another effect related to the polarization of the underlying Fe II emission line component, and probably has nothing to do with the particular transition where the rotation occurs. Perhaps the rotation is maximum at the wavelength of the Fe II UV 2 line because this is where the Fe II emission line flux peaks. This explanation requires the Fe II emission to be polarized at a low level and at a different position angle from the continuum.

4. 0105-265. This is the highest redshift object in our sample, with $z = 3.488$, so it shows the largest number of absorption troughs. The spectropolarimetry was presented by Cohen et al. (1995). The troughs are wide, smooth and deep, similar to those of PHL 5200 (see below). The continuum polarization rises steadily to the blue and the PA is constant across the entire spectrum, even in the troughs, blue-ward of Lyα, and below the wavelength of the Lyman edge (912 Å). The lack of a strong Lyman edge feature in direct or scattered flux suggests that both the BALR and scattering region are highly ionized.

There is a high contrast between the continuum and BAL polarization levels, with $P_c = 1.62 \pm 0.07\%$ and $P_t \simeq 10\%$. P increases in all of the troughs, including C IV, Si IV, N V/Lyα, Lyβ/O VI and S VI. Four of the troughs have nearly identical residual flux, suggesting that they are saturated. However, the peak trough polarization values do

not follow the trend of the continuum polarization. The troughs are almost completely detached, so they are not contaminated by the BEL.

5. 0137-0153. This BAL QSO has low polarization and the spectra are somewhat noisy. The troughs have a complex morphology with several subcomponents, including a deep narrow component at low velocity. The continuum polarization increases to the blue. P increases in the C IV and Si IV BAL troughs, especially in the deep narrow component. The polarization drops at all of the emission lines and they do not appear in the polarized flux spectrum. The spikes seen in the polarized flux and PA spectra at 1250 Å are probably due to a cosmic ray event.

6. 0146+0142 (UM 141). This object is distinguished by high-velocity absorption extending past 0.12c. The Si IV emission line appears to be completely occulted by the C IV BAL. There is a strong absorption feature at 1072 Å which may be a P V BAL (Barlow, 1993). The continuum polarization is wavelength independent. P rises in the NV/Lyα BAL, and the C IV BAL. P is above the continuum level at the wavelength of the Si IV BAL, but there is no distinct polarization rise in the deepest portion of this BAL. There is a hint of a polarization increase in the P V BAL, which if real would confirm its identification as a BAL. The spectrum is too noisy to determine the polarization at the O VI BAL. The PA rotates by ~ 10 degrees in the Lyα/N V, C IV, and Si IV troughs. P decreases at the emission lines, but there is residual polarized emission line flux in O VI/Lyβ, N V/Lyα, and C IV. However, the semi-forbidden C III] BEL does not appear in polarized flux. The difference between the polarization of the permitted and semi-forbidden BEL is discussed in Chapter 5.

7. 0226-1024. This is the brightest high-z BAL QSO in our sample, with $V = 16.9$. It has several distinct sub-components to its BAL. 0226-1024 was the target of further observations to study the polarization behavior at higher resolution with the 600 groove/mm grating. These observations are presented and discussed in Chapter 5, and confirm and extend the results of the lower resolution observations presented here.

The continuum polarization rises to almost 2% in the blue and the continuum PA is independent of wavelength. P increases to 7% in the C IV BAL and to 4% in the Si IV BAL. P does not rise in the sub-trough with lowest outflow velocity, suggesting that the corresponding BAL cloud covers the polarized light source more completely than the higher velocity BAL systems. The low-velocity associated absorbers have a different geometry and

may have a different origin from the other BAL clouds. This is discussed in more detail in Chapter 5. There are PA rotations of 15 degrees in the BAL due to partial coverage of the polarized continuum source. PA rotations in the opposite direction outside of the troughs indicate the presence of resonantly scattered flux.

There is a large peak in polarized flux just red-ward of the N V BEL. It is difficult to tell if this peak belongs to the polarized continuum or BEL because the continuum is not well defined at its wavelength. A similar peak is seen in BAL QSO 1524+5147. These features and the excess N V emission in BAL QSO may be due to Rayleigh scattering by neutral hydrogen. (See Chapter 4 for details.) P dips across all broad emission lines, including Fe II. There are deficits of polarized flux at the locations of the Lyα, Si IV, and C IV BEL, indicating that the BEL are polarized nearly perpendicular to the continuum. This may be an important clue to the geometry of the BELR.

8. IRAS 07598+6508. This is a low-redshift object with strong Fe II emission and a weak Na I BAL. The continuum polarization and polarized flux rise to the blue, but there are few windows in the spectrum which are not heavily contaminated by broad emission lines. We confirm the rise in P in the Na I BAL seen by Hines & Wills (1995), and also find a PA rotation across the BAL. The PA rotates away from the BEL value, suggesting that the Fe II BEL is absorbed to a greater extent than the continuum. This is also consistent with the unusually large polarization rise across the shallow BAL.

Our high S/N observations reveal that the BEL are polarized at a low level and at a PA different from the continuum. The PA rotates in one direction in the red wing and line core and in the opposite direction in the blue wing of Hα, an effect which is commonly seen in broad line radio galaxies (Cohen et al., 1998). The PA rotations are seen out to a velocity of $\pm 12,000$ km/s in the line wings. Most of the line flux contributes to a positive rotation across the Fe II line blends.

9. 0842+3431 (CSO 203). This BAL QSO has narrow, detached BAL troughs including a weak Al III trough. The continuum polarization is low ($P_c = 0.51 \pm 0.01$) and rises to the blue. P rises to 3% in the C IV BAL, a large contrast to the continuum polarization. The polarization drops at the N V emission line and there is no evidence for BEL in the polarized flux spectrum.

The trough depths vary between the two observational epochs, by up to 60% in the deepest portion of the C IV trough. The Si IV, C IV, and Al III troughs all show variability.

The peak C IV trough polarization is the same for both epochs within the uncertainties. The continuum polarization varies by ($\sim$ 0.2%) between the two epochs. Variations in the polarized flux spectrum should lag the continuum variations if light is scattered in the BELR. Trough variability was also reported for this object by Barlow et al. (1992) over the years 1989-1991.

10. 0856+1714. The BAL are deep and show several sub-components, similar to 0226-1024. There is weak Al III absorption. The polarimetric data are very noisy since the object is faint and there were clouds. They are only useful for an estimate of the continuum polarization, which rises to the blue.

11. 0903+1734. The troughs of this BAL QSO are deep and show several sub-components. There are two intervening metal absorption systems. The continuum polarization is low and the polarization spectra are quite noisy. P rises in the C IV, Si IV, and Lyα/N V BAL troughs and there is a large contrast between the trough and continuum polarization. P drops in the broad emission lines, but the spectra are too noisy to provide accurate BEL polarization measurements.

12. 0932+5006. This object has multiple distinct BAL sub-troughs which are well separated in velocity. There are low equivalent width Mg II and Al III BAL which show the same velocity structure as the C IV trough. However, the relative depths of the sub-troughs are different for the C IV and low ionization lines. The sub-trough at -13,600 km/s is anomalously shallow in C IV relative to its counterpart in the other ions. This could be a result of either velocity-dependent ionization or saturation of the C IV trough.

P rises in the multiple Si IV and C IV troughs, but the low-ionization troughs are too shallow to affect the polarization. The polarization rises by only a factor of 2.3 in the deep portion of the C IV trough, a small contrast relative to other objects in our sample. In polarized flux, the anomalous C IV sub-trough is significantly weaker than in total flux. This strongly suggests that the shallowness of this trough is due to an excess of scattered light. It is likely that this particular sub-trough covers a smaller fraction of the scattering region than the other sub-troughs. The effect of this is not seen in the low-ionization troughs because they are far from saturation and the scattered flux represents a small fraction of the residual flux.

The polarized continuum flux is reddened below 2000 Å, which is similar to 0019+0107. The reddening is accompanied by a 15 degree PA rotation across the continuum, another

effect seen also in 0019+0107. The reddening and PA rotation may be due to preferential and patchy absorption of the scattered flux by dust in the scattering region.

13. 1212+1445. The C IV BAL of this object has three narrow components at low velocity and a broad component at high velocity. The lowest velocity component is extremely narrow and unresolved in our spectrum, and cuts into the peak of the BEL. The narrow components are visible in the weak Al III and Mg II BAL. The continuum polarization rises strongly to the blue and there is a $\sim$ 10 degree PA rotation red-ward of C IV. The other BEL are unpolarized and the polarization dilution signatures of the Fe II blends and C III] are prominent.

The polarization changes drastically in magnitude and position angle across the broad portion of the C IV BAL trough. It appears that the narrow low velocity components do not participate in this behavior. The polarization drops below the continuum level at a velocity of -14,300 km/s and the PA rotates wildly (by as much as 120 degrees) at the same velocity. For this object, Q' is not a reliable estimate of P in the trough because of the large PA rotation. Therefore, we use $P = \sqrt{Q^2 + U^2}$ in the vicinity of the trough, and $P = Q'$ elsewhere. The net effect is that the high velocity BAL is deeper in polarized flux than in total flux and is also blue-shifted. The PA rotation begins in the red wing of the C IV BEL at +6000 km/s, strongly suggesting a resonantly scattered component to the C IV flux.

14. 1235+0857. This object has deep, narrow, low-balnicity troughs which cut into the broad emission lines. In addition there is a weak broad component which extends to -24,100 km/s and has a ragged profile containing at least 7 sub-troughs. There is a weak Al III doublet at a velocity of -4100 km/s which corresponds to the blue end of the deep C IV trough. As in 0932+5006, there is a suggestion of velocity-dependent covering fraction or velocity-dependent ionization.

The continuum polarization is moderately high ($P_c = 2.53 \pm 0.07\%$) and constant with wavelength. The BAL have no discernible effect on the polarization, suggesting that they uniformly cover the continuum sources and BELR. P drops in both the red and blue wings of the BEL, including the portion which is absorbed by the BAL. Most of the BEL do not appear in the polarized flux spectrum, but there is an emission spike at the wavelength of O VI/Lyβ which is probably due to noise. The BEL profiles are nicely recovered in the unpolarized flux spectrum (Fig. 4.6), which shows that they are uniformly absorbed by the BAL. The apparent PA rotations in the BAL troughs are not significant since they occur

where the absorption lines go nearly black, and do not appear in the shallower Si IV BAL.

15. 1246-0542. This is the brightest high-redshift object in our sample. The BAL troughs consist of a shallow component which extends from $v = 0 - 0.08c$ and a deep component centered at -17,400 km/s. Closer inspection reveals a number of narrower sub-troughs in the shallow region of the trough. There are weak Al III and Mg II BAL, also centered at -17,400 km/s. There are two intervening metal absorption line systems.

The continuum polarization rises steadily to the blue and the polarized continuum flux closely follows a power law with $\alpha = 0.2$. The broad emission lines have low polarization with PA perpendicular to the continuum and are only weakly present in the polarized flux spectrum (Chapter 5). The polarization rises from 1.3% in the continuum to 7.2% in the C IV BAL, a large contrast. The BAL are shallow in polarized flux and appear to be blue-shifted. This indicates a very small local covering fraction of the polarized light source by the BALR. The local covering fraction is also highly dependent on outflow velocity. The blue-shift is a projection effect due to the different geometry of the direct and scattered rays. This is discussed in detail in Chapter 5.

16. 1331-0108. This low-ionization BAL QSO was observed for a short time to determine the continuum polarization, which is moderate. There is very strong Fe II emission, which seems to be common in objects with strong low-ionization BAL. The deep Al III trough has a smaller velocity range than the C IV trough; it is missing the high-velocity absorption tail. The Mg II trough is not as deep as the Al III trough and has an indistinct high velocity edge because it is partially filled in with Fe II emission. Due to the short exposure time, there is little information about emission line and trough polarization.

17. 1333+2840 (RS 23). This classic object has P-Cygni line profiles. The BEL have unusually large equivalent widths for a QSO. We observed RS 23 on the suggestion of R. Goodrich, who hypothesized that large BEL equivalent widths may be an indicator of high polarization and attenuation of the continuum (Goodrich, 1997). This is indeed the most highly polarized object in our Keck sample, polarized up to 6% in the continuum.

The polarization rises by only 4.5% in the C IV trough, not nearly as dramatic a rise as in other BAL QSO such as 0105-265. This is consistent with a picture where the direct continuum light is attenuated and the spectrum is dominated by scattered light. Further absorption of direct light by the BALR has small effect on the polarization. Dilution by the low-polarization C IV BEL and resonantly scattered photons from the BALR also serve

to reduce the trough polarization. There is a +10 degree PA rotation in the C IV trough from selective absorption of the scattered continuum light.

Other than C IV, the BEL are not polarized and do not show up in the polarized flux spectrum. There is a -10 degree PA rotation in the blue wing of the C IV BEL, in the opposite direction from the trough PA rotation. In addition, there is negatively polarized flux in the red wing of C IV from photons resonantly scattered in the BALR. The complicated polarization spectrum across the C IV line results from multiple sources of scattered light,

18. 1413+1143 (Cloverleaf). This object is lensed into a quadruple source by an intervening galaxy (Magain et al., 1988). This complicates the analysis of the spectra, but may also prove to be a useful tool for studying the structure of this BAL QSO. The line profiles are P-Cygni like, but the troughs show more velocity structure than RS 23 (see above) and the C IV trough is nearly black. There is a weak Al III BAL and a number of intervening metal-line absorption systems.

The polarization properties of 1413+1143 have been reported by Goodrich & Miller (1995), including evidence for variable continuum polarization. In spite of the variability, they suggest a scattering origin for the polarization. The continuum polarization rises to the blue and the continuum PA is constant with wavelength. The polarization rises strongly in the BAL troughs, including Lyα, N V, Si IV, C IV, and perhaps P V. P reaches 17% in the C IV trough, but this is highly biased by the low S/N in the deep portion of the trough. There is a consistent 15 degree PA rotation across all BAL.

The permitted BEL are polarized at a lower level than the continuum, while the semi-forbidden C III] line is unpolarized. This is opposite to the BEL polarization behavior in 2225-0534 and 0019+0107, where only the C III] BEL is polarized. The permitted lines in 1413+1143 are probably polarized by scattering in the same region as the continuum, and the scatterers must be relatively cold to preserve the BEL width.

19. 1524+5147 (CSO 755). This is a very bright BAL QSO with multiple, shallow troughs. Its polarization properties were first reported by Glenn et al. (1994). The continuum polarization is high (3.5%) and rises to the blue. The BAL and BEL profiles are quite different from those of the other two HPQ in our Keck sample (PHL 5200 and RS 23). The BAL of CSO 755 are detached, narrow, and shallow, while the BAL of the other HPQ have deep P-Cygni profiles. The BEL have normal equivalent widths, in contrast

to the high equivalent width BEL of the other HPQ. This argues against the continuum attenuation model for the high polarization in CSO 755. As we discuss further in Chapter 4, there is no indication of a correlation between BAL and BEL properties and continuum polarization in our sample as a whole.

The polarization rises by only 1-2% in the Lyα and C IV troughs, because they are not very deep. There is no polarization increase in the two low-velocity associated absorption systems because they cover the polarized light source more completely than the other absorption systems. In addition, the low-velocity systems only partially cover the BELR.

There is a 5 degree PA swing across the N V BAL, but not across C IV. In addition, the polarized flux peaks in the red wing of N V. As in 0226-1024, this may be due to polarization by Rayleigh scattering in the Lyα BEL. There is a small deficit of polarized flux in the red wings of all permitted lines because they are polarized at a low level, perpendicular to the continuum.

20. 2225-0534 (PHL 5200). Results on this object were reported by Cohen et al. (1995). It is the prototypical BAL QSO, and like most prototypes is not well representative of its class. Its BEL have extreme equivalent widths like 1333+2840 (see above). This may be indicative of an attenuated continuum seen primarily in scattered light. Its deep, broad BAL start at 0 km/s and absorb the blue wing of the BEL. There is a modest Mg II BAL corresponding to the deepest (probably saturated) portion of the C IV trough.

PHL 5200 is the second-most highly polarized BAL QSO in the Keck sample with P rising to 5% in the blue. This is another sense in which it is an extreme example of its class. The continuum PA is roughly constant with wavelength. The polarization increases to 10% in the BAL, indicating an excess of scattered light which is unabsorbed by the BALR. This is one of the first objects where this phenomenon was detected.

P drops in the emission lines, including the blended Fe II features, but dilution by Fe II is insufficient to completely account for the wavelength dependence of the continuum polarization (Chapter 4). There is residual polarized flux and a small PA rotation at the C III] BEL. However, the C IV BEL is completely unpolarized. The difference in polarization between C III] and C IV has been attributed to resonance scattering in the low-optical depth C III] line (Cohen et al., 1995).

Figures 2.2-2.21.

Keck spectropolarimetry of 20 BAL QSO. From top to bottom the four panels display (1) total flux F_λ, (2) polarization fraction (rotated Stokes parameter Q'), (3) polarized flux $Q' \times F$, and (4) position angle (PA) θ. Total and polarized flux are plotted in units of 10^{-16} erg/s/cm^2/ Å . Prominent emission lines are indicated in the top panel of Figure 2.2, and tick marks above the other figures identify the same set of lines. The horizontal line in panel 4 is the mean PA which is listed in Table 2.5. Except for Figure 2.3, the formats of Figures 2.2-2.21 are the same. In Figure 2.3, we display F_λ and the unrotated Stokes Q and U parameters only, since UM 275 is unpolarized. Individual objects are discussed in the text.

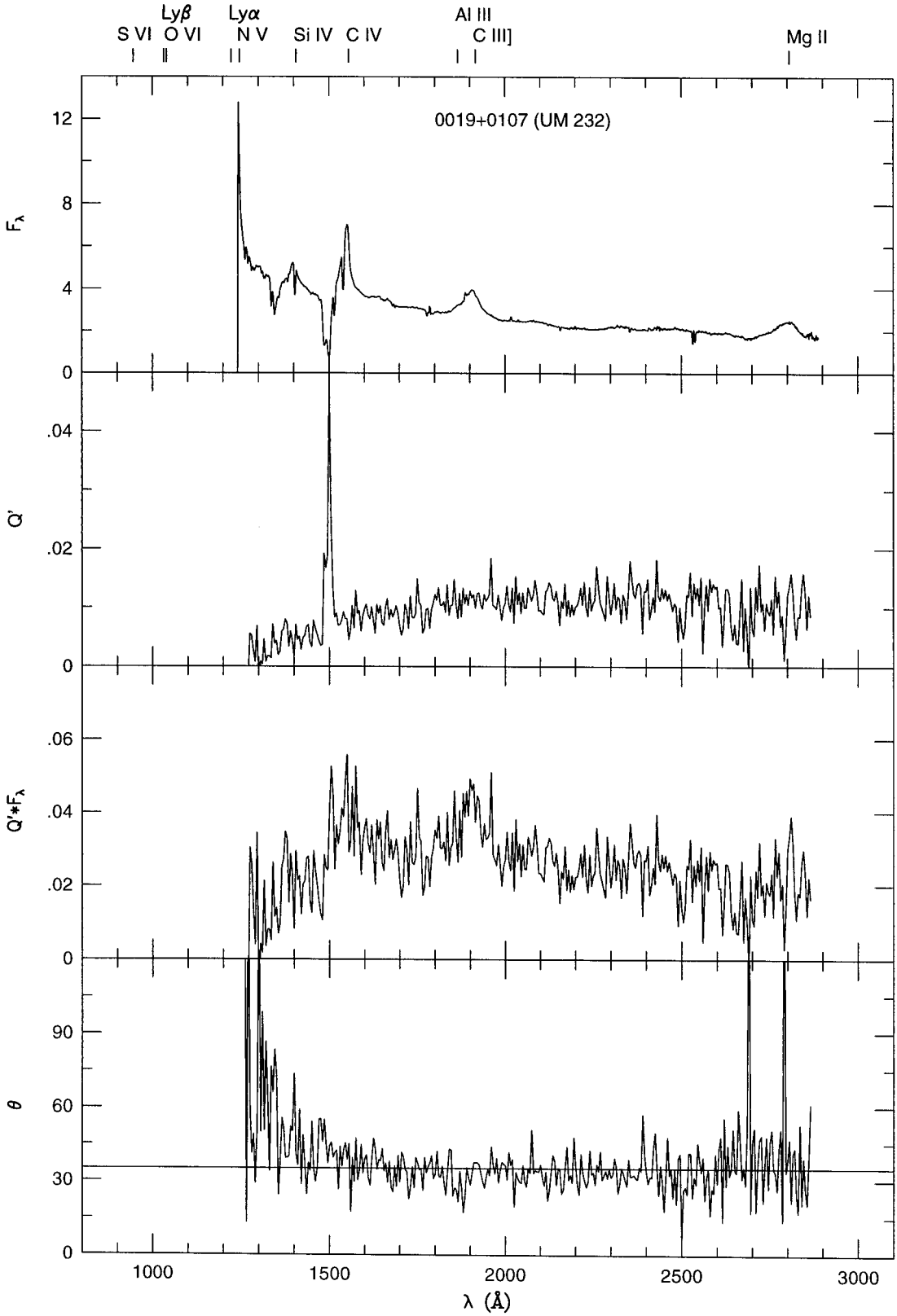

Figure 2.2: 0019+0107.

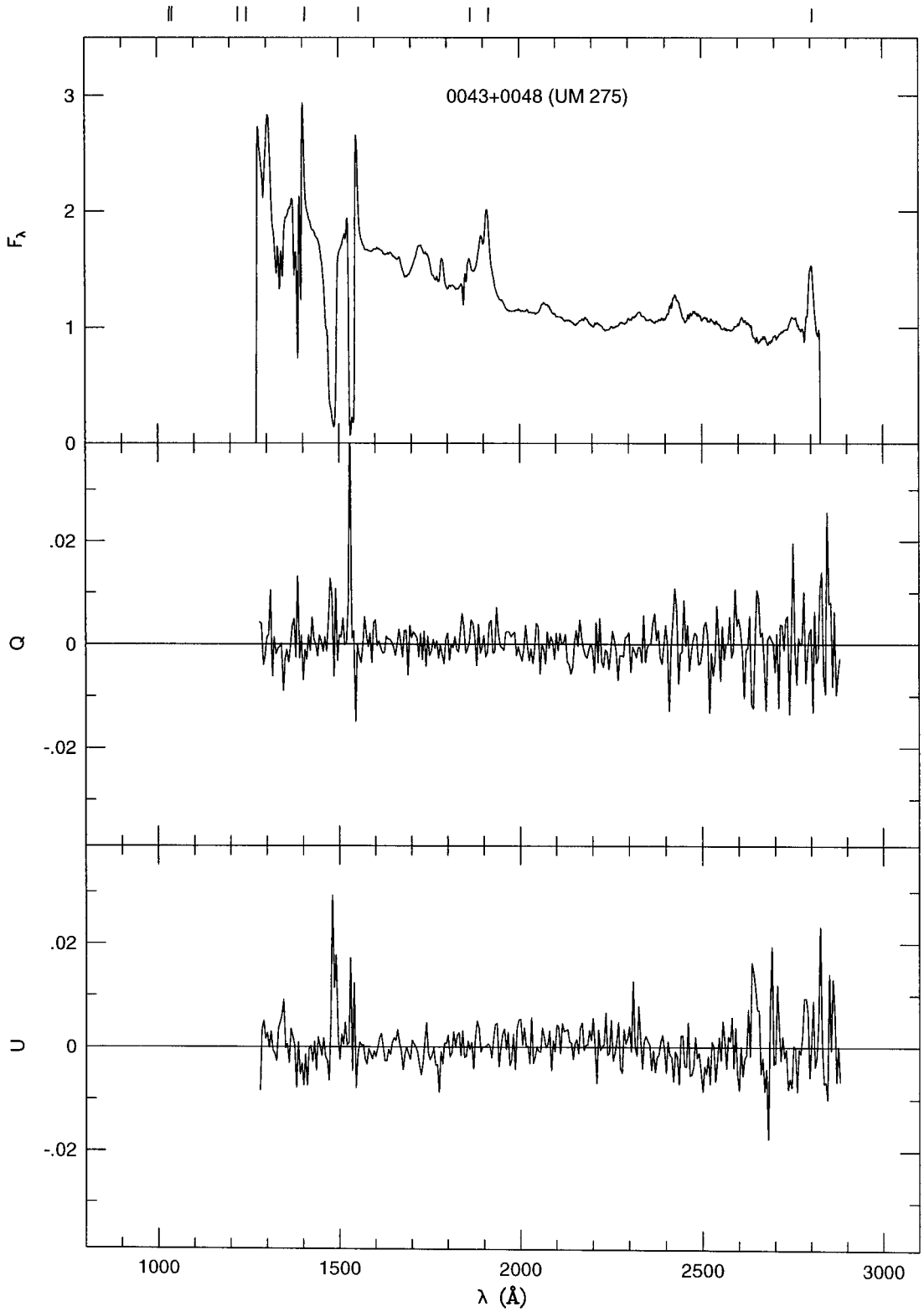

Figure 2.3: 0043+0048. This object is unpolarized so we show the Stokes parameters (Q,U) instead of Q', and we don't show polarized flux or PA.

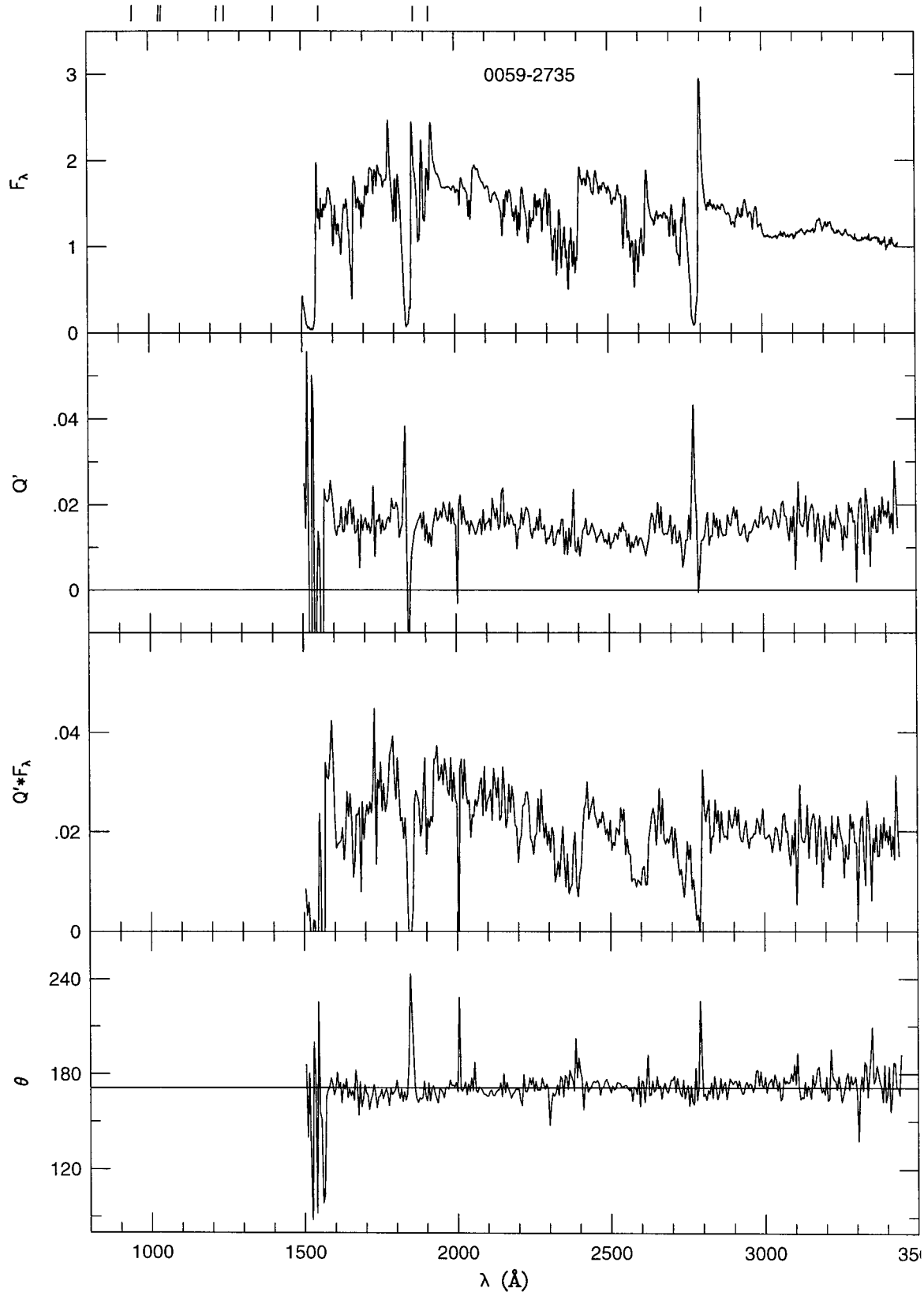

Figure 2.4: 0059-2735

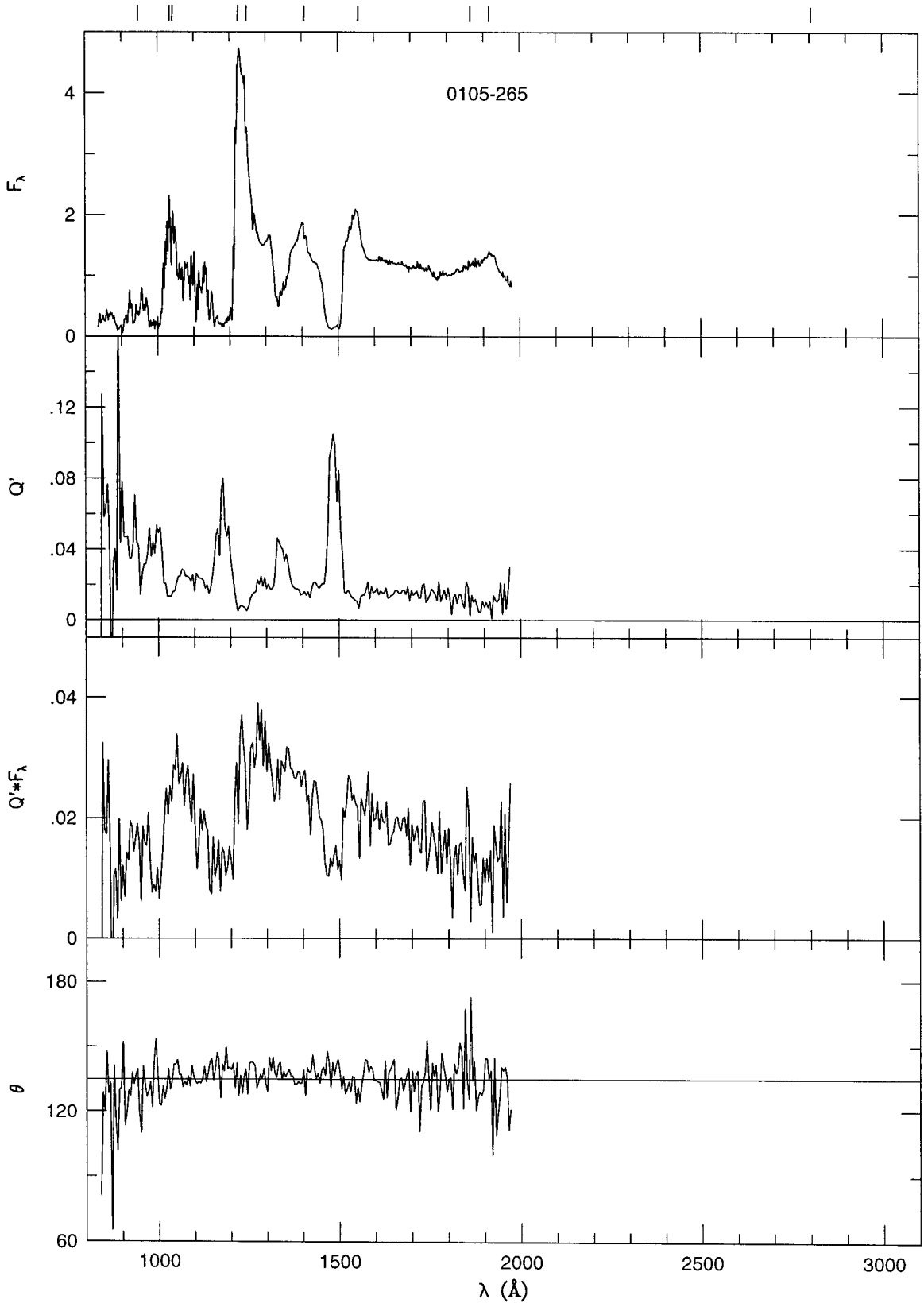

Figure 2.5: 0105-265

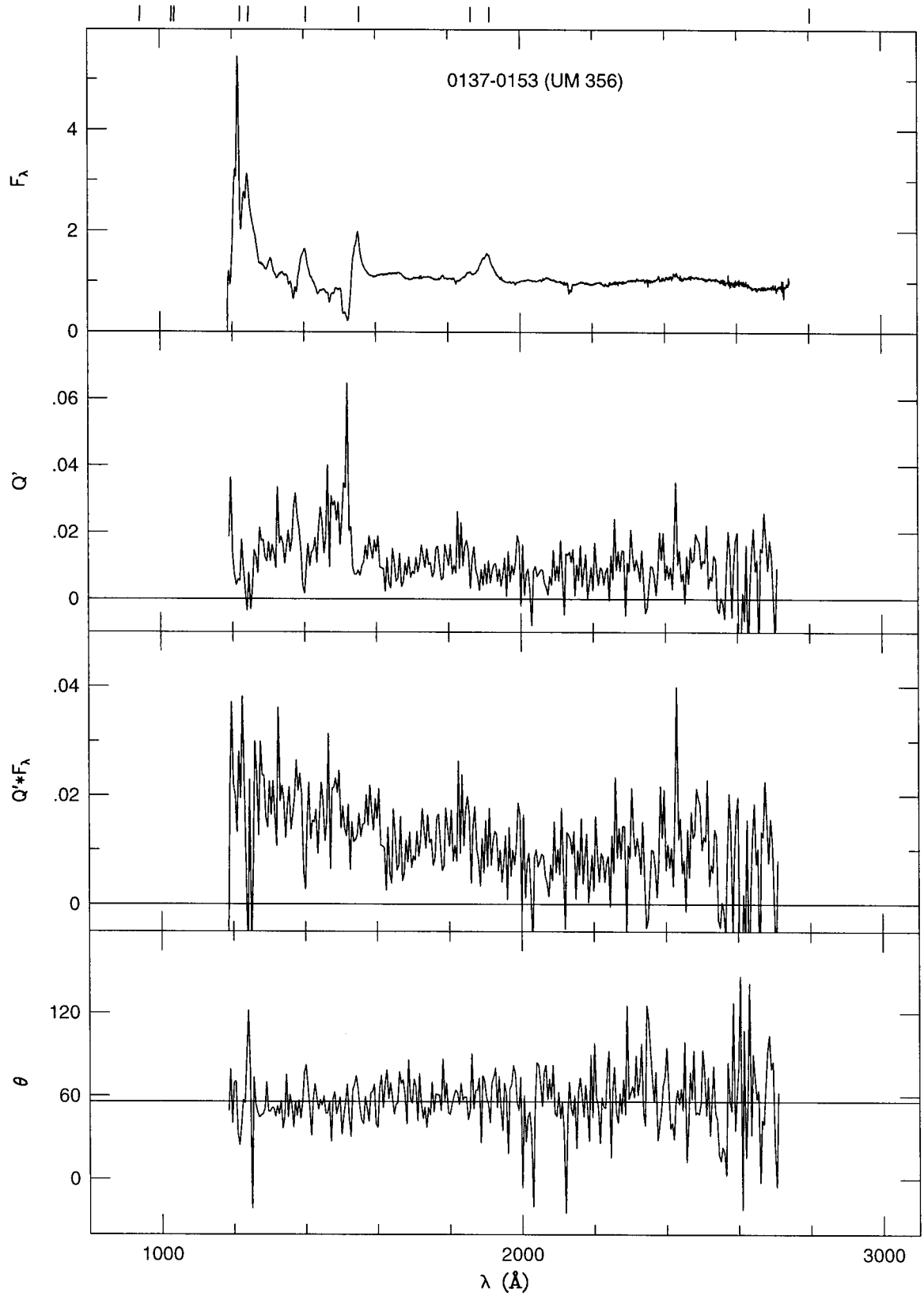

Figure 2.6: 0137-0153

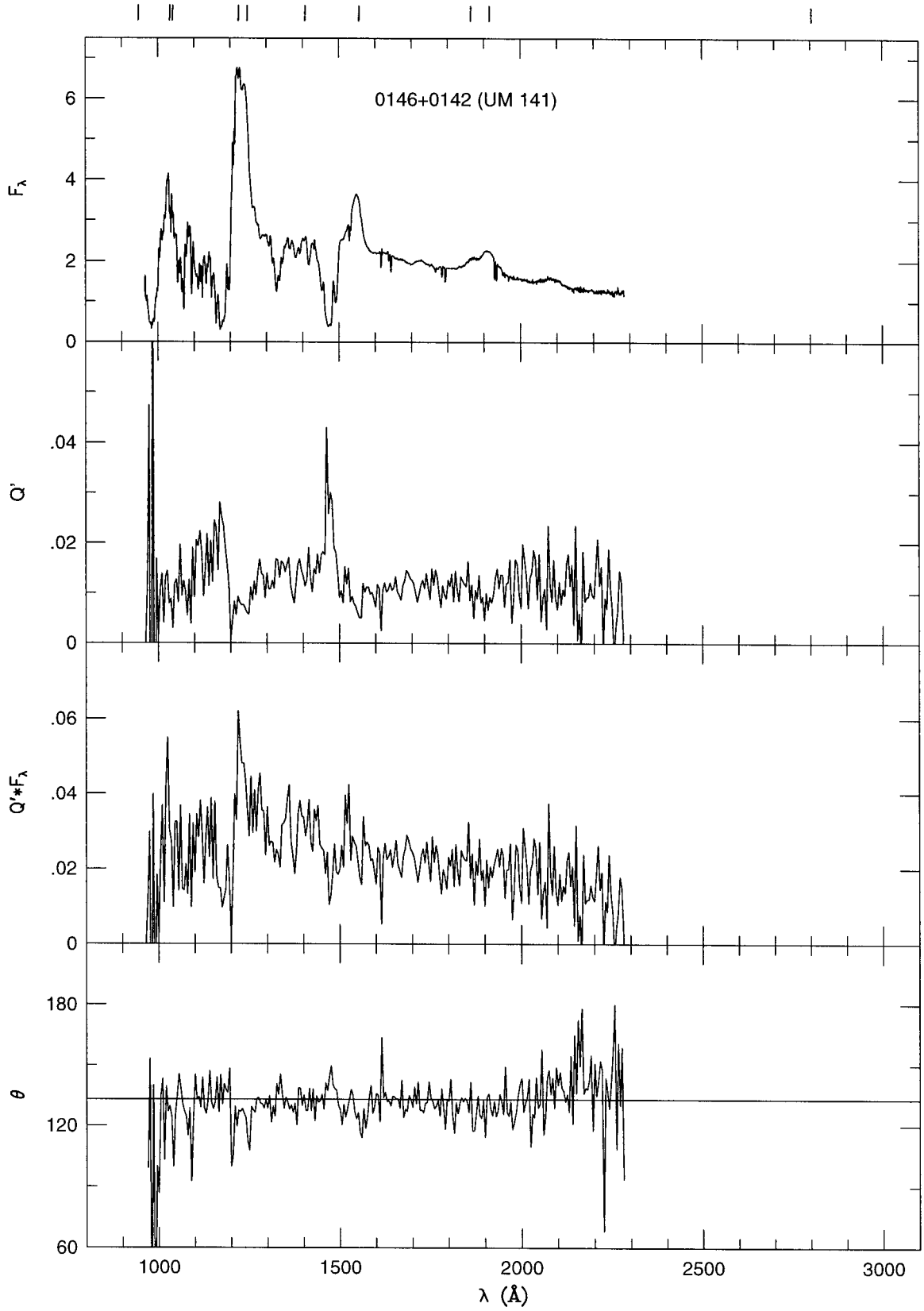

Figure 2.7: 0146+0142

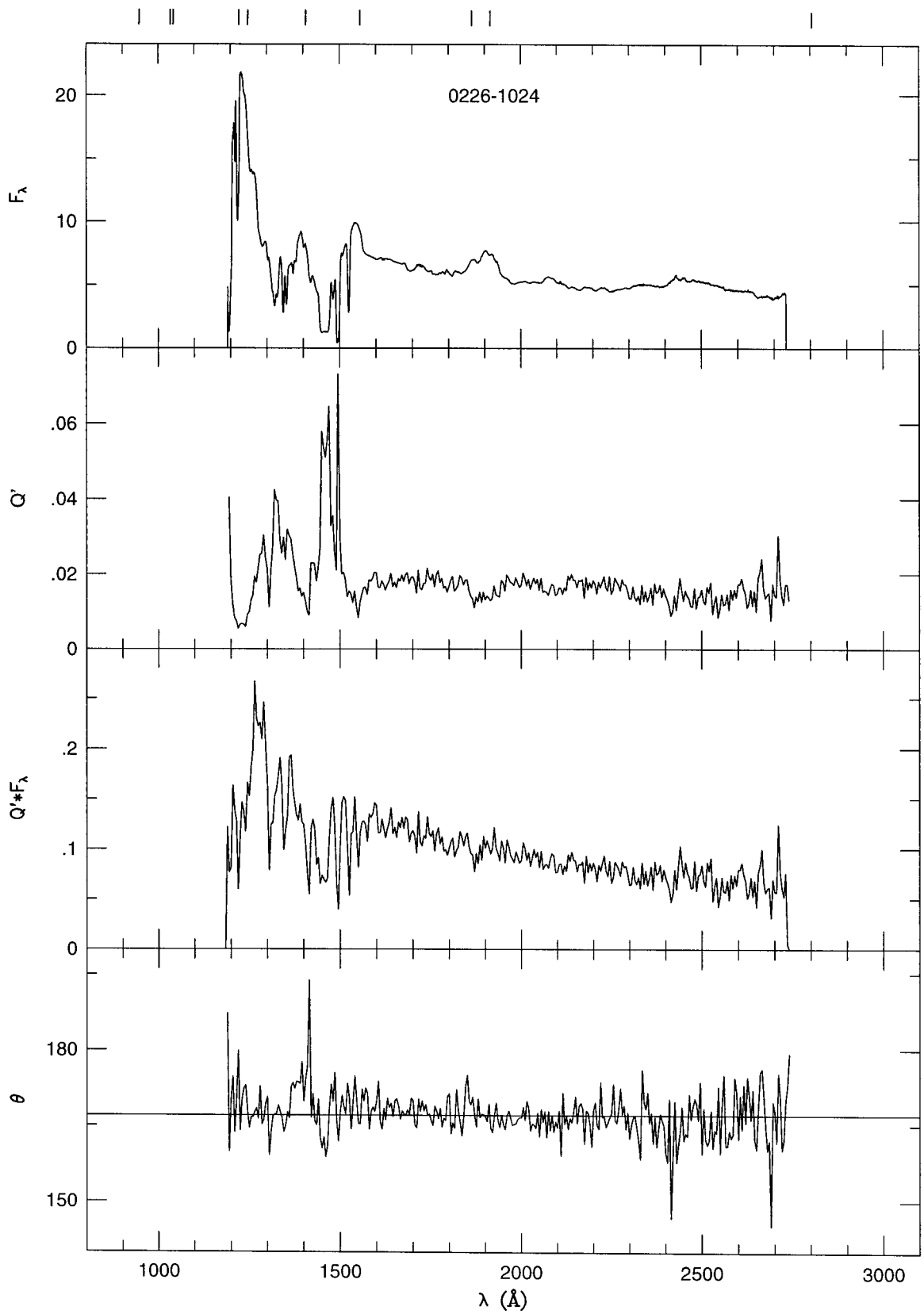

Figure 2.8: 0226-1024

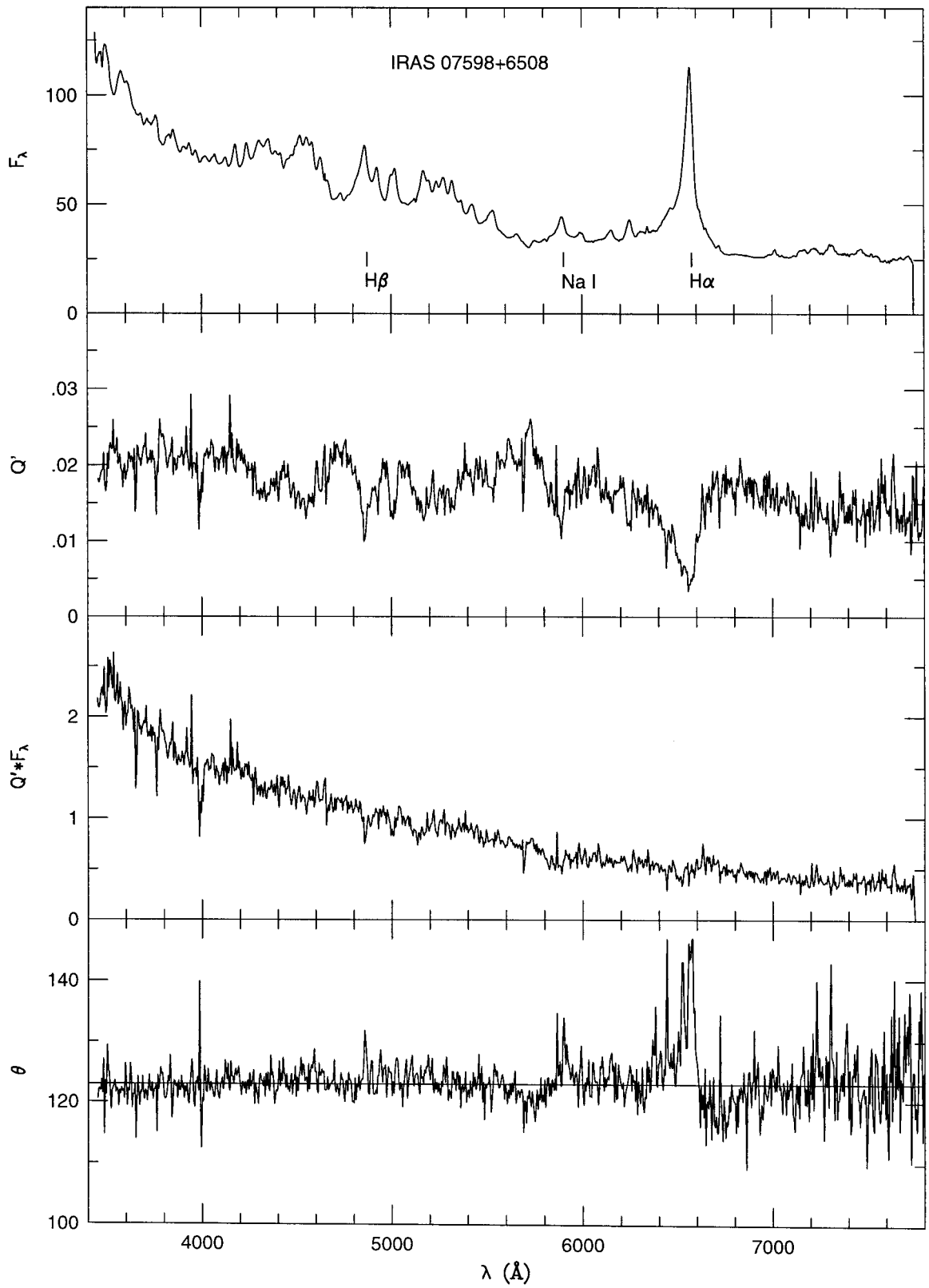

Figure 2.9: IRAS 07598+6508

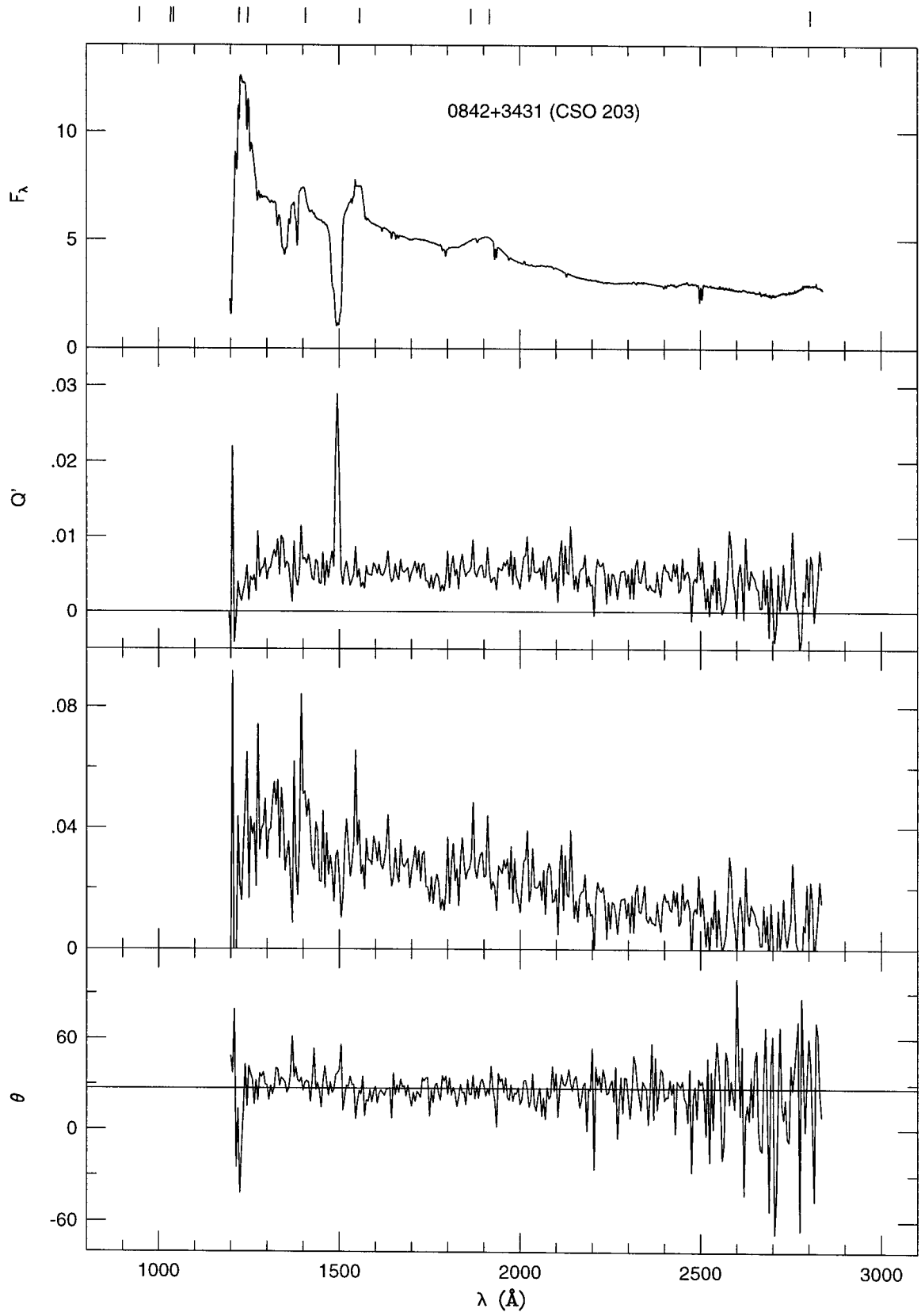

Figure 2.10: 0842+3431

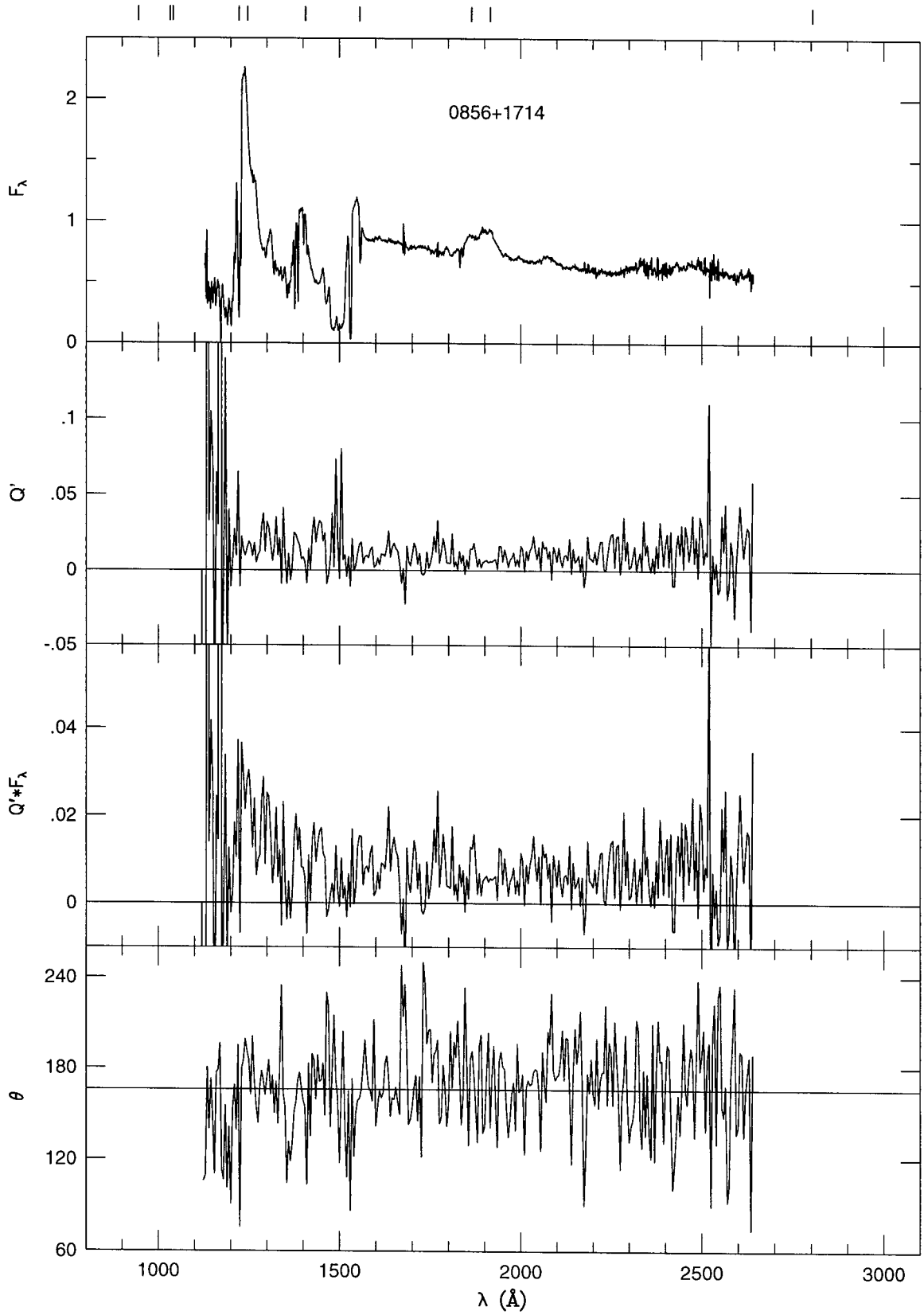

Figure 2.11: 0856+1714

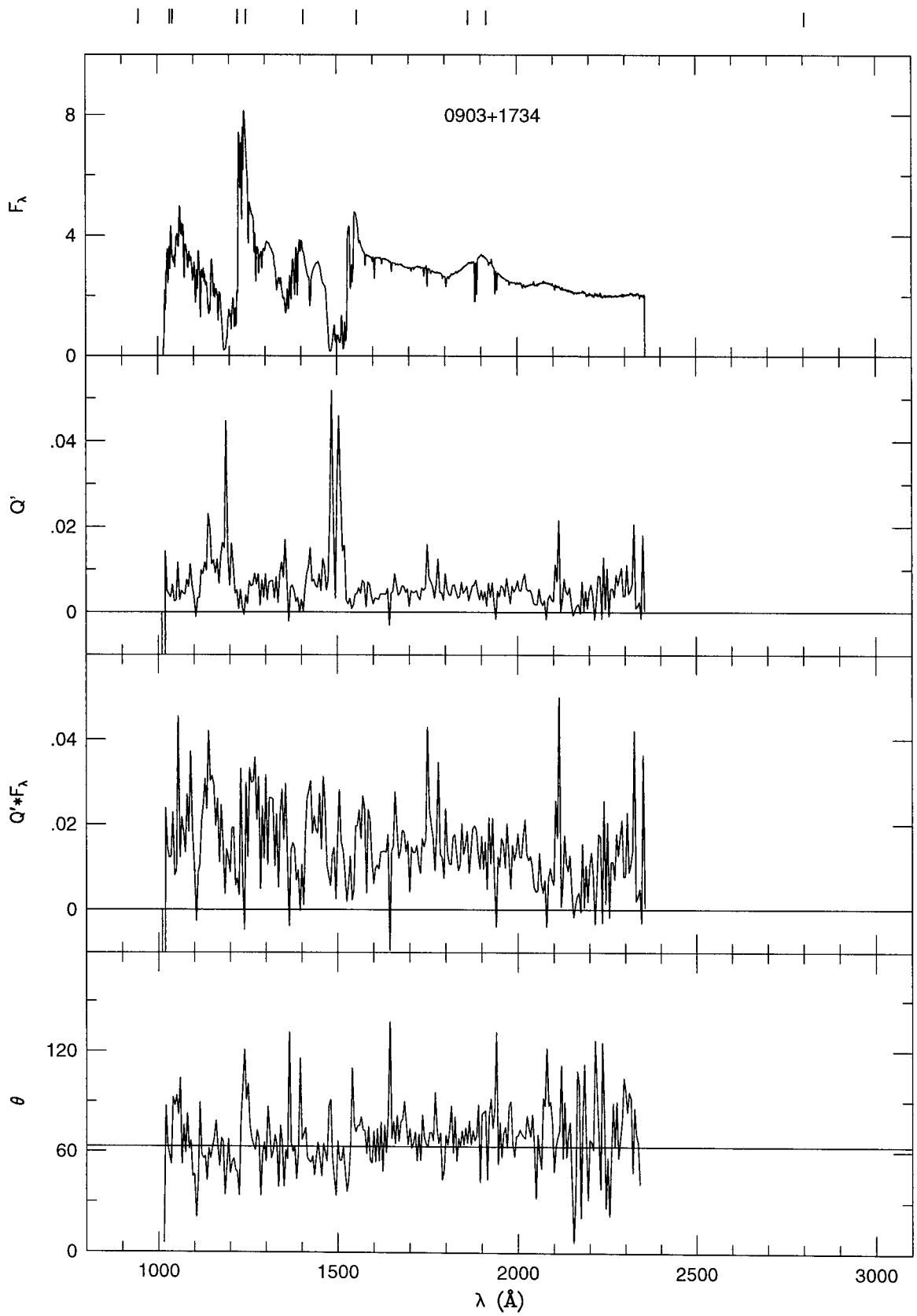

Figure 2.12: 0903+1734

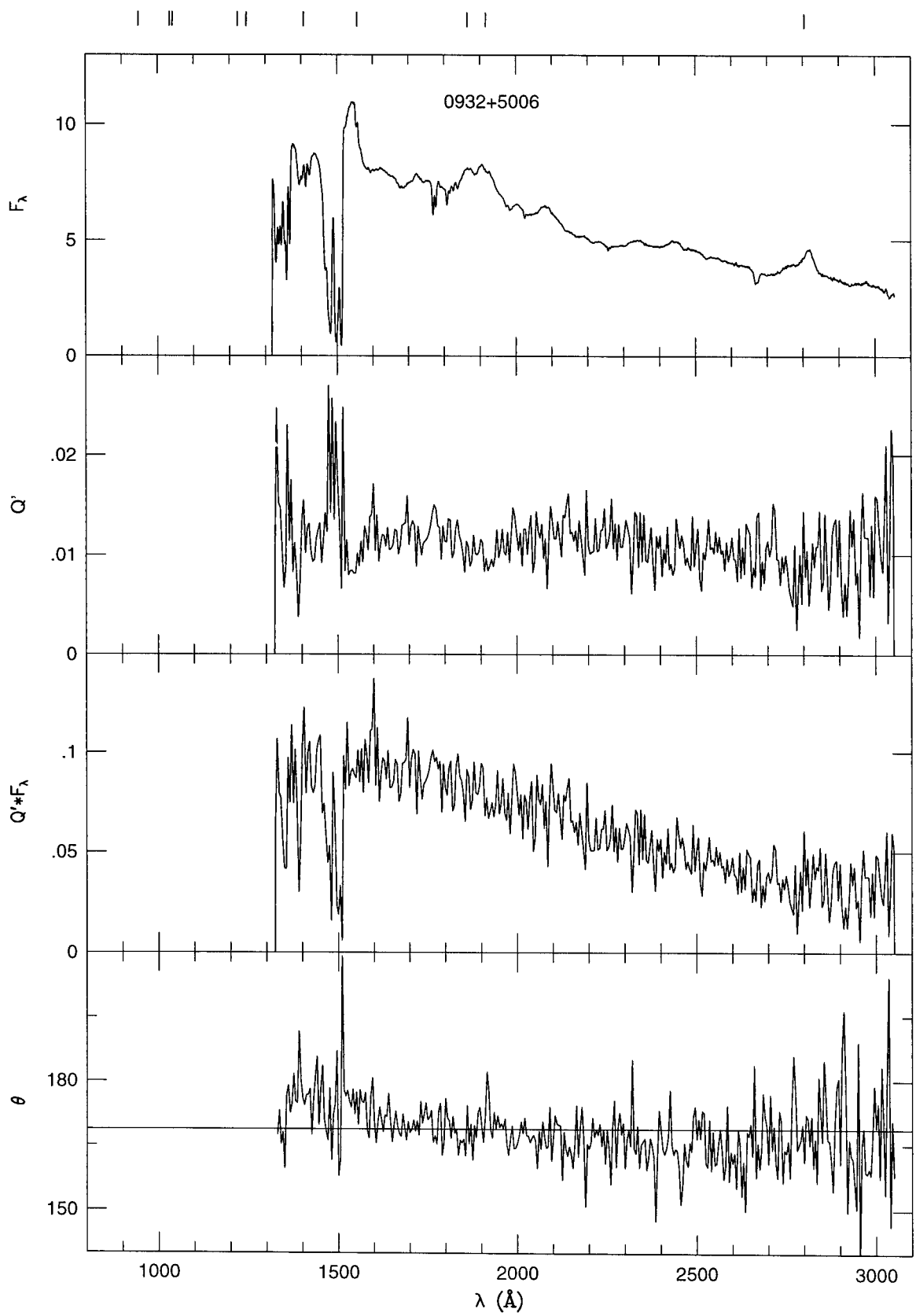

Figure 2.13: 0932+5006

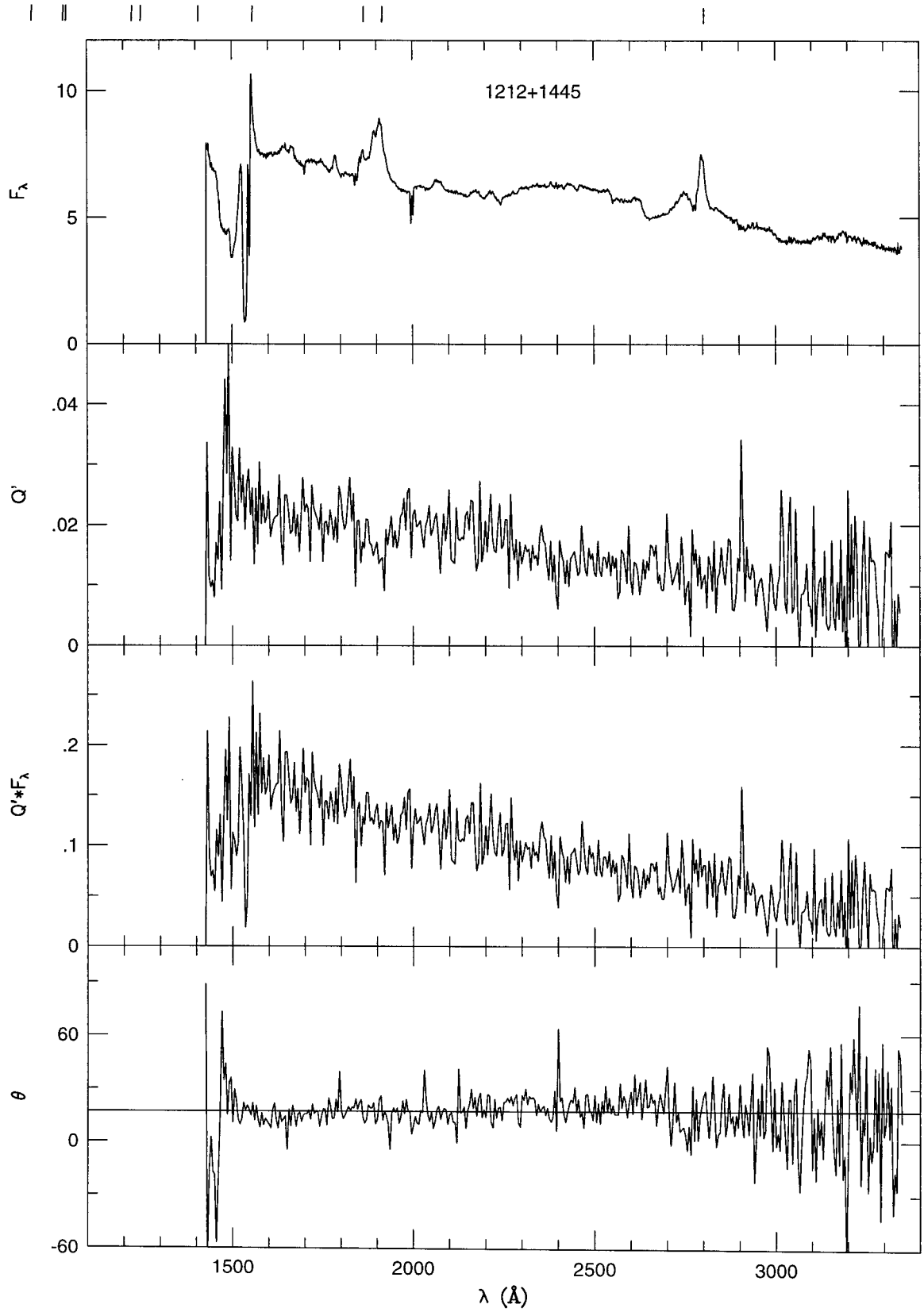

Figure 2.14: 1212+1445

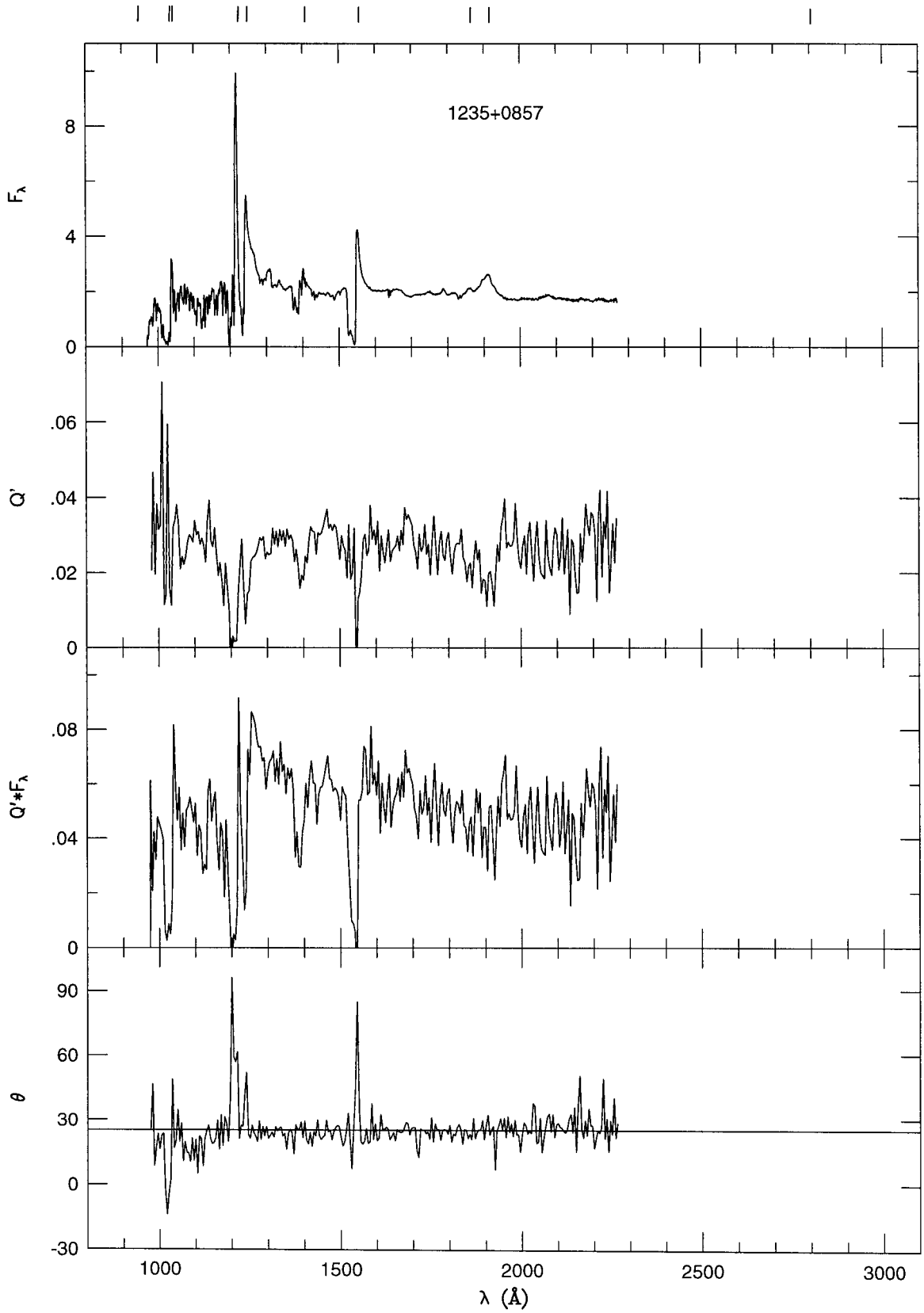

Figure 2.15: 1235+0857

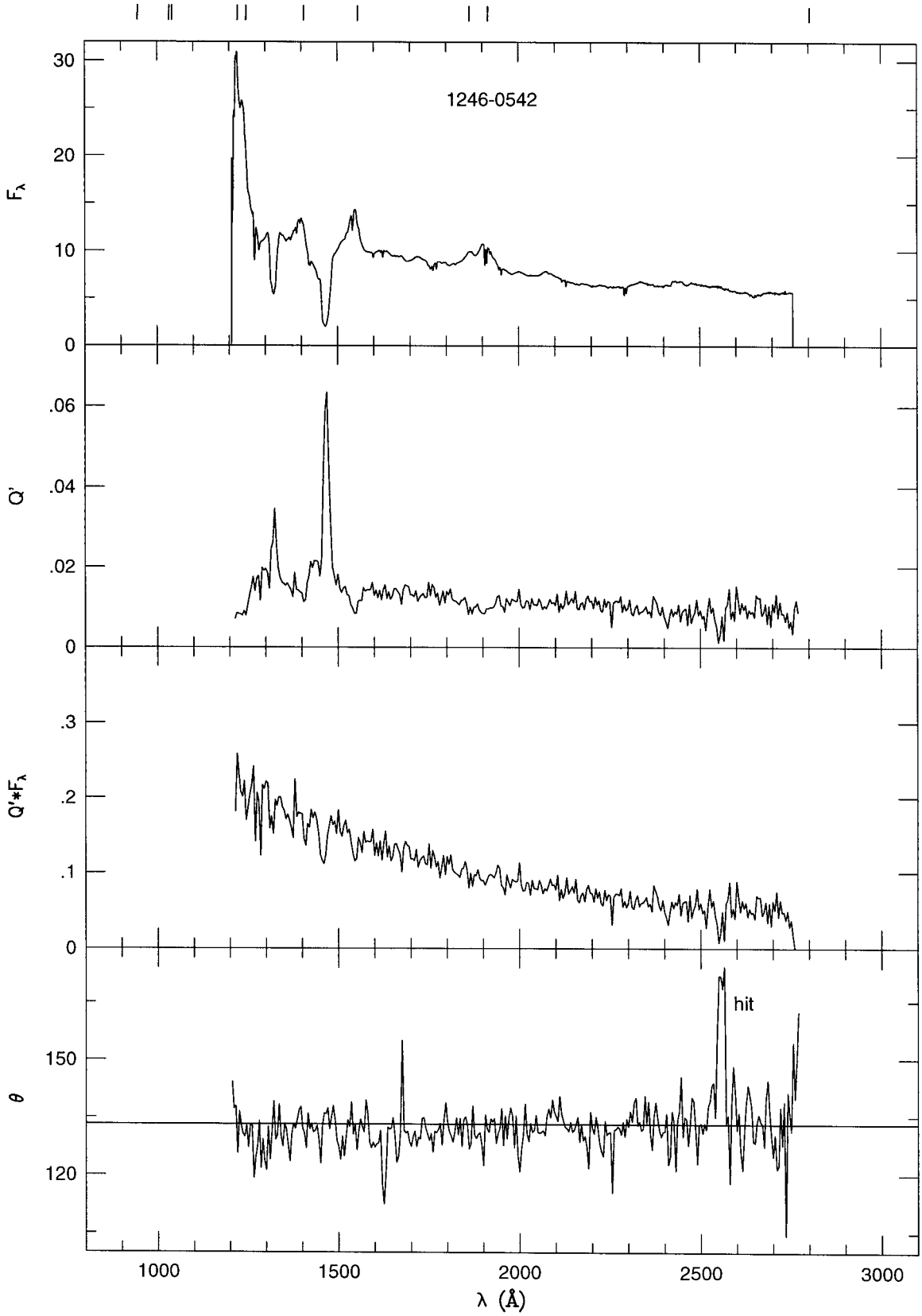

Figure 2.16: 1246-0542

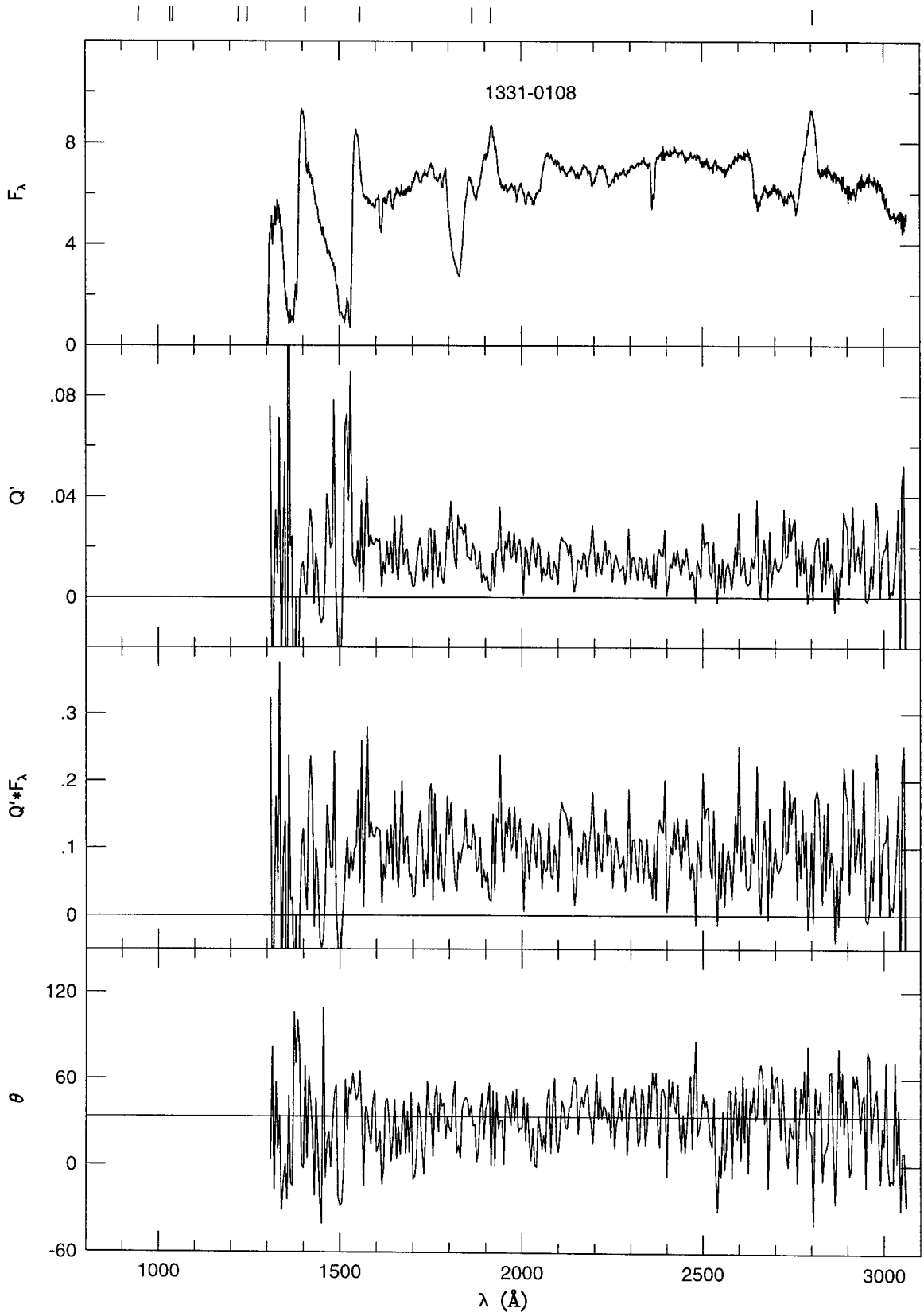

Figure 2.17: 1331-0108

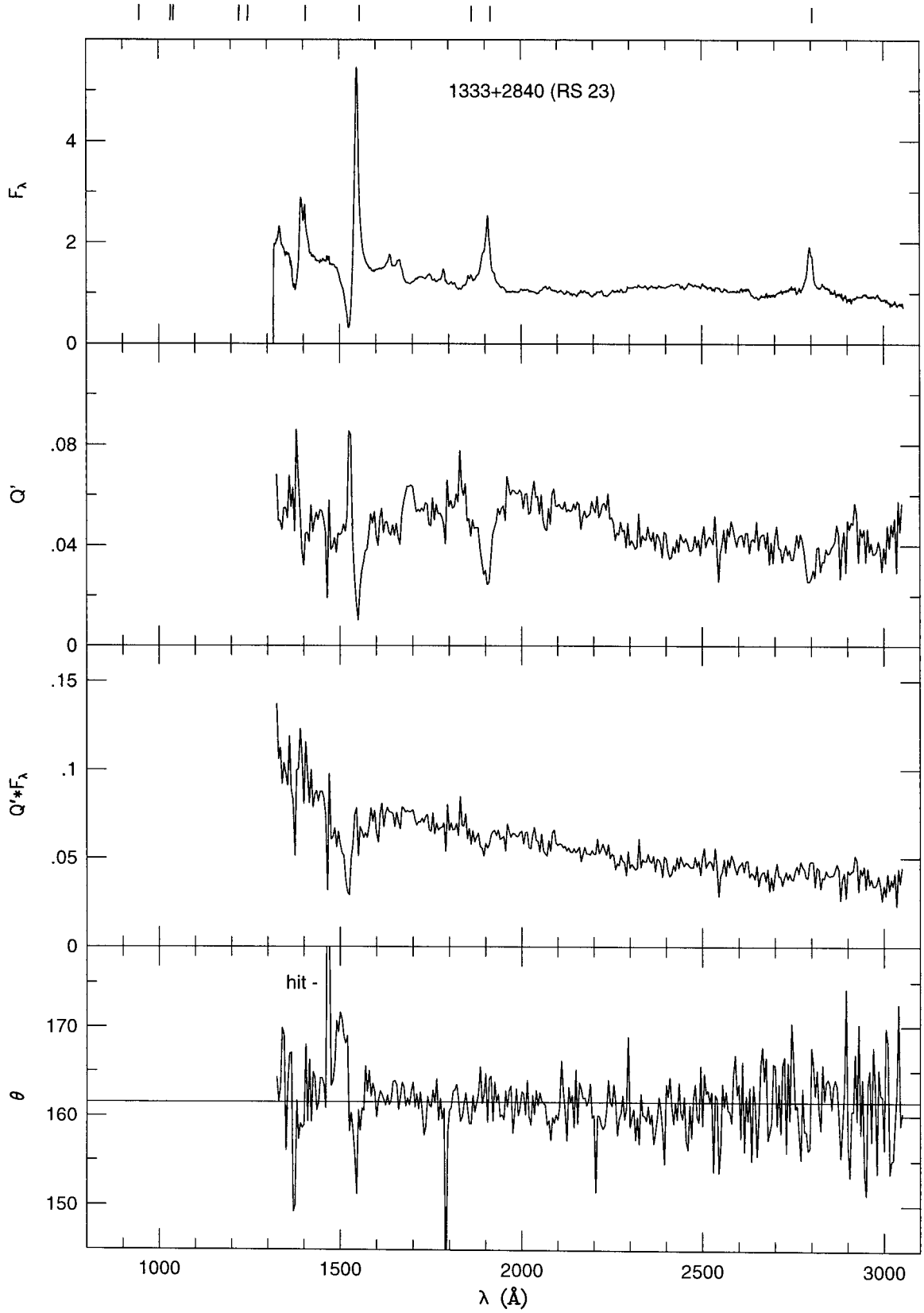

Figure 2.18: 1333+2840

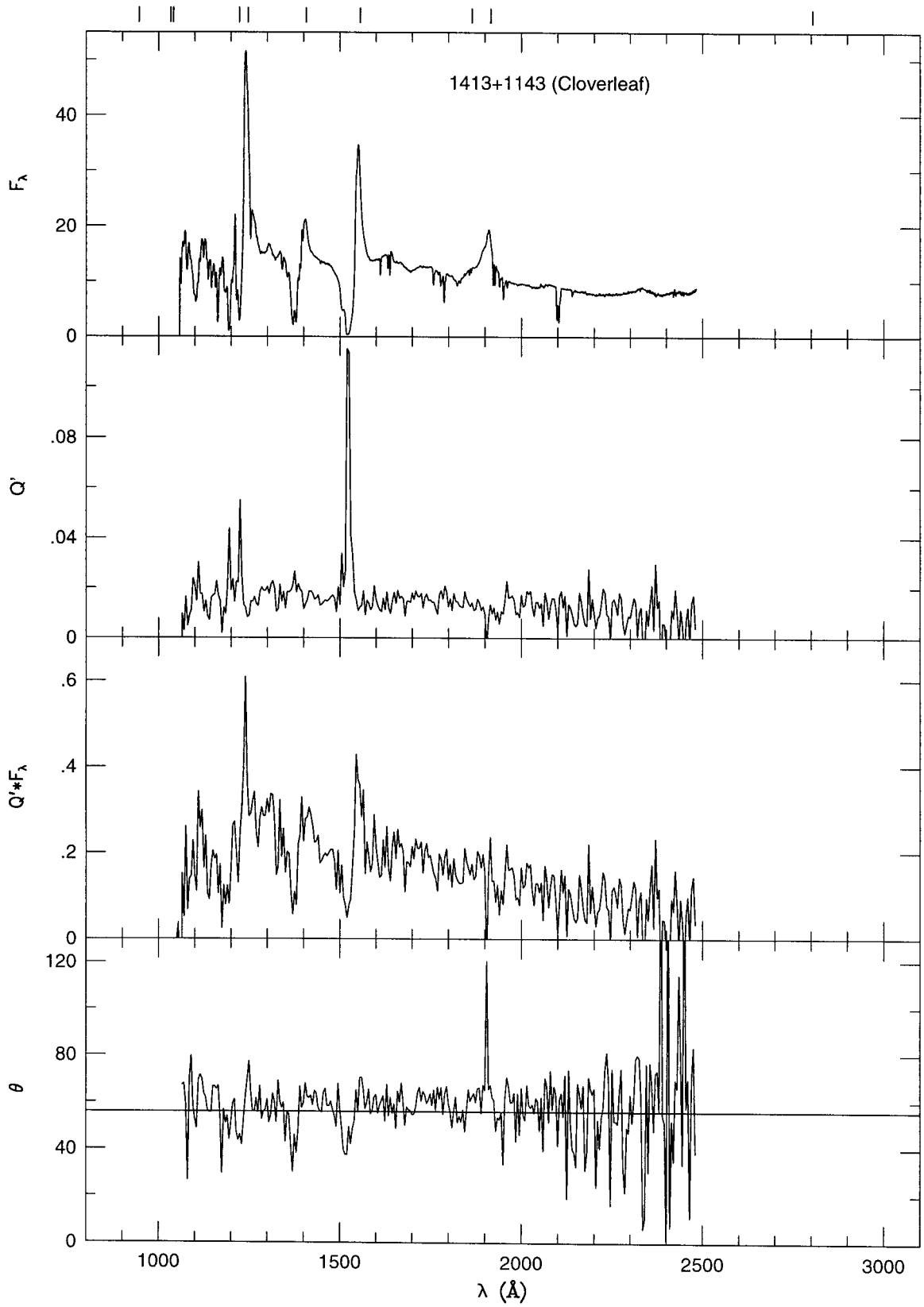

Figure 2.19: 1413+1143

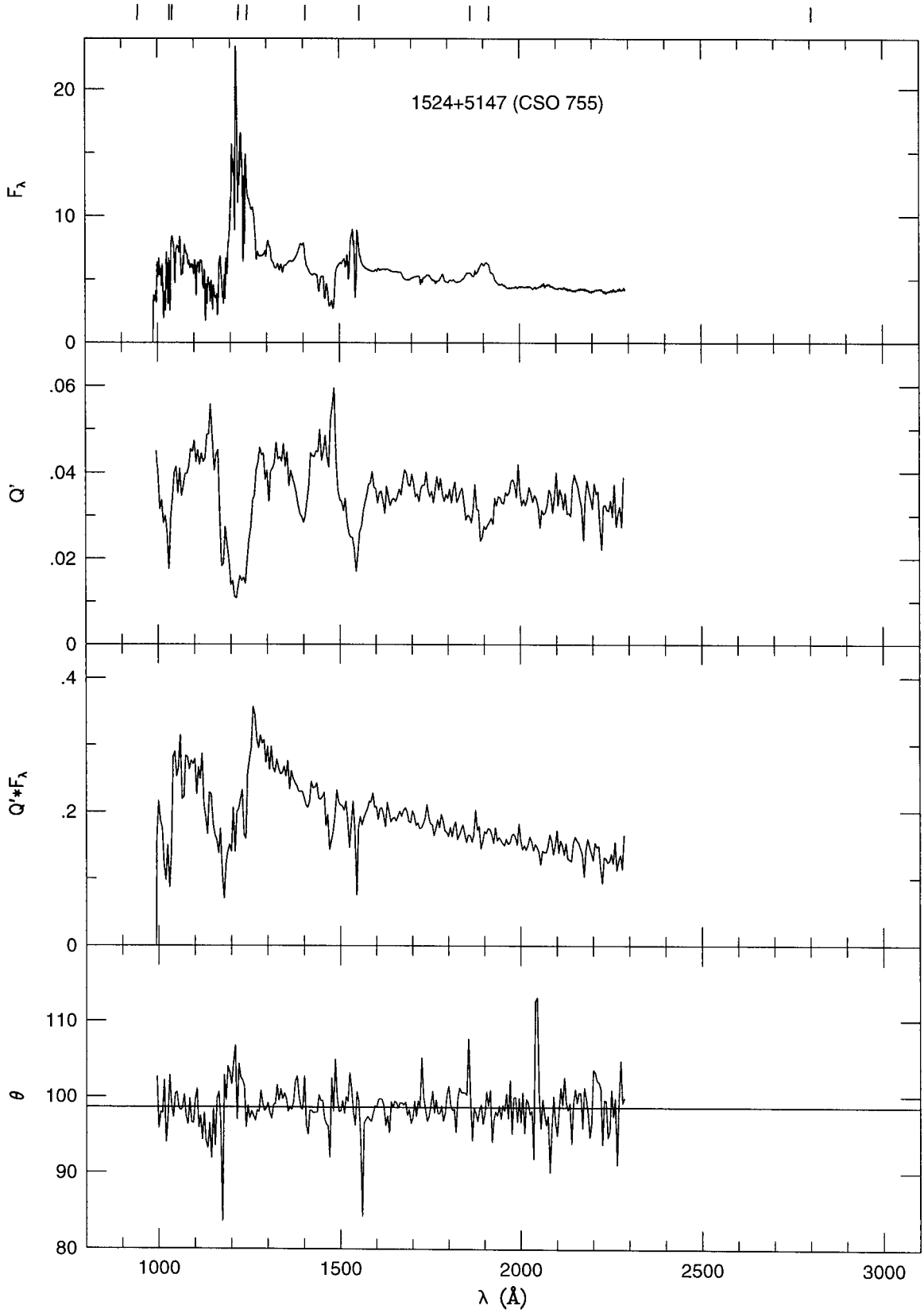

Figure 2.20: 1524+5147

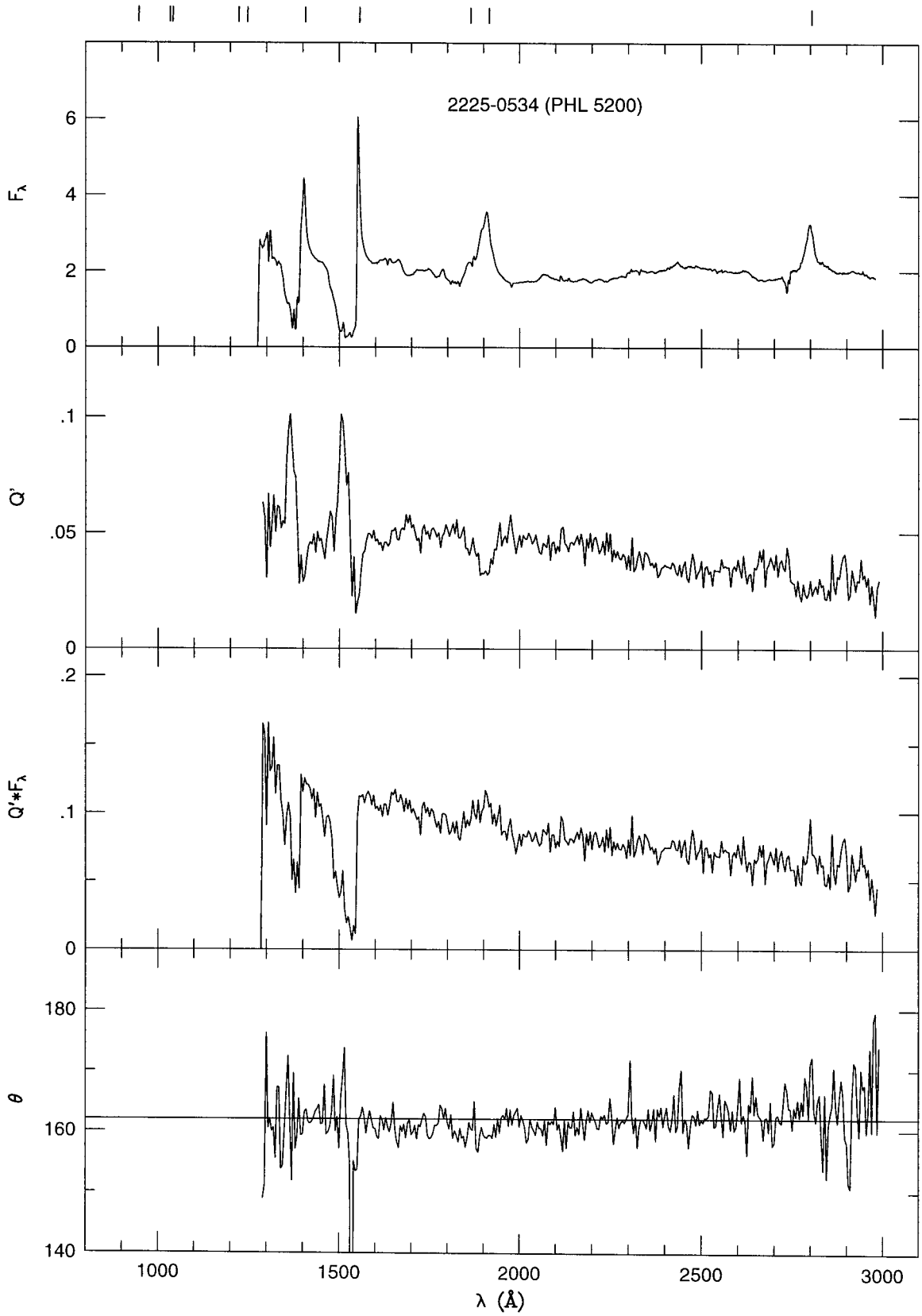

Figure 2.21: 2225-0534

Chapter 3 Palomar Spectropolarimetry

3.1 Sample Selection

A spectropolarimetric survey of BAL QSO was undertaken at Palomar to obtain continuum polarization measurements for a large sample of objects. The Keck survey (presented in Chapter 2) was originally intended to provide follow-up high S/N BAL and BEL polarization measurements of polarized objects from the Palomar survey. This strategy was partly successful, and 8 BAL QSO from the Palomar survey were re-observed at Keck. Because of poor weather at Palomar and good weather at Keck Observatory, 12 additional BAL QSO were observed at Keck. In cases of overlap between the two surveys, the high S/N data from Keck surpass the Palomar data in quality. The net result is that we have continuum polarization measurements of 20 objects from Keck and 16 objects from Palomar.

A total sample of 24 BAL QSO was observed with the Double Spectrograph polarimeter on the 5-m Hale telescope to determine their polarization spectra. Of these, 21 were selected from the (Weymann et al., 1991, WMF) sample of 40 BAL QSO. This was augmented by 3 other BAL QSO which fit into gaps in the observing schedule. The WMF sample was derived from the LBQS and a number of other surveys. This sample is useful because it contains most of the well-studied bright BAL QSO accessible from northern latitudes. However, due to haphazard selection and serendipitous discovery of most BAL QSO, the sample should not be considered uniform or complete. This heterogeneity, along with optical selection effects can insert biases (which are discussed in Chapter 4) into a systematic analysis of BAL QSO polarization.

The latitude of Palomar Observatory restricts observations to declinations $\delta > -30$ degrees. All objects have galactic latitudes $b > 30$ degrees, so interstellar polarization is typically less than 0.2%. (See Chapter 2 for a table of estimated interstellar polarization.) The visual magnitudes of the objects ranges from V=15.4-18.5.

IAU	Name	z	Mag	UT date	t(sec)	PA	
0021−0213		2.293	18.5	10 17 96	7200	0	np
0025−0151	UM 245	2.075	18.1	10 18 96	3600	25	np
0043+0048	UM 275	2.146	18.4	10 27 94	3600	25	
0059−2735		1.593	18.0	10 27 94	5400	0	
0119+0310	NGC470D8	2.10	18.1	10 18 96	3600	30	np,nw
0137−0153	UM 356	2.234	17.8	11 24 95	6480	30	np
0145+0416	UM 139	2.028	18.2	10 17 96	6000	20	np
0226−1024		2.256	16.9	10 27 94	3600	10	
0846+1540		2.912	17.9	10 18 96	3360	305	np,nw
0903+1734		2.773	17.4	11 24 95	6000	310	np
0932+5006		1.911	16.9	11 23 95	7500	220	np
1011+0906		2.262	17.3	02 23 96	7200	10	np
1212+1445		1.626	17.4	05 12 96	3600	20	
1231+1320		2.383	17.9	05 12 96	6000	45	
1232+1325		2.361	18.0	02 23 96	6000	0	np
1235+0857		2.887	17.5	05 13 96	3600	34	
1235+1453		2.686	18.4	05 13 96	7800	30	
1243+0121		2.790	18.1	02 23 96	5400	30	np
1442−0011		2.216	18.0	05 12 96	6000	35	
1443+0141		2.444	18.2	05 13 96	7200	35	
1700+5153	PG,IRAS	0.292	15.4	05 13 96	2400	130	nw
2154−2005		2.029	18.1	10 27 94	3600	0	
2201−1834		1.814	17.5	11 25 95	5400	20	np
				10 17 96	5400	5	np
2350−0045		1.624	18.5	10 18 96	7200	10	np

Table 3.1: Palomar observation log. The columns are 1) IAU designation, 2) Name, 3) redshift, 4) visual magnitude, 5) date, 6) exposure time, and 7) spectrograph slit PA. Non-photometric nights are marked "np," indicating clouds or fog. Objects not in the Weymann et al. (1991) sample are marked "nw." Data for columns 3 and 4 are primarily from the NASA Extragalactic Database (NED).

3.2 Observations and Data Reductions

The methodology of observation and data reduction is largely the same for the Palomar and Keck samples, and is primarily described in Chapter 2. Here we concentrate on the the issues which are peculiar to the Palomar data. BAL QSO were observed for 60-90 minutes, depending on their magnitude and polarization. Polarization spectra are measured with an accuracy of 0.06-0.7% in 50 Å (rest) bins.

The Palomar observations are summarized in Table 3.1. Spectropolarimetry was taken with the Double Spectrograph (Oke & Gunn, 1982) on the 5-m Hale Telescope. This system uses a dichroic filter to separate the blue and red portions of the spectra. Separate gratings are used to disperse the spectra in the blue and red arms of the spectrograph. This has the advantage of extending the available spectral range and optimizing the grating efficiency in each part of the spectrum. The dichroic filter has the additional advantage of blocking out second-order blue light in the red portion of the spectrum. The disadvantage of the Double Spectrograph is that there are twice as many spectra to reduce for each object.

We used the D55 dichroic filter, which splits the spectrum at 5500 Å. The transmittance of the dichroic is better than 90% red-ward of 5500 Å. This means that only a small fraction of the photons are lost to the dichroic filter. Some spurious polarization effects are introduced near the wavelength of the split which are difficult to calibrate out. Note that the polarization distortions are even greater for the D52 dichroic, so we did not use it. We set the gratings on the blue and red side to exclude the region of the dichroic split, so there is typically a 200 Å gap in our spectra. For most objects, this gap falls in between the C IV and C III] BEL. However, the gap falls in the C IV BAL region for three objects (0903+1734, 1235+1453, and 1243+0121), and on the C III] emission line for two objects (0932+5006 and 2201-1834).

We used a 300 groove/mm grating blazed for maximum efficiency at 3990 Å for the blue spectra. This gave a dispersion of 2.17 Å per pixel at the focus of the blue camera. We used a 316 groove/mm grating blazed at 7500 Å, which gave a dispersion of 2.46 Å per pixel in the red spectra. The wavelength coverage was typically 3600-5400 Å in the blue and 5600-8100 Å in the red. The Double Spectrograph can be used down to 3100 Å in the UV, but the low efficiencies at wavelengths less than 3600 Å are not adequate for polarimetric observations of faint QSO.

The spectrograph slit had a 2 arcsec aperture and a useful (un-vignetted) length of 35 arcsec in polarimetry mode. We used a wider slit at Palomar than at Keck because of the worse seeing. The spectral resolution was 6 Å in the red and 8 Å in the blue, slightly better resolution than in the Keck observations.

The polarimeter in the Double Spectrograph is an earlier version of the one at Keck. It is a dual-beam instrument with rotating half-wave plate analyzer. The calcite beam-splitter has a slightly different design from the Keck beam-splitter. The main difference is that there is no focus compensation between the ordinary and extraordinary beams. The foci of the cameras were typically set at a compromise position between the optimal foci of the two beams. The polarimeter sits above the dichroic in the optical path, so it serves both the blue and red arms of the spectrograph.

The detectors in the blue and red cameras were both 800×800 pixel CCDs. The blue detector suffered from dead columns and transient gain variations near the blue end of the spectrum. In addition, there was a jump in the efficiency in a segment of one beam due to an experimental coronene application on a localized portion of the chip. We located our spectra on chip locations with the best cosmetics, but the flux spectra may still be afflicted by nonlinearities at a level of 5% in localized wavelength regions. In fact, the flux standards of Oke (1990) were taken with the Double Spectrograph and suffer from some of the same defects. These glitches in the system efficiency were at a low enough level to cause negligible damage to the polarization spectra.

The red camera CCD chip suffered from a warped surface, which caused focus variations along the spectra. We set the focus to provide the sharpest image along the largest possible wavelength range. These focusing difficulties should not affect the polarimetry (except for lowering the S/N) since focusing and seeing variations are mitigated by the dual-beam method. During the last year of our observing program (1995-1996), the red camera was upgraded to a 1024×1024 pixel CCD and other changes were made to its optics. Since the completion of our program, the blue camera has also been upgraded. The upgrades of the blue and red cameras have removed the problems of multiple detector flaws and some of the focusing difficulties.

3.3 Flux and PA Calibrations

The Palomar calibration procedures are quite similar to the Keck procedures, except they were made separately for the blue and red sides of the spectrograph. The following is a quick recapitulation of the general calibration procedures. (See Chapter 2 for a detailed discussion.) Flux calibrations were made using the standards of Oke (1990). Spectra were corrected for absorption by the atmospheric oxygen and water bands. The flux spectra are all well-matched across the dichroic split, which enhances confidence in our flux calibrations.

The PA correction curve was determined using observations of bright stars through a UV Polaroid. The PA zero-point was determined using broad band polarimetric standards (Schmidt et al., 1992). There appears to be a 3 degree discrepancy between the Palomar and Keck observations of secondary standard Hiltner 102. The origin of this discrepancy is unknown, so the data from the two telescopes were calibrated independently. However, a comparison of Palomar and Keck BAL QSO PA values does not reveal any apparent systematic differences in the PA zero point. Before PA correction, the polarization data were corrected for instrumental polarization, which is discussed in the next section.

3.4 Instrumental Polarization

There is a large instrumental polarization correction for the Palomar observations taken after 10/94. Figure 3.1 shows the mean instrumental polarization curves for 11/95-10/96 , derived from observations of null polarization standards. The curves are displayed in instrumental coordinates for a slit position angle of $PA = 0$ degrees. The blue curve is corrected for an extra reflection at the dichroic filter, which is equivalent to a 90 degree rotation of the half-wave plate. All data were corrected by fitting splines to the raw instrumental polarization curves and subtracting them from the Stokes parameters. The instrumental polarization correction is of the same magnitude as the typical BAL QSO continuum polarization, so it is important to use accurate curves. The instrumental polarization rises from 0.6% at 8100 Å to 2% at 3700 Å . Except for some noise just blue-ward of the dichroic split, the curves match across the dichroic split.

The instrumental polarization varied less than 0.2% from run to run, and the small variations were probably due to weak polarization in the null standards. The one exception is the 10/94 observing run, where there was no measurable instrumental polarization.

Typically 2 or 3 null standards were averaged to obtain the correction curve for each run, reducing the effect of slight interstellar polarization in some standards. It is assumed that the correction is additive and does not depend on the true polarization of the object. This is similar to interstellar polarization correction, where the intervening dust can be approximated by a single partial-polarizing screen. The second-order corrections are less than the linear correction by a factor of the object polarization P_c (Goodrich, 1986), so are of order 0.01% in our observations. We checked the accuracy of the correction by comparing Palomar and Keck observations of the same objects. These agree to within the uncertainties of the measurements, giving confidence in the correction (see Fig. 3.2). However, residual instrumental polarization effects may give rise to some of the rotations seen in the blue PA spectra of a few objects (See, e.g., Fig. 3.4).

The Double Spectrograph and polarimeter are mounted on a ring at Cassegrain focus. When the instrument is rotated by the angle θ, the PA of the instrumental polarization rotates by 2θ in instrumental coordinates. This means the source of instrumental polarization is not the instrument, but either the primary or secondary mirror of the telescope. The 10/94 observing run showed little or no instrumental polarization. It is possible that cleaning and subsequent realignment of the telescope secondary mirror is to blame for the large increase in instrumental polarization between 10/94 and 11/95. If the secondary mirror is not aligned perfectly normal to the primary mirror, then the projection of the secondary will be slightly elliptical and induce a net polarization. This is also the reason why polarimetry must be done at Cassegrain instead of Naysmith focus.

The chromatic nature of the instrumental polarization suggests that it is not simply due to misalignment. Another possibility is spotty re-aluminization of the primary mirror. If the surface of the primary mirror is not evenly aluminized, this can induce a net polarization. The wavelength dependence could come from tarnished spots which selectively absorb blue light. In fact, re-aluminization of the 200 inch primary at Palomar is a very tricky business, and sometimes gives less than uniform coverage. There is similar difficulty with instrumental polarization in Lick Observatory spectropolarimetry (Martel, 1996), which is also due to irregular aluminization of the telescope mirrors. The wavelength dependence of the instrumental correction is somewhat different at Lick; it does not increase monotonically to the blue as at Palomar. Also, the magnitude of the effect is somewhat less ($\sim$ 1.5%) at Lick.

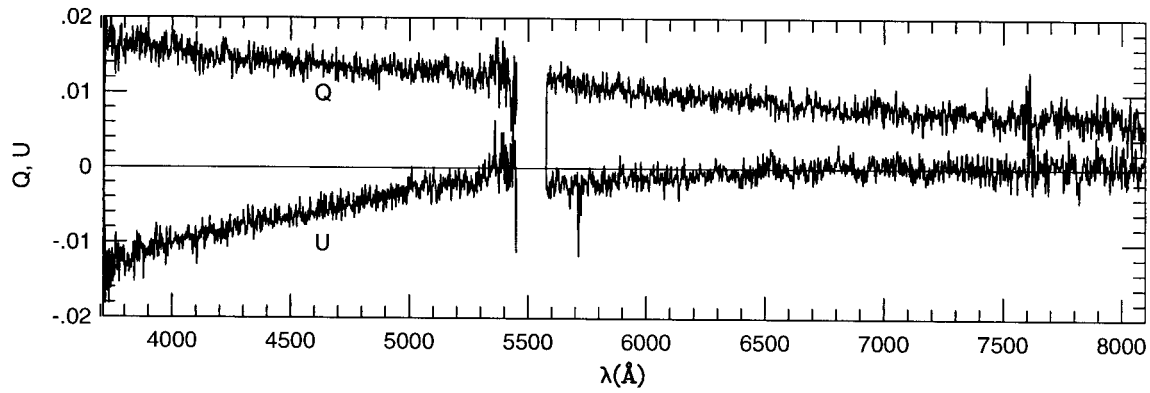

Figure 3.1: Mean Palomar instrumental polarization correction fraction for Stokes Q and U parameters. Note that these are in instrumental coordinates, not sky coordinates.

3.5 Continuum Polarization

As we did for the Keck data, we measured the continuum polarization of the Palomar BAL QSO in two continuum bands, one on either side of C III] λ1909 (1600-1840 Å and 1960-2260 Å). These regions are relatively free from contaminating emission lines and give a good estimate of the continuum polarization. For most objects, only one of these two bands was available and the other fell in the dichroic gap. Except for a few observations which were heavily affected by clouds, we were able to measure continuum polarization with an uncertainty of $< 0.3\%$. This approaches the level of the uncertainty in the instrumental polarization curve.

The results of our continuum polarization measurements at Palomar are presented in Table 3.2. The polarizations of the BAL QSO in the Palomar sample are similar to the polarizations in the Keck sample, ranging from 0.2-3.5%. We have identified one new HPQ in the sample–1232+1325, with $P_2 = 3.5 \pm 0.2\%$. This is a low-ionization BAL QSO, with BEL and BAL properties that are quite dissimilar from the other HPQ in our total sample. Several objects (8/24) are rated as polarization non-detections, and have $Q/\sigma_Q < 3$ and $U/\sigma_U < 3$. We list Q and U only for these objects, since P and PA are biased at low S/N.

We present a comparison of polarization and PA values for objects measured both at Palomar and Keck in Figure 3.2. All of the measurement pairs are within 2σ of the equality line. There is no indication of gross systematics or variability between the two sets. We study the continuum polarization variability in Chapter 4, to help determine the source of polarized radiation.

The continuum polarizations of the Palomar BAL QSO are only weakly wavelength-dependent. For many objects, the S/N in the polarization spectra are not great enough to detect the $\sim 0.5\%$ variation which we typically see across the Keck polarization spectra. In retrospect, Palomar spectropolarimetry can only measure the wavelength dependence in the brightest and most highly polarized objects, which we typically re-observed at Keck. However, we did not know the wavelength dependence of BAL QSO polarization would be so weak before we began this project. The observations are useful in ruling out polarizing mechanisms such as Rayleigh scattering, which would induce a polarization $P \sim \lambda^{-4}$. The analysis of the polarization wavelength dependence in Chapter 4 concentrates on the Keck data. However, the addition of eight objects from the Palomar sample helps to bolster the

case that polarization wavelength dependence is weak in all BAL QSO. We would also like to stress that spectropolarimetry was essential to ensure that the continuum polarization values would not be contaminated by emission lines and absorption lines.

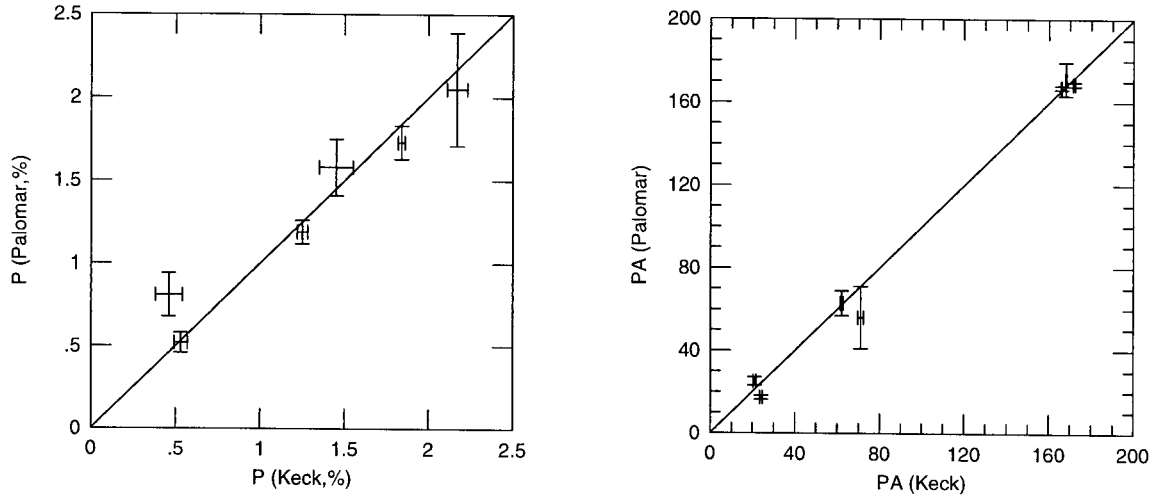

Figure 3.2: Comparison of Palomar and Keck polarization measurements. Note that there are no systematic differences between the two data sets. Also, there is no evidence of intrinsic variability between the sets.

3.6 Individual Objects

Polarized BAL QSO (and a few interesting unpolarized BAL QSO) are discussed individually in this section. Polarized BAL QSO are shown in Figures 3.3-3.11. Spectropolarimetry of objects which were observed at Keck are presented in Chapter 2. We show the Palomar flux spectra of these objects in Figure 3.12, which typically reach further into the blue than the Keck flux spectra. For example, the Palomar spectrum of 0059-2735 shows the entire C IV BAL, which was not accessible at Keck. The flux spectra of the polarization non-detections are displayed in Figure 3.13.

1. 0025-0151 (UM 245). This object has very shallow BAL troughs, punctuated by narrow absorption components. The C IV BAL varied between 11/95 and 10/96. The presence of variability in such a weak BAL suggests that weak BAL may be missed in some QSO, depending on the BAL equivalent width in the discovery spectrum. This would decrease the apparent BAL QSO fraction. The polarization is low, and may increase to

IAU	Name	$P_1\% \pm$	$P_2\% \pm$	$PA \pm$
0025−0151	UM 245	....	0.57 0.16	108 9
0059−2735		1.45 0.17	....	168 8
0137−0153	UM 356	....	0.46 0.13	71 15
0145+0416	UM 139	....	2.14 0.10	126 1
0226−1024		....	1.84 0.10	166 1
0903+1734		0.53 0.06	....	62 6
0932+5006		1.17 0.30	1.25 0.07	172 1
1011+0906		....	2.00 0.08	132 2
1212+1445		2.17 0.34	....	24 1
1231+1320		....	0.17 0.08	91 14
1232+1325		....	3.49 0.19	92 3
1235+0857		2.16 0.15	....	21 2
1235+1453		0.75 0.13	....	175 12
1243+0121		1.68 0.20	....	136 4
1700+5153	PG,IRAS	....	1.07 0.04*	53 1
2154−2005		....	0.90 0.17	142 8
IAU	Name	Q ±	U ±	band
0119+0310	NGC470D8	0.34 0.16	0.00 0.20	2
0021−0213		0.28 0.12	-0.42 0.23	2
0043+0048	UM 275	0.12 0.19	0.06 0.19	2
0846+1540		0.30 0.33	0.01 0.36	1
1442−0011		0.63 0.66	-0.50 0.38	2
1443+0141		0.80 0.33	0.29 0.27	2
2201−1834		0.16 0.07	0.00 0.12	2
2350−0045		-0.58 0.53	0.09 0.30	1

Table 3.2: Palomar continuum polarization measurements. The objects are split into polarization detections and non-detections (top and bottom sections). P_1 and P_2 are the polarizations in two narrow wavelength bands (1600-1840 Å and 1960-2260 Å, rest) to either side of C III] λ1909. (* 1700+5153 was measured in the band 3700-4100 Å, rest.) PA is the electric vector position angle in degrees. For most objects, only one of the two bands is available, due to the dichroic split. Stokes Q and U are listed for the objects which are undetected in polarized flux ($< 3\sigma$).

the blue. The PA spectrum is quite noisy and the apparent rotation in the blue is not statistically significant. The PA only settles on a significant value once the polarization rises above the noise threshold. The true PA may be 90 degrees, a value 2σ away from that given in Table 3.2. This would cause a small underestimate of the polarization.

2. 0145+0416 (UM 139). This object has a trough which is similar in shape and depth to 1246-0542. There is a deep main trough superimposed on a broader trough of moderate depth. However, the main trough is less detached from the BEL in 0145+0416. The continuum polarization is moderate and may rise to the blue. There is a strong continuum PA rotation from 126 degrees in the red to 98 degrees in the blue. The rotation starts blue-ward of the C III] BEL, similar to the rotations in 0019+0107 and 0932+5006 (see Chapter 2). However, it is not accompanied by a red polarization spectrum like 0019+0107 (Figure 2.2).

A strong PA rotation requires at least two sources of polarized light with different PA and different spectral slopes. The maximum interstellar polarization is 0.25%, which could only cause a PA rotation of < 2.4 degrees. We conclude that the PA rotation is due to multiple polarizing agents intrinsic to the QSO. Perhaps there is a competition between electron scattering in the BELR and dust scattering in a warped torus, which is tilted with respect to the symmetry axis of the BELR.

3. 0846+1540 (Fig. 3.13). The data for this BAL QSO are noisy, and the polarization is low. It has low equivalent width associated absorption line (AAL) systems, which do not qualify as BAL using the WMF balnicity criterion (Weymann et al., 1991). We observed it during a scheduling gap to see if objects with narrow or weak associated systems have polarization properties similar to BAL QSO. This question is not answered by viewing a single object, especially since this one has a $P < 0.8\%$ (2σ) upper limit. With such a polarization, it could fit into either the BAL QSO or non-BAL QSO polarization distribution (Chapter 4).

If a moderate or high polarization QSO with AAL could be found, it would be useful to determine the trough polarization at Keck. If the polarization showed a rise in the trough, the intrinsic nature of the system would be confirmed. This would be a difficult observation since the AAL troughs are shallow and narrow and would show only a small polarization effect. In addition, some of the BAL QSO in our Keck sample show low-velocity AAL which do not affect the polarization. If this is true of all AAL, then spectropolarimetry would

demonstrate that AAL have a different geometry and a larger local covering factor than BAL.

4. 1011+0906 (Fig. 3.5). This is a low-ionization BAL QSO, with a prominent Al III BAL and unusually strong Al III BEL. There are two intervening metal absorption line systems, one of which falls on the C III]/Al III BEL. The continuum polarization is a moderate 2% and shows no significant variation with wavelength. The marginal PA rotation at the blue end of the spectrum is of low significance. Both the total flux and polarized flux spectra are redder than spectra of typical high-ionization BAL QSO, suggesting dust extinction and reddening. There can only be a small difference between the reddening of the direct and scattered flux, otherwise there would be a large polarization wavelength dependence.

5. 1231+1320. This is another low-ionization BAL QSO with a strong Al III BAL and a large ratio of Al III/C III] emission. The spectrum is extremely unusual for a BAL QSO, for a number of reasons. There are multiple high velocity sub-troughs in Al III, C IV and Si IV, with the highest velocity sub-trough the deepest. The Si IV and C IV BAL overlap because of their large velocity ranges. The Si IV BAL appears to be deeper in some of its sub-troughs than the C IV BAL. This would imply an unusually low ionization state. However, some of the extra depth in the Si IV trough may be due to extremely high velocity C IV absorption. The Lyα/N V BEL is quite weak. This could be due to reddening of the spectrum, or absorption of the BEL by the Si IV BAL. Unfortunately, while the flux spectrum of 1231+1320 is quite interesting, the polarization is very weak and only marginally detected at $P_2 = 0.17 \pm 0.08$. Such a low polarization is only seen in two other BAL QSO–0043+0048 and 2201-1834, which don't have much else in common with 1231+1320.

6. 1232+1325. This is a low-ionization BAL QSO, which like 1011+0906 and 1231+1320, has a strong Al III BAL and a large Al III/C III] BEL flux ratio. The C IV and Lyα/N V BAL are saturated and go nearly black in the low velocity portion of the trough, which is reminiscent of 0059-2735 (Fig. 3.12). However, unlike the other low-ionization BAL QSO in our sample, there is no indication of reddening in the flux spectrum and the strong Lyα/N V BEL is more characteristic of a high-ionization object. The Si IV trough shows sub-structure at high-velocity which is not apparent in the C IV BAL because of its saturation.

This object officially qualifies as an HPQ, with continuum polarization $P_2 = 3.5 \pm 0.2\%$.

This makes it a rare QSO in three senses–BAL, lo-ionization, and HPQ. It definitely deserves further study with the Keck Telescope. Unfortunately, we were not able to fit this object into our Keck observing schedule. Now there are four known high polarization BAL QSO (RS 23, PHL 5200, CSO 755, and 1232+1325). Their BEL and BAL show a wide range of properties, suggesting that high polarization is independent of these (Chapter 4).

It is difficult to determine the wavelength dependence of the continuum polarization of 1232+1325 from our Palomar data because there are very few continuum windows in the spectrum. The polarization is roughly constant from 1700-2350 Å and there is no PA rotation. There are also hints that P drops in all of the BEL.

7. 1235+1453. This object has unremarkable flux and polarization spectra. The polarization is low and wavelength-independent. The interesting deep part of the C IV BAL is lost in the dichroic split between the red and blue spectra.

8. 1243+0121. The ragged velocity profile of the C IV BAL is similar to that of 0137-0153 (Fig. 3.12), with the deep portion of the trough only slightly detached from the BEL. There is a deep O VI/Hβ BAL. The continuum polarization is moderate and wavelength-independent. The polarization drops at all of the BEL, though this is of low significance in each instance.

9. 1700+5153 (PG, IRAS). This low-redshift BAL QSO has Mg II and high ionization BAL in the observed UV (e.g., Pettini & Boksenberg, 1985). There is no evidence of a Na I BAL. PG 1700+5153 belongs to a class of QSO with strong Fe II emission and extremely weak [O III] emission, which includes 07598+6508 (Boroson & Meyers, 1992). This is one of the few known low-redshift BAL QSO, which are difficult to identify because the BAL are in the UV. It is bright and nearby, allowing us to take high S/N spectropolarimetry of it from Palomar. The continuum polarization is low (1.1%), and increases weakly to the blue. This is the same behavior seen in the UV spectra of high-z BAL QSO, making it an extremely broad-band phenomenon which covers a range of at least 900-6400 Å . P drops in Hβ and the Fe II emission lines, so they do not show up in the polarized flux spectrum.

There is a moderate PA rotation (12 degrees) across the continuum. This may be partly due to interstellar polarization, which can be as large as 0.3% at the Galactic latitude of 1700+5153 (b=37.8 degrees). Depending on the orientation of the interstellar polarization, it could cause a rotation of up to 7 degrees. It is necessary to measure a nearby interstellar polarization probe star to determine the proper correction.

This is one of the very few BAL QSO which is bright enough and near enough to have a resolved radio structure, which consists of two point sources separated by 1 arcsec at a PA of roughly 100 degrees (Kellermann et al., 1994). This can neither be considered parallel nor perpendicular to the PA of the optical polarization vector at $PA = 53$ degrees. This is contrary to the suggestion of Goodrich & Miller (1995), who claim that the polarization PA and radio axis are parallel in PG 1700+5153, which would be evidence for scattering in the equatorial plane. If the radio structure is due to a weak double-lobed jet, it is likely that it is not well collimated and may not give a reliable indication of the spin axis of the central black hole. The misalignment of the radio jet and polarization axis is therefore not surprising and may not be fundamental to the QSO structure.

Ground-based and HST images have shown that there is an interacting companion galaxy to the QSO (Stockton et al., 1998, and references therein), located 2 arcsec to the north at $PA \simeq 0$ degrees (roughly perpendicular to the radio axis). Keck spectroscopy by Canalizo & Stockton (1997) shows a strong starburst component in the companion, which may be indirectly related to the QSO activity, and has a flux $\sim 1000\times$ weaker than the QSO. We see no evidence of this stellar component in our spectrum, which is not surprising given its faintness and location on the edge of our slit.

10. 2154-2005. This object has very weak BAL which appear to have varied in depth from the spectra of Weymann et al. (1991). The C IV BAL is shallower in our spectrum. This is similar to the case of 0025-0151, which also has weak variable BAL. The continuum polarization is low and rises gradually to the blue, and the PA is independent of wavelength. 2154-2005 has typical BAL QSO polarization characteristics in spite of its unusually weak BAL.

11. 2201-1834 (Fig. 3.13. This is an unusual BAL QSO in several ways. First, the spectrum is highly reddened. There aren't any low-ionization BAL, which are typically present in reddened BAL QSO. The C IV BAL has a very low equivalent width (16.3 Å), which is also atypical of reddened BAL QSO. Finally, the continuum has very low polarization ($P = 0.16 \pm 0.07$), which is unexpected for an object with high extinction. Perhaps we are viewing a normal high-ionization BAL QSO through a foreground dust screen which is not directly connected to the AGN phenomenon, such as dust in the host galaxy ISM. The dust grains are not aligned, or they would induce a measurable polarization.

Figures 3.3-3.11.

Palomar spectropolarimetry of 9 BAL QSO. From top to bottom the four panels display (1) total flux F_λ, (2) polarization fraction (rotated Stokes Q'), 3) polarized flux $Q' \times F$, and 4) electric vector position angle θ. Total and polarized flux are plotted in units of 10^{-16} erg/s/cm^2/ Å . Prominent emission lines are indicated in the top panel of Figure 3.3, and tick marks in the other figures identify the same set of lines. The continuum PA from Table 3.2 is indicated by a horizontal line. Individual objects are discussed in the text.

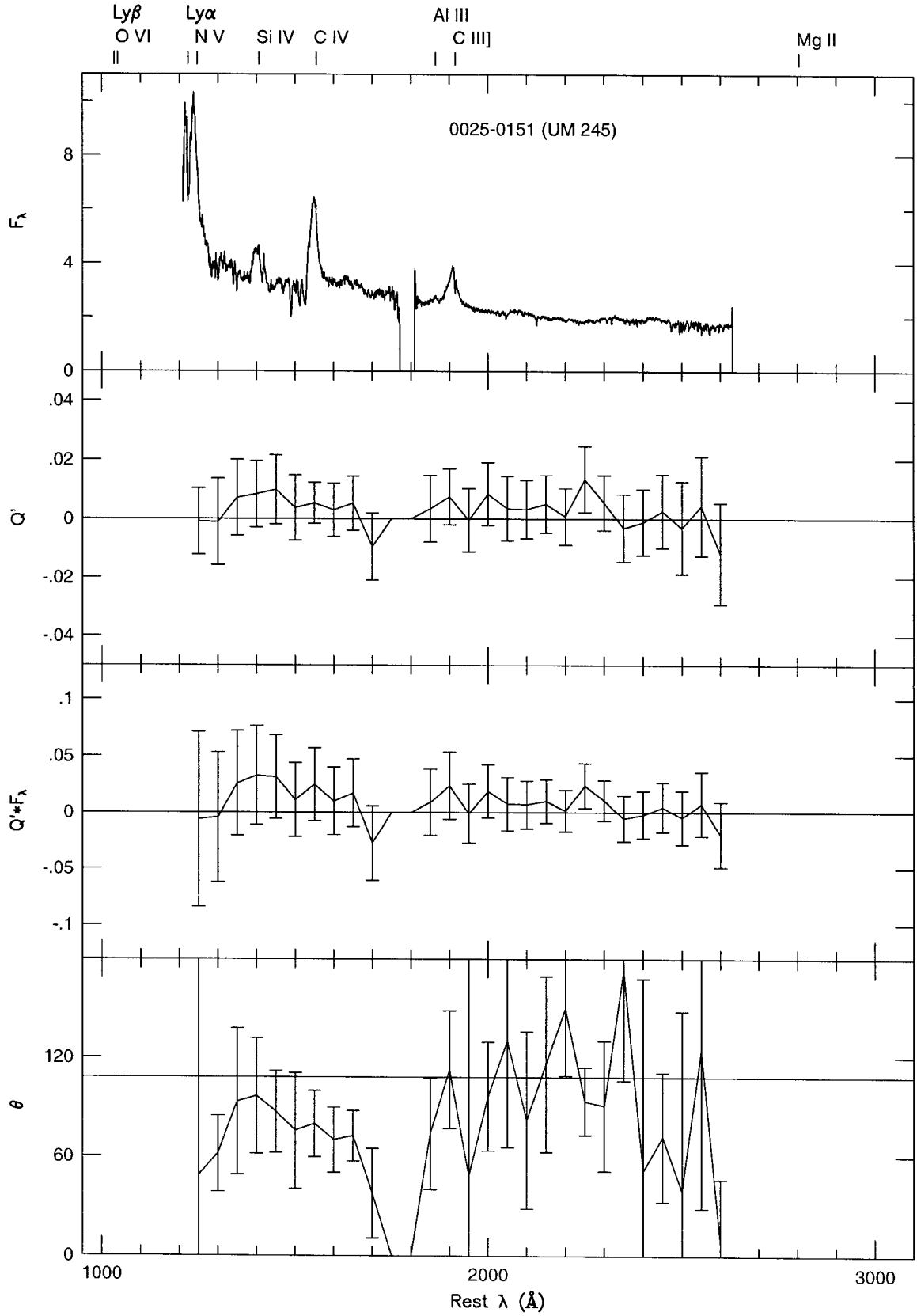

Figure 3.3: 0025-0151.

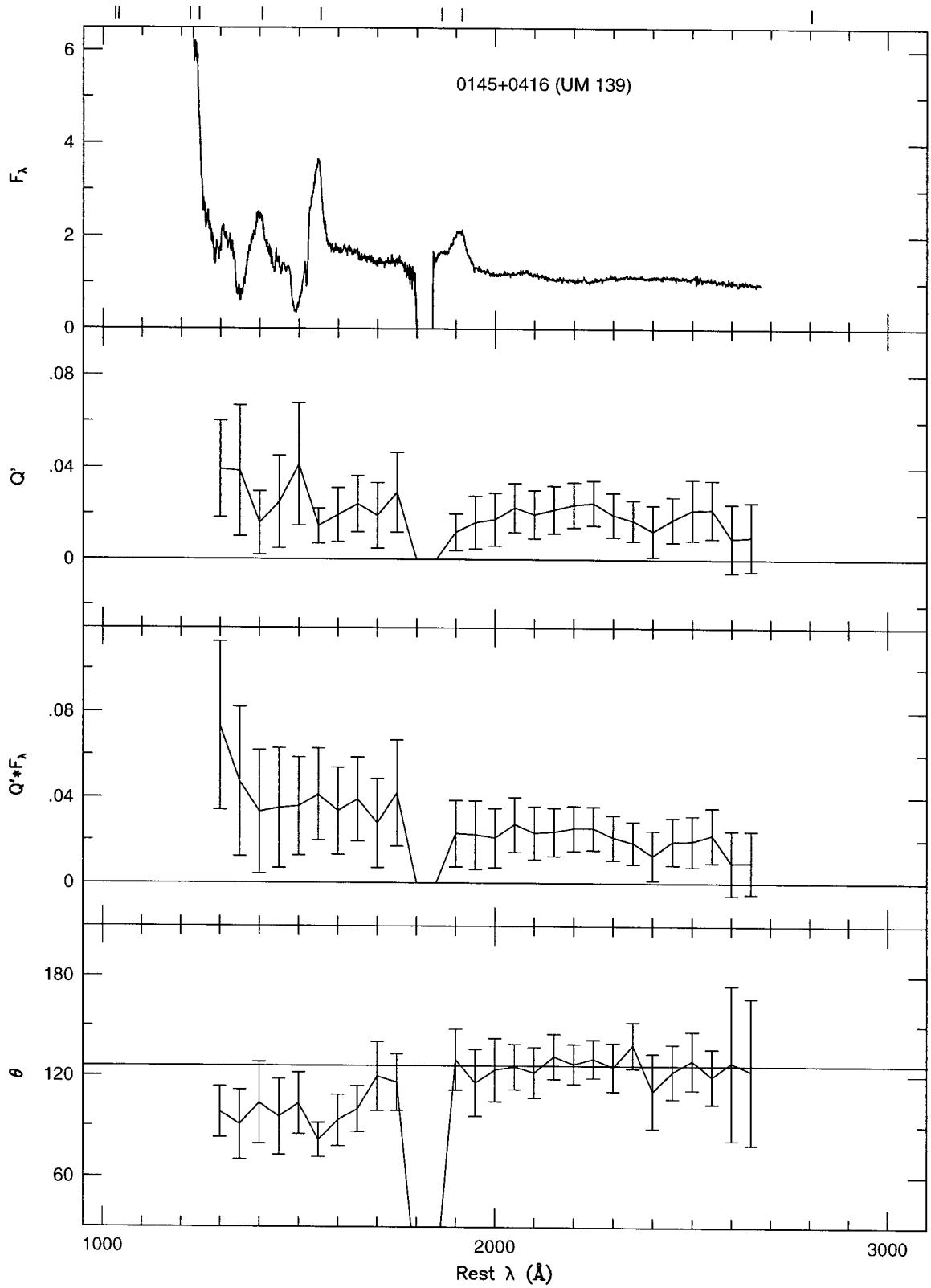

Figure 3.4: 0145+0416.

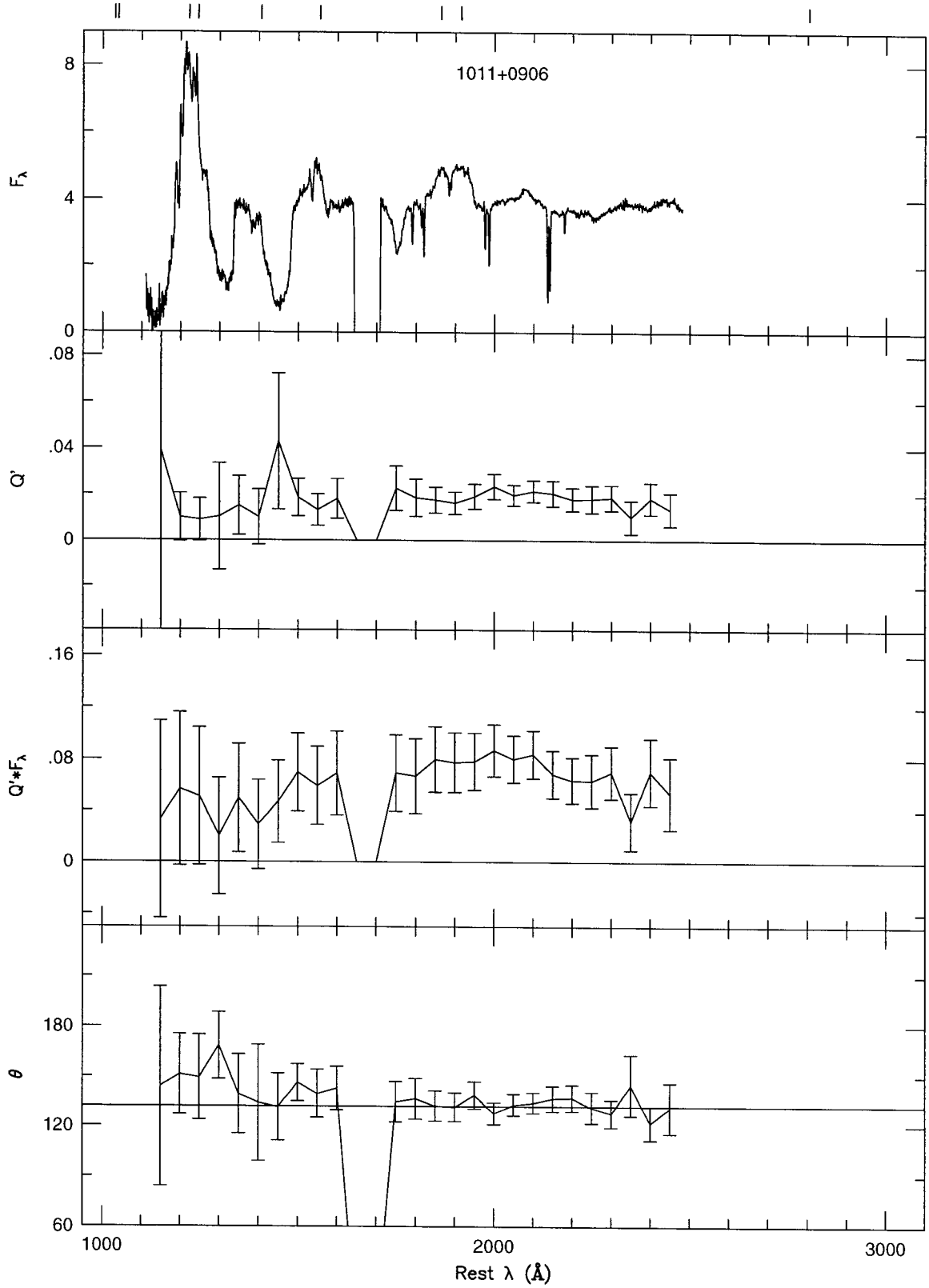

Figure 3.5: 1011+0906.

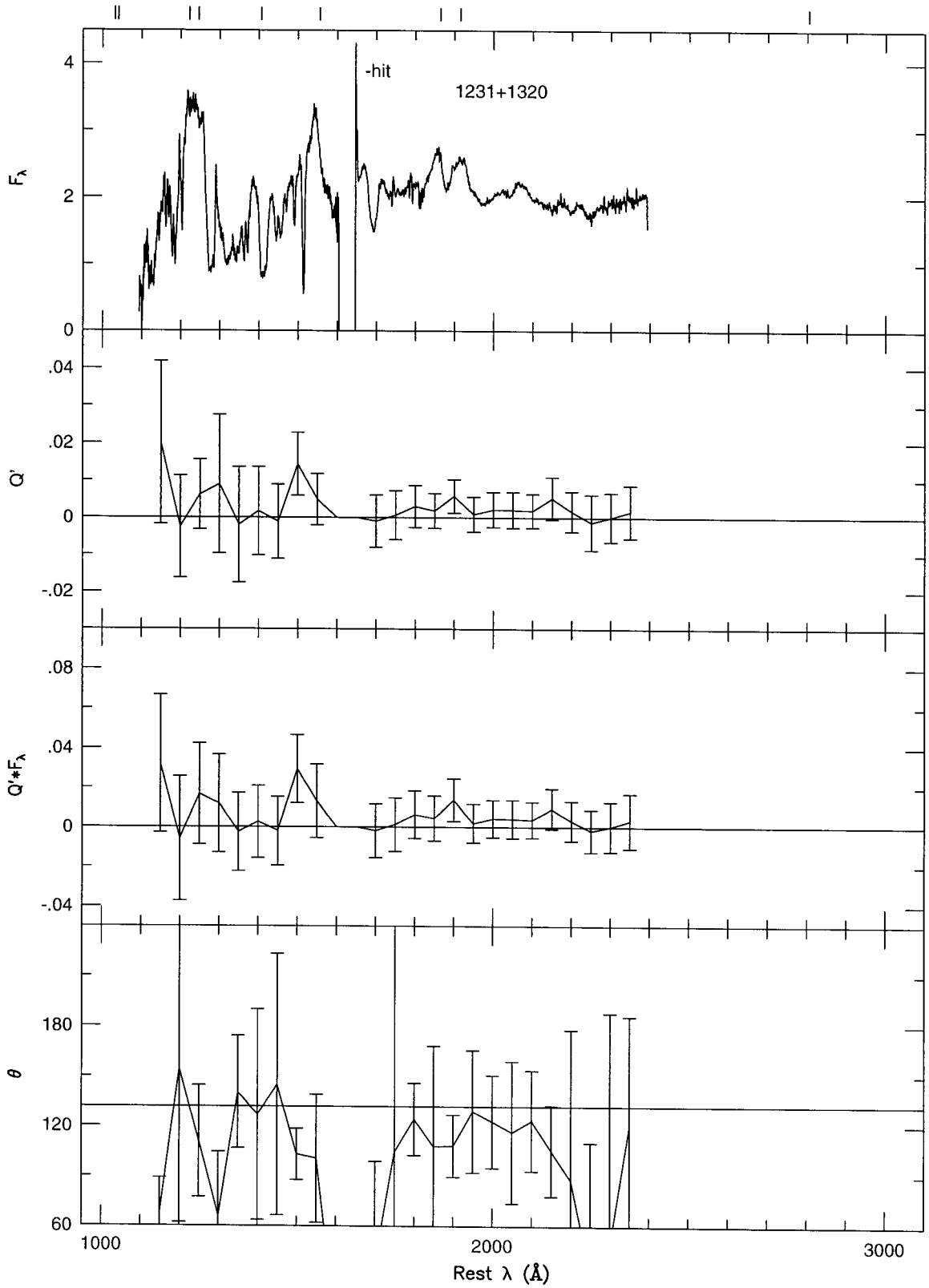

Figure 3.6: 1231+1320.

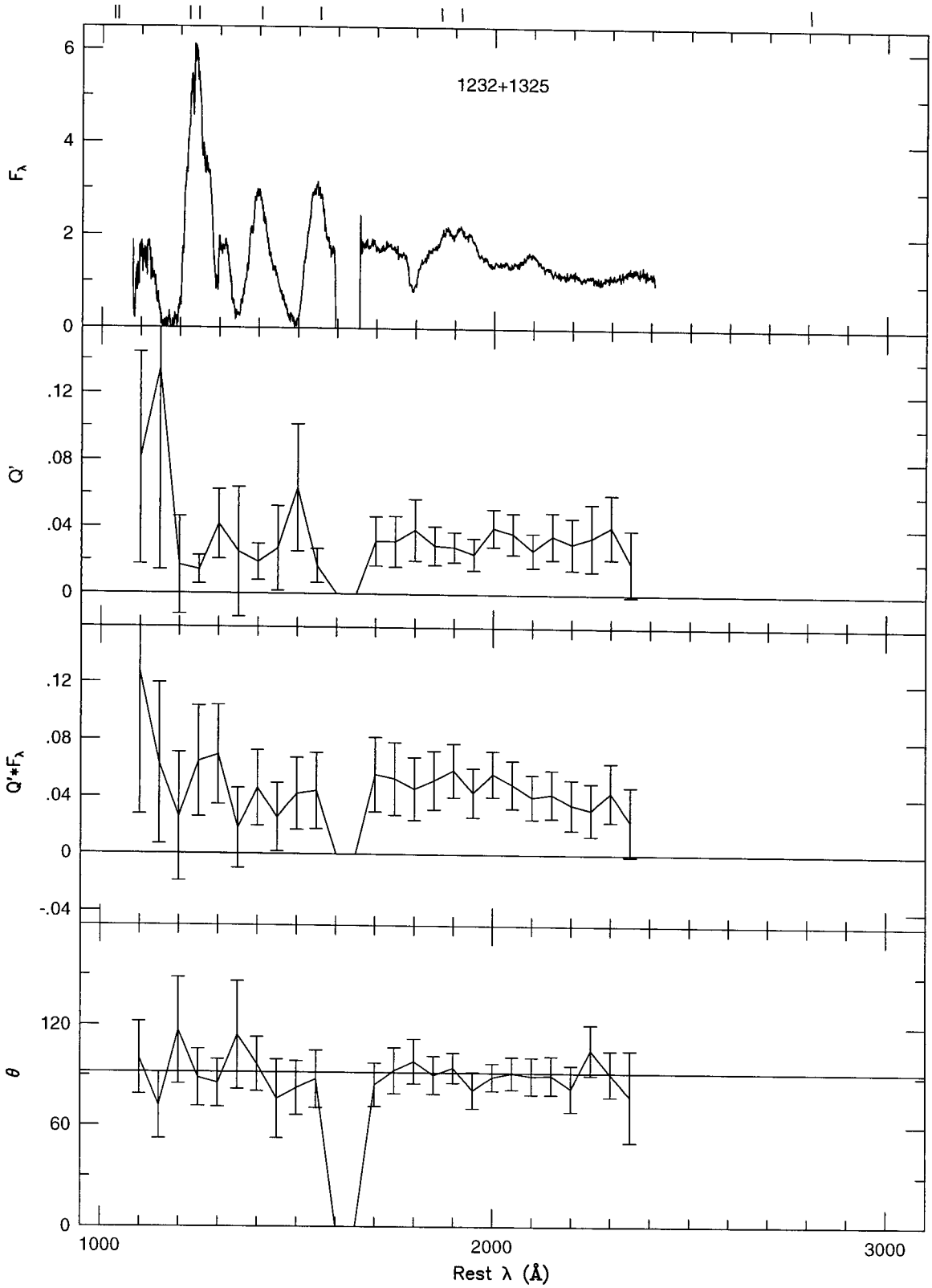

Figure 3.7: 1232+1325.

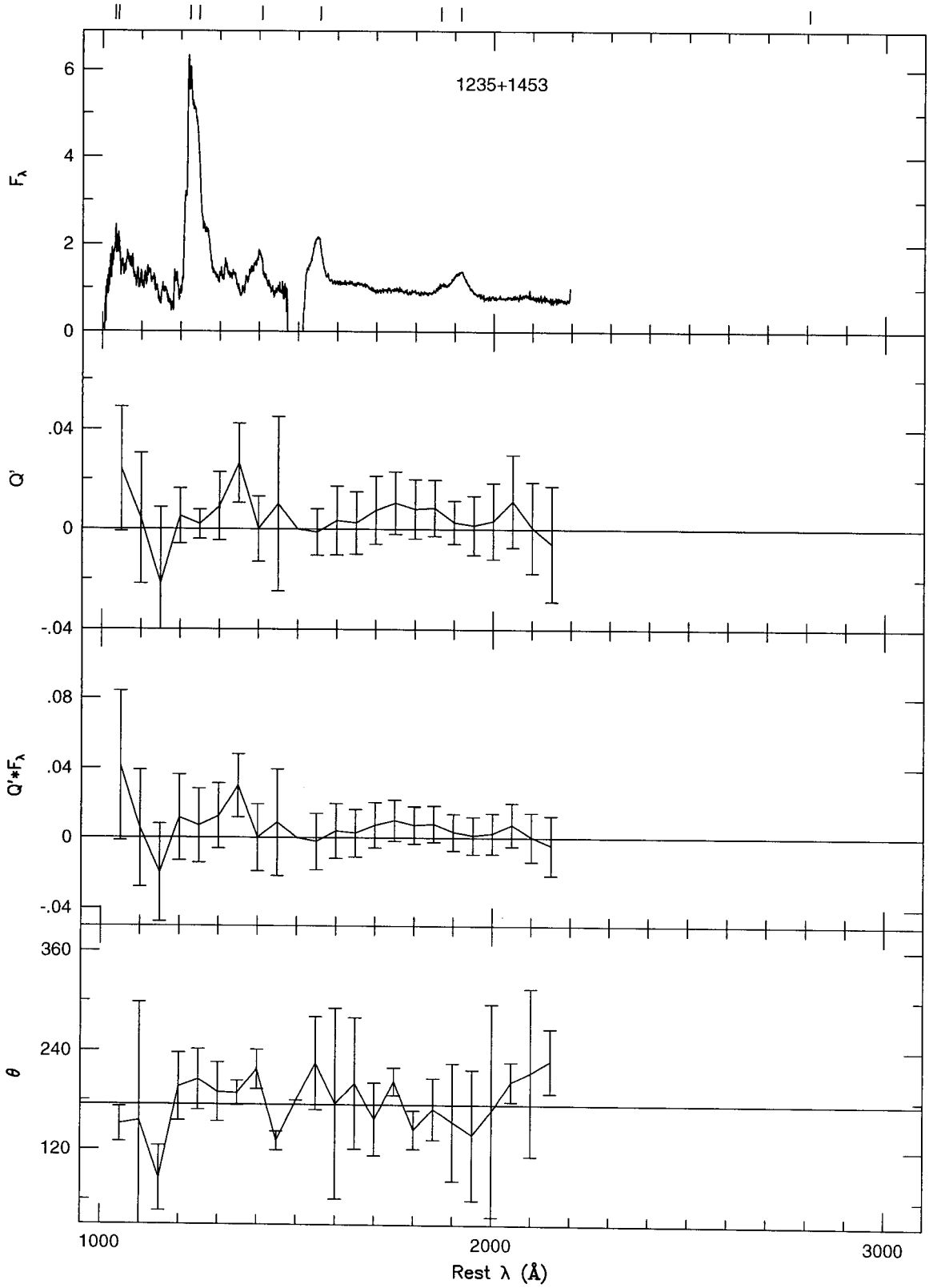

Figure 3.8: 1235+1453.

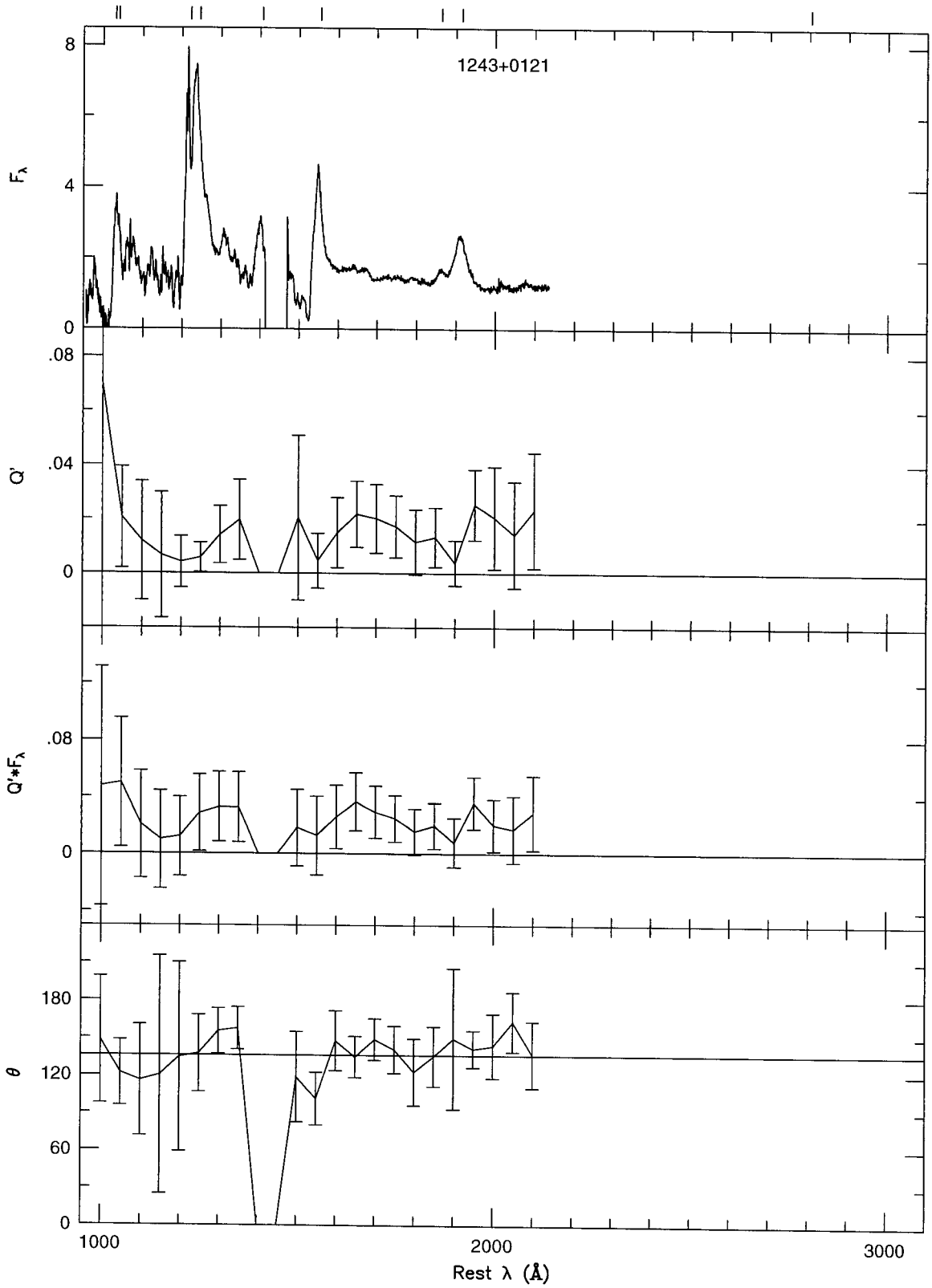

Figure 3.9: 1243+0121.

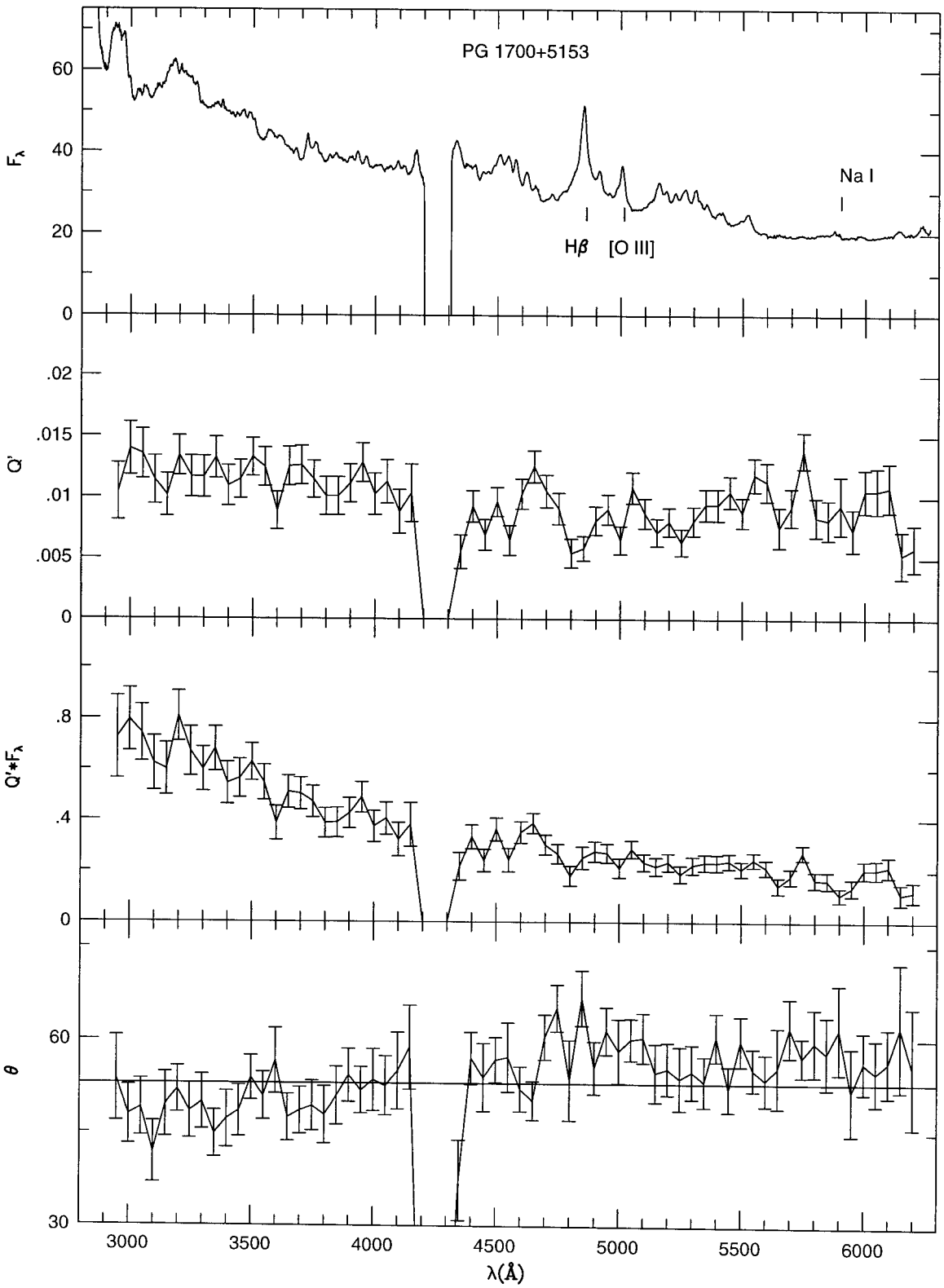

Figure 3.10: 1700+5153.

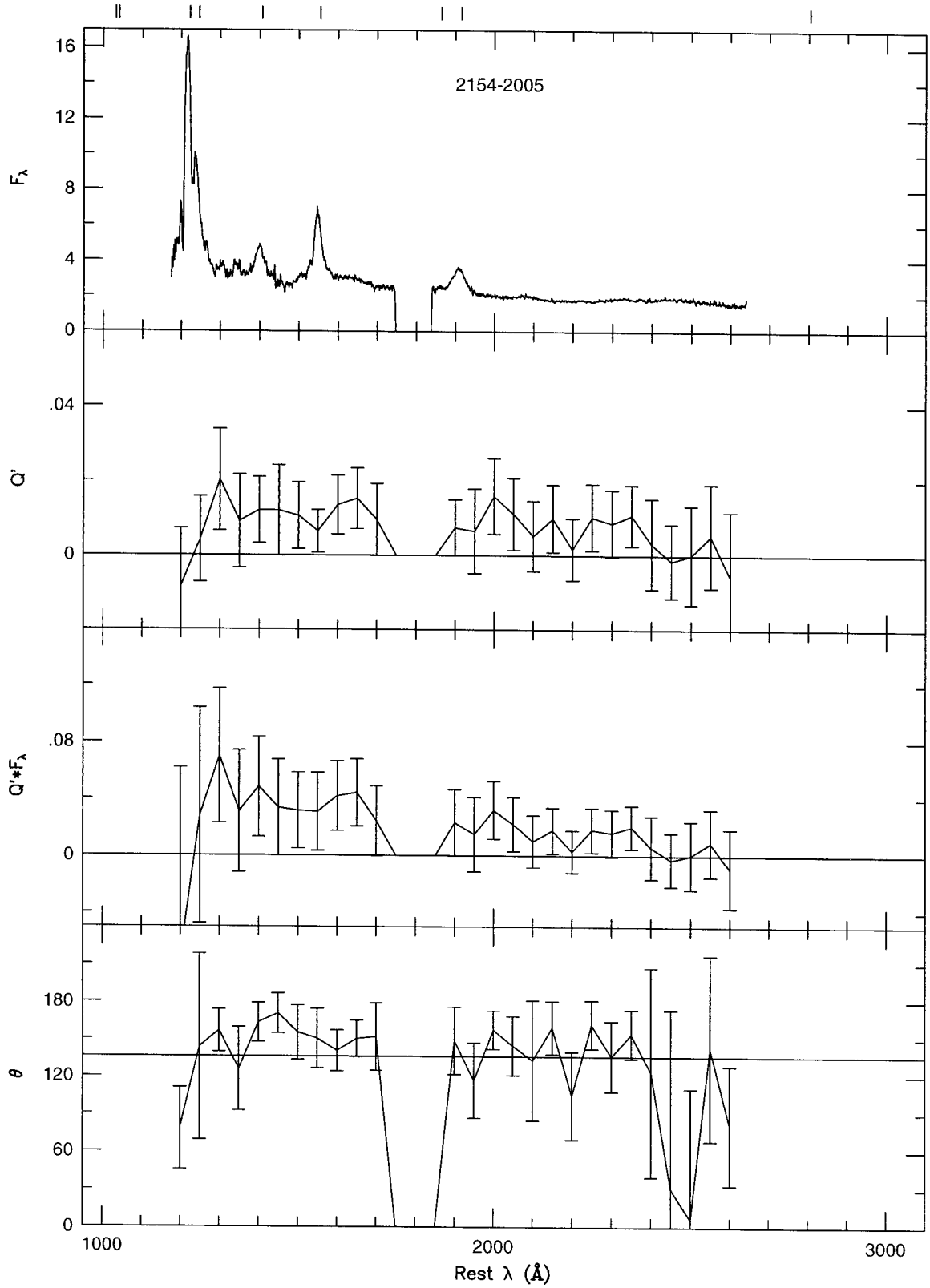

Figure 3.11: 2154-2005.

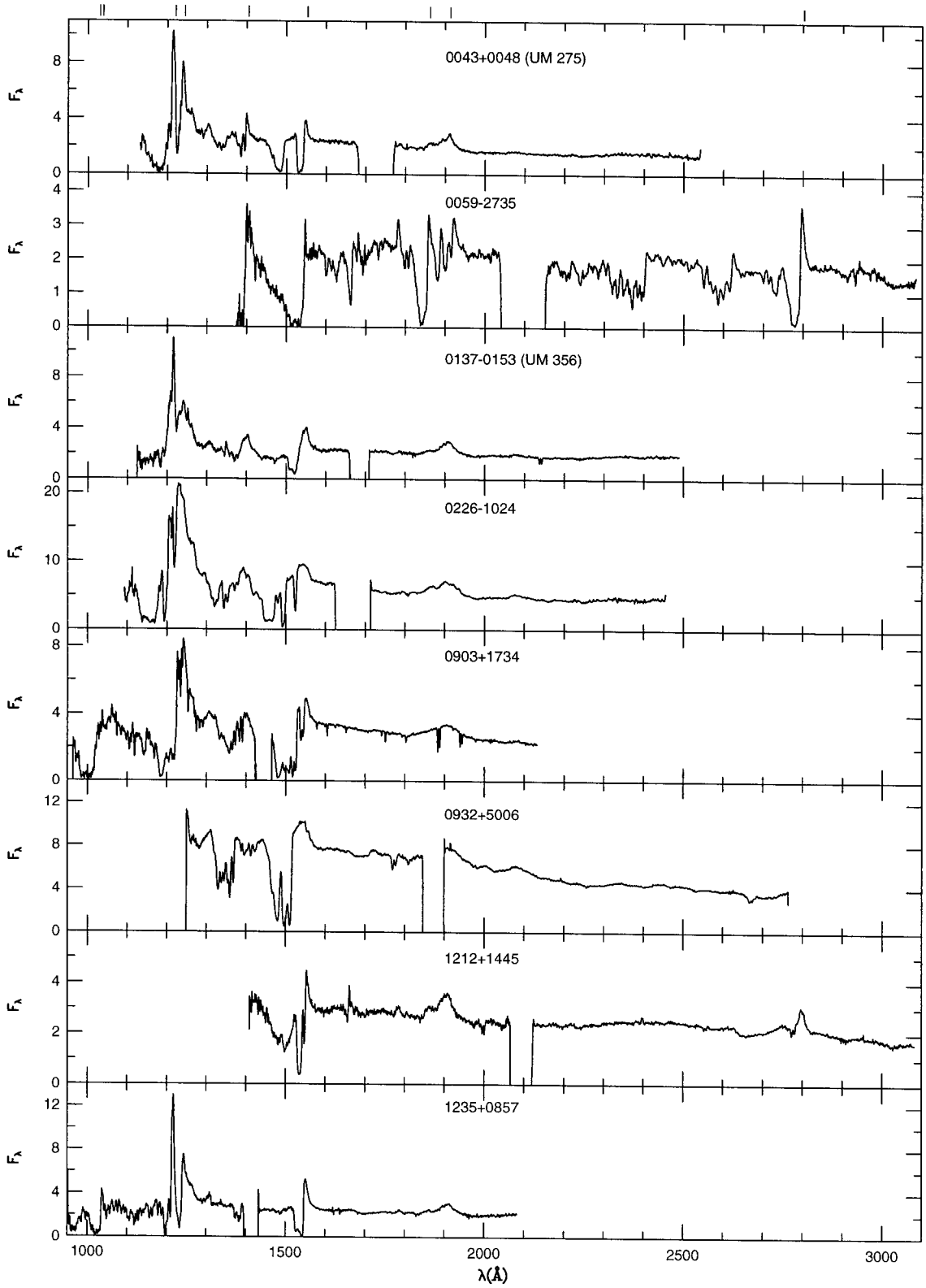

Figure 3.12: Palomar flux spectra of objects re-observed at Keck. Keck spectropolarimetry for these objects is presented in Chapter 2. Flux is in units of 10^{-16}erg/s/cm^2/ Å .

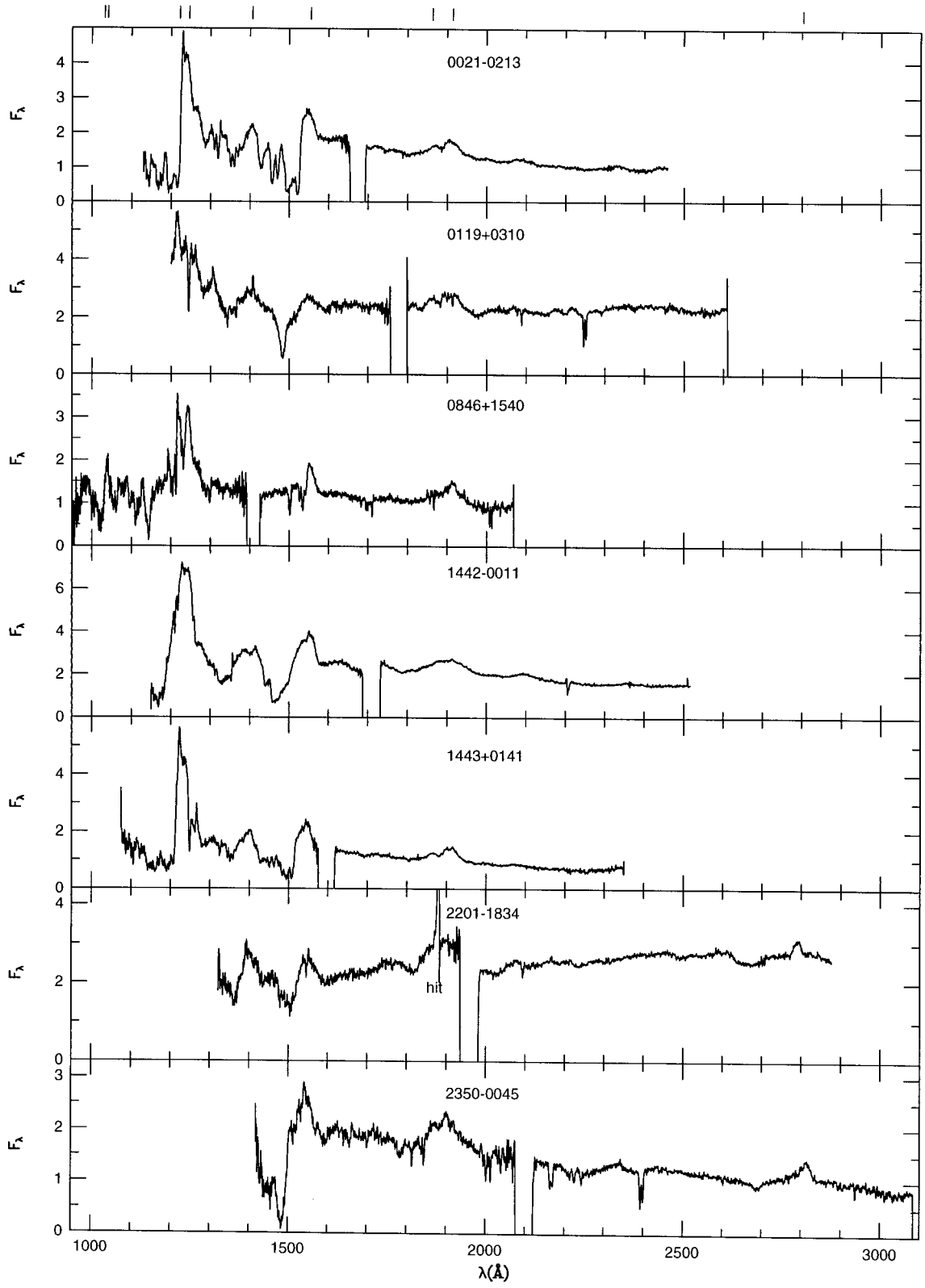

Figure 3.13: Palomar spectroscopy, polarization non-detections. Flux is in units of 10^{-16}erg/s/cm^2/Å.

Chapter 4 QSO Continuum Polarization

4.1 Chapter Outline

This chapter discusses the continuum polarization of BAL QSO and its origins. The distribution and wavelength dependence of the continuum polarization are examined and compared to simple scattering models. The polarization distribution is connected to the geometry of the broad absorption line region and unification with non-BAL QSO. The wavelength dependence of the polarization may be due to a number of factors. We evaluate the wavelength dependence in terms of electron scattering, dust scattering and reddening, and dilution by unpolarized emission lines. We look for correlations between polarization and BEL and BAL properties to see if there is a dependence on viewing angle.

The continuum polarization measurements in this chapter were made with the Keck and Hale telescopes. The observational and measurement techniques are described in Chapters 2 and 3. In this chapter we present some additional measurements of polarization wavelength dependence, BEL and BAL equivalent widths, and continuum polarization variability.

It is thought that the low static polarization of quasars, with the exception of blazars, is due to scattering by material in the nuclear environment (e.g., Stockman et al., 1984). The location of the scatterers is uncertain, but can be constrained by comparing line and continuum polarization. Emission and absorption line polarization are studied in detail in Chapter 5. One result from that chapter is that the scattering region is located at a radius comparable to that of the broad emission line and absorption line regions. The results from Chapters 4 and 5 are interdependent, but we split them up to focus separately on the continuous and emission line scattering processes.

4.2 Introduction–Scattering

The most conclusive proof of scattering in AGN comes from polarimetric imaging of the extended emission regions in Seyfert 2 and NLRG. In these objects, the electric vectors show a centro-symmetric pattern which is explained by scattering of a central continuum

source by a reflection nebula. The extended nebulae are biconical and roughly aligned with the radio axis, so the net polarization vector is roughly perpendicular to the radio axis. In the unification scenario, type 1 Seyferts and BLRG are simply type 2 objects viewed from a pole-on orientation. However, the light from these objects is dominated by nuclear emission, and the relatively weak emission from the extended regions is swamped. Imaging polarimetric techniques do not yet have significant dynamic range to detect the extended scattering regions in type 1 objects. Polarimetric images show that the sources of polarized flux in type 1 objects are concentrated in the unresolved nucleus. Since information on the spatial distribution of the polarized flux is lacking for unresolved Seyfert 1 and QSO nuclei, we can not be certain that it has a scattering origin and must resort to indirect arguments involving the spatially integrated polarization.

The spatially integrated continuum polarization depends on the geometry of the scattering region, its optical depth, and the nature of the scatterers. These aspects of the scattering phenomenon are considered below and compared with the polarimetric data.

Geometry is important because the orientation of the polarization vector is always perpendicular to the plane of scattering, and the magnitude of the polarization vector depends upon the angle between the incident and scattered rays. Greatest polarization will be seen for photons which are side-scattered at 90 degrees, and least polarization for those which are forward or back-scattered (0 or 180 degrees). The total amount of scattered light is proportional to the global covering fraction of the light source by the scatterers. There is a competition between scattered flux and polarization in the following sense. A spherical distribution of scatterers gives maximum coverage of the source and the most scattered light, but the net polarization of this configuration is zero because of its symmetry. A single scattering cloud with small covering fraction can yield scattered light with a polarization approaching 100%, but the intensity of the scattered light relative to the direct light will be low.

Polarized flux increases linearly with optical depth for optically thin scattering, when the number of scatterings per photon is much less than one. Depending on the geometry of the scattering configuration, multiple scattering can either decrease or increase the polarization of the scattered light. Additional opacity sources may become important for large column densities of gas, and will alter the relative intensities of the direct and scattered flux in a wavelength-dependent fashion. In cases where multiple scattering is important, it is

necessary to run Monte Carlo simulations to get a reliable estimate of the polarization (e.g., Wood et al., 1996).

The nature of the scatterers is fundamental to the scattering process in two respects. First, if the scattering cross-section is a function of wavelength, then the fraction of scattered polarized flux will be wavelength dependent. Second, the scattering phase function and radiation pattern is dependent on quantum physics in the case of atoms and molecules and on optical interference and absorption in the case of dust grains. It has proved very difficult to determine the type of scatterers responsible for the continuum polarization in AGN, though examples of both electron and dust scattering have been claimed.

4.3 Polarization Distribution of BAL QSO

Figure 4.1 shows the polarization distribution for the combined Palomar and Keck BAL QSO samples (34 objects). Two low-redshift objects are excluded from this plot because their polarizations were measured in the rest optical, not rest UV. Continuum polarization values are from Tables 2.5 and 3.2, using the greater of the two values (P_1, P_2) in the two rest UV continuum bands (1600-1840 Å and 1960-2260 Å). Objects are placed in 0.5% polarization bins, and 2σ polarization non-detections are indicated by the flag 'n.' Uncertainties in the polarizations are $< 0.3\%$ for all but two objects, so there should not be much leakage between adjacent bins.

The BAL QSO polarization distribution peaks at low polarization and there is a high-polarization tail out to 6%. The distribution is smooth and there is no indication of separate high and low-polarization populations. There is a 1.2σ difference between the number of objects in the 0-0.5% and 0.5-1.0% bins, which has low significance. There is significant positive bias in the polarization values of the two non-detections in the 0.5-1.0% bin, so they may move to the 0-0.5% bin with better S/N measurements. There are 4 objects (12%) with high polarization (HPQ, $P > 3\%$), 13 objects (38%) with moderate polarization (MPQ, $1\% < P < 3\%$), and 17 objects (50%) with low polarization (LPQ, $P < 1\%$).

There may be a selection bias towards objects with high polarization in our total sample. In particular, the objects 2225-0534 (PHL 5200), and 1524+5147 (CSO 755) were observed at Keck because they were known to have high continuum polarization. The objects 0105-265 ($P = 1.4\%$) and 1246-0542 ($P = 1.3\%$) were also known to be polarized. If we restrict

our attention to the Weymann et al. (1991) (WMF) sub-sample, which was not selected for polarization, the HPQ fraction is 11%, which is essentially the same as the 12% HPQ fraction in the total sample. Similarly, the MPQ fractions are 46% and 41% in the subsample and total sample, respectively. Any selection bias towards high polarization is therefore not apparent when we compare the two samples, and is less than the uncertainty due to Poisson statistics.

The incompleteness of our sample is also a cause for concern, since we may have inadvertently selected objects for characteristics which correlate with polarization. In fact, no such correlations exist, as we discuss in Section 4.16. The initial sample was selected from the WMF sample of 40 BAL QSO, 37 of which survived our magnitude and declination selection criteria. We observed 28 objects from this list, for a completeness of 76%. Given an 11% HPQ fraction, it is likely that we missed one HPQ from the complete list. If we didn't miss any HPQ, then the HPQ fraction drops to 8%.

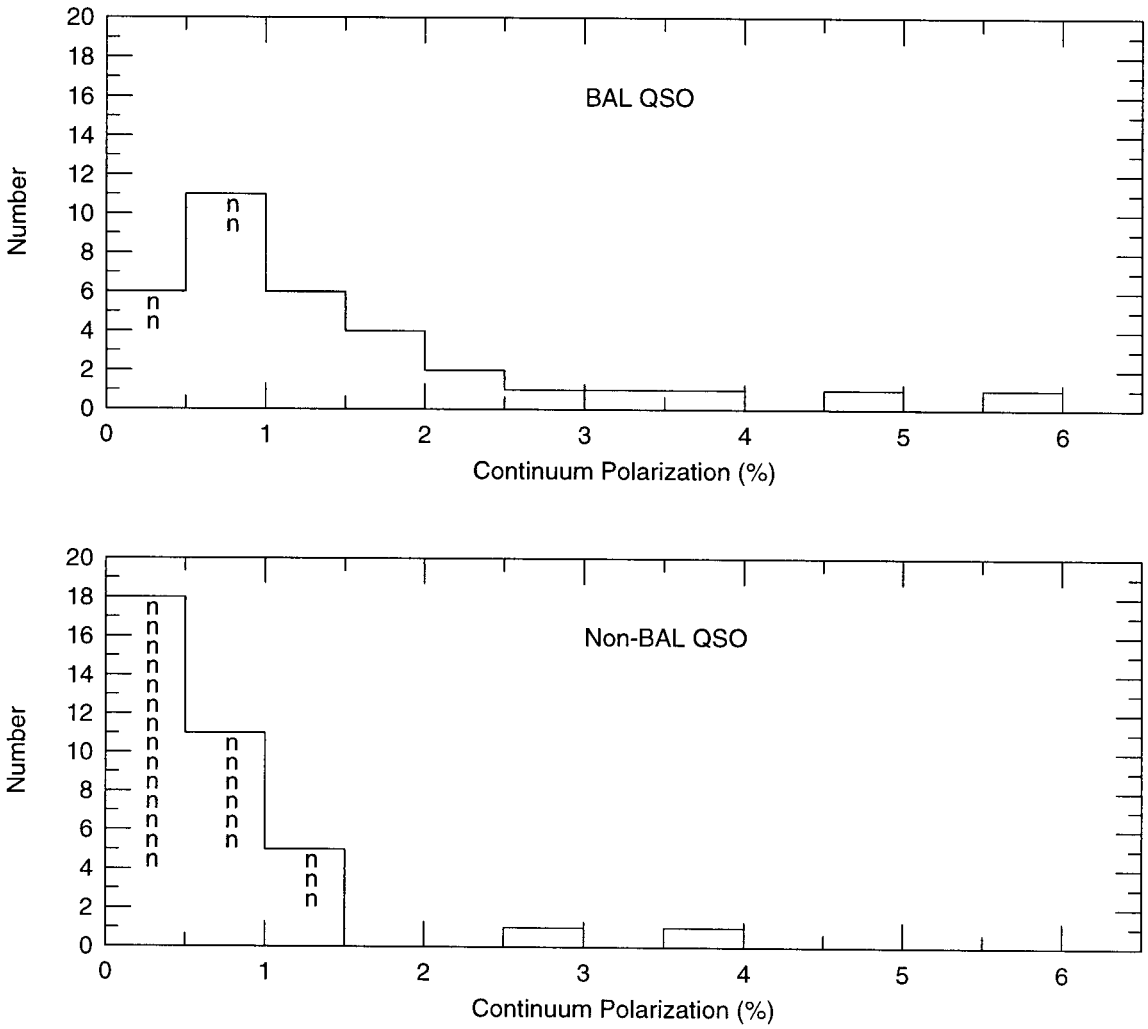

Figure 4.1: QSO continuum polarization distributions. The top panel shows the distribution of BAL QSO polarization measurements from this thesis (34 objects). The bottom panel shows the polarization distribution of the non-BAL QSO (NBAL) sample (36 objects), taken from the literature. Objects which are not detected in polarized flux at the 2σ level are indicated by the flag "n." There is a large number of non-detections in the NBAL sample.

4.4 Comparison with Non-BAL QSO Polarization Distribution

If BAL QSO and non-BAL QSO are distinguished by viewing angle, then it should be possible to match their polarization distributions. There have only been limited spectropolarimetric observations of high-redshift non-BAL QSO (e.g., Antonucci et al., 1996) because of their faintness and low polarization. There have been large broad band-polarization surveys of bright QSO, but these contain relatively few high-z objects and have large (0.5-1.0%) polarization uncertainties. However, we shall compare the polarization measurements of non-BAL QSO which are available in the literature to our results for BAL QSO.

First we compare our BAL QSO polarization distribution (BAL sample) with a combined sample (NBAL) of high-redshift non-BAL QSO measured by Stockman et al. (1984) and Antonucci et al. (1996) (SMA and AGG). The BAL and NBAL polarization distributions are shown in Figure 4.1. Objects with polarization $P < 2\sigma_P$ are indicated as non-detections with the letter "n." There is a much larger fraction of non-detections in the NBAL sample than the BAL sample. The NBAL sample contains 1 (3%) HPQ, 6 (17%) MPQ and 29 (80%) LPQ.

The SMA sample consists of 142 bright radio and optically-selected QSOs ($m_v < 17$) from the catalog of Burbidge et al. (1977). The broad-band polarizations are measured in white (un-filtered) light. We chose a subsample of all 24 non-BAL QSO with $z > 1.5$. Most of these objects are LPQ, and there are no known blazars. The typical uncertainties in the SMA polarization measurements are 0.2-0.7%, which is comparable to the uncertainties in our Palomar polarization measurements, but much larger than the uncertainties in the Keck measurements.

The AGG sample is a heterogeneous collection of bright high-z QSO chosen for spectropolarimetric measurement. There is a bias towards objects with detectable polarization and with weak radio cores because AGG were looking for objects with polarized accretion disk emission. As we will see, this bias only reinforces our conclusions below. We use the broad-band polarizations tabulated by AGG which cover various wavelength ranges between 912 and 3000Å. The polarization uncertainties are 0.03-0.5%, generally smaller than the uncertainties in the SMA sample.

A Kolmogoroff-Smirnoff (K-S) test shows that the probability that the BAL and NBAL

samples were chosen from the same polarization distribution is 0.27%. There is therefore a significant difference between the BAL and NBAL polarization distributions. A Chi-squared test comparing the binned BAL and NBAL distributions gives $\chi^2/DF = 15.1/9.0$, with a probability of 9% that the BAL and NBAL were drawn from the same distribution. The difference in the binned distributions is apparent from the much larger width of the BAL distribution in Figure 4.1. The Chi-squared test gives a lower significance than the K-S test because information is lost in binning the data.

The K-S test treats all polarization measurements equally, regardless of their S/N and whether or not they are formal non-detections. This is appropriate as long as the polarization uncertainties in the two samples are similar, otherwise there will be differential smearing between the two distributions. However, since the K-S test measures the maximum difference between the two cumulative distributions, it is most sensitive to differences in the medians of the distributions and less sensitive to outliers (e.g., Press et al., 1992). The median of the BAL polarization distribution is 1.13% and the median of the NBAL distribution is 0.5%, so non-BAL QSO are more weakly polarized than BAL QSO.

While the BAL and NBAL polarization distributions are significantly different, this could in principle be caused by sample selection effects or different observation techniques in the two samples. The first concern is that the errors in the Keck polarimetry are much smaller than in the broad-band polarimetry of SMA, and there are a large number of non-detections in the NBAL sample. Since the BAL distribution is broader than the NBAL distribution, the true difference between the widths of the two distributions must be even larger than the observed difference, reinforcing the conclusion that BAL QSO are more highly polarized than non-BAL QSO.

A second worry is that the band-passes used for the BAL and NBAL polarization measurements are different. As we discuss in Section 4.7, there is a weak but significant variation of continuum polarization with wavelength in BAL QSO; the polarization can vary by a factor of two per octave of wavelength. In addition, emission line dilution, especially by blended Fe II broad lines, can reduce the polarization by up to a factor of two. There is a similar wavelength dependence of the polarization in the SMA sample (Stockman et al., 1984), with the polarization rising weakly to the blue. A great advantage of spectropolarimetry over previous broad-band continuum polarization studies is that it allows us to measure the polarization in a narrow band which is fixed in rest wavelength. In order to

compare our results with broad-band measurements, we study the effect of bandpass choice.

There are two conflicting color corrections to the polarization. First, the narrow-band measurements generally have higher polarization than the broad-band measurements in objects where there is strong dilution by line emission. Second, for objects with polarization rising strongly to the blue, broad-band measurements blue-ward of 1600 Å will give higher polarization than measurements in the narrow bands near C III] λ1909. The best way to assess the net effect on the BAL QSO polarization distribution is to compare the narrow-band and broad-band polarization distributions. However, there is no easy accounting for the different wavelength-dependent efficiencies used in the broad band polarization measurements by SMA.

The NBAL sample includes a roughly even mix of radio and optically selected objects. It is questionable to compare the polarization of radio-loud and radio-quiet QSO for two reasons. The first reason is that some radio-loud quasars may contain polarized mini-blazar components in their spectra, while BAL QSO probably do not. The second reason is that there may be fundamental differences between the geometries of radio-loud QSO and BAL QSO. As discussed above, the median polarization of the NBAL sample is less than the median polarization of the BAL sample, and except for one object, all radio loud QSO in the NBAL sample have $P < 1.4\%$. This argues against a significant blazar contribution to the polarization. If the RQ and non-blazar RL QSO have the same polarization mechanism, such as scattering, then we have made a fair comparison between the BAL and NBAL samples.

In spite of the caveats discussed above, we conclude that BAL QSO have more highly-polarized continuum emission than non-BAL QSO. This conclusion would be greatly strengthened by high S/N spectropolarimetry of a large sample (> 30) of optically selected non-BAL QSO. This would eliminate the uncertainties due to wavelength-dependent polarization, mixing radio-loud and radio-quiet objects, and the large number of non-detections in the NBAL sample. However, this is difficult work and the low-polarization values of non-BAL QSO make line-polarization studies not as fruitful as for BAL QSO.

4.5 Axisymmetric Scattering Geometries

The polarization of an optically thin axisymmetric scattering geometry can be computed analytically using the formalism introduced by Brown & McLean (1977) in their study of Be stars. In this treatment, light is scattered by a tenuous envelope centered on an illuminating point source. This formalism has been adopted by Miller & Goodrich (1990) and Goodrich & Miller (1994) to explain the polarization of Seyfert galaxies. We repeat this analysis for QSO using the following equations. The polarization of the scattered light is given by

$$P_s = \frac{\sin^2 i}{2\alpha + \sin^2 i} \tag{4.1}$$

where

$$\alpha = \frac{1+\gamma}{1-3\gamma} \tag{4.2}$$

and

$$\gamma = \frac{\int\int n(r,\mu)\mu^2 dr d\mu}{\int\int n(r,\mu) dr d\mu} \tag{4.3}$$

are shape parameters which are integrals over the spatial distribution of scatterers. The density distribution of the scatterers with radius r and $\mu = \cos i$ is $n(r,\mu)$. For optically thin scattering in an axisymmetric geometry, the polarization increases with inclination from the pole as $\sin^2 i$.

The net polarization of the scattered (F_s) plus direct (F_d) continuum flux is then

$$P = \frac{P_s \times F_s}{F_d + F_s} = 2\tau(1-3\gamma)\sin^2 i\left(\frac{F_d}{F_d + F_s}\right) \tag{4.4}$$

where τ is the optical depth to scattering.

The polarization distribution can give information about the geometrical distribution

of the BALR around the central source. If the polarization is due to scattering by an axisymmetric structure such as an ionization cone or accretion disk, it will be maximum when viewed from the equatorial plane of this structure, and zero when viewed from the poles. If the geometry and optical depth of the scattering region were known, it would be possible to determine the viewing angle for each object. Alternatively, if the distribution of viewing angles were known, it would be possible to learn about the geometry and optical depth of the scattering region.

In the simplest case, the axis of symmetry of the scattering region corresponds to the fundamental axis of the quasar (if such an axis exists). We assume that the fundamental axis is defined by the angular momentum of the central black hole. In fact, the fundamental axis of a radio-quiet QSO is poorly defined. The radio jets are very weak compared to the jets in radio-loud QSO, and are difficult to detect. The next-best marker of the fundamental axis is the ionization cone. This assumes that there is a opaque structure, such as an obscuring torus, which collimates the radiation from the central source into oppositely directed cones. Even if this is the case, there is no guarantee that the angular momentum vector of the torus will line up with the angular momentum vector of the black hole.

Consider an ensemble of identical axisymmetric QSO oriented randomly on the sky, within some range of viewing angles $i_1 - i_2$. The range of viewing angles corresponds to lines of sight to the continuum source which are not occulted. For example, non-BAL QSO may be confined to a polar cone ($i_1 = 0$, $i_2 < 60$ degrees) and BAL QSO to an equatorial wedge ($i_1 > 60$, $i_2 = 90$ degrees). Assume that on average there are no preferred viewing directions inside this range. Regardless of the detailed geometry and the specific values of i_1 and i_2, there are always more objects viewed at high inclination because there is more solid angle there. Therefore the distribution of viewing angles $N(i)$ peaks at $i = i_2$ and the polarization distribution $N(P)$ peaks at $P = P(i_2) = P_{max}$. (Fig. 4.3, model δ). The observed polarization distributions for non-BAL and BAL QSO fail to match this type of distribution; instead they peak at low polarization.

Since the BAL QSO polarization distribution does not peak at high polarization, it is likely that object-object differences in viewing angle are small. In other words, the BALR occupies a small inclination range and has a small covering fraction. This is consistent with the QSO unification hypothesis. The width of the observed distribution is then mainly due to intrinsic object-object variation in scattering efficiency, scattering geometry, or continuum

dilution. In that case, we can use the observed BAL QSO polarization distribution to compute the polarization distribution expected for non-BAL QSO under the unification hypothesis. We use a simple model where non-BAL QSO are visible from $0 - i_1$ degrees, BAL QSO are visible from $i_1 - i_2$ degrees, and obscured QSO (QSO 2) have $i = i_2 - 90$ degrees (Fig. 4.2). We assume that the BAL coverage is smooth so that the global covering fraction is given by

$$f = \cos i_1 - \cos i_2 \tag{4.5}$$

Non-BAL QSO are viewed from a polar direction, while BAL QSO are viewed at an intermediate inclination. This is a common representation of the unification model, where the outflow is axisymmetric. We have generalized the model by including an obscuring torus of opening angle i_2. If all QSO contain a smooth BAL outflow which covers 10% of the central continuum source, then the BAL phenomenon will only be visible from a small range of angles. This implies that the geometrical variation of the polarization among BAL QSO is small. For example, if the BAL flow is equatorial, covering $i = 84 - 90$ degrees, the polarization will only vary by a factor of 0.99 from the equator to the top edge of the flow. Including an obscuring torus or accretion disk in the unified model changes the global covering fraction inferred from the BAL QSO fraction. Since some of the solid angle around the central source is excluded by obscuration, the global covering fraction is less than the BAL QSO fraction.

We assume that all orientations are equally likely, so the probability distribution of inclination is $P(i) = \sin i$. The polarization distribution of non-BAL QSO is obtained by integrating over the inclination range ($i = 0 - i_1$) in which they are visible.

$$N_{NBAL}(P) = \int_0^{i_1} N_{BAL}(P(i_2) = P\frac{\sin^2 i_2}{\sin^2 i}) \sin i \, di \tag{4.6}$$

where $N_{BAL}(P)$ is the BAL QSO polarization distribution. Note that this assumes $\sin^2 i_1 \simeq \sin^2 i_2$, which is true for a BALR which covers a narrow inclination range. The polarization of a non-BAL QSO is smaller by a factor $\sin^2 i / \sin^2 i_2$ than the corresponding BAL QSO.

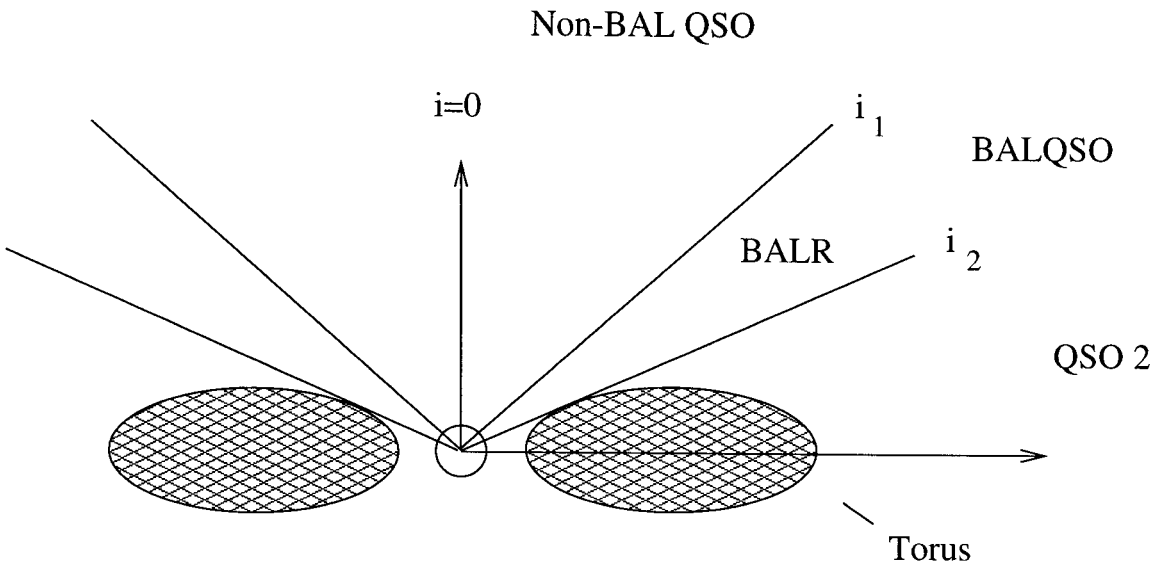

Figure 4.2: Simple unification model.

The BAL wind inclination i_2 is a free parameter which we can fit to the observed non-BAL QSO polarization distribution.

We fit the unification model (Equation 4.6) to the data using a χ^2 test. We varied i_2 and constrained i_1 by forcing the global covering factor to be $f = 0.1$. Figure 4.3 shows the best-fitting model in comparison to the observed NBAL polarization distribution. There is a 92% probability that the polarization distributions match. This means that the observed BAL QSO and non-BAL QSO polarization distributions are consistent with the simple unification scenario. Remember that a we found a 9% likelihood that the binned BAL and NBAL polarization distributions were the same (Section 4.4). Therefore the unification model gives a definite improvement to the match between BAL and NBAL polarization distributions.

Unfortunately, the inclination i_2 of the BAL wind is not well constrained because of the small number of objects and bins in the polarization distributions. Table 4.1 gives χ^2, the number of degrees of freedom, and the probability that model and observed non-BAL QSO polarization distributions are the same for i_2 =45, 60, and 90 degrees. The three models are plotted in Figure 4.3. A BAL wind inclination of 60 degrees gives the best match to the data, but the other inclinations are also consistent. Note that the model distributions shift to lower polarization as i_2 is decreased. This happens because the non-BAL QSO are confined to smaller inclinations and the polarization decreases most rapidly near the polar

i_2	i_1	χ^2	DF	Prob.
45	36	4.14	8	0.85
60	53	4.54	10	0.92
90	84	8.26	11	0.69

Table 4.1: χ^2 fits of the unification model to the non-BAL QSO polarization distribution. Columns 1 and 2 list the maximum and minimum inclinations of the BAL wind, constrained to give a smooth global covering fraction $f = 0.1$. Columns 3 and 4 list χ^2 and the number of degrees of freedom for the fits, and column 5 gives the probability that χ^2/DF will exceed the measured value. Therefore high probabilities indicate a good fit. A BAL wind with inclination range $i = 60 - 53$ degrees gives the best match between the model and data, however the other fits are also acceptable.

axis. Alternatively, we can use the lowest polarization bin with the largest number of objects to discriminate between the models. Since there are 18 objects in this bin, the uncertainty due to counting statistics is ± 4 objects. This is similar to the predicted difference between each of the models. A 3σ discrimination between each of the models would require a sample of about 180 non-BAL QSO, which would be costly in terms of observing time, but feasible using broad-band polarimetry.

4.6 Selection Effects

There may be an observational selection effect against highly polarized BAL QSO if they are either intrinsically dimmer, or partially obscured. Goodrich (1997) points out that there is a natural connection between high polarization and obscuration of the unpolarized central continuum source. This effect is prominent in radio galaxies, where the central source is blocked by dusty molecular clouds and the continuum is dominated by the fainter scattered component. The putative dusty torus serves as an occulting bar, blocking out the glare of the unresolved central regions.

In BAL QSO, obscuration could be provided by dust or electrons associated with the BAL wind (Goodrich, 1997). This is an attractive scenario for a number of reasons. First, if the BAL gas is ablated off the accretion disk or torus, then it is reasonable to expect that dust is carried along with the gas. Second, X-ray observations of BAL QSO indicate that the column of gas along the line of sight is much greater than that estimated from measurements of UV BAL optical depths. A large column of ionized gas may provide

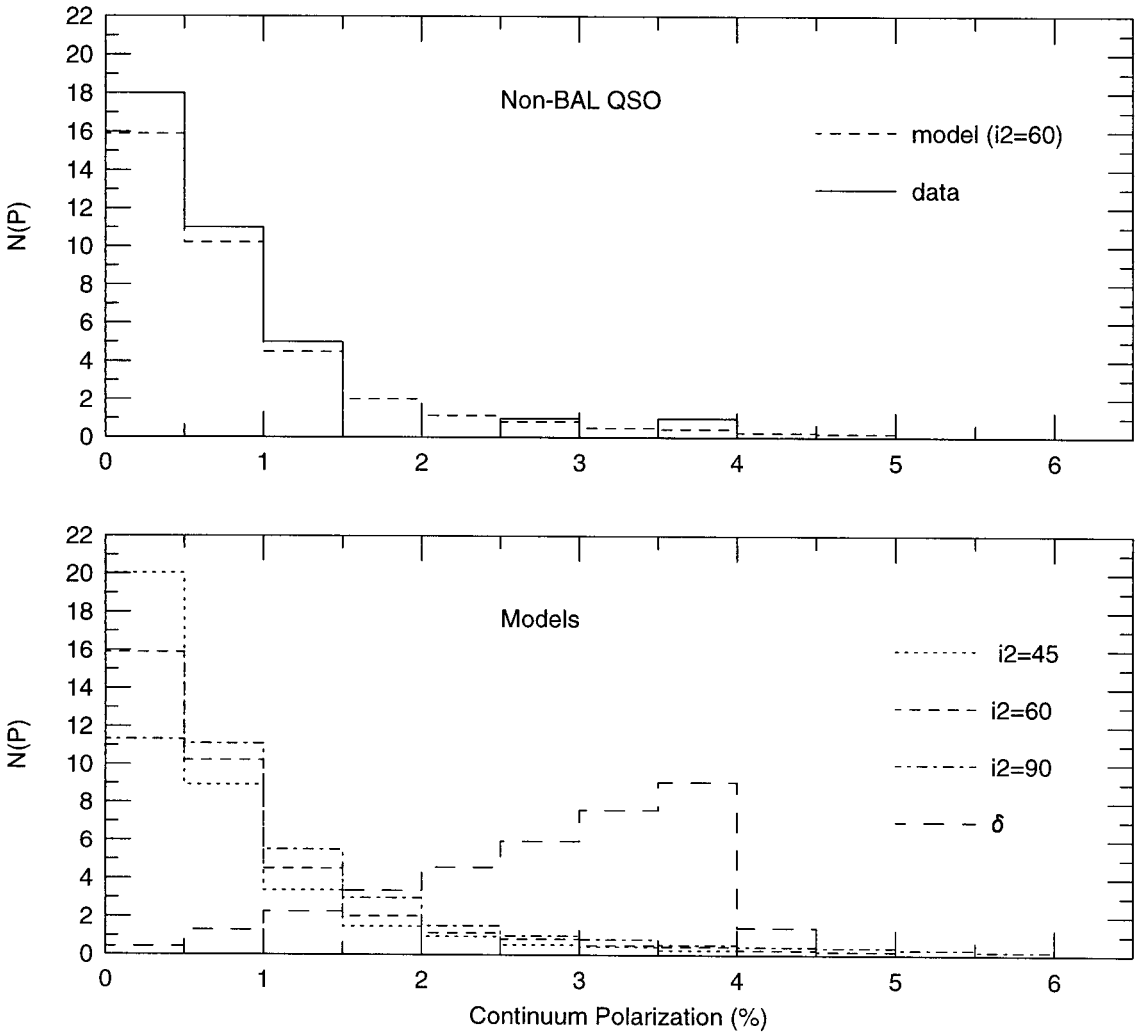

Figure 4.3: QSO Polarization distributions. The top panel compares the best fit unification model ($i_2 = 60$ degrees) to the observed NBAL polarization distribution. The bottom panel shows the distributions derived for a variety of BAL wind inclinations ($i_2 = 45$, 60, and 90 degrees), assuming the BAL polarization distribution holds for equatorial views. The model labeled δ assumes a δ-function at $P = 4.75\%$ for the intrinsic BAL QSO polarization distribution, and $i_2 = 60$ degrees. This gives an NBAL distribution which peaks at high polarization and does not match the observations.

sufficient optical depth for electron scattering and attenuation of the central source. If there is dust obscuration, then the highly polarized objects should be reddened; attenuation by electrons would be grey.

Krolik & Voit (1998) recently suggested that the anisotropy of emission from an accretion disk could serve a purpose similar to obscuration by intervening dust or electrons. It is expected that a hot accretion disk should appear dimmer along the equator than from the poles because of the smaller projected surface area and limb-darkening effects. If BAL outflows are equatorial, then BAL QSO will appear dimmer than if BAL outflows are polar. However, as we discussed at length in Chapter 1, the accretion disk model has serious difficulties matching the spectropolarimetric data for QSO. This aside, anisotropic disk emission could introduce a strong selection effect against objects viewed from the equator.

Both the obscuration and anisotropic disk radiation possibilities would have an impact on the inferred covering fraction of the BALR. They would serve the same purpose as a dusty molecular torus. Goodrich (1997) and Krolik & Voit (1998) suggest that the BALR covering fraction could be as large as 50%, instead of the 10% that is inferred from the BAL QSO fraction. Dim objects viewed from the equator would be missed from flux-limited samples. The resonance scattering limits derived by Hamman et al. (1993) from the ratio of emission to absorption equivalent widths would not necessarily be violated. The large covering fraction of the BALR would be counteracted by the weaker continuum emission in the direction of the equatorial wind (Krolik & Voit, 1998).

If there is significant continuum anisotropy (due to disk emission or dust obscuration) in QSO, then the objects in our BAL sample would tend to be viewed at the minimum possible angle at which the line of sight still passed through the BALR (i.e., $i = i_1$). In addition, the polarization would drop faster than $\sin^2 i$, due to dilution by beamed continuum towards the poles. Our models in Section 4.5 would have to be modified for orientation-dependent selection effects in the magnitude-limited BAL and NBAL samples. Since the available data are not sufficient to distinguish different BAL wind inclinations in the simple model, they will certainly not be sufficient to distinguish between various limb-darkening and obscuration models. A better way to deduce the angular dependence of the continuum radiation would be to search for and study type 2 QSO with extended reflection nebulae like those seen in narrow-line radio galaxies.

4.7 Wavelength Dependence

Here we discuss the observed wavelength dependence of the polarization, before correction for line dilution. Table 4.2 gives the spectral indices for the total and polarized flux spectra and the ratio P_b/P_r of blue to red continuum polarization. The spectral indices α were measured between blue (b) and red (r) bands and are defined by $F_\nu \propto \nu^{-\alpha}$. For objects with $1.5 < z < 2.0$, b is red-ward of C IV (1575-1600 Å) and r is red-ward of Mg II (2900-2925 Å). For objects with $z > 2.0$, b is red-ward of N V (1275-1300 Å) and r is red-ward of C III] (2225-2250 Å). These bands were chosen to minimize contamination from BEL and BAL. The formal uncertainties in $\alpha(F)$ are < 0.1, so the errors are dominated by systematic effects including possible BEL and BAL contamination. The uncertainties in $\alpha(PF)$ are much larger and dominated by photon noise in the narrow continuum bands. We have included objects from the Keck sample with $z > 1.5$, except for UM 275, which is unpolarized.

As was noted in Chapter 2, the polarization rises to the blue for most objects ($P_b/P_r = 1.0 - 2.2$). Consequently, the polarized flux is bluer than the total flux ($\alpha(PF) < \alpha(F)$). Two objects (1235+0857 and 1333+2840) have flat polarization spectra, and one object (0019+0107) has polarization falling sharply blue-ward of 2000 Å. The redshift range of the full sample gives a wavelength coverage of 1300-2900 Å for our continuum polarization measurements. This large wavelength coverage helps to constrain the polarizing mechanism in BAL QSO. In Figure 4.4, we plot P_b against P_r to graphically demonstrate the "color" of the polarization spectra. Simple Thomson (or grey) scattering with no emission line dilution is represented by the line with unity slope. We also plot the trend expected for optically thin dust scattering with a cross section that goes as λ^{-1}. Several objects fall near this line, but we must be wary because the data are not corrected for Fe II line dilution, which can bluen the polarization spectrum (Section 4.8). A similar wavelength dependence is seen in the polarization of non-BAL QSO (Stockman et al., 1984), who suggest a dust scattering origin.

IAU	$\alpha(F)$	$\alpha(PF)$	$\pm$	P_b/P_r	$\pm$
0019+0107	0.4	3.2	1.0	0.22	0.13
0059−2735	1.8	1.4	0.2	1.29	0.14
0137−0153	1.4	0.0	0.5	2.17	0.64
0146+0142	0.6	-0.2	0.7	1.59	0.58
0226−1024	0.9	0.4	0.3	1.36	0.17
0842+3431	0.5	0.0	0.4	1.31	0.28
0856+1714	1.4	0.2	0.7	1.96	0.76
0903+1734	1.1	0.8	1.0	1.11	0.63
0932+5006	0.5	-0.5	0.4	1.75	0.40
1212+1445	1.2	0.7	0.4	1.37	0.35
1235+0857	1.3	1.5	0.2	0.92	0.12
1246−0542	1.0	-0.1	0.2	1.81	0.23
1331−0108	2.1	1.8	0.4	1.21	0.29
1333+2840	1.2	1.2	0.1	0.99	0.08
1413+1143	0.8	-0.2	0.4	1.72	0.42
1524+5147	1.0	0.5	0.1	1.30	0.06
2225−0534	1.8	0.9	0.1	1.76	0.13

Table 4.2: Blue and red continuum polarization measurements. The two-wavelength spectral indices in total and polarized flux are listed in columns 2 and 3. The ratio of blue to red polarization is listed in column 5. The wavelength bands for these measurements depend on the redshift of the object, and are given in the main text.

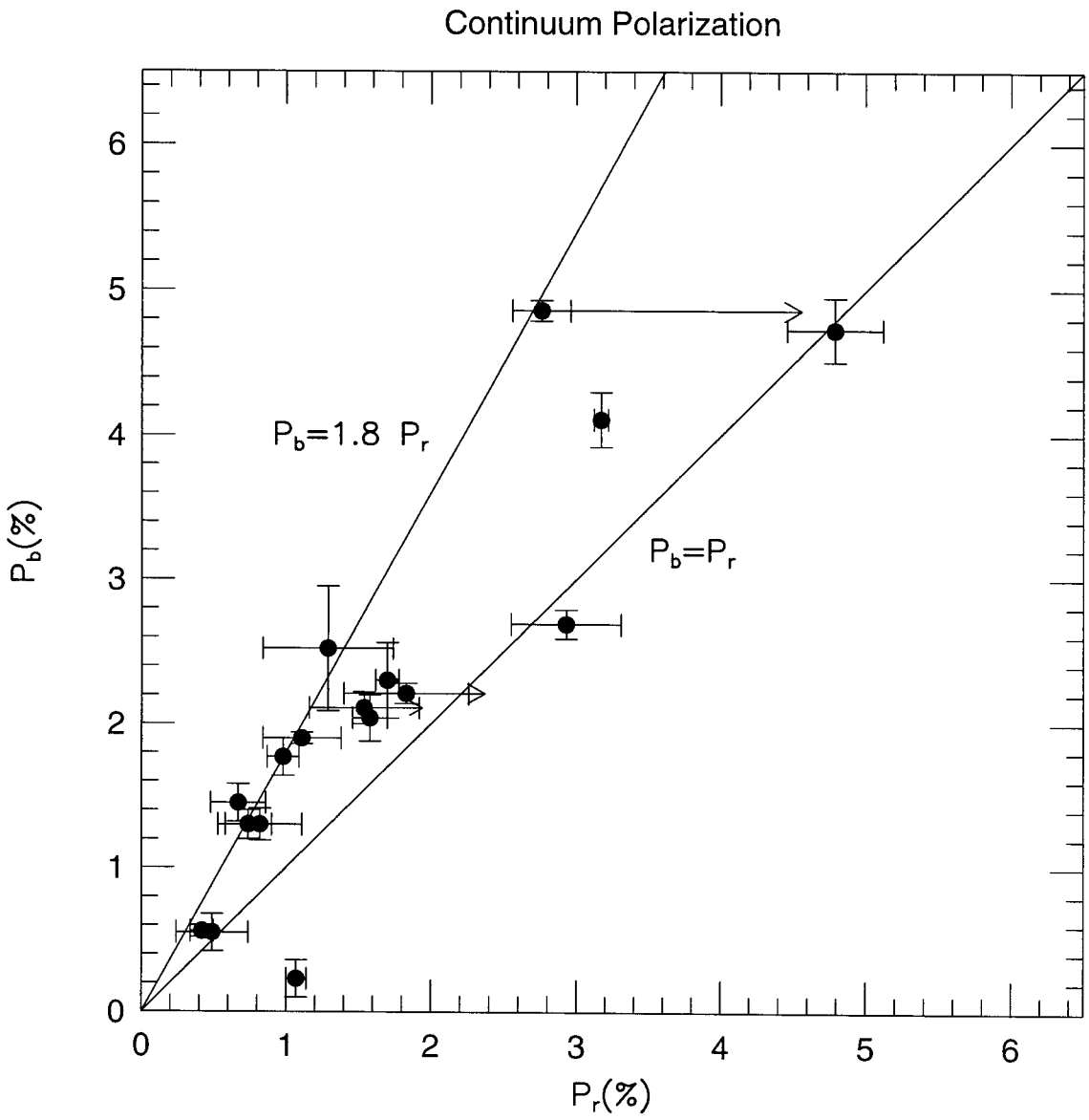

Figure 4.4: Polarization color dependence. Blue polarization P_b is plotted vs. red polarization P_r to show the continuum polarization wavelength dependence in BAL QSO. The two lines represent Thomson scattering ($P_b = P_r$) and a λ^{-1} polarization law ($P_b = 1.8P_r$). Fe II dilution correction vectors are plotted for objects which have them (Section 4.9). Only one object (0019+0107) has a red polarization spectrum.

4.8 Emission Line Dilution

The wavelength dependence of the continuum polarization provides important clues to its origin. However, it is often difficult to distinguish between the effects of dilution by an unpolarized component and a true wavelength dependence of the polarizing agent. For example, in Seyfert 2 galaxies (Tran, 1995) the polarization appears to rise to the blue because of dilution by red unpolarized starlight. After correcting for starlight, the polarization level is independent of wavelength in most Seyfert 2s, suggesting that electron scattered light dominates the polarized flux.

Cohen et al. (1995) suggest that the rise in polarization to the blue in BAL QSO PHL 5200 is mainly due to dilution by broad Fe II emission. There is a broad bump extending red-ward of 2200 Å in the total flux spectrum which is absent in the polarized flux spectrum. This so-called "little blue bump" is commonly identified with a complex of blended Fe II emission lines (e.g., Wills et al., 1985). Most of the UV spectral region in quasars is contaminated by Fe II emission lines. (See Fig. 2.17 for an extreme example.) There can also be a strong Balmer continuum component which adds to the blend of emission lines.

It is readily apparent from looking at the Keck polarization spectra in Chapter 2 that the BEL do not share the same polarization as the continuum. For most objects the polarization drops in the BEL, but the BEL polarization is not necessarily zero. We wish to study the polarization of the continuum separately from the emission lines. The flux F and polarized flux PF can be decomposed into continuum and line components:

$$F = F_c + F_l \tag{4.7}$$

$$PF = P_c F_c + P_l F_l \tag{4.8}$$

where F_c and F_l are the continuum and line fluxes and P_c and P_l are the corresponding polarizations. The problem is that there is no unique decomposition. There are two equations in four unknowns, so to solve them it is necessary to make some assumptions about the form of the line and continuum flux or the wavelength dependence of the line and continuum polarization. This would not be difficult if the emission lines were well separated from one another. In that case a continuum could be fit to F and PF by interpolating between

continuum windows. However, the BEL in our spectra are hopelessly blended together (especially the Fe II BEL) and there are few (if any) continuum windows.

The simplest assumption to make is that the BEL are unpolarized ($P_l = 0$) and the continuum polarization is wavelength independent (P_c = constant). Of course, this defeats the purpose of trying to determine the wavelength dependence of the polarization. But, it allows us to decompose the flux into line and continuum components. The continuum polarization must be at least as great as the maximum polarization observed away from the BAL, $P_c = P_{c,max}$. Using this value for the continuum polarization yields the minimum amount of diluting line flux

$$F_l = F - PF/P_{c,max} \tag{4.9}$$

The error in the line flux caused by assuming $P_c = P_{c,max}$ is given by

$$\frac{\Delta F_l}{F} = \frac{P}{P_c}(1 - \frac{P_c}{P_{c,max}}) \tag{4.10}$$

Figures 4.5-4.7 show the unpolarized line flux for the Keck BAL QSO computed from Equation 4.9. In most cases, the decomposition appears to be reasonable in the sense that the unpolarized flux is dominated by emission lines identified in the total flux spectrum (c.f., 1524+5147). Also notice that the unpolarized flux in the BAL troughs is negative because the trough polarization is greater than the continuum polarization.

It is clear for a few BAL QSO that the 2-component model with constant continuum polarization and unpolarized lines is inadequate. The simple model fails drastically for 0019+0107, which has an unpolarized blue continuum component below 2000 Å. While dilution by a blue continuum component could explain the rapid fall in the polarization below this wavelength, the correspondence between the drop in continuum polarization and PA rotation (Fig. 2.2) point instead to a real wavelength dependence in the polarizing mechanism.

There are four objects in the Keck BAL QSO sample which might be better decomposed into a continuum component with polarization increasing to the blue plus an unpolarized

line component. These are 0105-265, 1212+1445, 1246-0542, and 2225-0543, which show unusually red unpolarized flux components in the simple decomposition (Figs. 4.5-4.7). This is a qualitative judgment, since we have no knowledge of the intrinsic range in color displayed by the Fe II emission bump and the range in Fe II/C III] intensity ratios. Perhaps reddening is important along the line of sight to the Fe II BELR and is present in varying amounts from object to object.

Are there are other possible sources of dilution in addition to the BEL which could contribute to the wavelength dependence of the polarization? Such a component would have to be extended with respect to the scattering region to dilute the polarization, and would also have to have a relatively mild wavelength dependence. This is analogous to the so-called "FC2" component which dilutes the continuum polarization in Seyfert 2 and radio galaxies. In these objects, the direct continuum light is mostly obscured so that the relatively faint extended continuum emission (probably from hot young stars) can compete with the scattered light and cause a reduction in the net continuum polarization. It is unlikely that a stellar source of continuum emission, even from a nuclear starburst, can contribute significantly to the total flux from a quasar. Lyman and Balmer continuum emission from the BELR, on the other hand, may be an important component in the quasar spectrum, and should have similar polarization to the broad emission lines.

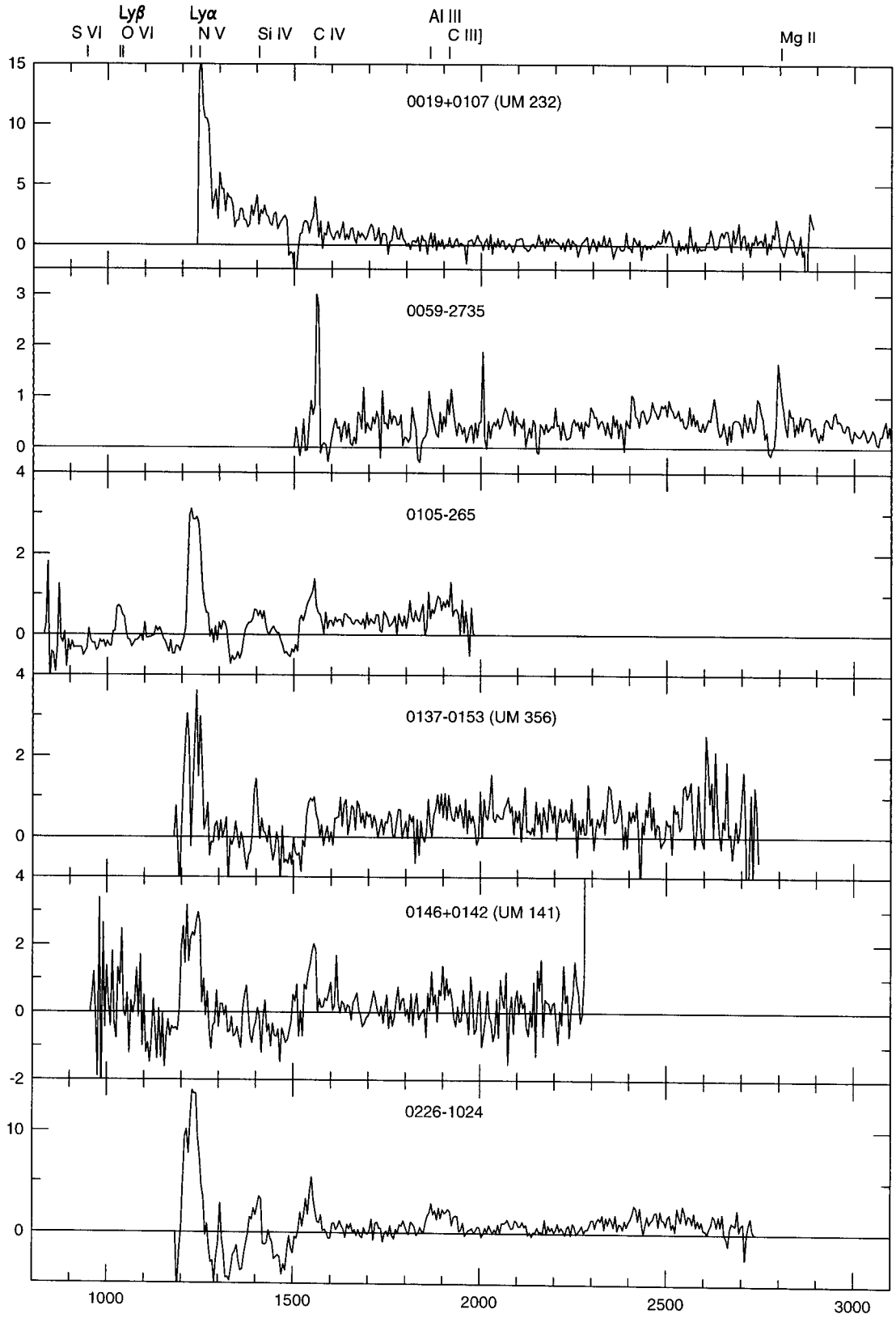

Figure 4.5: Unpolarized flux spectra.

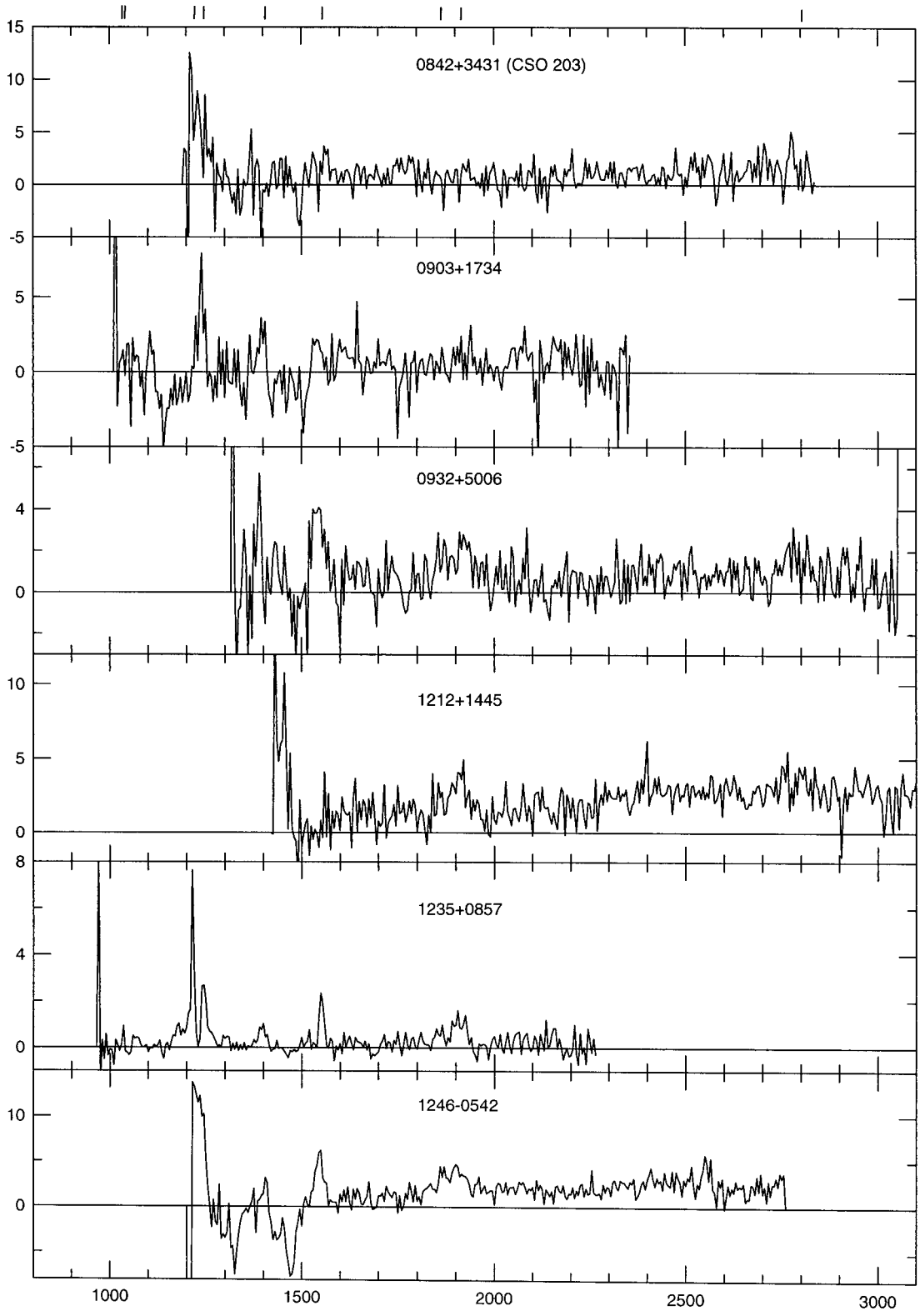

Figure 4.6: Unpolarized flux spectra.

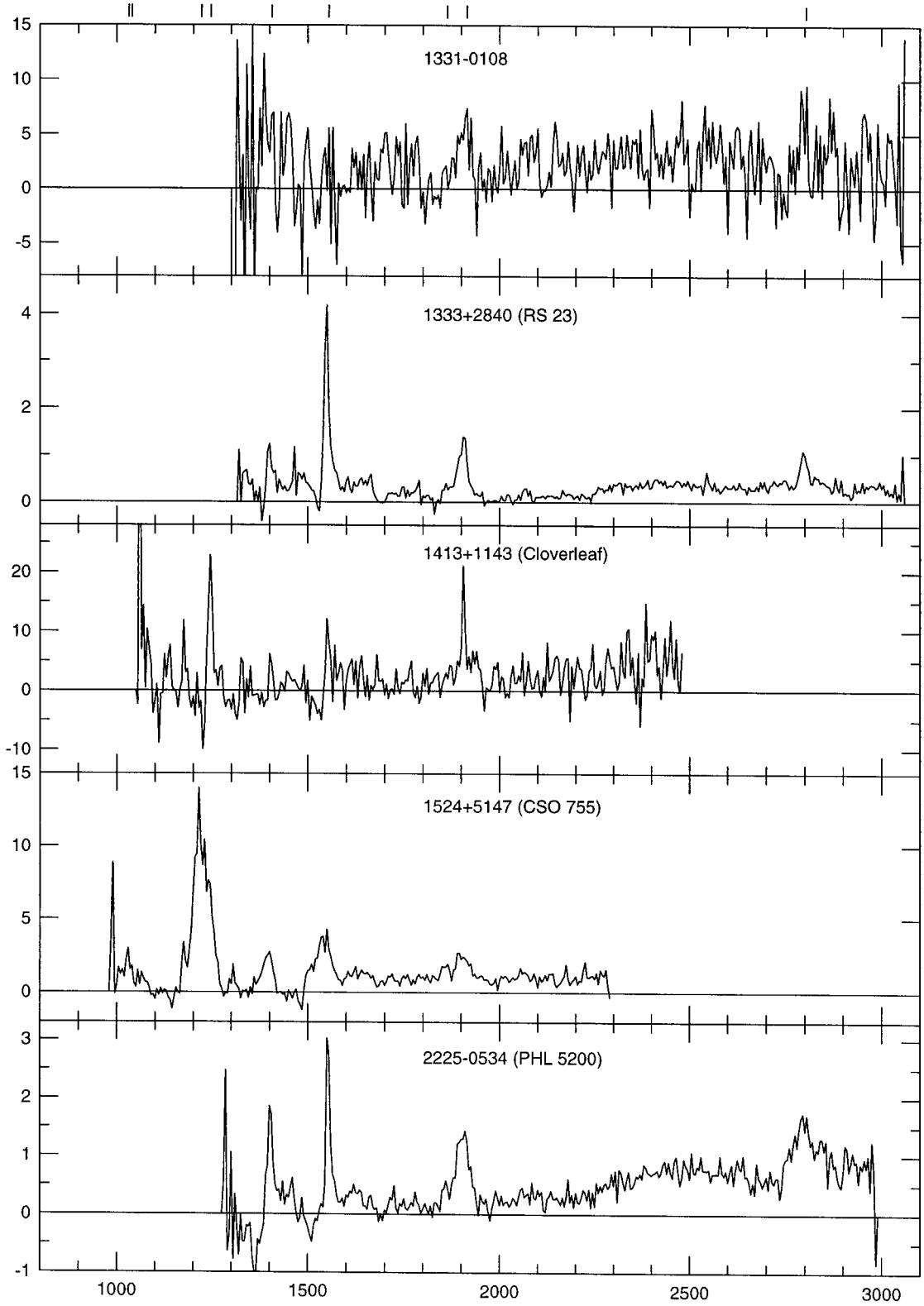

Figure 4.7: Unpolarized flux spectra.

4.9 Fe II Template Fitting

In the last section, we decomposed the flux into line and continuum components by assuming constant polarization for the continuum and unpolarized lines. Another way to decompose the flux is to use an emission line template for F_l and a polynomial (or power-law) curve for F_c. The intensities of these components can be fit to the total flux spectra. If we assume that the emission lines are unpolarized ($P_l = 0$), then the continuum polarization can be derived by dividing the polarized flux spectrum by the continuum fit

$$\frac{PF}{F_c} = P_c + P_l \frac{F_l}{F_c} = P_c \tag{4.11}$$

If the emission lines are polarized, then the error in P_c equals the line polarization multiplied by the emission line fraction. This error is small in most cases, judging from the lack of emission lines in most polarized flux spectra. (See Chapter 5 for a discussion of polarized emission lines.)

We use the unpolarized flux of 1333+2840 (RS 23) as our emission line template. This assumes that RS 23 has a wavelength independent continuum polarization so that the decomposition in the previous section is valid. While there is no guarantee that the polarization of RS 23 is wavelength independent, it appears to have a relatively flat spectral index and a smooth polarized flux spectrum between 1600 and 3000 Å. It also has a large Fe II content and high polarization, which makes it ideal for constructing an Fe II template.

A BEL template was made by fitting a power law to the Stokes flux with $\alpha = 0.75$ and scaling by $1/P_{c,max}$, where $P_{c,max} = 0.062$ is the maximum observed fractional polarization blue-ward of C III]. The scaled power law fit was subtracted from the total flux to give the unpolarized flux spectrum. This is equivalent to the flux decomposition from Section 4.8, but has much lower noise because we fit a smooth curve to the polarized flux. The systematic error in the line flux that comes with assuming constant polarization is given by Equation 4.10. The value for $P_{c,max}$ was determined by assuming there is no line emission in the continuum window from 1820-1840 Å. If there is residual Fe II emission in this continuum window, we underestimate $P_{c,max}$ and the emission line flux. However, using a greater value for $P_{c,max}$ gave worse results in the Fe II fitting below.

An Fe II template was derived from the BEL template by interpolating across prominent

non-Fe II BEL. The Fe II emission underneath the C III]/Al III, Mg II, He II, and O III] BEL was interpolated with a straight line. The flux decomposition and resultant Fe II template are shown in Figure 4.8.

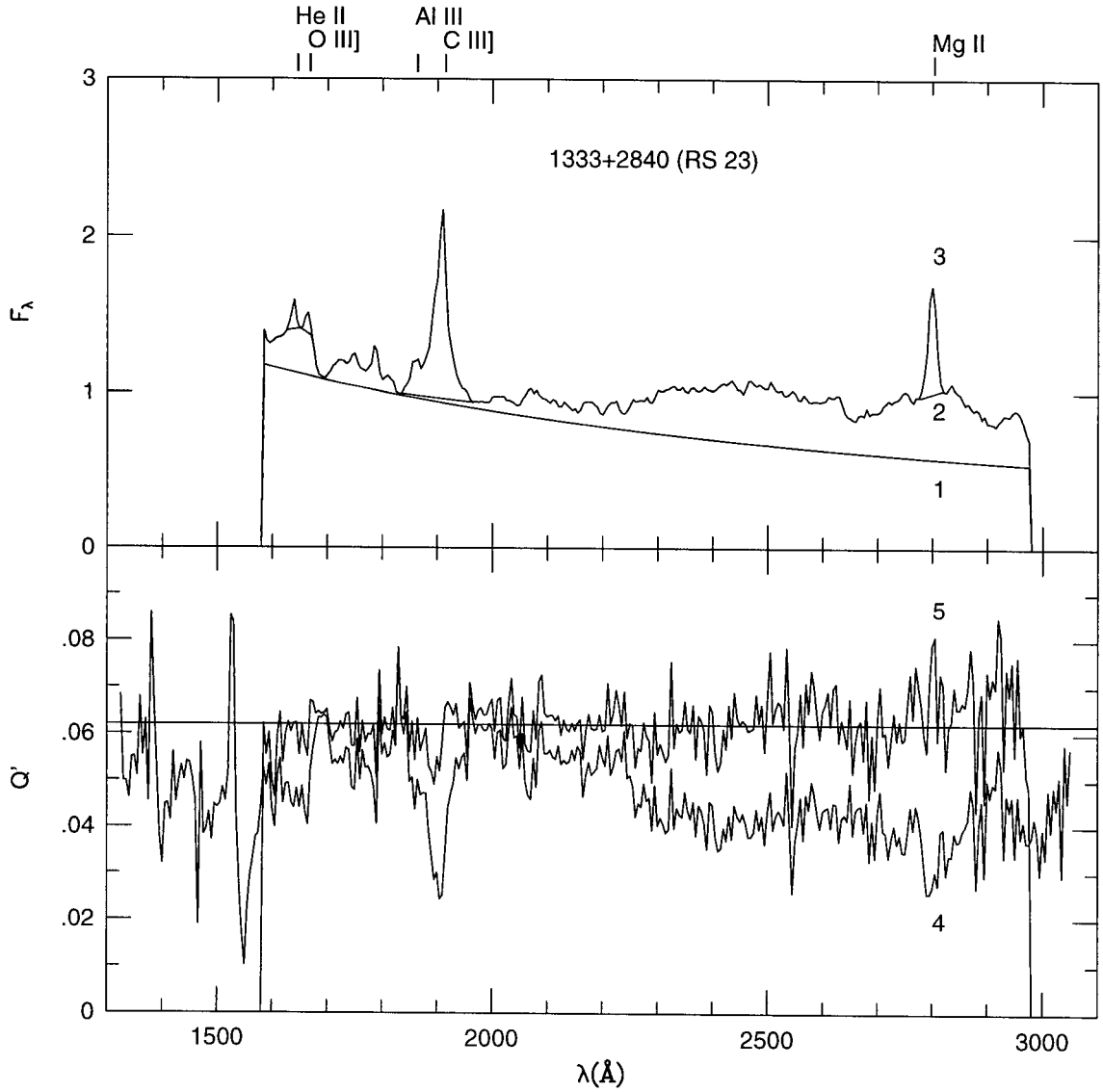

Figure 4.8: (a) Decomposition of RS 23 into polarized power law continuum and unpolarized emission lines. Curves 1, 2, and 3 are the continuum F_c, continuum plus Fe II, and total flux $F_c + F_l$. (b) Comparison of uncorrected (4) and dilution-corrected (5) fractional polarization. No correction is made blue-ward of C IV. The horizontal line is at $P_c = 0.062$.

A third order polynomial ($F_{c,fit}$) plus Fe II template fraction were fit simultaneously to each Keck BAL QSO with spectrum extending past 2650 Å (11 objects). The other objects in the Keck sample can not be properly fit because the Fe II bump is not in their spectra. We used a modified version of the procedure by Tran (1995), which was written

to fit and subtract host galaxian starlight from AGN spectra. The redshift of either Fe II UV 191 or Mg II low ionization BEL was used to align the spectra with the Fe II template when available, since these lines are thought to better represent the QSO rest frame. In some cases the low ionization BEL redshift is significantly different from the C III] redshift, a well known phenomenon (e.g., Weymann et al., 1991). The Fe II fraction (2255-2650 Å) and the RMS deviation of the fits are given in Table 4.3.

The polarization spectra were multiplied by the factor $F/F_{c,fit}$ to correct for line dilution. The corrected polarization spectra are presented in Figure 4.9. The polarization spectrum of 1333+2840 is not included in the figure because it was used to construct the Fe II template. BAL QSO 0043+0048 is not included because it is unpolarized, and the polarization spectrum of 1331-0108 is too noisy for the polarization correction to be useful. We plot the Fe II dilution correction vectors for the (3/9) objects which have corrections $\Delta P_r > 0.1\%$ in Figure 4.4.

The emission lines (Except for C III] in two cases) are properly corrected for and little trace of them remains in most polarization spectra. This confirms our assumption that the BEL are mostly unpolarized. The wavelength-averaged Fe II fraction ranges from 6-31%, corresponding to a line dilution factor of 0.94-0.76 in the observed polarization. The fit is poor (RMS> 4%) and the fit Fe II fraction appears to be too low in two cases (0932+5006 and 1331-0108), apparently because the Fe II template is not the right shape. The extreme widths of the BEL in 0842+3431 give them little contrast against the continuum, and so the Fe II fraction may also be underestimated in this object. It is easier to identify and separate the Fe II emission component in objects with relatively narrow lines, such as RS 23.

The result of our Fe II template fitting is that the continuum polarization is still wavelength dependent for some BAL QSO after correcting for line dilution. Four of eight objects show a distinct rise in polarization to the blue (0226-1024, 1212+1445, 1246-0542, and 2225-0534). Three of these are objects which did not appear to be well-fit by a constant continuum polarization in Section 4.8. BAL QSO 0019+0107 shows a drop in polarization to the blue even after correction for line dilution. The other three objects (0137-0153, 0842+3431, and 0932+5006) show a wavelength-independent polarization after correction, but the first of these has a noisy spectrum and the other two of these were not fit well by the Fe II template.

We conclude that there is some weak intrinsic wavelength dependence in the continuum

polarization. We discuss the implications of this in detail below. The best candidates for source of the wavelength dependence are scattering by large dust grains and differential dust absorption of the direct and scattered rays.

The results of this section depend strongly on the RS 23 emission line template. The template was derived by assuming the intrinsic continuum polarization of RS 23 is wavelength independent, which is not necessarily true. If the true continuum polarization of RS 23 rises to the blue, then the template Fe II flux is overestimated in the red. This would tend to reduce the Fe II fraction in the fits to other objects, and cause a false reddening of their dilution-corrected polarization spectra.

It is possible that the Fe II broad line ratios differ from object to object, either from reddening or ionization differences. For QSO which have heavily reddened BEL (relative to RS 23 and their own continua), the polarization would be over-corrected for line dilution in the blue, causing a false bluing of the polarization. One way around this dilemma is to take greater S/N spectropolarimetry so that every peak in the Fe II blend stands out distinctly in dilution of the polarization spectra. We approach the necessary S/N in the most highly polarized bright BAL QSO in our sample, and are encouraged to see no residual line dilution features in the corrected polarization spectra of these objects.

Another method to construct a line template is to model the Fe II emission and reddening in each object using a photoionization code. Progress has been made in this task by Wills et al. (1985), but the physical conditions and ionizing SED are not yet well enough understood to make theoretical line templates of the required accuracy. The relative strengths of the Fe II UV multiplets vary with conditions in the line-emitting gas. Wills et al. (1985) find that the strengths of the Fe II and Balmer continuum components depend on a number of factors, including intrinsic reddening, Balmer continuum absorption, and resonance fluorescence. The broad line widths can also have an impact via radiative transfer effects.

IAU	FeII	±	RMS%	$P_{r,c}$	±
0019+0107	0.111	0.009	3.5	1.09	0.07
0043+0048	0.207	0.013	3.0	....	....
0137−0153	0.203	0.008	2.4	0.73	0.21
0226−1024	0.184	0.012	3.9	1.78	0.08
0842+3431	0.059	0.010	3.4	0.42	0.08
0932+5006	0.092	0.012	4.6	0.85	0.19
1212+1445	0.179	0.005	1.8	1.94	0.48
1246−0542	0.132	0.011	3.7	1.01	0.11
1331−0108	0.193	0.013	4.5	2.37	0.55
1333+2840	0.305	.....	0.1	....	....
2225−0534	0.186	0.010	2.3	4.56	0.34

Table 4.3: Fe II and continuum fits. Columns 2 and 3 give the Fe II fraction averaged over the wavelength range 2255-2650 Å . The root-mean square deviation for the fit is listed in column 4. The Fe II-corrected red polarization $P_{r,c}$ is listed in column 5.

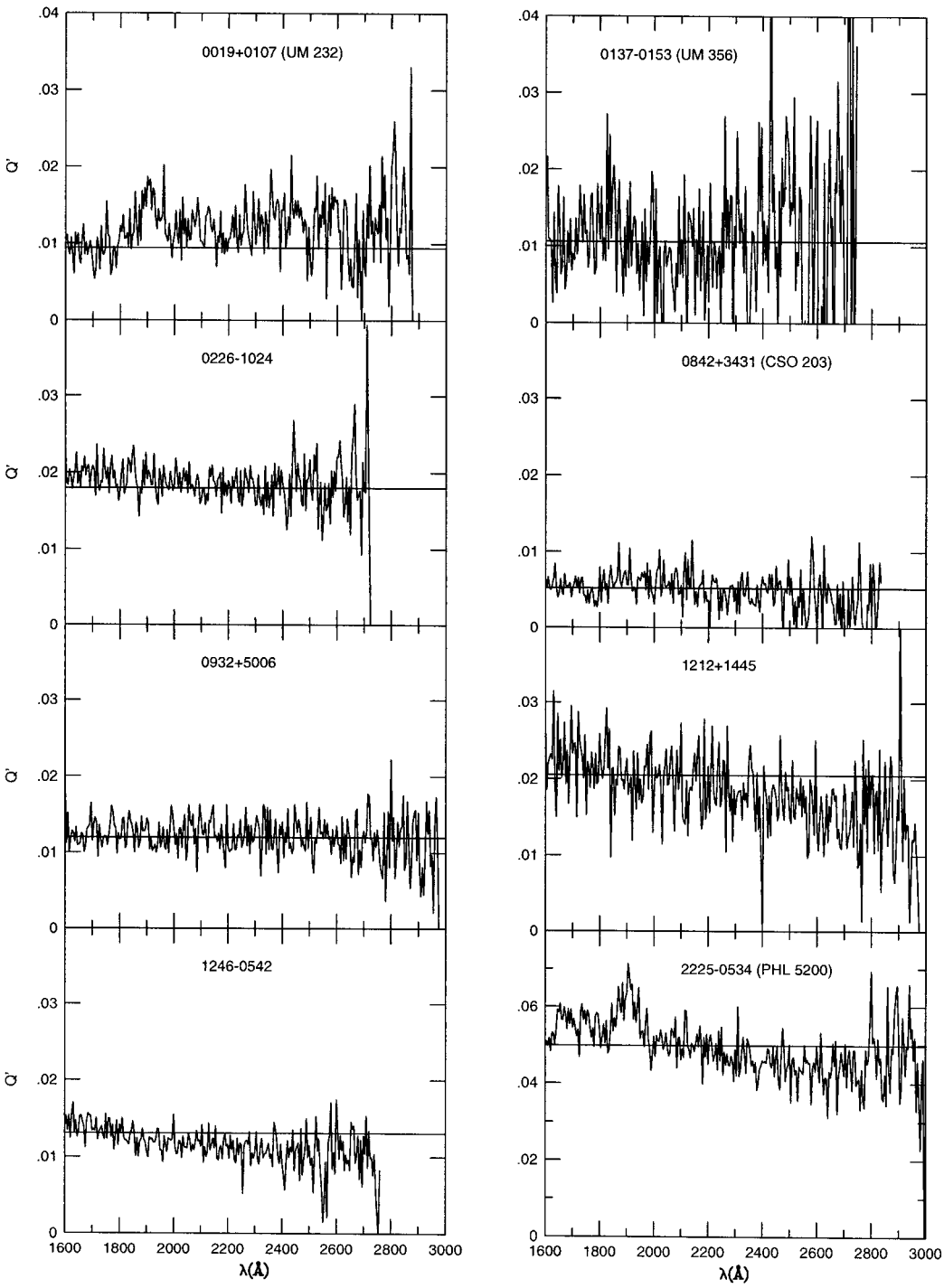

Figure 4.9: BAL QSO polarization corrected for line emission. The emission lines were fit using the RS 23 Fe II template and the procedure described in the text. Note the residual polarization in the C III] BEL of UM 232 and PHL 5200. Also note how the polarization spectra of four objects rise to the blue. The horizontal lines are drawn at the continuum (P_1) polarization level tabulated in Table 2.5.

4.10 Fe II Dilution in 0059-2735

The low-ionization BAL QSO 0059-2735 is a special case where emission line dilution is essential to understanding the polarization spectrum. The flux and polarized flux spectra are chopped up by a plethora of narrow absorption lines (NAL) and BAL, complicating the interpretation. Figure 4.10 shows an expanded view of the 0059-2735 spectra. As noted in Chapter 2, the NAL are deeper in polarized flux than in total flux, and the NAL polarization seems to vary unpredictably from one absorption feature to the next. This is contrary to what is observed in the BAL of this and most other objects, where partial coverage of the polarized light source causes polarization to rise in the troughs. Two other Lo-BAL QSO show similar polarization behavior in their NAL. The polarization drops in all NAL of FIRST 1556+3517, while it rises in some NAL and drops in other NAL of FIRST 0840+3633 (Brotherton et al., 1997). For both of these objects, the polarization of the NAL never rises above the polarization of the continuum.

We hypothesize that the wavelength-dependent polarization across the NAL in Lo-BAL QSO is merely a result of BEL dilution of the continuum. In the case of FIRST 1556+3517, the polarization drops to 0% in the NAL because they completely absorb the polarized continuum source and have a local continuum covering factor of 100%. The residual flux in the NAL is from unpolarized emission lines, including Fe II. In 0059-2735 and FIRST 0840+3633, some NAL are saturated, but the polarization doesn't drop to 0% because the local continuum covering factor is $< 100\%$. Our polarimetry is reinforced by high resolution observations of 0059-2735 (Wampler et al., 1995, WCP), which show that many of the NAL components are saturated, but have a range of non-zero residual flux levels. WCP also suggest that the residue may be Fe II line emission. In the case of unpolarized BEL, the polarization level in the NAL is given by

$$P = P_c d = P_c \frac{1}{1 + \frac{F_l}{F_c}} \tag{4.12}$$

$$\frac{F_l}{F_c} = \frac{F_{l,o}}{F_{c,o}} \frac{1 - f_l + f_l e^{-\tau}}{1 - f_c + f_c e^{-\tau}} \tag{4.13}$$

In Equation 4.12, d is the line dilution correction. In Equation 4.13, $F_{l,o}$ and $F_{c,o}$ are the unabsorbed line and continuum flux, f_l and f_c are the local line and continuum covering

factors, and τ is the optical depth of the NAL. Note that $P < P_c$, which is consistent with the observations.

We can make progress in deciphering the polarization spectrum by studying the unpolarized line flux F_l (computed via Equation 4.9 in Section 4.8). We tried a range of values $P_{c,max} = 0.018 - 0.025$, and $P_c = 0.022$ gave the best results. Figure 4.11 shows the unpolarized flux component in 0059-2735, which shows many of the same emission line features as the RS 23 BEL template in the bottom panel. This confirms that the polarization drop in the NAL is due to dilution by unpolarized line emission. The polarization decreases in the various NAL by the dilution factor d in Equation 4.12.

In addition to Fe II, strong C IV and Mg II BEL are seen in the unpolarized flux spectrum. This is particularly striking in the case of C IV, which is quite weak in the total flux spectrum. In fact, the C IV BEL unpolarized flux is greater than the total flux at the same wavelength. This means that C IV is polarized perpendicular to the continuum, which is quite different from all the other unpolarized BEL in the spectrum. This suggests that the C IV BEL photons are resonantly scattered by an equatorial BALR. The contribution from resonantly scattered continuum photons must be relatively small since the C IV BEL is quite narrow. The C IV BEL in the unpolarized flux spectrum extends from -2900 km/s at the bottom of the C IV BAL to 4400 km/s. The peak is redshifted by 2200 km/s with respect to the peak in total flux; which makes sense if the flux in the blue wing is absorbed by the near-side BAL clouds. Resonance scattering is considered in detail in Chapter 5.

The C III] BEL is present in the total and unpolarized flux spectra but is quite weak compared to Mg II, and Fe III. This suggests that the high-ionization BEL are largely obscured, while the low-ionization BEL are not. This requires stratification of the BELR, which is seen also in the reverberation mapping of Seyfert 1 galaxies.

There is no indication of the Fe II NAL in the unpolarized line spectrum (Fig. 4.11), but they are plainly present in the polarized continuum flux spectrum (Fig. 4.10). This suggests that the NAL cover at most a small fraction of the BELR ($f_l << 1$) and a large fraction of the direct and scattered continua ($f_c \simeq 1$). The NAL at 2393 Å has local covering fraction $f_l = 0.7$, assuming it is saturated. There are a few narrow dips in the unpolarized flux spectrum, but we could not identify these with absorption lines in the high-resolution spectrum of WCP, so they are probably just noise.

The Mg II, Al II and Al III BAL are present in the unpolarized line spectrum, and the

Mg II and Al III BAL have negative unpolarized flux. This is partly due to the excess polarized continuum flux in the BAL, an effect seen in other objects such as 0226-1024 (Fig. 4.5). In other words, we underestimated P_c in the bottom of the BAL by using the continuum value, and therefore underestimated F_l. The blue wings of the Mg II and Al III BEL may be partially absorbed, as in C IV. We expect that the resonance scattering contribution to these lines is much lower than in C IV, and most of the flux comes directly from the low-ionization BELR.

We require five separate lines of sight to explain the flux spectra and polarization behavior in 0059-2735–two lines for continuum, and three for the BEL. The unpolarized and polarized continua are both absorbed by the NAL and BAL, but to different degrees. The low-ionization BEL are absorbed by the BAL, but not the NAL. The high ionization BEL are highly obscured, perhaps by dust; the weak remainder of the BEL is absorbed by the BAL, but not the NAL. The C IV BEL is resonantly scattered by the far side of the BALR and comes booming through in polarized flux. We can infer that the NAL clouds have a smaller local covering fraction than the BAL clouds; they only absorb the direct and scattered continuum, which have relatively small angular extent. The continuum scattering region is extended, since it is only partially covered by the BAL clouds. The low-ionization BELR has the largest angular extent, but is still partially covered by the BAL. We discuss the geometry in more detail in Chapter 5.

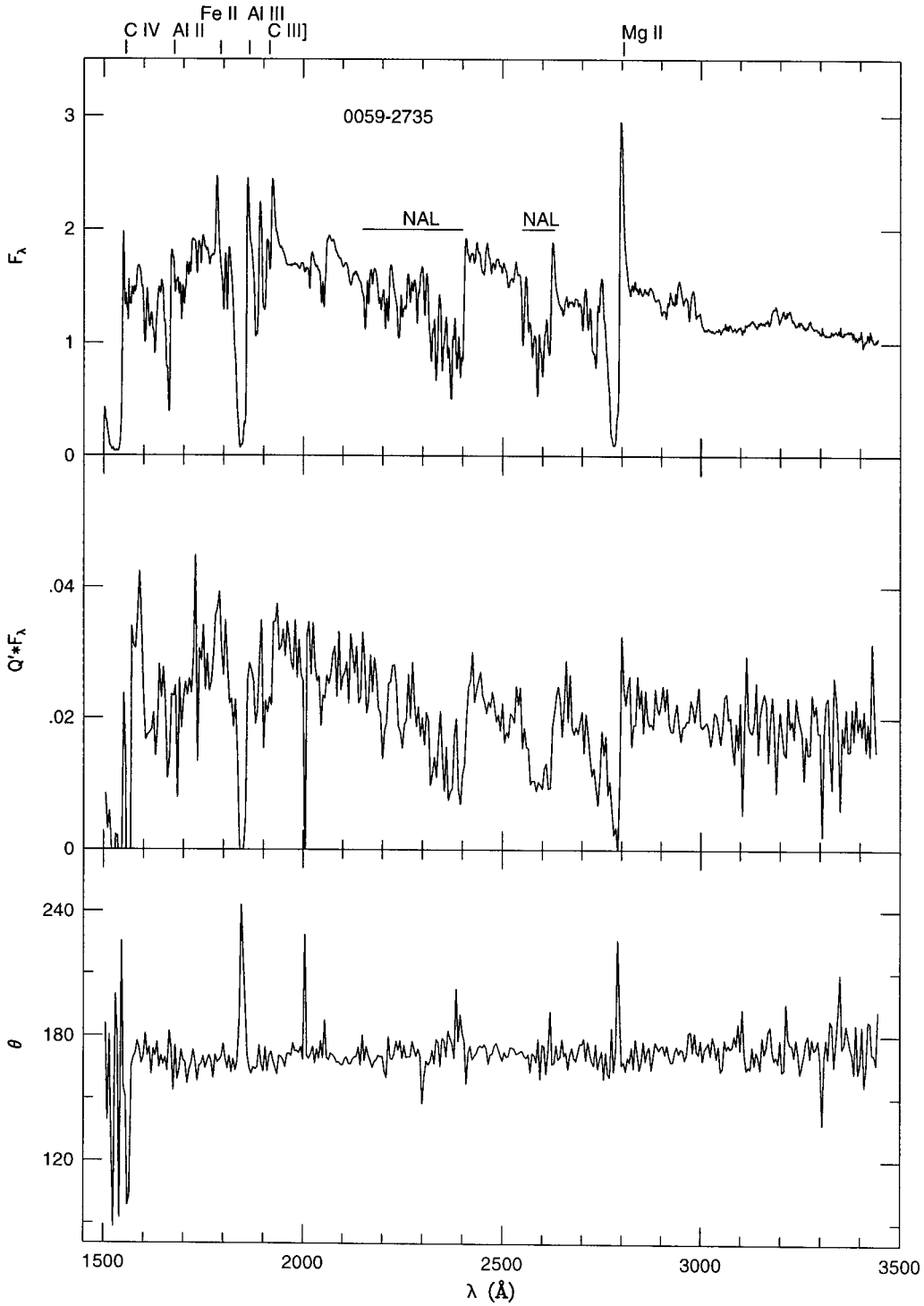

Figure 4.10: BAL QSO 0059-2735. Panels 1, 2, and 3 display the flux, polarized flux and PA. Note that the emission lines are absent in the polarized flux spectrum and the NAL are deeper in polarized flux than in total flux. In the bottom panel, there are PA rotations in the BAL and NAL.

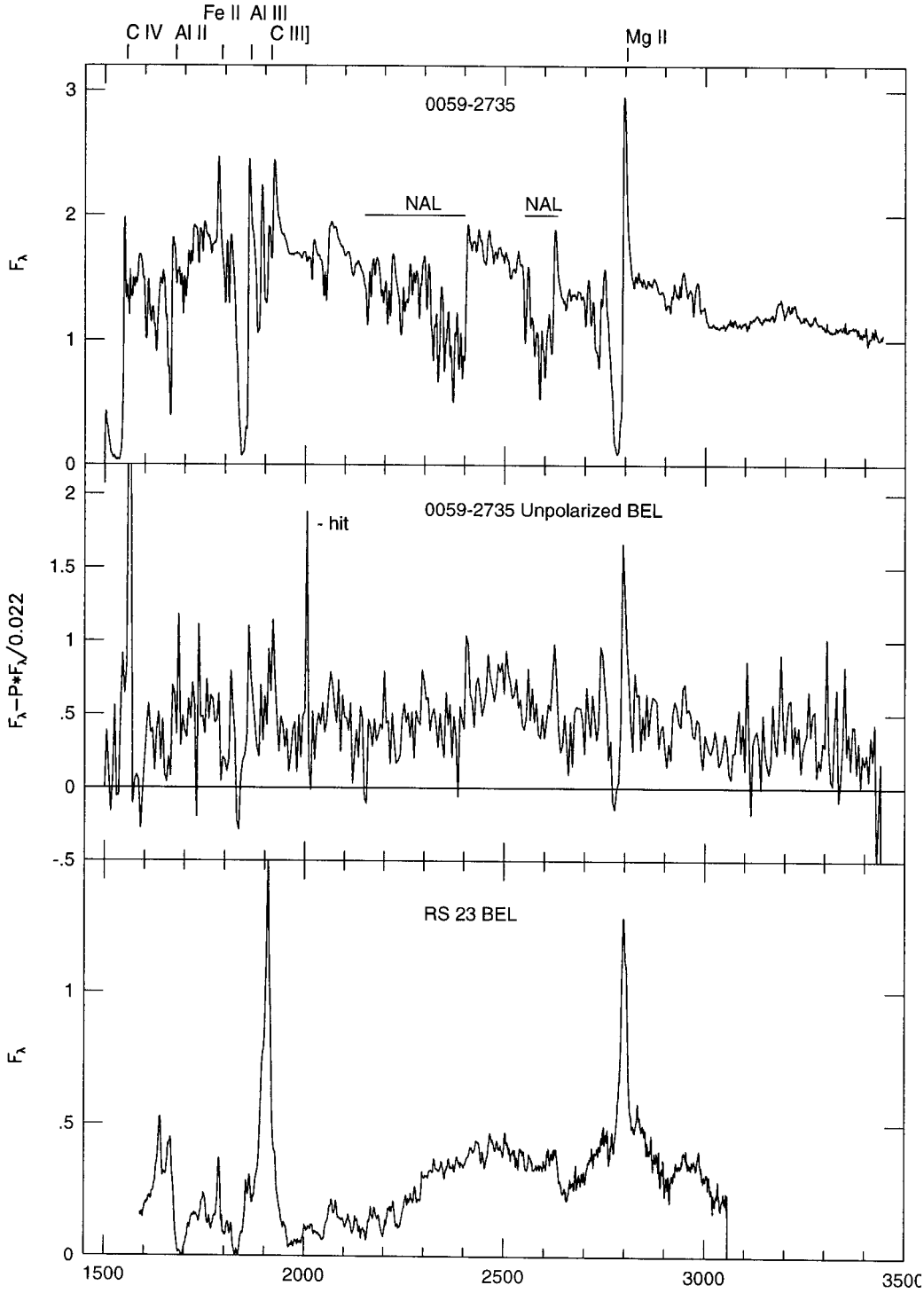

Figure 4.11: 0059-2735. The total flux is in panel 1. The unpolarized flux in panel 2 was computed by scaling the polarized flux by $1/P_{c,max}$ and subtracting it from the total flux. Several Fe II emission features are present, as well as Mg II and C IV emission lines. The unpolarized flux in panel 2 has a similar shape to the RS 23 BEL template in panel 3, demonstrating that the NAL polarization variations are due to line dilution. Also note that the NAL are not apparent in panel 2, so the BEL are not absorbed by the NAL.

4.11 Electron Scattering

Electrons are the simplest scattering particles, and behave as dipole oscillators in the non-relativistic regime. Optically thin Thomson scattering leads to a polarization which is independent of wavelength. However, wavelength-independent polarization is not unique to Thomson scattering and can be copied by large dust grains over fairly wide wavelength intervals. Electron scattering is likely to dominate in regions of the nucleus which are exposed to and completely ionized by hard continuum emission from the central source. However, dust may exist at radii smaller than the dust sublimation radius if it is shielded by a large column of gas, such as may be present in the accretion disk which feeds the nucleus.

There is evidence for scattering by warm ($T \sim 3 \times 10^5$K) electrons in the broadening of scattered emission lines in NGC 1068 (Miller et al., 1991). Some radio galaxies, such as Cygnus A (Ogle et al., 1997) show extremely broad scattered emission lines. It is unknown whether the large line widths in these radio galaxies are due to thermal broadening by the scatterers or motion intrinsic to the broad emission line region.

The BAL QSO in our sample with wavelength-independent continuum polarization may be polarized by Thomson scattering in the BELR or BALR. An optical depth $\tau_{es} = 1$ requires an electron column density of $N_e = 1.5 \times 10^{24}\mathrm{cm}^{-2}$. This greatly exceeds the column densities derived for the BALR from the depths of UV BAL. However, as we noted in Chapter 1, these estimates may be unreliable. In addition, X-ray observations yield much larger column densities, $N_H \sim 10^{23}\mathrm{cm}^{-2}$. With a high ionization parameter, this would give an optical depth to electron scattering of $\tau_{es} \sim 0.1$, which is the right order of magnitude for optically thin scattering.

4.11.1 Scattering in the Broad Absorption Line Region

The first possibility is that the scattering occurs entirely in the BALR. This is attractive because it naturally leads to partial coverage of the polarized continuum by the BAL clouds. For the geometry of Figure 4.2 and a constant electron density, we can compute the polarization due to electron scattering in the BALR using Equation 4.4. The shape parameter is obtained from Equation 4.3,

$$\gamma = \frac{1}{3}\frac{\cos^3 i_2 - \cos^3 i_1}{\cos i_2 - \cos i_1} \tag{4.14}$$

For our best fit model with $i_2 = 60$, $i_1 = 53$ degrees, we get $\gamma = 0.30$. If we assume that the scattered light is a small fraction of the direct light (which is true for the optically thin case), and a viewing angle of $i = 60$ degrees, then we get $P = 1.5\%$ for $\tau_{es} = 0.1$. If there is indeed a sufficient optical depth to electron scattering in the BALR, then it is easy to produce the observed continuum polarization within the unification scenario. Note that the scatterers will produce a significant grey attenuation of the direct continuum (10% for $\tau_{es} = 0.1$) since they lie in the line of sight.

The continuum polarization distribution is readily understood if it is produced by electron scattering in the BALR. There is likely to be a significant range in BALR column densities and scattering optical depths. For objects with $N_H < 1.5 \times 10^{22}$ and $\tau_{es} < 0.01$, the polarization will be very low ($P < 0.15\%$) and not detected in our survey. In this context, the extremely low polarization of UM 275 ($P_c = 0.11 \pm 0.06\%$) can be accommodated into an equatorial BALR model with little difficulty. Here we are only considering scattering on the scale of the BALR. The lack of polarization of the light emitted by the central continuum source in UM 275, before it is scattered by the BALR, is still mysterious and will be discussed in more detail below.

The upper limit to the BAL column density is set by Thomson attenuation. First of all, we are not likely to detect objects with $\tau_{es} > 1$ because they are attenuated. Perhaps more importantly, Thomson-thick clouds will not be accelerated to high speeds by radiation pressure.

4.11.2 Scattering in the Broad Emission Line Region

One clue to the nature and location of the scatterers comes from the low BEL polarization (see Chapter 5), which suggests that the scattering region is internal to or coincident with the BELR. The continuum may be scattered by electrons in the BELR. The geometry of the BELR is not well constrained, but may be similar to that of the BALR (Murray et al., 1995, MCG). We know that the BELR lies at least partly interior to the BALR. A plausible scenario is that the BAL wind is swept outward from the BELR. In this model, the

BELR could provide the large X-ray absorbing column which shields a lower column density BALR, as required by the dynamical calculations of MCG. The polarization calculations for an optically thin ($\tau_{es} < 1$) BELR are identical to those for an optically thin BALR. The main difference between the two models is the coverage of the electron scattering region by the BALR. The BELR need not lie along the line of sight to the continuum. An alternate geometry for the BELR would put it at an intermediate elevation where it is only partly occulted by the BALR. The BELR may be composed of chaotically orbiting clouds with a low volume filling factor, but it is more likely to induce a high continuum polarization if it is organized in a jet or a disk structure. The column density of the BELR is not as well constrained in such models. For some viewing angles a BELR cloud could occult the continuum source, and might reveal itself as a narrow associated absorber.

Korista & Ferland (1997) calculate the albedo of ionization-bounded BEL clouds, including the effects of Thomson scattering, Rayleigh scattering in the wings of Lyα by H I, and the ionization edges and absorption breaks of a number of ions. The relative contributions of Rayleigh and Thomson scattering are determined by the ionization level in the cloud. These models predict an albedo which increases slowly to the blue from 3650 to 1600 Å, corresponding to decreasing absorption below the Balmer jump. This nicely matches the slow rise in polarization to the blue seen in our BAL QSO observations.

From 1600 to 1100 Å the albedo can increase dramatically, approaching unity in the vicinity of the Lyα resonance (Korista & Ferland, 1997, KF). We may see a hint of this effect in 6 BAL QSO (0146+0142, 0226-1024, 0856+1714, 1333+2840, 1524+5147, and 1235+0857). These objects show a moderate rise in the polarized continuum flux between C IV and Lyα, which appears to peak in the red wing of N V. Unfortunately, this effect is masked at the peak of Lyα by residual BEL polarization and N V absorption.

The albedo blue-ward of Lyα should be significantly reduced by C I, O I, and H I absorption edges (KF), but this effect is difficult to measure because of intervening and associated absorption in this region. In the one object (0105-265) for which there is data below the Lyman limit (912 Å), the polarization persists at a level of 2-4%. This indicates that absorption edges do not significantly modify the polarization, consistent with a highly ionized scattering region. Another important prediction of scattering in ionization-bounded BEL clouds is a drop in albedo at the Balmer jump. This should be readily visible near 3646 Å in polarized low-z BAL QSO. We do not see this effect in PG 1700+5153, which

suggests that neutral hydrogen opacity is not large in the scattering region.

While the rise in polarization near Lyα is suggestive of weak Rayleigh scattering in some BAL QSO, and the rise in continuum polarization to the blue could be attributed to neutral hydrogen opacity, the lack of a polarization signature at the absorption edges is difficult to reconcile with scattering by a low-ionization cloud. It instead appears that the scattering region must be highly ionized, and the scattering dominated by electrons.

4.11.3 Scattering in an Accretion Disk

Theorists have long predicted that a thermally radiating accretion disk should produce continuum light polarized at a level of up to 12% (Chandrasekhar, 1960) in the case of electron scattering. More realistic disk models include opacity effects due to hydrogen and other ions which modify the wavelength dependence of the polarization and tend to reduce its magnitude. General relativistic effects are also important since the UV-optical radiation originates within $10R_G$ of the central black hole (Laor et al., 1990). Shorter wavelengths are generally emitted closer to the black hole where gravitational effects are stronger. Gravitational lensing tends to de-polarize the radiation by rotating the plane of the electric vector. Laor et al. (1990) predict wavelength dependent polarizations of 1-5%, with polarization rising to the blue in the UV region due to decreasing absorption opacity, and a significant drop in polarization near the Lyman edge.

As with the BELR scattering model above, we expect the Lyman edge feature to be prominent in the polarization spectrum of an accretion disk. Since it is not seen in our data, or spectropolarimetry of non-BAL QSO (Koratkar et al., 1995), it is unlikely that the polarization wavelength dependence in BAL QSO is due to hydrogen opacity. As we argued above, the scattering region must be optically thin and highly ionized if electrons are the scattering agent. It is difficult to reconcile this with optically thick accretion disk models.

If the continuum polarization were produced entirely in the accretion disk, at a radius of $10R_G$, then the polarized light source would appear point-like at the scale of the BALR. It would be completely covered by the BALR, and the polarization would not vary across the BAL due to partial coverage of the continuum source. In this scenario, the extra scattered polarized flux in the BAL would have to come entirely from resonance scattering in the BALR. This conclusion can be avoided if the BALR consists of very small cloudlets

($r \simeq 10^{14}$cm) with local covering fraction $f_l < 1$.

Optically thin and thick accretion disks are distinguished by the position angle of the scattered continuum. An optically thin disk produces polarization aligned with its axis, while a thick disk is polarized in the plane of the disk. This effect can lead to PA rotations in the continuum in the presence of wavelength-dependent opacity sources.

4.12 Dust Scattering

In this section we explore the possibility that the wavelength dependence of BAL QSO polarization is due to dust scattering. Since the scattering regions are of the same size scale as the BELR and BALR, the dust has to survive the harsh conditions and energetic radiation field in the nucleus. First we review the evidence for dust in AGN, then we consider the wavelength dependence of dust scattering.

4.12.1 Evidence for Dust in AGN

There is a large body of evidence pointing to significant amounts of dust in AGN. One reliable dust indicator is the Balmer decrement (ratio of Hα to Hβ). Recombination generally leads to a $\sim$ 3:1 Balmer decrement in photoionized nebulae (Osterbrock, 1989). In the presence of dust, this ratio is increased by reddening. Extended emission line imaging of radio galaxies such as Cygnus A (Jackson et al., 1998) indicates an extensive amount of dust. Continuum reddening is also apparent in a large number of radio-loud quasars (e.g., Masci, 1997). This evidence for dust is somewhat indirect since it requires knowledge of the intrinsic, un-reddened spectral energy distribution. Samples selected optically for blue continua, such as the LBQS, are biased against red objects with a lot of dust extinction.

Strong mm-FIR emission (above the extrapolated synchrotron component) has been detected in several high-redshift AGN, including radio galaxies and BAL QSO (e.g., Hughes et al., 1997). This emission appears to be thermal and its source is dust, heated either by a starburst or the nuclear continuum source. The estimated dust masses are in the range $10^8 - 10^9 M_\odot$, but are subject to large uncertainties (Hughes et al., 1997). It is unknown if the dust is located in the nucleus or extended star-forming regions, but in any case it is plausible that dust can provide a significant optical depth to scattering in high-redshift AGN.

In the extended scattering regions of narrow line radio galaxies, dust is preferred over electrons. Dust has a typical scattering efficiency per unit mass of 6×10^4 times that of ionized gas, and for a Galactic dust-to-gas ratio, the efficiency of dust scattering is about 400 times greater than electron scattering (Dey et al., 1996). Especially in distant radio galaxies with scattering regions several kpc in extent, an enormous mass of gas ($\sim 10^{11}$ solar masses) would be required for electron scattering (Dey et al., 1996).

Dust is a necessary component in unified AGN models. In these models, a dusty molecular torus obscures the central regions from an equatorial perspective. The torus serves to collimate the radiation from the AGN and also serves as a source of fuel for the central engine. While there is strong evidence for unification in a number of Seyfert and radio galaxies, and a handful of ultra-luminous infrared galaxies, it has by no means been demonstrated that all AGN are unified. In particular, the absence of a detected population of type 2 QSO makes it unclear if there is a dusty torus in any type 1 radio-quiet QSO. If an obscuring torus is a fundamental component of QSO, then it is likely that dust is accreted from the more extended regions and funneled along with the molecular gas down into the central regions.

The survival of dust in the interior regions of QSO is an important problem. The harsh radiation field can heat dust to its sublimation temperature, which is in the range 1400-1750 K for graphite and silicate grains. At a given radius from the central continuum source, small grains are hotter than large grains. Large grains will therefore survive closer in to the central source than small grains. Hence we might expect a grey dust scattering albedo near the inner edge of the dusty torus. Laor & Draine (1993) note that the outer edge of the broad emission line region is about the same as the dust sublimation radius. So the question is: does the dusty torus or the dust-free ionized inner region scatter the most light?

4.12.2 Wavelength Dependence

Dust scattering provides a possible explanation for the wavelength dependence of QSO continuum polarization. Dust is a catch-all word for small particles which can range in size from $10^{-3} - 10$ microns. Dust has a complex wavelength-dependent scattering efficiency, absorption efficiency, and phase function. The wavelength dependence of the dust albedo and absorption depend on its chemical composition and distribution of dust grain sizes (e.g., Laor & Draine, 1993). If the dust consists of mostly large grains (10 microns), then the IR to

X-ray scattering and absorption efficiencies are essentially grey. If the dust instead consists of small grains (10 Å), then the scattering efficiency decreases to the red as λ^{-4} (Rayleigh scattering). Intermediate size dust grains which are larger than 0.1 μm can impose a weak wavelength dependence on the scattering efficiency and polarization.

Depending on the composition of the dust, there may be resonant absorption features in the UV. For example, graphite has a prominent absorption feature which has been used to explain interstellar absorption at 2175 Å. Evidence for such a feature is not present in our data, and has been elusive in most extragalactic observations. The presence of dust features in the scattered light spectrum depends sensitively on the geometry and optical depth to scattering (Manzini & di Serego Alighieri, 1996). There is a competition between scattering and absorption; at wavelengths where there is enhanced absorption, scattering is also enhanced. Both UV absorption and IR emission features from dust are small if the dust grains are large. This would help explain why the 2175 Å absorption and SiC emission features are not seen in AGN.

4.13 Dust Absorption

In addition to its role as a possible scattering agent in QSO, dust may cause significant extinction and reddening. Differential reddening between the scattered and direct continuum light could introduce a wavelength dependence to the polarization. This is suggested as a possibility by Goodrich & Miller (1995) and Hines & Wills (1995). In this scenario, the scatterers are electrons along the axis of the QSO. If the direct ray is reddened by dust and the scattered rays are not, then the continuum dilution will decrease and the polarization will increase to the blue. As we discuss in Chapter 5, the polarized scattered light is absorbed to a lesser extent than the direct light by the BALR. If there is dust associated with lines through the BALR, then the direct continuum would naturally be more highly extincted and reddened than the scattered continuum. The dust could either be mixed in with the BAL clouds or belong to a separate phase. This is a natural scenario if BAL QSO are viewed on dusty lines of sight which skim the accretion disk or torus.

Sprayberry & Foltz (1992) have shown that the red colors of low-ionization BAL QSO can be explained by absorption from SMC-type dust or silicates. Some of the deepest troughs are seen in the low ionization broad absorption line objects, which have the reddest

continua of all BAL QSO. However, high-ionization BAL QSO show little evidence for reddening relative to non-BAL QSO. This is readily explained if there is a correlation between BAL optical depth and dust optical depth. Low-ionization BAL QSO have greater BAL and dust optical depths and greater reddening than high-ionization QSO. Hines & Wills (1995) correct for Fe II dilution in IRAS 07598+6508 using the I Zw 1 template of Boroson & Green (1992). The corrected polarization spectrum rises to the blue, consistent with a λ^{-1} wavelength dependence. After Fe II correction, the increase of polarization to the blue may be completely accounted for by decreasing dilution by the unpolarized, reddened, direct continuum. We have observed this same object with higher S/N at Keck and confirm the conclusions of Hines & Wills (1995).

Another possible source of continuum polarization is dichroic absorption by magnetically aligned dust grains. This would imprint a characteristic spectral shape on the polarization (Serkowski et al., 1975). It would also be accompanied by strong extinction and reddening by the same dust grains. Sufficient reddening is only observed in a small number of Lo-BAL QSO, so dichroic absorption is probably not a large contributor to the polarization in most BAL QSO.

4.14 Continuum PA Rotations with Wavelength

A few BAL QSO show PA rotations with wavelength in the continuum. This may indicate the presence of multiple sources of continuum polarization. We concentrate on the most conspicuous rotators in our Keck sample, which are 0019+0107, and 0932+5006. These two objects show PA rotations in the continuum of > 10 degrees, away from the noisy edges of the spectrum.

Galactic interstellar polarization by magnetically aligned dust grains is one possible culprit. The maximum PA deviation due to interstellar polarization P_{is} for an object with intrinsic polarization P is given by

$$(\Delta\theta)_{max} = 0.5 \arctan(\frac{P_{is}}{P}) \tag{4.15}$$

The maximum PA deviation was estimated using the maximum interstellar polarization

IAU	$(\Delta\theta)_{max}$	$\Delta\theta(obs)$	$\pm$
0019+0107	7.2	13.3	5.0
0932+5006	0.6	8.0	2.6

Table 4.4: Interstellar PA rotation. Maximum PA rotations due to absorption by Galactic dust are listed in column 2. The observed PA rotations and their uncertainties are listed in columns 3 and 4. Interstellar contamination can not fully account for the observed rotations.

$P_{is} = P_{max}$ (estimated in Table 2.4). The PA variation with wavelength was determined from a Serkowski curve (Serkowski et al., 1975) which peaks near 5450 Å in the observed frame. The differential change from 4050 Å to the peak of the Serkowski curve is approximately $\Delta P_{max} = 0.12 P_{max}$. Using this and $P_c(\lambda)$ in Equation 4.15, we tabulate $(\Delta\theta)_{max}$ for 0019+0107 and 0932+5006 in Table 4.4. The maximum interstellar polarization effect is inadequate to account for the PA rotations observed, so some of the PA rotation must be due to an extragalactic source.

It is possible that the PA rotation is due to absorption by aligned dust grains in the QSO host galaxy or the QSO itself. The Serkowski formalism was derived for wavelengths $\lambda > 3100$ Å and for Galactic dust, so it may not apply to the UV spectra of QSO. However, both 0019+0107 and 0932+5006 have normal UV spectral indices ($\alpha = 0.4$ and 0.5), which are not far from the canonical $\alpha = 0.7$ (Francis et al., 1991, and references therein). They are actually bluer than most BAL QSO in our sample, which have a mean UV spectral index of $\alpha = 1.1 \pm 0.5$. There is therefore no indication of an extra amount of reddening in the total flux spectra of these objects.

The PA rotation in 0019+0107 coincides with a rapid drop in polarization blue-ward of 2000 Å (Fig. 2.2). It appears that the main source of scattered light is extincted and a weaker source with a different PA takes over. Note that the wavelength dependence must come from extinction of the scattered light since dust scattering efficiencies are flat or increase to the blue in the UV spectral region. We have not been able to positively identify the opacity source which is responsible for the absorption of scattered light in 0019+0107, but dust outside the scattering region is a possible candidate. In particular, small dust grains ($\sim 0.01\mu$m) have an absorption cross-section which peaks near 1200 Å (Laor & Draine, 1993), and might survive outside of the BELR. This model is somewhat awkward because it requires more dust along the scattered line of sight than the direct line of sight. However,

this is the only object in a sample of 34 high redshift BAL QSO which has a red polarization spectrum. There may be a fluke dust cloud along the scattered line of sight. This model can be tested with UV polarimetry; the polarization should recover blue-ward of 1200 Å (rest).

The PA rotation in 0932+5006 is more difficult to explain, because the polarization has a flat wavelength dependence (Fig. 2.13). Two sources of polarized radiation with different spectra and different PA would have to conspire to give a constant polarization. Laor et al. (1990) predict PA rotations due to general relativistic effects near the central black hole in QSO. These occur if the polarization is produced by scattering in a thermally emitting accretion disk. The rotations in this model increase with frequency because higher energy photons are emitted closer to the black hole. However, this effect should amount to < 3 degrees in the 1300-3000 Å interval of our spectrum.

4.15 Continuum Polarization Variability

We did not undertake a variability monitoring campaign for this thesis, but seven objects were observed on more than one epoch, separated by intervals of 2 months to 2 years. The S/N of the Keck continuum polarization measurements is high enough that we can detect polarization variations at the level of 0.1% in some objects. Table 4.5 breaks down the polarization of the multi-epoch observations, listing P_1 and PA_1 (1900-2200 Å) for each epoch. Four out of seven BAL QSO have P and PA variations of $< 3\sigma$, and we do not consider them variable. The remaining three (0019+0107, 0105-265, and 0226-1024) are variable at the $> 3\sigma$ level (99.73% confidence). The change in the percentage polarization ranges from 0.15-0.44%, and the change in PA ranges from 3.4-7.6 degrees for the variable objects.

Continuum flux in the variable BAL QSO can not be dominated by a blazar component since the polarization is low and varies by only a small fraction of a percent. A mini-blazar component is still a possibility. Synchrotron emission from relativistic electrons spiraling in a magnetic field is thought to be responsible for the high and variable polarization seen in blazars. All blazars are strong radio sources, and many show apparent superluminal motion in their radio jets. Flares in optical flux and polarization appear to be connected to activity at other wavelengths, including the radio, and may be associated with the ejection of new components in the radio jet. Lower level mini-blazar activity is seen in some quasars.

BAL QSO are radio-quiet for the most part, with radio-to-optical flux ratios of less than unity. It therefore seems unlikely that the blazar mechanism is operating in BAL QSO. While BAL QSO are radio-quiet, they aren't necessarily radio-silent. Francis et al. (1993) find an excess of BAL QSO among radio-moderate ($0.2 < \log R < 1.0$) objects. However, they also find that relativistic beaming models are inconsistent with the observed distribution of radio-to-optical flux ratios. It is possible that attenuation of the optical flux relative to the radio is responsible for increasing the $\log R$ values in BAL QSO (Goodrich, 1997).

A second explanation for the polarization variability is dilution by variable emission lines. Variability in the blended Fe II lines could mimic continuum variability. However, the variability extends uniformly over the entire range of the spectrum in 0019+0107 and 0226-1024, ruling out variable BEL dilution.

If the continuum polarization is due to scattering, which is most likely the case, then variability in the scattered flux will be delayed with respect to variability in the direct continuum flux. It may be possible to use this effect to do reverberation mapping of the scattering region (as discussed in Chapter 1). In this model, we would expect the polarization to return to its equilibrium value after a light-crossing time of ~ 0.1 yr (rest frame). Motions within the scattering region may also change its configuration on a time scale of ~ 1 yr. Variable ionization and electron density are unlikely to be a large effect in a highly ionized scattering region, but may be important for scattering in a partially ionized region.

4.16 Line and Polarization Correlations

We measured the rest equivalent widths (REW) of the BEL and BAL of all objects in the Keck and Palomar samples. We used a low-order spline fit to the continuum, which was conservative in the sense that it gave a lower limit for the flux in the Fe II line blends. Knot points were set at continuum windows, including but not restricted to 1680-1710 Å, 1820-1840 Å, 1960-1990 Å, and 2640-2700 Å. The BEL REW were measured at a velocity width of 16,200 km/s, and include only flux above the continuum level. Half REW (HREW) were measured for the red side of the C IV BEL, since the blue side is often contaminated by C IV absorption. The NV/Lyα and Al III/C III] BEL blends are measured as single lines. The BAL REW were measured from 0-29,400 km/s, and include only absorption below the

IAU	UT Date	P_1%	±	PA_1	±	ΔP_1	±	ΔPA_1	±	
0019+0107	07 29 95	0.87	0.04	32.6	1.1					
	12 15 95	1.26	0.04	40.2	1.2	0.39	0.06	7.6	1.6	v
0059−2735	12 30 94	1.66	0.12	170.4	1.7					
	07 28 95	1.48	0.11	172.2	3.3	0.18	0.16	1.8	3.7	
0105−265	08 03 94	1.72	0.09	132.4	1.8					
	10 28 94	1.51	0.10	138.4	2.9	-0.21	0.13	6.0	3.4	
	11 06 94	1.28	0.08	135.5	2.7	-0.44	0.12	3.1	3.2	v
0146+0142	11 06 94	1.12	0.05	130.1	1.7					
	12 15 95	1.15	0.05	135.4	1.1	0.02	0.07	5.3	2.0	
0226−1024	12 31 94	1.80	0.02	167.8	0.4					
	10 05 96	1.95	0.01	171.2	0.2	0.15	0.02	3.4	0.4	v
0842+3431	11 06 94	0.56	0.03	21.7	1.7					
	12 17 95	0.49	0.03	28.5	1.8	0.07	0.04	6.8	2.5	
1333+2840	01 28 95	5.63	0.11	160.5	0.5					
	04 17 96	5.61	0.06	161.3	0.4	-0.02	0.13	0.8	0.6	

Table 4.5: Continuum polarization variability. BAL QSO observed on multiple epochs are listed, along with their polarization measurements P_1 and PA_1 in the 1600-1840 Å continuum band. (1333+2840 was measured in the 1960-2200 Å band because of a contaminating cosmic ray event in the other band.) The changes in polarization ΔP_1, and in position angle ΔPA_1 are given with their uncertainties. Objects which are variable at a level of $> 3\sigma$ are indicated with a 'v'.

continuum level.

Table 4.6 lists the results of our REW measurements for Lyα/N V, Si IV, and C IV BAL, and the Lyα/N V, Si IV, C IV, and Al III/C III] BEL. The Keck values are listed in precedence of the Palomar values because they have higher S/N. A number of measurements are missing either because the BEL or BAL was out of the range of our spectra or fell near the dichroic split.

We searched for correlations between pairs of observables using the non-parametric Spearman correlation coefficient. We expect one chance correlation out of 30 tests for a Spearman probability of 3.3%; we found 5 correlations which are more significant than this. The significant correlations among the BEL and BAL equivalent widths are listed in Table 4.7. A low probability (P_s or $P_d < 3.3\%$) indicates that the correlation is present at a high confidence level. The only significant correlations which we found were between pairs of BEL equivalent widths and between pairs of BAL equivalent widths. For example, the REW of the Si IV BAL correlates strongly with the REW of the C IV BAL, and the HREW of the C IV BEL correlates with the REW of the C III]/Al III BEL. We plot these two most highly significant correlations in Figure 4.12.

The BEL-BEL correlations are not surprising; they tell us that the amounts of emission from two different ions in the BELR are related. The BAL-BAL correlations are consistent with the hypothesis that the absorption from different ions comes from the same clouds. This was already known, since the BAL of different ions share similar velocity structure. If the C IV BAL are saturated, then there will still be a correlation with the REW of the Si IV BAL because Si IV and C IV have the same velocity widths.

We searched for correlations between the BAL or BEL properties and the polarization of BAL QSO. If viewing geometry is the main discriminant between BAL and non-BAL QSO, it may also be important in the classification of BAL properties. For example, we might expect BAL QSO viewed from an equatorial aspect to have the deepest BAL and greatest polarization. This would lead to a positive correlation between BAL equivalent width and continuum polarization. On the other hand, if BAL QSO are viewed from a very narrow range of angles, then variation in BAL depth and polarization may be unrelated. The BEL properties of BAL QSO and non-BAL QSO show only subtle differences (Weymann et al., 1991, WMF). The strongest correlation found by WMF was between the Fe II emission strength and balnicity (C IV BAL equivalent width), and they suggested that these two

IAU	Lyα/N V BAL	Lyα/N V BEL	Si IV BAL	Si IV BEL	C IV BAL	C IV BEL	Al III/CIII] BEL
0019+0107	....	.....	8.07	3.19	22.95	13.20	37.65
0021−0213	....	25.18	23.95	1.39	54.43	9.89	32.53
0025−0151	....	.....	16.49	1.78	19.21	11.14	32.53
0043+0048	....	42.61	18.05	6.15	41.31	6.02	32.92
0059−2735	....	.....	.....	.....	66.63	2.26	11.04
0105−265	71.28	70.74	21.71	5.98	51.49	9.12	35.18
0119+0310	....	.....	9.27	3.56	24.52	4.20	33.09
0137−0153	....	68.62	16.25	4.31	44.58	8.79	38.83
0145+0416	....	.....	26.30	5.09	38.37	16.30	32.26
0146+0142	51.07	63.90	15.16	0.26	34.21	9.83	22.45
0226−1024	....	61.57	25.88	2.46	52.09	7.24	33.28
0842+3431	....	.....	10.81	2.92	25.03	7.45	22.80
0846+1540	22.45	55.37	.....	.....	.....	12.55	37.66
0856+1714	....	34.65	29.59	3.83	65.95	4.45	29.25
0903+1734	60.03	24.63	30.34	0.07	65.74	5.66	27.04
0932+5006	....	.....	25.88	0.06	43.57	4.01	27.44
1011+0906	....	51.13	35.26	0.03	48.46	4.17	34.78
1212+1445	....	.....	.....	.....	.....	3.39	20.79
1231+1320	....	32.41	42.64	0.56	26.64	3.99	27.23
1232+1325	73.25	65.16	45.06	9.89	59.47	9.67	51.42
1235+0857	51.08	38.39	10.81	1.65	28.29	15.08	33.31
1235+1453	40.27	99.32	14.36	5.63	.....	14.92	59.07
1243+0121	51.17	66.25	16.55	.....	.....	24.16	64.11
1246−0542	....	.....	15.02	3.70	31.60	4.96	30.97
1331−0108	....	.....	.....	19.02	44.47	6.99	20.13
1333+2840	....	.....	.....	8.43	20.44	20.95	45.42
1413+1143	49.20	37.99	20.42	9.09	33.90	22.38	35.21
1442−0011	....	53.23	21.31	5.45	36.10	11.94	45.37
1443+0141	46.87	55.10	15.23	3.93	46.55	.....	54.49
1524+5147	35.19	54.58	3.77	5.12	20.02	7.07	30.22
2154−2005	....	89.10	10.32	5.62	17.30	13.51	39.44
2201−1834	....	.....	.....	7.40	16.32	6.19	.....
2201−1834	....	.....	.....	11.86	11.04	6.96	.....
2225−0534	....	.....	.....	10.87	53.54	19.83	54.80
2350−0045	....	.....	.....	.....	.....	5.27	39.44

Table 4.6: BAL and BEL equivalent widths. Rest equivalent widths (in Å) are given for the BAL and BEL in our Keck+Palomar sample. REW are listed for all lines but the C IV BEL, for which we list the HREW instead. Uncertainties are dominated by continuum placement, not photon noise.

var1	var2	N	r_s	P_s%	P_d%
Lyα/N V BAL	Si IV BAL	10	0.794	0.61	1.72
Lyα/N V BEL	Al III/C III] BEL	20	0.630	0.29	0.60
Si IV BAL	C IV BAL	24	0.729	0.005	0.048
Si IV BEL	Al III/C III] BEL	28	0.485	0.89	1.2
C IV BEL	Al III/C III] BEL	32	0.656	0.005	0.026
Lyα/N V BAL	P	11	0.291	38.5	35.8
Lyα/N V BEL	P	20	0.263	26.2	25.1
Si IV BAL	P	26	0.055	79.1	78.4
Si IV BEL	P	30	0.150	42.8	41.8
C IV BAL	P	30	0.252	17.9	17.4
C IV BEL	P	34	0.274	11.7	11.5
Al III/C III] BEL	P	33	0.098	58.8	58.0

Table 4.7: BAL, BEL, and polarization correlations. The two variables are listed in columns 1 and 2. The number of objects, Spearman coefficient r_s, and probabilities are listed for significant correlations among BEL and BAL REW in the top half of the table. Low P_s and P_d indicate a low probability that the correlation occurred by chance, and therefore high significance. There are no significant correlations of line REW with continuum polarization P in the bottom half of the table.

quantities could be related via viewing angle.

We find no significant correlations between the BEL or BAL equivalent widths and the continuum polarization. Table 4.7 gives the Spearman coefficients and probabilities for correlation between P and the various REW. It is possible that the intrinsic object-object variation in the BAL and BEL properties swamps any dependence on geometry. In addition, the BAL and BEL are known to be variable, while polarization variability is weak (Section 4.15). This suggests that the polarization is not directly linked to the BEL and BAL intensities, but the polarizing mechanism could still reside in the general vicinity of the BELR or BALR.

There is no correlation between polarization and C III] REW (Figure 4.12 and Table 4.7). Goodrich (1997) suggests that the large equivalent width of C III] and high polarization in PHL 5200 is due to attenuation of the unpolarized central continuum source. He correctly predicts that RS 23 has high polarization, from its large C III] REW. However, this trend does not hold for objects with lower polarization. The other HPQ in the sample (1232+1325, and CSO 755) do not have BEL with unusually large REW.

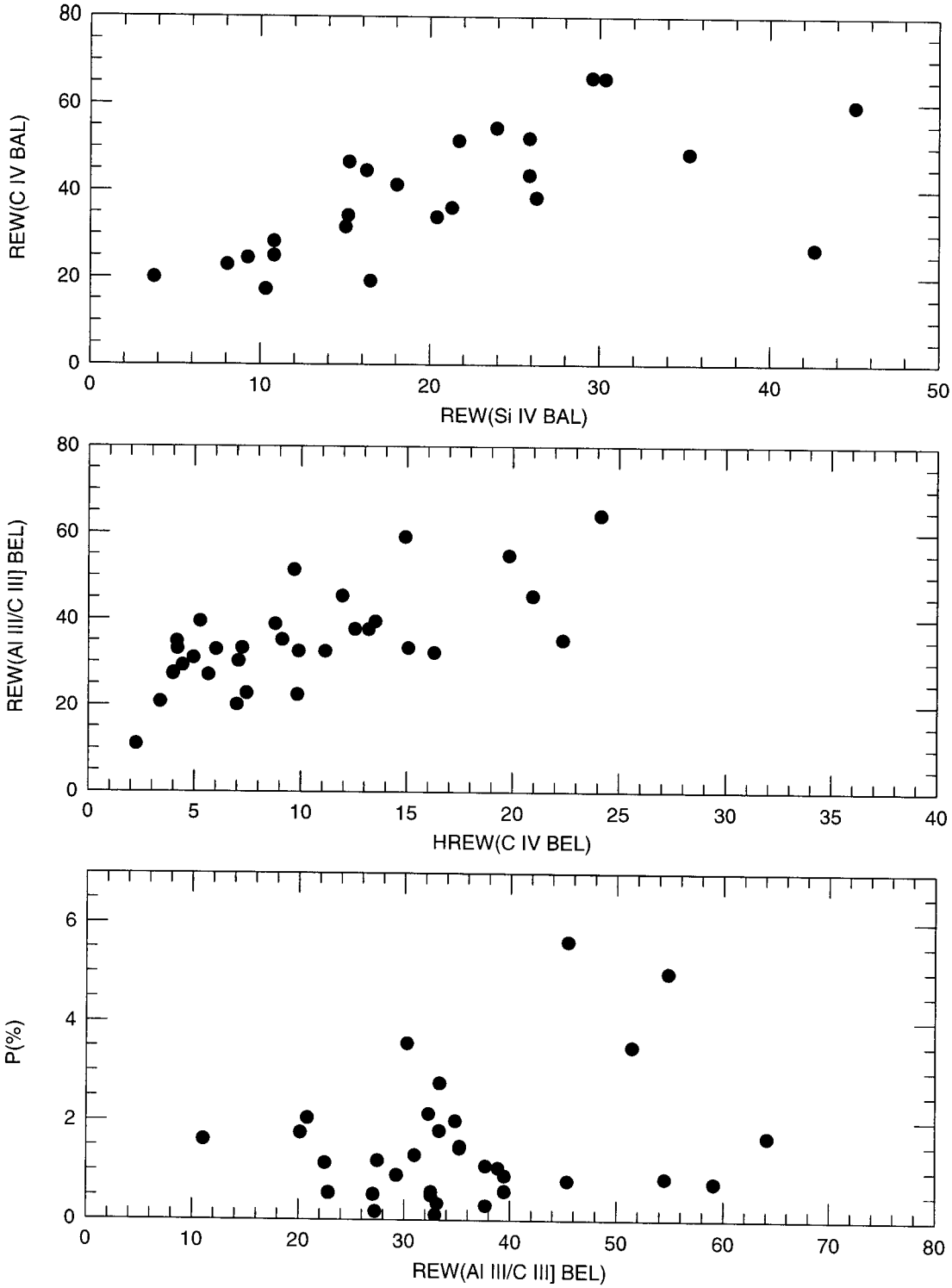

Figure 4.12: BEL, BAL, and polarization correlations. Panel 1 shows the strongest correlation between the REW of two BAL. Panel 2 shows the strongest correlation between the REW of two BEL. Panel 3 demonstrates that there is no correlation between BAL QSO continuum polarization and Al III/C III] REW.

4.17 Conclusions

The polarization distribution of BAL QSO is not dominated by viewing angle effects. In addition, there are no correlations between BEL and BAL equivalent widths and polarization. This is consistent with a small range of BAL QSO viewing angles. The large range of continuum polarization reflects a large range in scattering optical depths or geometries. The polarization distributions of BAL QSO and non-BAL QSO are consistent with the unification hypothesis. The median BAL QSO polarization is greater than the median non-BAL QSO polarization because BAL QSO are viewed from a more equatorial aspect. Further constraints on the BAL wind inclination from the polarization distribution will require high S/N polarimetric observations of a much larger sample of non-BAL QSO. Selection effects due to obscuration and anisotropic continuum emission may also be important.

The wavelength dependence of the continuum polarization is weak in most objects. Dilution by unpolarized emission lines can account for part of the wavelength dependence. The constant polarization in some objects can be accounted for by Thomson scattering. The remaining weak wavelength dependence in the other objects is likely due to scattering by large dust grains or differential dust absorption between the scattered and direct rays. The polarization spectra are useful for separating the unpolarized BEL spectrum from the polarized continuum. This technique gives clues about the different spatial distributions of the high and low ionization BELR and scattering regions. The polarization variations across the NAL of 0059-2735 are due to dilution by unabsorbed BEL photons. In addition, there is evidence for resonant scattering of C IV BEL photons by the BALR in 0059-2735.

There are significant PA rotations with wavelength in the continuum of 0019+0107 and 0932+5006. This may be due to absorption of scattered light by small dust grains in 0019+0107. No satisfactory explanation was found for the PA rotation in 0932+5006.

Weak continuum polarization and PA variability were found at a levels of $\Delta P < 0.5\%$ and $\Delta PA < 8$ degrees. We favor a reverberation model for the variability, where there is a delay between variations of the direct and scattered flux. This may be used in the future to determine the characteristic size of the scattering region via the reverberation mapping technique.

There are several possible scattering locations, corresponding to various structures in the standard AGN model. These include (in order of increasing distance from the center):

the central accretion disk where the thermal continuum is produced, the broad emission line region, the inner edge of the dusty torus, and the BALR. The results of this chapter are consistent with electron scattering in a highly ionized region such as the BELR or BALR. We discriminate between these two possible scattering regions in Chapter 5, which covers the BEL and BAL polarization of BAL QSO.

Chapter 5 BAL QSO Absorption and Emission Line Polarization

5.1 Introduction

We observed 36 BAL QSO with the Keck and Hale Telescopes to study their continuum and line polarization. The results of the continuum polarization study were presented in Chapter 4. We suggested that electron scattering in the BALR or BELR polarizes the continuum, and that BAL QSO are more highly polarized than non-BAL QSO because they are viewed from a more equatorial aspect. In this chapter we concentrate on the trough and emission line polarization. We have observed 7 BAL QSO with sufficient accuracy to make a detailed study of polarization in the BAL troughs.

Early studies of BAL QSO polarization were limited to broad band measurements of the continuum polarization (e.g., Stockman et al., 1984). Heroic efforts, requiring exposure times of up to 16 hours were made to measure the emission line and trough polarization with 3-m class telescopes (Goodrich & Miller, 1995). These observations indicated that the emission lines were polarized at a lower level than the continuum, but gave only hints of interesting polarization behavior in the BAL (Stockman et al., 1981; Glenn et al., 1994). With the advent of the Keck Telescope, it has become possible to measure the polarization of the residual light in the BAL with reasonable exposure times. Cohen et al. (1995) found that the polarization rises in the troughs of 0105-265 and 2225-0534 (PHL 5200). This showed that the polarized light is absorbed to a lesser extent than the unpolarized light by the BAL clouds. The velocity dependence of the polarization also indicated complex phenomena at work, possibly the result of multiple sources of scattered light.

We explore two possible explanations for the high trough polarization, suggested by Cohen et al. (1995). The first possibility is that the BALR only partially covers the polarized continuum source from the observer's point of view. The second possibility is that resonantly scattered polarized light from the BALR partially fills in the BAL. In both cases, light is scattered by particles in a region which has an angular extent comparable to the BALR. Some of the light is scattered around the BAL clouds and is absorbed to a

lesser extent than the direct continuum light. This extra polarized scattered light fills in the troughs, causing the polarization to rise above the continuum polarization level. An equivalent statement is that in the troughs there is less dilution of the polarization by direct continuum light, which is attenuated more than the scattered flux.

The distinction between the two explanations for the trough polarization is subtle but important. In both cases, the first scattering may be followed by subsequent scattering/absorption in the BALR. In that sense, both processes are affected by what we call partial coverage. Some of the scattered rays may miss the BALR entirely, but some may suffer additional attenuation by the BAL clouds. It is difficult to observationally distinguish between scattered continuum and resonantly scattered light in the absorption troughs. Both resonance scattering and partial coverage of the continuum can produce modulation of the polarization and position angle with outflow velocity in the BAL. Probably both partial continuum coverage and resonance scattering effects are occurring at some level, and we would like to determine their relative importance for the trough polarization.

The best location to look for a unique signature from resonantly scattered light is redward of the BEL, where there is no absorption. This requires high S/N since the polarization is dominated by the continuum in this region. Resonantly scattered light should be confined to a region within $\pm 3 \times 10^4$ km/s of the BEL, and its profile determined by the geometry and velocity structure in the BAL outflow (Hamman et al., 1993). Resonantly scattered light must be present because it is resonance scattering which creates the BAL. The amount of resonantly scattered light is primarily determined by the covering fraction of the BALR, which is thought to be roughly $f = 0.1$. However, resonantly scattered light will escape preferentially in the direction of minimum optical depth, which may not be along the line of sight if the BAL are optically thick or directed non-radially.

While the BEL generally have lower polarization than the continuum, they are not completely unpolarized. In this chapter, the BEL polarization is analyzed to put constraints on the size and geometry of the BELR. There are several possible sources of BEL polarization, including electron and dust scattering in the BELR or BALR, and resonance scattering in the BELR or BALR. If BEL photons are scattered by electrons or dust in the same region as the continuum photons, then their polarization is reduced by geometric dilution (e.g., Goodrich & Miller, 1995). Geometric dilution occurs when the scattering region is smaller than or of comparable size to the source of photons. There is cancelation of polarization due

to the large angular size of the source and a reduction in polarization due to the reduced solid angle covered by the scattering region relative to the source. We can use this idea and our BEL polarization measurements to make a rough estimate of the size of the BELR relative to the scattering region.

5.2 BEL Polarization

We measured the rest equivalent widths (REW) of the BEL and BAL in polarized flux. We used a similar procedure and the same velocity intervals which we used to measure the REW of the lines in total flux (see Chapter 4). The BEL REW were measured at a velocity width of 16,200 km/s, and the BAL from 0-29,400 km/s. A low-order spline was used to fit the continuum. This was actually somewhat easier for the polarized flux than the total flux because there are few BEL in polarized flux.

In Table 5.1, we list the REW in polarized flux of the Lyα/N V, C IV, and Al III/ C III] emission lines of BAL QSO with significant line polarization ($> 2\sigma$ significance). We also list the red half-REW of C IV, since the blue side is contaminated by absorption in many cases. There is also contamination of the Lyα/N V BEL by the BAL, which can masquerade as negatively polarized flux. Individual cases are assessed below.

There are three objects (0226-1024, 1246-0542, and 1333+2840), which show significant polarized emission on the red side of C IV. Two other objects (0059-2735 and 1413+1143) also have polarized C IV emission, but their REW measurements were compromised by their narrow width and ill-defined nearby continua. The HREW in $Q' \times F$ are in the range of -3 to -8 Å , while the HREW in $U' \times F$ are not significant (< 0.6 Å). Negative REW correspond to negatively polarized flux, so the PA of the C IV BEL electric vector is perpendicular to the PA of the continuum. Figure 2.8 shows this effect in N V, C IV and perhaps Si IV in 0226-1024. The shape and velocity range of the negatively polarized line flux matches that of the BEL in total flux. The HREW in total flux from Chapter 4 for these same objects range from 5 to 20 Å , so the BEL are polarized at a level of roughly one half of the continuum polarization. The remaining objects in Table 5.1 show possible polarization in Lyα and C IV, but it is difficult to evaluate because of BAL contamination.

Four objects show polarized C III] emission, but no significant polarization in the permitted lines. The detection of polarized C III] in 1413+1143 is contaminated by a cosmic

ray event, and should not be trusted. The detection is questionable in 0059-2735 because of the difficulty of setting the continuum level amongst a forest of NAL. The remaining two objects (0019+0107 and 2225-0534) show strong polarized C III] BEL which are readily apparent in their polarized flux spectra (Fig. 5.1). The PA of the C III] BEL is rotated from the continuum PA in both cases. The C III] full widths at half-maximum (FWHM) are somewhat broader in polarized flux ($12,000 \pm 2500$ km/s) than in total flux (6900 km/s), but the difference has only marginal (2σ) significance. If the scatterers are electrons, this puts an upper limit on the electron temperature of 1.4×10^5 K.

It is remarkable that objects with strong C III] polarization have unpolarized C IV emission, and vice versa. A possible explanation is that C IV BEL photons are polarized by resonance scattering in in the BALR (Section 5.12), while C III] is polarized by resonance scattering in the BELR. We do not have enough objects to tell if the two phenomena are truly anti-correlated; it is just as likely that they are independent. If polarized C IV is resonantly scattered by the BALR, then its orthogonality to the continuum PA indicates that the BALR is oriented perpendicular to the electron scattering region. This would be the case if the BAL outflow is equatorial and the electrons are distributed in plasma along the symmetry axis of the QSO. We discuss additional evidence for resonance scattering in the BALR below .

Resonance scattering of the C III] emission in the BELR of 2225-0534 was suggested by Cohen et al. (1995), using the prediction of Lee (1994). C III] is the only emission line in our spectra which may have low enough optical depth ($\tau = 1 - 10$) to preserve the polarization of photons emerging from the BEL clouds. Now that we have found a second object with polarized C III], the case for resonance scattering is strengthened. It is also significant that the PA of the C III] BEL is different from the PA of the continuum in both objects, suggesting a similar polarizing mechanism. However, 0019+0107 has an unusually red polarization spectrum, and there is a hint of polarized C IV emission. There is a worry that wavelength dependent absorption by dust could lower the polarization of C IV relative to C III] (see Section 4.14).

An alternate explanation of the line polarization is that all BEL are scattered by the same distribution of particles (e.g., electrons), but the various BEL sources are distributed in different locations with respect to the scatterers. For example, the C IV BEL could be distributed in a disk and polarized perpendicular to the axis by electron scattering in

		Lyα/N V	$\pm$	C IV	$\pm$	C IV (red)	$\pm$	Al III/ CIII]	$\pm$
0019+0107	Q'	....	....	15.9 *	7.0	8.0	5.0	22.1 *	8.3
	U'	....	....	5.1	7.3	4.5	5.3	20.5 *	8.6
0059−2735	Q'	....	....	....	....	-2.5	2.3	0.7	3.4
	U'	....	....	....	....	2.9	2.2	13.8 *	3.4
0146+0142	Q'	6.6	6.7	-6.7	6.7	-6.3	4.4	-3.2	12.2
	U'	13.9 *	6.8	5.6	6.7	4.20	4.3	-0.6	11.9
0226−1024	Q'	....	....	-9.0 *	2.0	-5.4 *	1.5	2.8	3.4
	U'	....	....	-1.2	2.0	0.1	1.4	4.0	3.3
1246−0542	Q'	....	....	-5.7 *	1.7	-2.8 *	1.2	-1.6	3.0
	U'	....	....	0.2	2.1	-0.6	1.4	0.9	3.5
1333+2840	Q'	....	....	-10.0 *	1.6	-8.2 *	1.3	-2.8	2.3
	U'	....	....	3.2	1.6	0.2	1.3	2.3	2.3
1413+1143	Q'	5.3	5.5	6.3	4.8	2.4	4.2	-16.5 *	8.1
	U'	-0.8	6.0	-3.1	5.6	-2.6	4.9	1.3	9.8
1524+5147	Q'	-11.1 *	1.9	-6.4 *	1.7	-2.0	1.1	-5.5	3.1
	U'	-2.6	1.8	3.6 *	1.7	3.9 *	1.1	-1.1	3.1
2225−0534	Q'	....	....	-1.6	1.3	-1.6	1.2	12.5 *	2.4
	U'	....	....	-0.4	1.3	-0.4	1.2	4.9 *	2.4

Table 5.1: Polarized BEL. The polarized REW (in Å of $Q' \times F$ and $U' \times F$) of Lyα/N V, C IV, and Al III/C III] are listed for objects with significantly polarized lines. Lines with significant polarization ($> 2\sigma$) are indicated with an asterisk. Several lines are polarized perpendicular to the continuum ($Q' < 0$ and $U' \simeq 0$).

the corona of the disk. In this geometry, the continuum would be polarized parallel to the axis by virtue of its central location. The skewed PA of the C III] BEL is not easily accounted for in this scenario unless it comes from a different radius in a warped disk. We evaluate the evidence for electron scattering and resonance scattering of the BEL in detail in Section 5.12.

5.3 C IV BAL Polarization

Figure 5.2 displays peak C IV trough polarization P_t vs. continuum polarization $P_c = P_1$ (measured in the 1600-1840 Å band, Table 2.5). The peak trough polarization and its uncertainty are measured in 5 Å bins. The large uncertainties and scatter in the trough polarization values are in part due to the small number of photons per bin. There appears to be a limit to the peak trough polarization of about 10%. Excluding objects which have

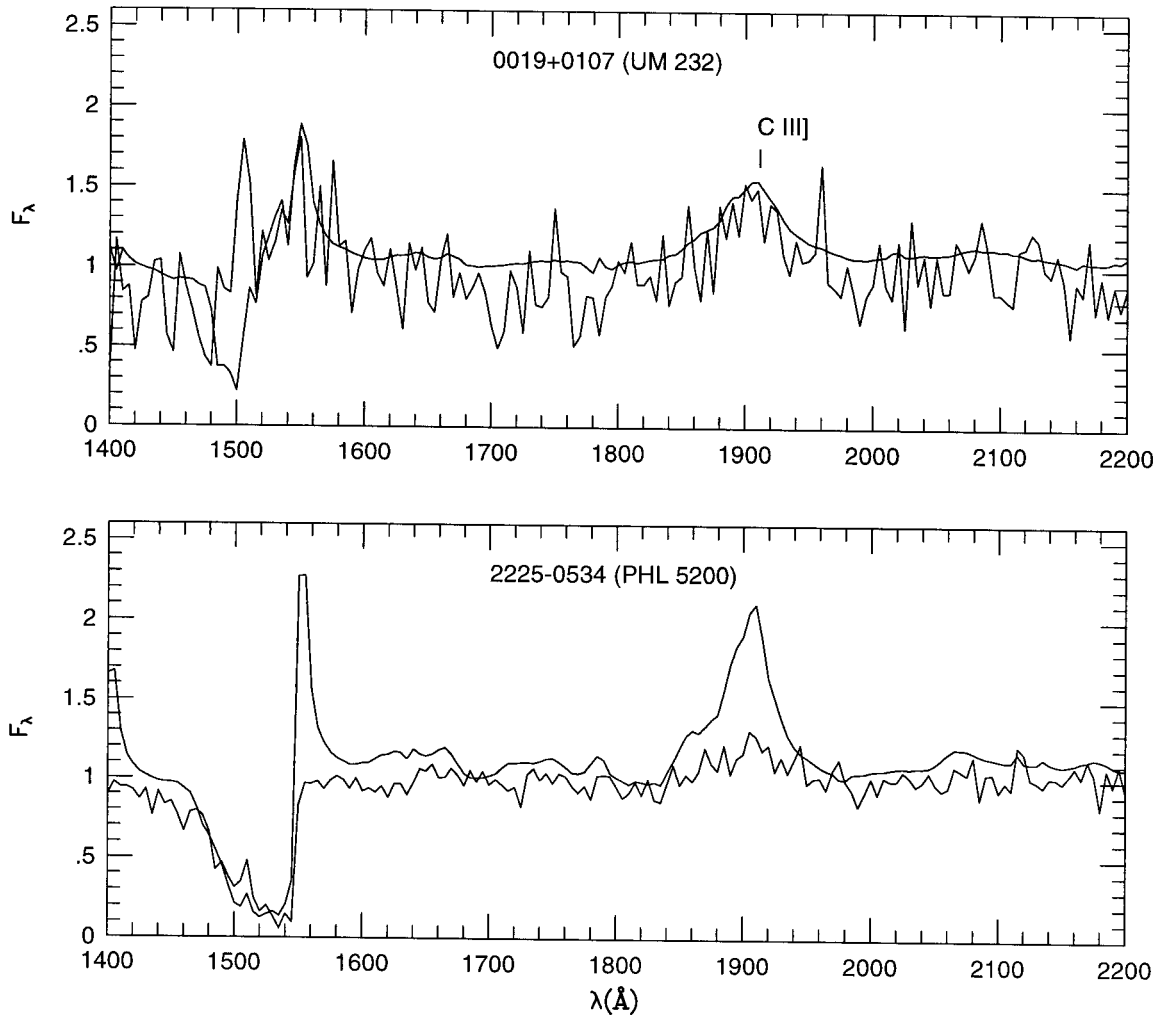

Figure 5.1: Polarized C III] BEL. BAL QSO 0019+0107 and 2225-0534 show polarized C III] emission. We have scaled the spectra by spline fits to the continuum to put the total and polarized flux (noisier curve) on the same scale. Note that C III] is polarized nearly as highly as the continuum in 0019+0107, but at a significantly lower level in 2225-0534.

$P_t < 2\sigma$, the highest polarization in any C IV BAL is $P_t = 10.5 \pm 3.3\%$ in 0105-265.

There is no correlation between the peak trough and continuum polarization. The Spearman correlation coefficient for the two variables is only 0.282, with a significance of 26%. There are no cases where the peak trough polarization is less than the continuum polarization, which puts a lower bound on the trough polarization of $P_t = P_c$. The lower bound on the trough polarization could in principle introduce an artificial correlation between P_t and P_c, but the scatter in our data overwhelms this effect.

It is possible to contrive a geometry where the trough polarization is less than the continuum polarization. For example, if we view the central source through a hole or weak spot in the BALR, the scattered continuum may be more highly absorbed than the direct continuum. Alignment with such holes must be rare, if they exist. In addition, BAL QSO are selected for large optical depths along the line of sight to the central source, so it is unlikely that the scattered rays would be on average more highly absorbed. A reduced polarization in the trough could also be achieved if the resonantly scattered photons were unpolarized or polarized perpendicular to the continuum photons. This is in fact seen in 1333+2840 (Section 5.8). In principle, it is also possible obtain 100% trough polarization with a suitable arrangement of scatterers and absorbers. The 10% maximum trough polarization provides another constraint on the geometry of the the scattering region and BAL outflow.

We measured the peak trough polarization in the wavelength band containing C IV absorption (Table 2.6). This measurement is plagued by a number of problems. Since the polarization peaks near the minimum in the trough, the photon numbers are small, and the uncertainty is high. Peak trough polarization measurements are biased high by their very nature since we are choosing to measure the bin with greatest polarization. This is especially true of low S/N observations. The spectral bins with the highest and lowest polarization are typically the ones with the greatest deviations from their true polarization values. For example, 0856+1714 has $P_t = 8.0 \pm 6.5\%$. The uncertainty is high because the object is faint and was observed through clouds, and because the peak polarization was measured in the most uncertain bin. Even objects with high S/N continuum observations can have very deep or truly black troughs (e.g., 1413+1143 and 0059-2735) so that the polarization is not well measured at the trough minimum.

We could improve the S/N in the trough by using larger wavelength bins. This would tend to lower the peak polarization for two reasons. First, the noise bias would be reduced.

Second, the polarization peak would be washed out by the reduced resolution. This can be carried to the extreme by measuring the polarization over the entire C IV trough.

Table 5.2 lists the equivalent widths of the C IV BAL in polarized flux ($Q' \times F$ and $U' \times F$). Figure 5.2 plots the C IV REW in polarized flux vs. the C IV REW in total flux. The BAL REW are negative, indicating absorption. We have left the sign to distinguish between absorption of positively polarized flux and emission of negatively polarized flux. Out of 16 objects, 11 have REW of equal or smaller absolute magnitude in polarized flux than in total flux. In other words, there is less net absorption of polarized scattered flux than of direct light. Of the remaining objects, 3 have polarized REW which are within 1σ of their REW in total flux, and 2 (1333+2840 and 2225-0534) have polarized REW which have greater magnitude than the REW in total flux.

		Lyα/N V	$\pm$	Si IV	$\pm$	C IV	$\pm$
0105−265	Q'	-52.8	4.2	0.3	3.3	-31.9	4.3
	U'	-7.4	4.6	-7.6	3.5	-9.1	4.6
0137−0153	Q'	....	....	7.7	18.4	6.3	18.1
	U'	....	....	4.6	19.3	1.3	18.7
0146+0142	Q'	-27.4	7.9	-17.6	5.6	-19.7	5.6
	U'	-14.0	8.1	-7.1	5.6	-11.9	5.5
0226−1024	Q'	....	....	-13.1	2.1	-41.3	1.7
	U'	....	....	3.2	2.0	0.2	1.6
0842+3431	Q'	....	....	-3.7	8.7	-22.5	6.6
	U'	....	....	-13.2	8.6	-10.0	6.6
0856+1714	Q'	....	....	-31.3	16.9	-65.2	16.6
	U'	....	....	23.8	16.1	-6.9	16.0
0903+1734	Q'	-29.0	14.9	-22.5	13.4	-31.8	12.6
	U'	53.4	15.0	32.1	13.5	47.1	12.7
0932+5006	Q'	....	....	....	....	-34.0	7.3
	U'	....	....	....	....	3.0	7.4
1235+0857	Q'	-48.6	6.3	-11.6	3.6	-33.2	4.4
	U'	2.5	6.3	2.2	3.6	1.9	4.4
1246−0542	Q'	....	....	-6.8	1.9	-7.6	1.4
	U'	....	....	7.5	2.3	-2.4	1.7
1331−0108	Q'	....	....	....	....	-52.6	32.0
	U'	....	....	....	....	21.0	29.4
1333+2840	Q'	....	....	....	....	-29.6	2.1
	U'	....	....	....	....	-8.2	2.1
1413+1143	Q'	-56.3	7.4	-24.1	4.3	-36.1	4.6
	U'	9.9	8.2	11.3	4.8	12.9	5.3
1524+5147	Q'	-30.0	1.8	1.1	1.2	-13.5	1.4
	U'	4.0	1.7	-2.3	1.2	-0.2	1.4
2225−0534	Q'	....	....	....	....	-56.9	1.8
	U'	....	....	....	....	-2.9	1.9

Table 5.2: BAL equivalent widths in polarized flux. The REW (in Å of $Q' \times F$ and $U' \times F$) of Lyα/N V, Si IV, and C IV BAL are listed. They are measured with respect to the continuum in $Q' \times F$. Three objects (0059-2735, 1212+1445, and 07598+6508) are at low redshift, so the C IV BAL are only partially or not at all accessible. 0043+0048 has no significant polarized flux, and is also omitted from the table. The uncertainties in the REW are derived from photon statistics.

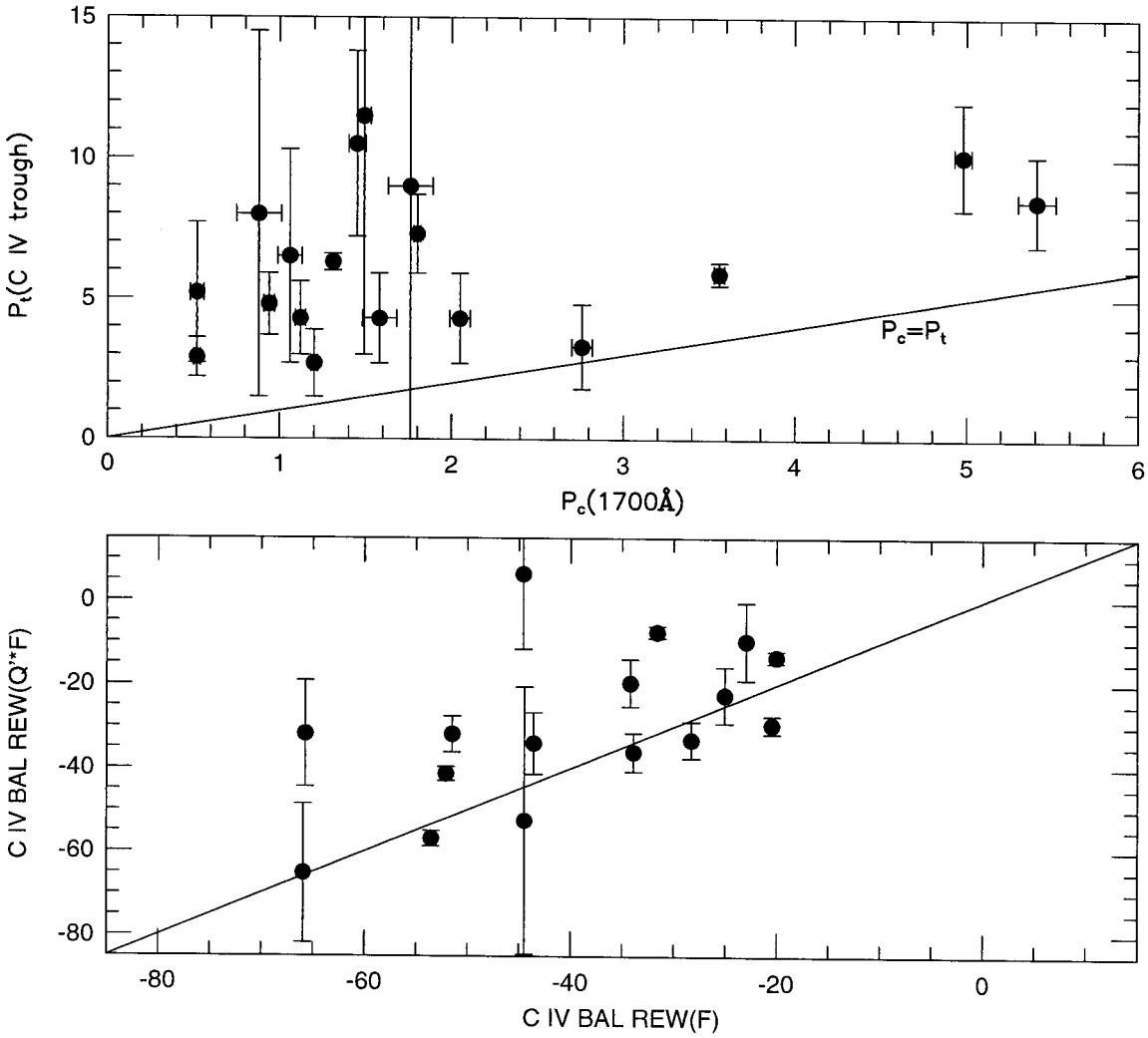

Figure 5.2: C IV BAL vs. continuum polarization. In the top panel, peak trough polarization (%) is plotted against continuum polarization for 18 objects. The polarization is greater in the trough than in the continuum for all objects. As a result, we see in the bottom panel that the REW of most C IV BAL are smaller in polarized flux than in total flux. (Negative REW indicate absorption.)

5.4 BAL Spectropolarimetry

Spectropolarimetric observations of BAL QSO are presented in Chapters 2 and 3. Only the Keck observations in Chapter 2 have sufficient S/N to be useful for BAL polarization studies. The trough polarization is significantly greater than the continuum polarization in 15/20 of the BAL QSO observed at Keck. The BAL QSO 0105-265, 0226-1024, 1246-0542, 1333+2840, 1413+1143, 1524+5147, and 2225-0534 show the most convincing polarization increases in the trough. In the following sections we discuss the C IV BAL and BEL polarization of these objects. For each object, we present normalized flux, rotated Stokes Q' and U' polarization parameters with error bars, and normalized polarized flux $Q' \times F$ (Figs. 5.3- 5.10). The continua were fit by a low order spline (which was also used to measure the line REW) and divided by it.

The maximum trough depth varies from object to object. In objects with shallow, unsaturated troughs, the polarization remains low in the trough because of dilution by direct continuum light. The best objects to study are those with fairly deep troughs with saturated portions (e.g. 0105-265). The polarization in the saturated portion is a good estimate of the polarization of the scattered light since there is little dilution by direct continuum. The signature of a saturated trough is a flat bottom, but this can be mimicked by unsaturated absorption. On the other hand, information about the velocity profile of the BALR can only come from the unsaturated portions of the trough. The larger the range in optical depth, the more information can be extracted from the trough polarization spectrum. Trough detachment from the BEL is also important when studying the trough polarization. Troughs which are well separated from the BEL are not contaminated by BEL emission, so they are easier to interpret. However, it is also important to study low velocity absorption which can give a handle on the geometry of the BELR.

Some caution must be observed when interpreting the polarized flux spectra of BAL QSO because polarized flux can be either positive or negative. Negatively polarized flux is due to photons with electric vector PA perpendicular to the continuum PA. If there are equal amounts of negatively and positively polarized flux, the net polarization is zero. Spatially selective absorption of scattered flux can in principle induce absorption line polarization in objects which have zero net continuum polarization (Section 5.14). Ideally, we would like to distinguish between absorption of positively polarized flux and emission of negatively

polarized flux. In practice, this can be done by identifying emission or absorption features in polarized flux with corresponding emission or absorption features in total flux. For example, if absorption features line up in total and polarized flux, then we can be fairly confident that there is absorption of positively polarized flux. However, if an absorption feature in polarized flux matches an emission feature in total flux, then it is likely that there is emission of negatively polarized flux. Similarly, there can be absorption of negatively polarized flux or emission of positively polarized flux.

It is difficult to distinguish between emission and absorption features in the BAL because the continuum is not well defined. In our interpretation of the BAL polarization spectra, we will assume that the velocity profile of the resonantly scattered light is in general much smoother than the velocity profile of the BAL absorption. This is justified by the following argument (and also by the data presented below). If the BAL outflow covers a large enough solid angle for resonance scattering to be an important source of polarized flux, then the line of-sight velocity of outflow will be smeared out by projection effects. Variation in the velocity profile along different lines of sight will also smear out the profile of the resonantly scattered light. On the other hand, if the BAL outflow only covers a small fraction of the continuum source, then resonance scattering will not contribute significantly to the polarized flux. So any polarization features due to resonance scattering should have large velocity widths and only slow velocity dependence. Any sharp features in the BAL which are localized in velocity will be interpreted as absorption features.

5.5 0105-265

0105-265 has a smooth, wide C IV absorption trough which we divide into four segments for discussion purposes (Fig. 5.3). The lowest velocity segment (1) is centered at roughly -9200 km/s. Segment 2 extends from -12000 to -17000 km/s, and is the deepest, most highly polarized portion of the trough. The third segment is a gradual ramp out to -22,000 km/s and the fourth segment runs into the red wing of Si IV at roughly -25,000 km/s. Segments 3 and 4 are shallow and have low polarization.

The polarization in the C IV trough of 0105-265 was discussed by Cohen et al. (1995). P rises to a maximum of $10.5 \pm 3.3\%$ at a velocity of -12,400 km/s. This is 6.6 times the continuum polarization red-ward of the C IV emission line. There is therefore considerably

more absorption in total flux (REW= -51 Å) than in polarized flux (REW= -32 ± 4 Å). That means that scattered light accounts for an extra 19 Å in polarized flux at the bottom of the BAL. This amount of resonantly scattered flux would be easily detected to the red of the C IV BAL in $Q' \times F$, yet none is seen. The HREW of the C IV BEL in polarized flux is -2 ± 4 Å , a non-detection. It seems unlikely that resonantly scattered flux would be confined to velocities where there is C IV absorption. We expect to see resonantly scattered flux red-ward of -6000 km/s, unless it is obstructed by a second scattering surface. We therefore conclude that electron (or dust) scattered continuum photons, and not resonantly scattered photons, are responsible for the high trough polarization. The resonantly scattered flux is below our detection threshold.

Trough segments 1 and 2 appear to be less saturated (i.e., the velocity structure has more contrast) in polarized flux than in total flux. The significance of this result is low considering that it hinges on a 2-3% (1σ) dip in polarization at -10,600 km/s which coincides with the split between segments 1 and 2. Reduced saturation in polarized flux would indicate that the optical depth is lower for the average scattered continuum ray than for the direct rays. It would also verify the hypothesis that the troughs are smooth in total flux because they saturated.

There is a possible rotation in the PA of the electric vector across the trough. This shows up as residual polarization in the Stokes U' parameter. The coordinate system was rotated so that $U' = 0$ across the continuum region, so any extra polarized flux in U' is peculiar to the BAL or BEL. The rotation in individual pixels is insignificant ($U' = 3 \pm 4\%$), but seven out of eight pixels rotate in the same direction. The REW of this feature in $U' \times F$ is 9.1 ± 4.6 Å , which is marginally significant. As in Q', the polarization feature in U' is confined to the trough, which strongly suggests that it is the result of partial coverage of the electron scattering region instead of resonance scattering. Some parts of the continuum scattering region are selectively covered by asymmetric BAL clouds, causing a PA rotation in the residual polarized flux.

0105-265 is the highest redshift object in our sample ($z = 3.488$), so it has the greatest number of high ionization absorption troughs available for study. Unfortunately, all of the troughs blue-ward of the Lyα emission line are contaminated by intervening absorption systems. The intervening lines should not effect the polarization since they should have equal equivalent widths in total and polarized flux. P rises in the Si IV, Lyα/N V, Lyβ/O VI,

Lyγ/C III and Lyϵ/S VI troughs (Fig. 2.5). In principle, high-resolution spectroscopy could be used to model and remove the intervening absorption lines. High resolution spectropolarimetry could also be used, but is beyond the capabilities of even the Keck Telescopes. There is an additional problem of overlapping absorption troughs, such as Lyα/N V and Lyβ/O VI.

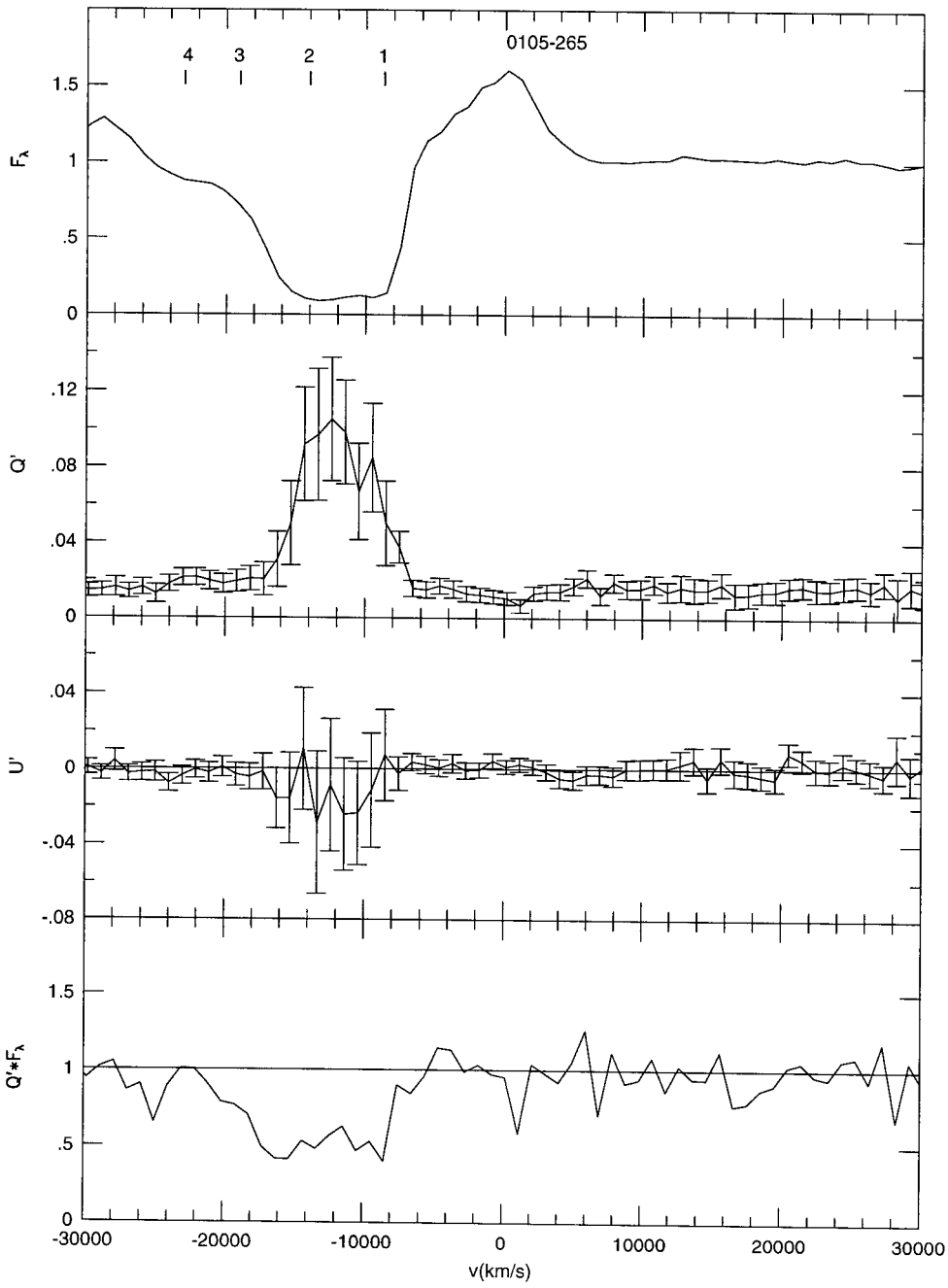

Figure 5.3: 0105-265 C IV BAL. Panels 1-4 show the normalized total flux, rotated Stokes Q', rotated Stokes U', and normalized polarized flux ($Q' \times F$). Sub-trough segments discussed in the text are labeled in panel 1.

5.6 0226-1024

We observed BAL QSO 0226-1024 for 1.7 hours with the 300 groove/mm grating, and these observations were presented in Chapter 2. We re-observed it for 4 hours with the 600 groove/mm grating to study the details of the trough and line polarization. This object is ideal for study because it is one of the brightest and shows fairly strong polarization, PA rotations, and multiple troughs. In addition, it has been studied in detail with HST (Korista et al., 1992). The spectropolarimetry of the C IV BAL is shown in Figure 5.4. The spectra are presented in velocity bins of 74 km/s, and have a resolution of roughly 300 km/s. A preliminary analysis is presented by Ogle (1997); here we expand on those results.

For the purpose of discussion, we break up the C IV trough into 6 sections, numbered from low to high speed. Segments 1-3 are narrow and well defined; segment 4 is broad and composed of at least 3 components; and segments 5 and 6 blend together in the high-velocity tail of the trough. The wavelength ranges and peak polarizations of each of these segments are listed in Table 5.3. The polarization peaks at 9% in the deepest trough segment (number 2), and is more than 2σ above the 1600-1800 Å continuum polarization in segments 3-6. The continuum polarization is rising to the blue, so it is difficult to tell if the polarization in the shallow segments 5 and 6 is greater than the local (1400 Å) continuum polarization. In any case, trough segments 2-4 show significant enhancements in polarization. Trough segment 1 shows no significant polarization increase even though it is deeper than segment 3. The net effect of the polarization increase in segments 2-4 is that the C IV BAL is shallower and less saturated in polarized flux than in total flux. In particular, the velocity structure in trough segment 4 is more apparent in polarized than in total flux. (Compare panels e and f.)

The polarization spectrum of 0226-1024 is complicated. There is evidence of partial continuum coverage in the BAL, polarized BEL, and resonance scattered flux red-ward of the BEL. It is difficult to establish a continuum baseline in the $Q' \times F_\lambda$ spectrum because of the deep BAL. However, it is easy to distinguish between resonantly scattered flux and scattered continuum in the $U' \times F_\lambda$ spectrum. The scattered continuum shows up as positively polarized flux and is restricted to the BAL. Resonantly scattered light is negatively polarized and dominates away from the BAL.

Resonantly scattered light shows up as negatively polarized flux in $U' \times F$ both red-ward

segment	λ	v(km/s)	$Q'\%$	$\pm$	v(km/s)	$U'\%$	$\pm$
1	1524-1536	-4200	2.4	0.4	-3900	0.7	0.5
2	1493-1509	-9800	8.9	2.8	-9500	4.6	2.0
3	1482-1493	-12100	3.9	0.4	-12100	2.4	0.4
4	1444-1482	-16500	7.2	1.0	-17300	3.5	0.9
5	1431-1444	-22200	3.0	0.4	-21700	0.5	0.4
6	1414-1431	-23600	2.8	0.4	-24300	0.9	0.4

Table 5.3: 0226-1024 C IV BAL sub-trough polarization measurements. Peak polarization values are listed for the sub-troughs 1-6 discussed in the text

and blue-ward of the C IV BEL (Figure 5.4, panel g). The resonantly scattered features are indicated with the label "r" and the scattered continuum features are labeled "c" in panels d and g. The red polarized flux extends to +13,000 km/s, well past the red wing of the C IV BEL, and has a rest equivalent width (REW) of 4.0 ± 0.4 Å. The REW was measured relative to the polarized (Q') continuum in a 216 Å wide band red-ward of C IV. The uncertainty was determined by varying the red end of the extraction window. We can not reliably measure the REW of the resonantly scattered flux blue-ward of C IV because of BAL partial coverage effects.

It is remarkable that away from the BAL the resonantly scattered flux displays a broad plateau. This plateau does not extend to the highest BAL velocities on the blue side of C IV (-25,000 km/s) nor to corresponding velocities on the red side. On the blue side, this is complicated by partial BALR coverage effects. The shape and velocity extent of the resonantly scattered flux profile is consistent with resonance scattering in an out-flowing BALR. The most highly polarized flux comes from photons which are side-scattered by BAL clouds which are moving across the line of sight and have low projected velocities. Clouds with greatest projected velocity are moving most directly towards and away from the observer. The polarization of light back and forward-scattered from these clouds is zero, so the highest velocities ($\sim 25,000$ km/s) are not seen in the polarized flux spectrum. It is difficult to distinguish between bipolar and equatorial outflow purely on the basis of the profile of the polarized resonantly scattered flux. Lee & Blandford (1997) calculate the expected profiles for bipolar and equatorial outflow using a Monte Carlo method. The residual flux and polarization in the BAL are similar for the two models (about 10%).

For a bipolar outflow, the red scattered flux might be blocked by the accretion disk. If

there is an optically thick accretion disk in the vicinity of the BALR, then the detection of red resonantly scattered flux in 0226-1024 definitively rules out a strictly bipolar model ($i_2 < 45$ degrees in Fig. 4.2). If we accept the conclusion that the BALR is non-bipolar, then some of its streamlines must be inclined from the pole by more than $i_1 = 45$ (see Fig. 4.2). Note that a non-bipolar outflow isn't necessarily equatorial.

The maximum intensities of the resonantly scattered polarized flux $U' \times F_{rs}$ and electron scattered polarized flux $U' \times F_{es}$ are similar ($U' \times F = 6.0 \pm 0.1 \times 10^{-18}$erg/s/cm^2/ Å). However, $U' \times F_{es}$ dominates over $U' \times F_{rs}$, in the BAL. This is evidenced in the BAL by the PA rotation away from the PA of the resonantly scattered light (Figure 5.4, panel d). Partial coverage of the scattered continuum source is the primary explanation for the polarization rise in the troughs. The effects from resonantly scattered light are secondary.

The PA rotations in the BAL are naturally explained if the flow crosses the line of sight at an angle to the axis of the scattering region (Section 5.14). The PA in the troughs is driven away from the PA of the obscured electron scattered light. PA rotations could therefore indicate a misalignment between the axes of the BAL outflow and the electron scattering region. Alternatively, they may be due to peculiar convolutions or gaps in the Sobolev surfaces of the BALR (e.g., Lee & Blandford, 1997).

Sub-trough 1 shows peculiar polarization behavior relative to the the other sub-troughs. As we noted above, Q' does not rise in this sub-trough, suggesting that the corresponding BAL cloud completely covers both the direct and electron-scattered continuum sources (Section 5.14). However, the sub-trough does show up in $U' \times F$ as absorption of the resonantly scattered flux (Fig. 5.4). This effect is subtle, and it is difficult to tell if the BAL cloud is truly blocking all of the resonantly scattered light at this velocity, or if there is an asymmetry in the coverage of the electron scattering region. If the former is true, then the BAL cloud must have a larger angular size than the low-velocity BALR. In addition, sub-trough 1 is seen in the unpolarized flux spectrum of N V and C IV (Fig. 4.5), indicating that it also covers the BEL.

Sub-trough 1 breaks up into a number of narrower components at high resolution, while the other troughs remain smooth (Keck HIRES data of T. Barlow and V. Junkkarinen, private communication). This is another clue to the unique nature of this absorption system, suggesting that it does not belong to the main BAL flow. A number of BAL QSO show low-velocity absorption systems that are narrower than the main BAL trough, yet are still broad

(e.g., 1524+5147). We discuss a possible geometry for these systems in Section 5.10. Similar (but weaker) low velocity associated absorption systems are seen in radio-loud quasars. It would be useful to search for a polarization increase in these associated absorbers with spectropolarimetry to determine if they behave the same as the low-velocity systems in BAL QSO. This will be difficult because non-BAL QSO have low polarization and the associated absorbers have small equivalent widths.

The Lyα/N V, Si IV, and C IV BEL show up in $Q' \times F$ as a flux deficit (Fig. 2.8 and Fig 5.4, panel f). This means that the permitted BEL are polarized with PA roughly perpendicular to the continuum PA. The polarized C IV BEL flux could be from resonantly scattered continuum, but the velocity profile of the polarized BEL in $Q' \times F$ is similar to the velocity profile in F, and dissimilar to the velocity profile of the resonantly scattered flux in $U' \times F$ (Figure 5.4, panels f and g). Another clue is that the C IV line is red-shifted in polarized flux by 1000 km/s. In addition, C III] is not polarized (Fig. 2.8). This suggests that we are seeing photons from the C IV BELR resonantly scattered by the BALR. An alternate possibility is that the C IV BEL is scattered by electrons but the C III] BEL is not. This would require a special geometry. (See Section 5.12.)

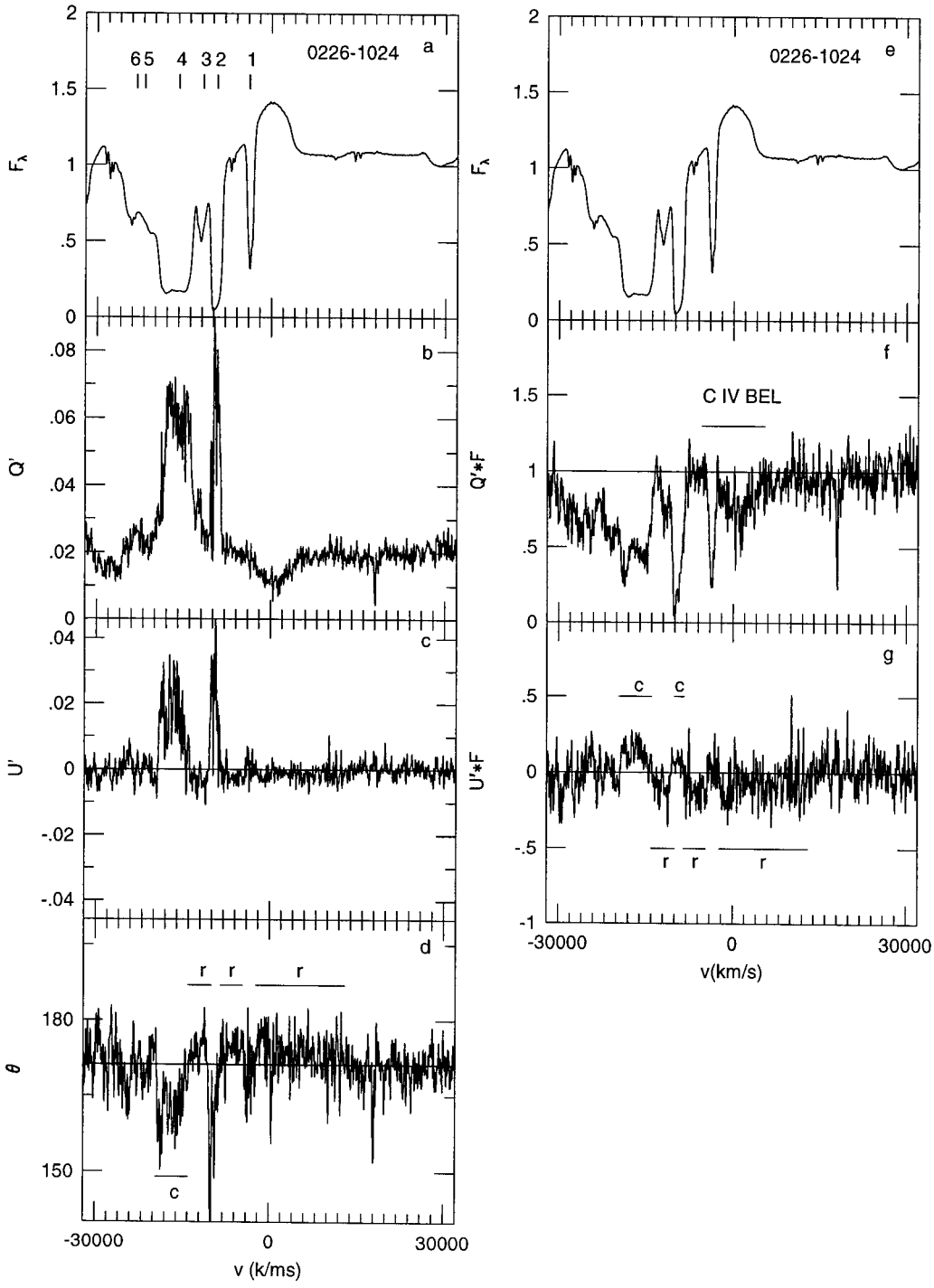

Figure 5.4: C IV BAL of 0226-1024 (z=2.246). (a,e) Total flux. (b,c) Fractional Stokes Q' and U'. (d) Position angle; the mean continuum PA indicated by the line is 171 degrees. (f,g) Stokes polarized flux $Q' \times F$ and $U' \times F$. The total and polarized flux spectra are normalized to a continuum level of 1.0. Features due to resonance scattering are labeled "r," while those due to partial coverage of the scattered continuum are labeled "c."

5.7 1246-0542

1246-0542 has very high signal to noise data and a strong polarization signature in the broad absorption line trough (Fig. 5.5). There are three main sub-trough components. There is a low-velocity shallow absorption sub-trough (1) from -5800 to -11,500 km/s which has additional substructure, an intermediate velocity deep sub-trough (2) from -11,500 km/s to -19,300 km/s, and a high velocity shallow sub-trough (3) which extends to at least -25,000 km/s. The detached nature of the BAL suggests that the central continuum source is viewed through a non-radial segment of the outflow. Otherwise, we would see absorption at 0 km/s.

The polarization rises to about 2% in the shallow sub-troughs, and to a peak of $6.3\pm0.3\%$ in the deep intermediate velocity sub-trough. The polarization is greater on the red (low speed) side of the trough than on the blue side of the trough for a given trough depth. This is seen even better in the unbinned data (Figure 5.13).

There is a marked difference between the REW of the C IV BAL in total flux (-31.6 Å) and in polarized flux (-7.6±1.4 Å). The excess polarized flux in the BAL has a REW of 24 Å, which is much larger than the red HREW of the C IV BEL (-2.8 ± 1.2 Å). It is therefore very difficult to account for the extra flux in the BAL by resonance scattering. This is one of five objects in which the C IV BEL is measurably polarized, at a PA perpendicular to the continuum (Sections 5.2, 4.10; and Fig. 5.5, panel 4). If this is resonantly scattered light, then the ratio of resonantly scattered light in the BEL to the extra electron scattered light in the trough is 0.12 ± 0.05. There is little doubt in this case that resonantly scattered light does not contribute significantly to the BAL polarization.

There are marginally significant PA rotations, especially in the deep, intermediate velocity C IV BAL. These rotations can be seen in the U' spectrum (Fig. 5.5, panel 3), and they line up with the BAL in $Q' \times F$ (panel 4). The localization of the PA rotations to the BAL suggests that they are due to asymmetric coverage of the scattered continuum by BAL clouds.

The intermediate velocity sub-trough (2) shows up in polarized flux, but the minimum is blue-shifted by 1,000 km/s. The trough minimum is at -16,300 km/s in total flux, and at $-17,300$ km/s in polarized flux. There is an even larger shift (-2,000 km/s) at the red and blue edges of the trough, which is indicated by the dotted lines in Figure 5.5.

The shallow sub-troughs 1 and 3 at low and high speed do not appear in polarized flux. The difference in the trough velocity structure strongly supports electron scattering over resonance scattering. It is unlikely that the velocity profile of resonantly scattered light would have the right shape to fill in the BAL just so.

For most electron scattering geometries, the scattered lines of sight should have a larger impact parameter than the direct line of sight. Larger impact parameter typically means less absorption of the scattered ray. In addition, if the BAL flow accelerates outward, then scattered lines of sight at large impact parameter will miss the low velocity absorption at the base of the outflow. The velocity shift between the BAL in polarized and unpolarized light is enhanced by the non-radial nature of the flow, which increases the projected velocity gradient. The BAL velocity structure in polarized light is therefore neatly explained by electron scattering in the BELR or BALR coupled with an outwardly accelerating BAL flow. (See Section 5.14 for a more detailed discussion.)

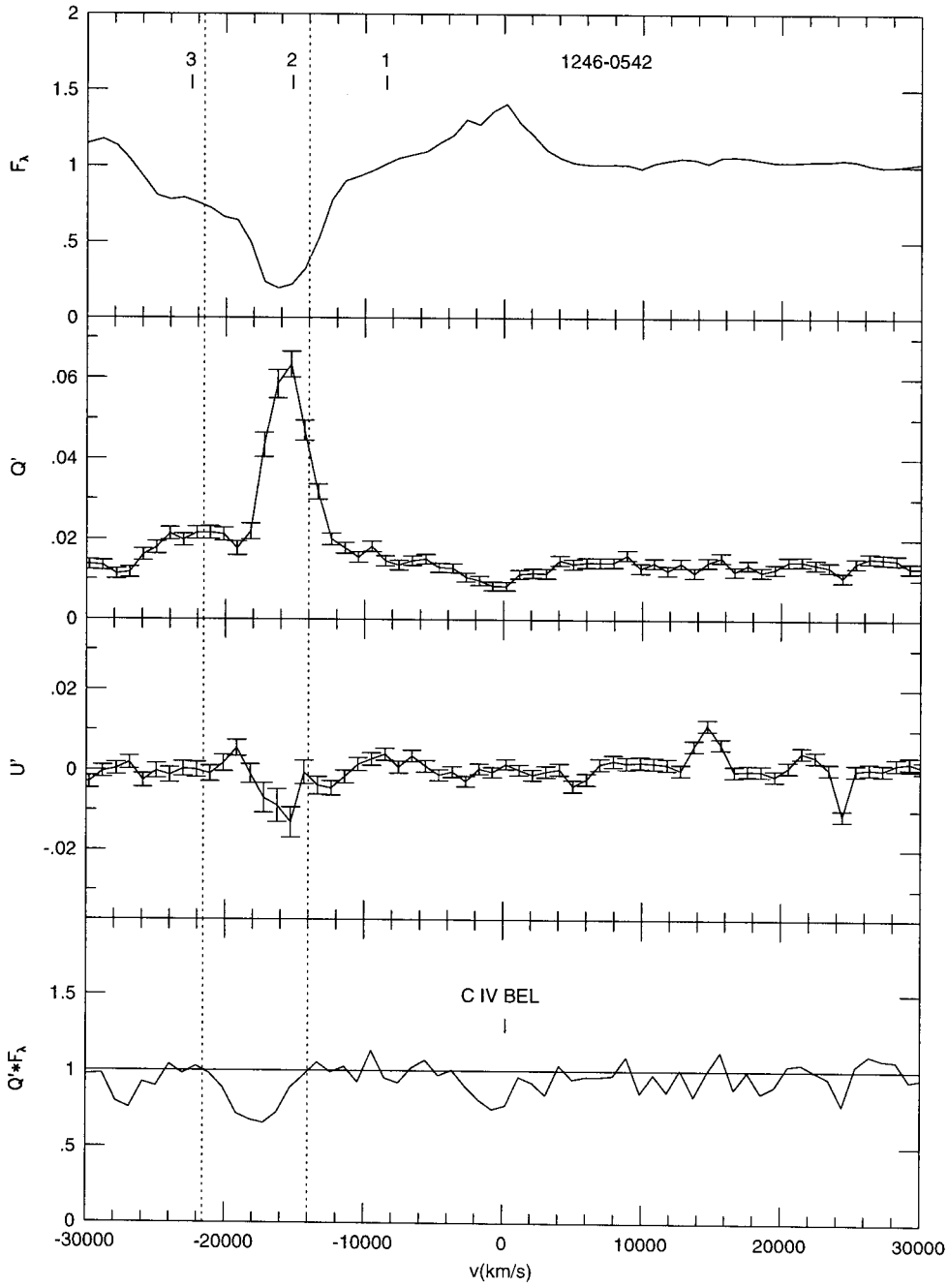

Figure 5.5: 1246-0542 C IV BAL. Panels 1-4 show the normalized total flux, rotated Stokes Q', rotated Stokes U', and normalized polarized flux ($Q' \times F$). Sub-trough segments discussed in the text are labeled in panel 1.

5.8 1333+2840 (RS 23)

The C IV line in 1333+2840 has a P-Cygni profile, with strong absorption in the blue wing (Fig. 5.6). The large equivalent width and sharply peaked profile of the BEL is unusual for BAL QSO. From the shape of the BEL, it appears that the BAL starts at 0 km/s, but this depends on the blueshift of the C IV BEL relative to the rest frame. The BAL doesn't dip below the continuum level until a velocity of -2600 km/s. It is likely that the BEL is only partially covered by the BAL and fills in the BAL to some extent. There is shallow absorption in the blue wing of the C IV BAL, which extends to -25,000 km/s. Unfortunately, there was an intense cosmic ray event which contaminated the spectra from -17,400 km/s to -14,400 km/s.

There is an interesting interplay between polarization effects in the emission and absorption lines (Fig. 5.6). The polarization rises to $8.5 \pm 1.6\%$ at -4800 km/s. This is only 2σ above the maximum continuum polarization value of 5.4%, but occurs in two adjacent bins. Also, the polarization increases by 4.5% above the local continuum, which is highly significant. The peak C IV BAL polarization in 1333+2840 is not much smaller than the 10% polarization seen in the most highly polarized troughs of 0105-265 and 2225-0534, but it is unusual that the contrast between the continuum and trough polarization is so small. As we discuss below, a number of effects are probably conspiring to reduce the trough polarization.

The polarized flux spectra show a very strong contribution from light resonantly scattered by the BALR on the red side of the C IV BEL (Fig. 5.6, panel 4). There is a dip in $Q' \times F$ from 0-12,000 km/s. This feature may extend to even higher velocities because the slope of the spectrum changes from negative to flat at 24,000 km/s (see also Fig. 2.18). Altogether, the polarized flux spectrum gives the impression of a large dip centered on the C IV BEL and extending 24,000 km/s in either direction. The red wing HREW of this feature is -13.1 ± 2.1 Å. The net REW of the C IV BAL is larger in polarized flux than in total flux (-30 ± 2 vs. -20.4 Å), in spite of the polarization rise at trough minimum. This indicates that the REW of the blue resonantly scattered polarized flux is about 10 ± 2 Å. The red "absorption" feature in $Q' \times F$ is too broad to be caused by gas in the BELR, confirming the BALR as its origin.

The red resonantly scattered photons are polarized roughly perpendicular to the con-

tinuum since $Q' \times F$ is negative and there is no significant red emission in $U' \times F$ (Fig. 5.6, panels 4 and 3; and Table 5.1). This is similar to the polarized BEL in 0226-1024 and 1246-0542. However, for 1333+2840 we are certain that we are seeing photons from the central continuum source which are resonantly scattered by the BALR, not just scattered photons from the BELR. The BALR and electron scattering structures must be roughly perpendicular to each other. For example, the BALR may be equatorial and the electron scattering region perpendicular to it in a polar outflow. The electrons could reside in the BELR or perhaps a more tenuous and highly ionized phase. The perpendicular nature of the two scattering regions probably rules out electron scattering of the continuum in the BALR. A polar location for the electrons also nicely explains why the BALR only partially covers the scattered continuum.

There are highly significant PA rotations across the blue side of the C IV BEL and across the deep portion of the C IV BAL, from 0 to -14,400 km/s. The Stokes U' flux is negative blue-ward of -5100 km/s and positive red-ward of this velocity (Fig. 5.6, panel 3). The net effect is a -10 degree PA rotation across the red wing of the C IV BEL and a +10 degree PA rotation in the BAL (Fig. 2.18). It is difficult to discern if the rotation is from resonantly scattered light or partial absorption of the polarized continuum by the BALR. The PA rotation switches sign near the trough minimum, so it is plausible that the geometry of the BAL streamer crossing the line of site changes at this critical velocity. In that case, the ratio of polarized continuum flux in $Q' \times F$ and $U' \times F$ would depend on the angle the streamer makes on the plane of the sky with respect to the electron scattering region.

1333+2840 shows the most convincing signature of BALR resonance scattering of all the objects in the sample. It is also the object with the greatest continuum polarization, and has a distinctive BEL and BAL velocity profile. These may just be coincidences, especially in light of our conclusions from Chapter 4. In that chapter we found no correlation between continuum polarization and line equivalent width. Apparently, there is a large variance in the properties of the electron scattering region which overwhelms any dependence on viewing angle. In spite of this, it is possible that 1333+2840 is viewed at an optimal angle to see continuum and resonance scattering polarization effects. For example, we may have a line of sight which is nearly perpendicular to the polar axis.

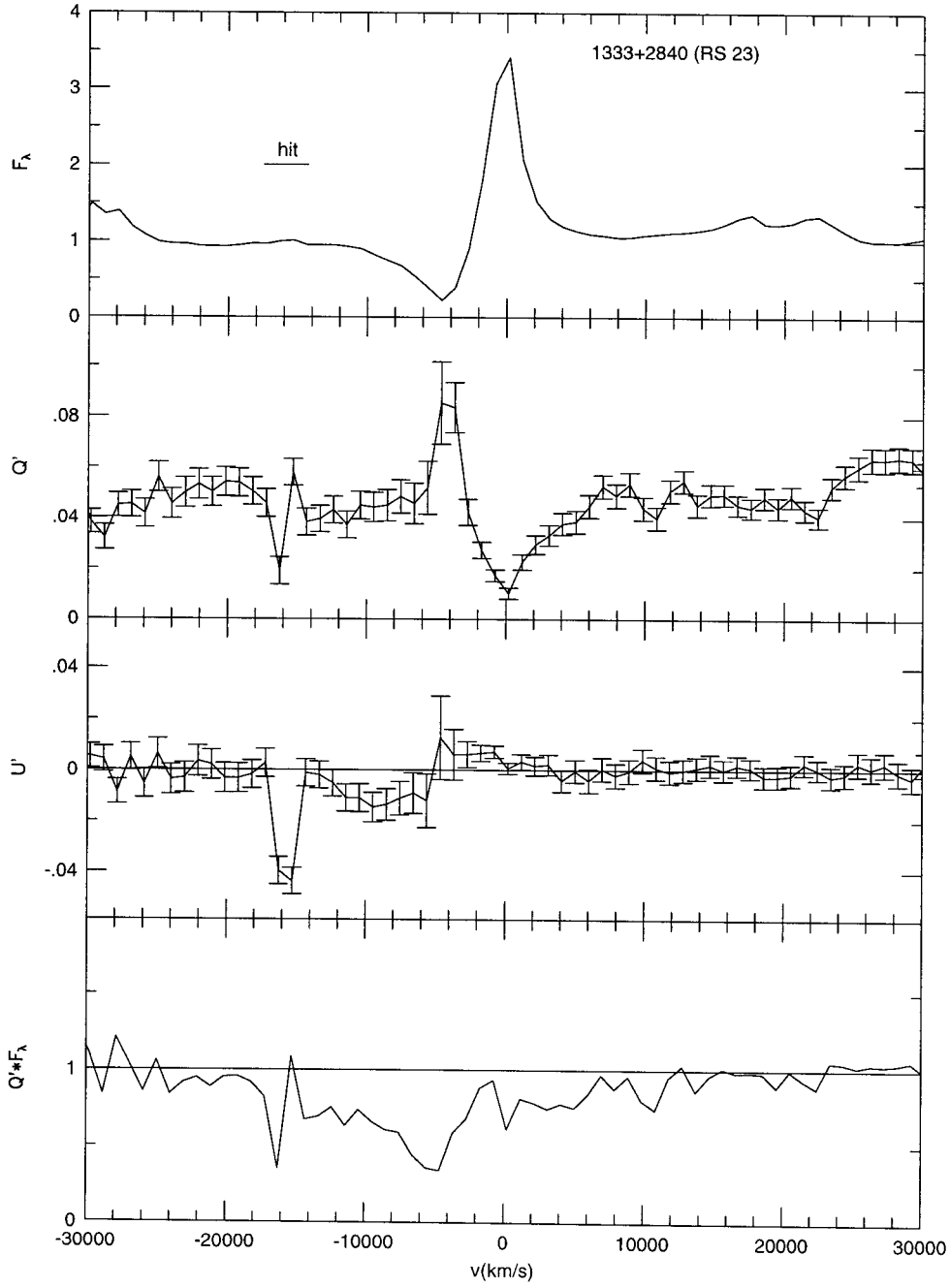

Figure 5.6: 1333+2840 C IV BAL. Panels 1-4 show the normalized total flux, rotated Stokes Q', rotated Stokes U', and normalized polarized flux ($Q' \times F$).

5.9 1413+1143

1413+1143 is well known as the Cloverleaf, a quadruple lensed BAL QSO. We show its flux and polarization spectra in Figure 5.7. Its polarization characteristics are somewhat peculiar for a BAL QSO, and this may be related to the fact that it is lensed. Goodrich & Miller (1995) claim that the continuum polarization is variable over the period 1985-1994, with $P = 1.2 - 2.7\%$ and $PA = 48 - 64$ degrees. They also measure non-zero polarization in the emission lines at a PA which is consistent with the continuum, suggesting a scattering origin for both. While we do see indications of low-level polarization variability in other objects, it is at a level of $< 0.4\%$ (Section 4.15).

If polarization variability is intrinsic to the QSO, then it may reflect changes in the distribution of scattering material or light travel-time effects (Section 4.15). In this case, the polarization of all four of the lensed components should track one another, and there should be consistent delays between component pairs. Alternatively, the polarization variability could be due to microlensing and the motion of the lens across the source. This would indicate that the polarization is highly sensitive to the viewing geometry, since the images are separated by only 1 arcsec. Microlensing effects should be independent in the four components. A third possibility is polarization by dust in the lensing galaxy. The polarization would be static in each component, but the polarization of the combined components would depend strongly on spectrograph slit location and seeing. It is feasible to distinguish between the three possibilities with high resolution imaging polarimetry monitoring.

Our Keck observations of the continuum polarization are consistent with those of Goodrich & Miller (1995). We find $P = 1.49 \pm 0.04$ and $PA = 56.8 \pm 0.6$ degrees in the continuum. We can not add much to the question of polarization variability with a single epoch of observations, but our measurement in 1996 June is consistent with no variation greater than 1σ from the 1994 June data (Goodrich & Miller, 1995, GM).

The C IV and Lyα/N V emission lines are present as positive spikes in the polarized flux spectra (Figs. 5.7, 2.19). However, their REW have low formal significance ($5 - 6 \pm 4$ Å). Since GM found polarized C IV at a level of 5σ, we will assume that it is truly present. It is likely that we underestimate the REW of the narrow C IV line by using a wide window (16,200 km/s) which includes the BAL on the blue side and noisy continuum on the red side; it would be better to use a 8000 km/s window. As we noted in Section 5.2, the C III]

polarization measurement was contaminated by a cosmic ray event. Positively polarized C IV BEL are unusual in our sample. More typical are negatively polarized BEL, which can in some cases be connected to resonance scattering in the BALR. The narrow widths of polarized BEL in 1413+1143, along with their similar PA to the continuum suggest that the BEL and continuum are scattered by the same (cool) electrons. The reduced polarization of the BEL relative to the continuum may be due to spatial dilution.

P is not well measured ($\sigma = 8\%$) in the deepest part of the C IV BAL (-4700 to -5700 km/s). However, the polarization rises convincingly in the shallower portions of the trough from -1800 to -3700 km/s and -6600 to -9600 km/s. The rise in individual wavelength bins has low significance ($\sim 1\sigma$), but is present in 6-8 bins. The polarization returns to the continuum value of 1.5% in the high speed tail of the trough.

Because the polarization increase is localized to the deep, low speed portion of the C IV BAL, the shape of the trough is smoothed out in polarized flux. The low-speed portion of the trough is de-emphasized with respect to the high speed portion. The shallow blue wing of the trough is relatively more prominent in polarized flux than in total flux. This is similar to the 2225-0534 C IV BAL (Fig. 5.10), and is consistent with a BALR local covering factor that increases with velocity. However, the high velocity absorption may also be enhanced by negatively polarized, resonantly scattered flux, as in 1333+2840. This a strong possibility, considering the similarity of the BEL and BAL profiles in 1413+1143 and 1333+2840. The data for 1413+1143 are noisier, which may cause us to miss the expected resonance scattering feature red-ward of the C IV BEL.

There are unusually strong PA rotations (~ 20 degrees) across the C IV and Si IV BAL in 1413+1143 (Fig. 2.19). This is also apparent in Figure 5.7 (panels 2 and 3), where the Stokes Q' and U' polarization are of equal strength in the C IV trough. A PA rotation this large means that $Q' \times F$ underestimates the total polarized flux ($P \times F$) by a factor of 0.77. The C IV REW in $U' \times F$ is 13 ± 5 Å, while the REW in $Q' \times F$ is -36 ± 5 Å. Like in other objects, the PA rotations are restricted to the trough, so we attribute them to partial coverage of the electron scattering region.

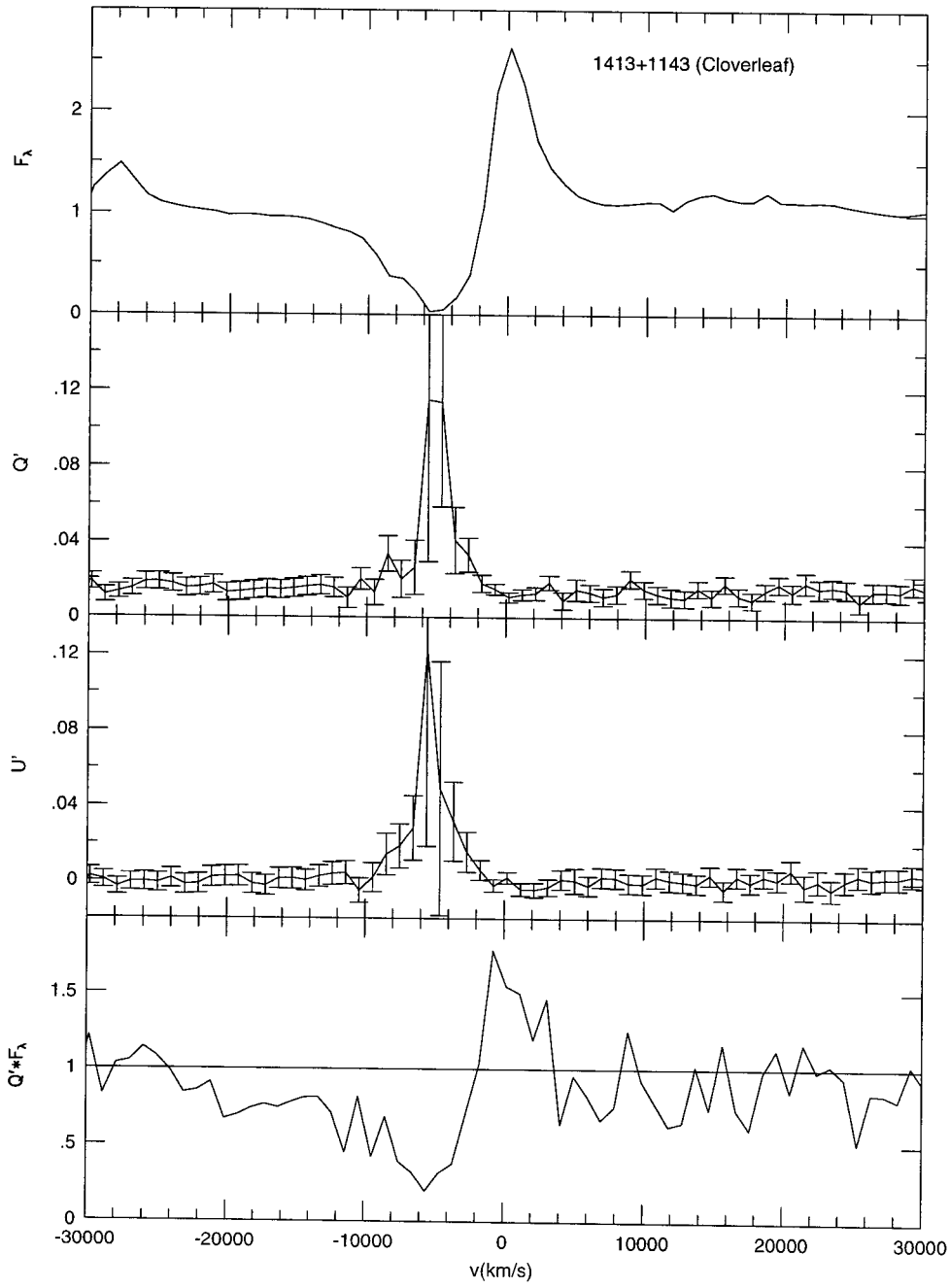

Figure 5.7: 1413+1143 C IV BAL. Panels 1-4 show the normalized total flux, rotated Stokes Q', rotated Stokes U', and normalized polarized flux ($Q' \times F$).

5.10 1524+5147 (CSO 755)

The C IV BAL in 1524+5147 is shallow, so the polarization effects in it are quite small (Fig. 5.8). However, this is a very bright BAL QSO with high S/N data and there is a significant detection of the polarization rise in the deepest sub-trough. There are multiple sub-troughs centered at the following velocities: 1) -800, 2) -4800, 3) -6700, 4) -14200, 5) -17300, 6) -20300, and 7) -24000 km/s.

The polarization rises to a maximum of $6.0 \pm 0.4\%$ on the red side of sub-trough 4. The polarization at the sub-trough minimum is $P = 5.2 \pm 0.5\%$. There is therefore a hint that polarization decreases to the blue in this trough. This is a marginal result, but it agrees with the trend seen in other objects (e.g., 1246-0542). There are 1σ increases in polarization in sub-troughs 3, 5, and 6, and no increases in the low-velocity sub-troughs 1 and 2. The deepest sub-trough (4) is significantly shallower in polarized flux than in total flux.

The low velocity sub-troughs 1 and 2 provide interesting constraints on the geometry of the BELR, low velocity BALR and scattering region. These narrow sub-troughs are deeper in polarized flux than in total flux, but they don't reveal themselves in the polarization spectrum (Fig. 5.8, panels 2 and 3). This means that absorption systems 1 and 2 cover the direct and scattered continuum sources equally, unlike the higher velocity BAL cloud 4. The geometry of the various emission regions and absorbing clouds is sketched in Fig. 5.9. In addition, sub-troughs 1 and 2 are much weaker in the unpolarized flux spectrum (Figure 4.7), so the corresponding clouds cover only a small fraction of the Lyα, N V and C IV BELR. This suggests that the BELR has a larger angular size on the sky than the electron scattering region (which is also consistent with the low BEL polarization). Absorption systems 1 and 2 must also be intrinsic to the quasar; intervening systems would cover all emission sources equally. This is similar to the behavior seen in the narrow low velocity sub-trough 1 of 0226-1024 (Figure 5.4). The angular size of the electron scattering region is intermediate between the angular sizes of the high and low velocity BAL clouds.

An unusual feature of 1524+5147 is absorption on the red side of the C IV BEL peak (sub-trough 1). Glenn et al. (1994) measure a redshift of 500 km/s for this feature relative to the peak. We have used a nominal redshift of 2.88, which puts the onset of the C IV BAL at 0 km/s. However, it is apparent from our spectra (Fig. 5.8, panel 2) that the dilution feature from the C IV BEL reaches minimum polarization at -800 km/s, which matches

the velocity of sub-trough 1 to within 1 velocity bin. This means that the C IV BEL is centered at -800 km/s and sub-trough 1 has a velocity relative to this of 0 km/s. This, along with the polarization behavior discussed above, strongly suggests that sub-trough 1 is due to absorption by gas directly associated with the BELR. In addition, it means we should revise the C IV redshift of 1524+5147 to 2.877.

Several BEL are seen in the unpolarized flux spectrum of 1524+5147 (Fig. 4.7). The dilution signature of Si IV can be seen as a dip at at -28,850 km/s in Figure 5.8 (panel 2). There also appears to be a small residual of negatively polarized flux from Si IV at this velocity (panel 4). The corresponding negatively polarized flux in C IV is seen weakly red-ward of sub-trough 1. It is not necessary to invoke resonantly scattered flux from the BALR for these features, since they do not extend past the wings of the C IV BEL. However, if they are due to resonance scattering, then this is yet another case where the resonantly scattered light is polarized perpendicular to the continuum.

There are small (5 degree) PA rotations across the deepest C IV sub-trough. These are due to 1% residual polarization spikes in U' (Fig. 5.8, panel 3). These are of marginal significance, but may be real since they correspond to the deepest part of the trough. There is a spike in U' at 2000 km/s on the red side of the BEL; this may be due to a weak cosmic ray event since it covers only one bin and doesn't line up with any feature in the total flux spectrum.

There is a steepening of the polarized flux spectrum blue-ward of the Si IV BEL (Fig. 2.20). The polarized flux begins to rise above the apparent continuum level at 1397 Å and peaks at 1261 Å. The peak wavelength corresponds to a bump in the total flux spectrum on the red wing of N V. This may be due to Rayleigh scattering in the wings of Lyα (see Chapter 4). There is also a significant PA rotation of ± 5 degrees across the Lyα/N V BEL and BAL (Fig. 2.20). It is peculiar that a similar feature is not visible in the C IV region. The PA rotation may also be from Rayleigh scattering in Lyα, or it may be due to resonantly scattered N V and Lyα photons.

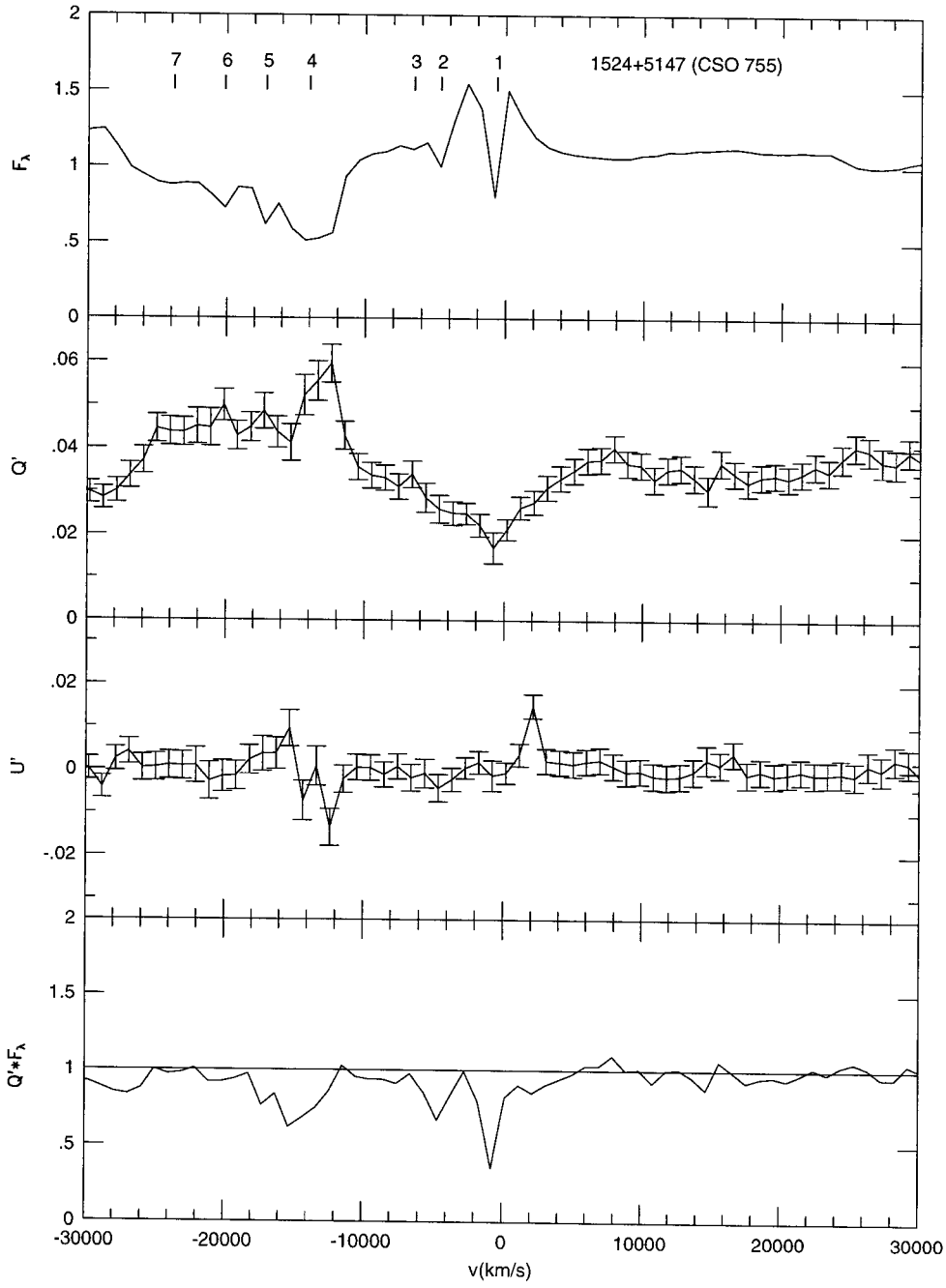

Figure 5.8: 1524+5147 C IV BAL. Panels 1-4 show the normalized total flux, rotated Stokes Q', rotated Stokes U', and normalized polarized flux ($Q' \times F$). Sub-trough segments discussed in the text are labeled in panel 1.

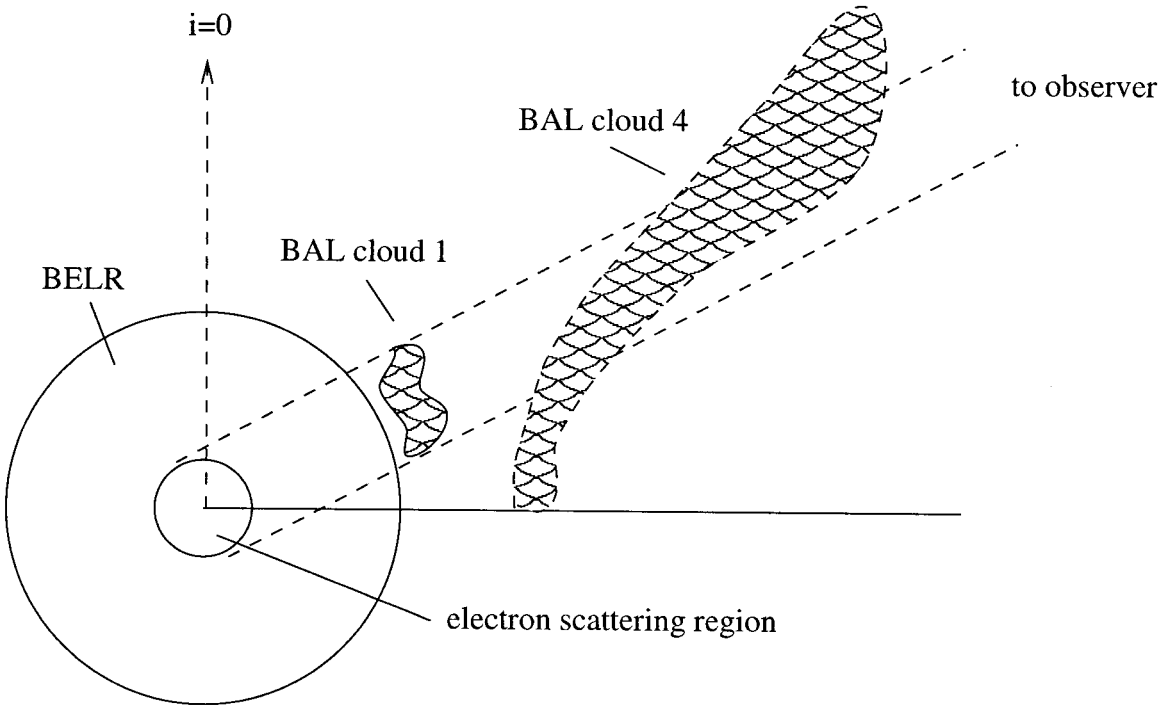

Figure 5.9: 1524+5147 model. This diagram shows the geometry of the low and high velocity BAL clouds. The low velocity cloud 1 completely covers the electron scattering region but only partially covers the BELR. The high velocity cloud 4 only partially covers the electron scattering region because the outflow is non-radial and accelerating outward.

5.11 2225-0534 (PHL 5200)

2225-0534 has a large equivalent width C IV BEL, which is cut at 0 km/s by the C IV BAL (Fig. 5.10). The BEL profile and lack of detachment of the BAL from the BEL are similar to 1333+2840 and 1413+1143, but the deep portion of the C IV BAL extends to a much higher velocity (-15,400 km/s) in 2225-0534. We have labeled 5 distinct features in the BAL (at (1) -2700 km/s, (2) -5600 km/s, (3) -7500 km/s, (4) -8900 km/s, and (5) -14400 km/s). Features 1, 2, 4 and 5 are sub-troughs. Feature 3 is a region of reduced absorption which is discussed by Turnshek et al. (1988).

The trough polarization of 2225-0534 is discussed by Cohen et al. (1995) (C95). These same data are presented in Figure 5.10. The polarization reaches a peak of $10.1 \pm 1.9\%$ at a velocity of -8400 km/s. This value is 2% lower than the value given by Cohen et al. (1995), because we have binned the data more. The trough polarization is greater than the continuum polarization in the velocity range -4000 to -11,500 km/s (sub-troughs 2 and 4).

C95 noted that the polarization peak in the C IV BAL is quite a bit narrower than the width of the trough, even though the trough has a fairly flat bottom. They suggested that the polarization is diminished in the low speed portion of the trough by residual flux from the C IV BEL. We affirm that suggestion by noting that the red wing of the BEL extends to at least 7400 km/s, while the BAL polarization reaches its maximum at -7500 to -8500 km/s. Note that the diluting power of the C IV BEL is enhanced in the trough because the BAL absorbs a smaller fraction of the BEL than the continuum. C95 suggested that the polarization drops at high speeds because the high speed BAL clouds more completely cover the scattered continuum than the lower speed clouds at -8500 km/s. This effect is difficult to judge in the binned spectra because it covers a narrow velocity range.

C95 also discussed a 10 degree PA rotation near the peak in polarization and associated it with feature 4 in the total flux spectrum. This is also visible as an excursion of in the U' spectrum (Fig. 5.10, panel 3) of $-0.04 \pm 0.02\%$. This has only marginal significance, but extends over two wavelength bins. Similar rotations were discussed above for a number of objects, and they appear to be due to partial coverage of the electron scattering region.

There is a hint of negatively polarized flux in $Q' \times F$ from 0 to 18,000 km/s (Fig. 5.10, panel 3). This feature has a REW of -4.2 ± 1.9 Å, a marginally significant detection. However, this measurement depends heavily on the continuum fit.

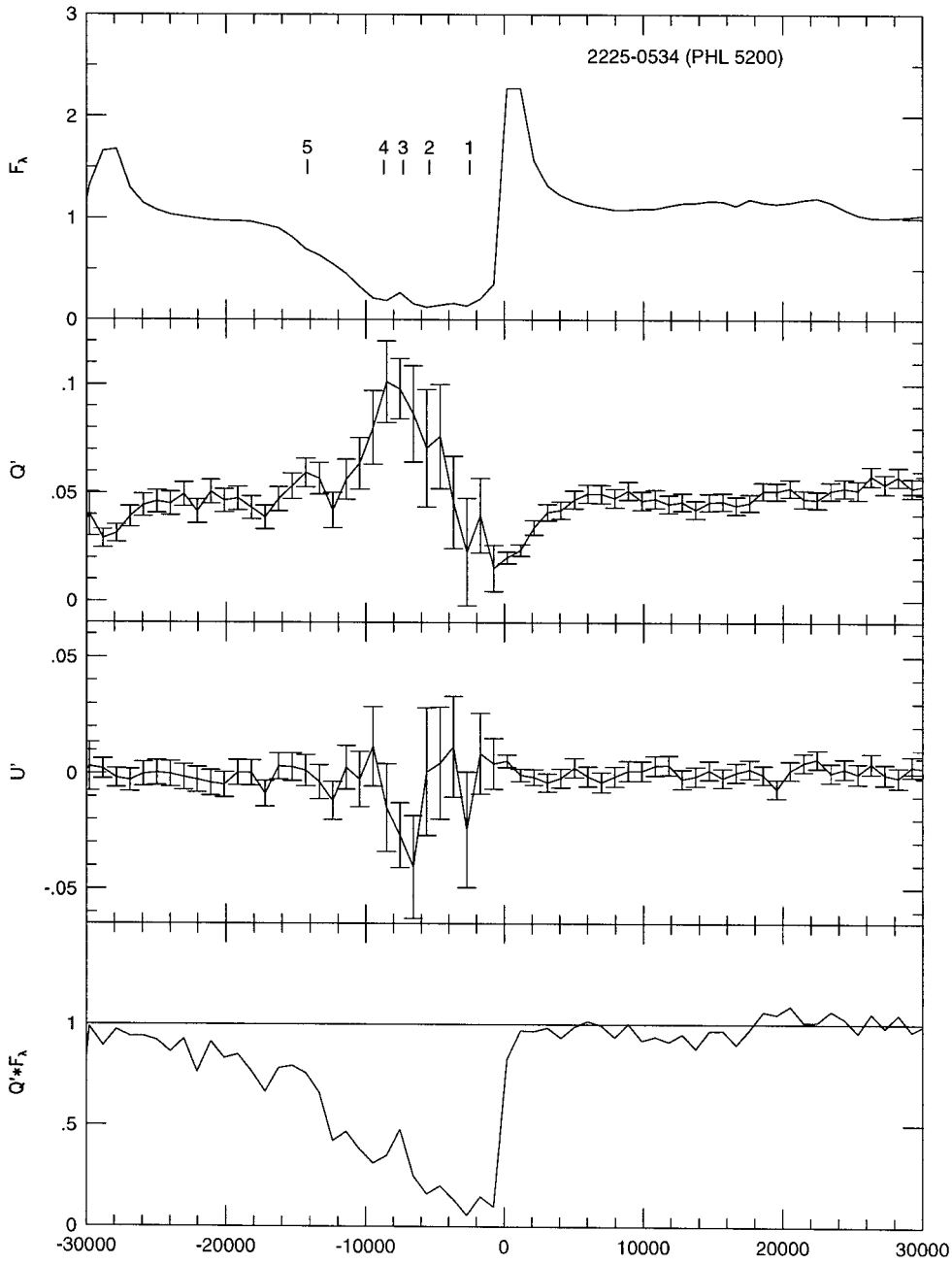

Figure 5.10: 2225-0534 C IV BAL. Panels 1-4 show the normalized total flux, rotated Stokes Q', rotated Stokes U', and normalized polarized flux ($Q' \times F$). Sub-trough segments discussed in the text are labeled in panel 1.

5.12 BEL Polarization Sources

There are 5 objects in our sample with significantly polarized permitted BEL (Section 5.2). The extremely broad, high velocity component of the polarized C IV flux in 0226-1024 and 1333+2840 is due to photons from the central continuum source resonantly scattered at a large range of velocities in the BALR. There is also a narrower component with a velocity width and profile shape comparable to the C IV BEL in 0059-2735, 0226-1024, 1246-0542, 1413+1143, and 1524+5147. We call the extremely broad component "resonantly scattered continuum" and the narrower component "scattered BEL," to distinguish the origins of the scattered photons.

In this section we consider two possible sources of BEL polarization which seem equally plausible. The BEL could be polarized by electron scattering, resonance scattering in the low velocity BALR, or both. We consider the extremely broad resonantly scattered continuum feature separately in the next section. Figure 5.11 presents our best model of the nuclear environment in QSO, based on the commonly favored equatorial outflow model. We show the relative dispositions of the continuum source, BELR, and BALR (not all to scale). The various direct and scattered rays are labeled 1-6.

First we consider the arguments for electron scattered BEL. The polarized BEL flux is greater than the (undetected) resonantly scattered continuum flux in 0059-2735, 1246-0542, 1413+1143, and 1524+5147. This suggests that the resonantly scattered BEL component is also weak and the electron scattered component is strong. However, detection of the resonantly scattered continuum component may be hampered by its extremely broad width relative to the BEL.

Since the C IV BEL profile is not greatly broadened in polarized flux, scattering by hot electrons can not explain the reduced polarization in the BEL relative to the continuum. The particles which scatter the BEL must be cold or massive (i.e. cool electrons, C IV ions, or dust). The lower polarization and different PA of the C IV BEL relative to the continuum suggests that the BEL clouds are distributed in a region larger than the electron scattering region. This reduction in polarization (relative to a point source) due to scattering of an extended source is called spatial dilution. The Fe II and C III] BEL may be completely unpolarized in most objects because they lie at a larger distance from the electron scattering region than the C IV, Si IV, and N V BELR. The C III] BEL photons are only polarized

in two objects (0019+0107 and 2225-0534). As we discussed in Section 5.2, this may be due to resonance scattering in the moderate optical depth C III] BELR, and is probably unrelated to the polarization of the other BEL. The C IV BEL is polarized parallel to the continuum in 1413+1143. This could occur if the C IV BELR had a smaller radius than the continuum scattering region.

Next we consider the arguments for resonantly scattered BEL. If the BEL photons are resonantly scattered by C IV ions in the BALR, then we don't have to worry about temperature broadening because the ions are relatively massive and move slowly. The width of the line is roughly preserved by resonance scattering if the velocity field of the BELR is isotropic. However, the line will be skewed to the red since the BAL outflow is redshifted in the rest frame of the BELR (Krolik & Voit, 1998). A redshift of 1000-2000 km/s is seen in the scattered C IV BEL of 0059-2735 and 0226-1204.

In 4/5 objects, the BEL polarization is perpendicular to the continuum polarization. This is consistent with resonance scattering in the geometry of Figure 5.11, where both the BELR and low-velocity BALR sit near the equatorial plane. Note that the BEL will only be scattered in the low velocity base of the BAL outflow. We find resonance scattering in the BALR a more appealing explanation for the C IV BEL polarization than electron scattering. Resonance scattering invokes a relatively simple geometry and cleanly explains the difference between the C III] and C IV BEL polarization.

BAL QSO IRAS 07598+6508 has polarized Hα, Na I, and Fe II emission lines (Fig. 2.9. There is a strong (20 degree) PA rotation between the blue and red wings of the BEL. Hα must be polarized by dust or electrons. It is not a ground-state transition and therefore can not be resonantly scattered in the BALR. It would be useful to observe the C IV line polarization of this object to see if it is similar to Hα. It would also be useful to do polarimetry of the UV lines in Seyfert 1 galaxies. This might indicate variations in the geometry of the various line-emitting regions.

Seyfert 1 galaxies generally have more highly polarized BEL than BAL QSO. Goodrich & Miller (1994) and Martel (1996) find striking polarization variations and PA rotations across the Balmer emission lines in Seyfert 1s. They attribute these effects to scattering on the size scale of the BELR. Similar phenomena are observed in broad-line radio galaxies (Cohen et al., 1998). The difference in line polarization between Seyfert 1s and QSO suggests that the BELR and scattering regions in Seyfert 1s can not be simply scaled up to match

QSO. Perhaps the BELR is smaller relative to the the scattering region in Seyfert 1s than in QSO.

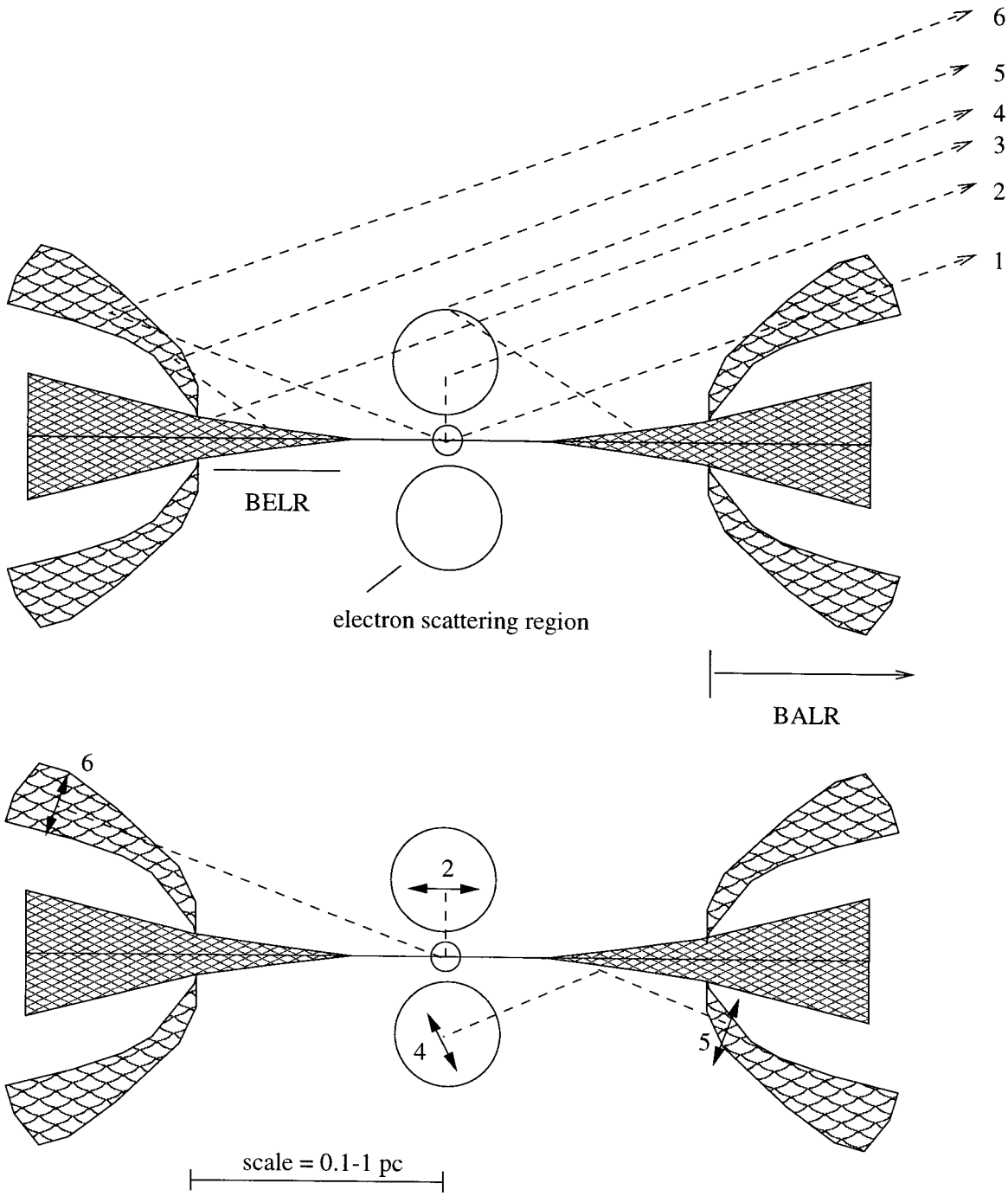

Figure 5.11: Scattering model. The BELR and BALR are located near the equator, and the electron scattering region is located along the polar axis. The central continuum source is the small circle at the center, not drawn to scale. The various direct and scattered rays are as follows: 1) direct continuum, 2) electron scattered continuum, 3) direct BEL, 4) electron scattered BEL, 5) resonantly scattered BEL, and 6) resonantly scattered continuum. The top drawing is a side view (observer to the right side). The bottom drawing is in the plane of the sky, and shows selected polarization vectors for the 4 scattered rays. Note that scattered rays from the bottom half of each drawing may be obscured by an accretion disk in the equatorial plane.

5.13 BALR Resonance Scattering

The BAL troughs are produced by scattering resonant photons from the continuum source out of the line of sight. Some photons originally directed away from the observer are scattered into the line of sight. The flux of resonantly scattered photons is determined primarily by the global covering factor of the BALR, but also by the shape and velocity profile of the outflow. So far, it has been impossible to detect resonantly scattered photons in the total flux spectra of BAL QSO because the intensity of the scattered light is low and it is difficult to separate from the BEL emission.

We have found strong evidence for resonantly scattered photons in the polarized flux spectra of two BAL QSO (0226-1024 and 1333+2840). We see polarized line flux which extends more than 12,000 km/s to either side of the C IV BEL, at much higher velocities than are present in the BELR. In other words, the velocity profile of the resonantly scattered flux is much broader than the BEL profile. We are therefore confident that the photons are scattered in the BALR. The intensity of the resonantly scattered flux is weak ($\sim 4 \times 10^{-18}$erg/s/cm^2/ Å), and the red HREW in polarized flux is 4-13 Å .

Two lines of evidence suggest that the BALR is equatorial and not bipolar. First, in Chapter 4 we showed that BAL QSO are more highly polarized than non-BAL QSO. The continuum polarization distributions of BAL QSO and non-BAL QSO are also consistent with the unification of these two classes of object. We concluded that non-BAL QSO are viewed from a polar perspective, while BAL QSO are viewed from a more equatorial perspective. Second, we see the resonantly scattered continuum flux extending to the red side of C IV. These photons should be blocked by the accretion disk if it is extensive enough and the BALR is bipolar. However, we expect to see these photons back scattered from the far side of the outflow in the case of an equatorial wind.

Hamman et al. (1993) (HKM) put limits on the resonantly scattered flux in BAL QSO by comparing the equivalent widths of the BEL and BAL in total flux. We can improve on this now that we have actually measured the equivalent width of the resonantly scattered light, and have a better grasp on the geometry of the outflow. We assume the simple unification geometry presented in Chapter 4. In this geometry, the BAL flow is confined to a range of inclinations $i = i_1 - i_2$, and equatorial views are obscured by a torus with opening half angle i_2. In the case of isotropic continuum emission and isotropic scattering,

the global covering fraction f can be estimated from the total flux spectrum using

$$f = 2f' = 2\frac{W_{rs}}{W_{BAL}} \tag{5.1}$$

where W_{BAL} is the BAL equivalent width and W_{rs} is the equivalent width of the resonance scattering feature. The factor of 2 accounts for the absorption of 50% of the resonantly scattered flux by the accretion disk. A covering fraction of f' is derived if there is no accretion disk. It is assumed that no scattered photons are destroyed along any other directions and that W_{rs} and W_{BAL} are independent of viewing angle through the BALR. This is not necessarily the case in an optically thick flow.

The equivalent width of the trough (W_{BAL}) must be corrected for scattered flux which partially fills in the BAL. The blue resonantly scattered contribution to this correction is $W_{rs,b}/P_{rs}$ and the electron scattered contribution is $W_{es,t}/P_{es,t}$. In addition, our measurements of the equivalent widths W_{rs} and $W_{es,t}$ in polarized flux must be scaled to correct for the different polarizations of the resonantly scattered and electron scattered light. The modified equation to estimate the global covering fraction from the polarized flux is

$$f = \frac{2p(W_{rs,r} + W_{rs,b})}{W_{BAL} + pW_{rs,b} + p_2 W_{es,t}} \tag{5.2}$$

$$p = \frac{P_{es}}{P_{rs}} \tag{5.3}$$

$$p_2 = \frac{P_{es}}{P_{es,t}} \tag{5.4}$$

$W_{rs,r}$ and $W_{rs,b}$ are the equivalent widths of the red and blue resonantly scattered polarized flux and $W_{es,t}$ is the equivalent width of electron scattered polarized flux in the trough. The polarization of the electron scattered continuum is P_{es} and the polarization of the resonantly scattered continuum is P_{rs}. $P_{es,t}$ is the mean polarization of the electron scattered light in the trough, which may be velocity-dependent. The ratio $p_2 \simeq 1$ depends on the details of the scattering and BALR geometries (Section 5.14).

We measured W_{BAL} and $W_{rs,r}$ for the C IV BAL in 0226-1024 and 1333+2840 (Table 5.4). We assume that the magnitudes of the blue and red resonantly scattered flux are roughly the same $W_{rs,b} \simeq W_{rs,r}$. We estimated the total scattered contribution to the

flux in the trough ($W_{s,t} = W_{rs,b} + W_{es,t}$) from the difference between the trough REW in total and polarized flux. However, the intrinsic polarizations of the electron scattered flux and resonantly scattered flux (P_{es} and P_{rs}) can not be directly measured since we can not identify these components in the total flux spectrum. The best we can do observationally is to estimate $P_{es} \simeq 10\%$ from the maximum trough polarization.

The polarization of the resonantly scattered light P_{rs} is determined by the geometry of BAL outflow and by the angular momentum of the resonance transition. Lee & Blandford (1997) find $P_{rs} \simeq 15\%$ at the bottom of the C IV ($J = 1/2 - 1/2, 3/2$) trough for a poloidal equatorial flow. Transitions with $J = 1 - 0$ should have much higher polarization ($\sim 50\%$). Unfortunately, the $J = 1 - 0$ transitions (e.g. C III λ977 and Al III λ977) are generally out of the wavelength range we observe, or they are not strong enough to give a polarization signature. Since the maximum C IV trough polarization and the polarization of resonantly scattered light from the BALR are roughly equal, $p \simeq 1$ in Equation 5.2.

The estimated global covering fractions of the BALR in 0226-1024 and 1333+2840 are listed in Table 5.4. We find a 25% covering fraction for 0226-1024 and an unphysical 181% covering fraction for 1333+2840. If we do not assume half of the resonantly scattered flux is obscured by an accretion disk, then we get $f' = 13\%$ for 0226-1024 and $f' = 90\%$ for 1333+2840. The estimate is so large for 1333+2840 because the C IV BAL equivalent width is small and there is a large amount of resonantly scattered flux. We may have underestimated $W_{s,t}$ for 1333+2840 because the resonantly scattered flux and electron scattered flux have opposite signs and may partially cancel in the BAL polarized flux spectrum (Section 5.8). This may have lead to an overestimate of the covering fraction.

The parameter p is a large source of uncertainty in our estimate, and may vary by a factor of two depending on the exact parameters chosen for the electron and resonance scattering regions. Our values of f' compare favorably to the values which HKM derive from their line-fitting of 0226-1024 ($f' = 10\%$) and 1333+2840 ($f' = 90\%$). (Note that HKM do not assume half of the resonantly scattered flux is absorbed.) This consistency is encouraging, and indicates that the amount of resonantly scattered flux is strongly constrained by the depth of the low speed ($|v| < 12{,}000$ km/s) portion of the trough (HKM). It also suggests our assumptions that $p \simeq 1$ and $p_2 \simeq 1$, are not far off the mark.

Two other uncertainties in our estimate of the BALR global covering fraction are important to consider. First, the REW of the C IV BAL in total flux is probably highly dependent

on the observer's line of sight through the BAL. It is unlikely that the particular pattern of multiple troughs and their depths are preserved as the line of sight is rotated in azimuth or altitude. The C IV BAL REW range from 19-66 Å in our sample, which must be partly attributable to a range of viewing angles. Therefore, line of sight effects can potentially introduce a factor of 3.5 uncertainty in the denominator in Equation 5.2.

Second, the assumption of isotropic scattering in the BALR may also be an over-idealization if the BALR is optically thick. This means that the amount of resonantly scattered flux is likely to depend on viewing angle, lending uncertainty to the numerator of Equation 5.2. However, the profile of the resonantly scattered light is probably less sensitive to viewing angle than the BAL REW, since it is integrated over the entire flow. Also, as we saw in Chapter 4, BAL QSO may be viewed from a very narrow range of inclinations.

Keeping in mind the large uncertainties in our estimates of the global covering fraction, what are the implications for the unification of QSO and non-BAL QSO? 0226-1024, with $f = 25\%$, would appear as a non-BAL QSO from most directions. It is consistent with the unification hypothesis and a global BALR covering fraction of $f \simeq 0.1$. 1333+2840 , however, does not easily fit into this scheme. Its P-Cygni profile and large flux of resonantly scattered continuum photons are consistent with a more spherical outflow. On the other hand, the high polarization of the continuum and a polarized resonance scattering feature require a non-isotropic distribution of scatterers. We may view 1333+2840 from near the equatorial plane so that the underside of the BAL flow is not obscured by the accretion disk and f' is a better estimate of the global covering fraction than f. Our dilemma may also be alleviated if p has a low value (e.g., $p = 0.1$), or if we are looking through a weak portion of the flow. Finally, we did not detect the resonantly scattered continuum flux in our very high S/N observations of 1246-0542 and 1524+5147, implying a low global BALR covering fraction in these objects. (The 2σ upper limits are $f < 0.14$ and $f < 0.30$, respectively.)

5.14 BALR Partial Continuum Coverage and Dynamics

While resonance scattering effects are important for determining the covering fraction and geometry of the BALR, they only affect the polarized flux at a detectable level in a few objects. The C IV BEL polarized HREW range from undetectable (< 2 Å) to 8 Å (Table 5.1). This leads us to believe that the strong polarization effects in the C IV BAL of most BAL

BAL QSO	W_{BAL}	$W_{rs,r}$	$\pm$	$W_{s,t}$	$\pm$	f
0226-1024	52.09	4.0	0.4	10.8	1.7	0.25
1333+2840	20.44	13.4	2.1	9.2	2.1	1.81

Table 5.4: BALR global covering fraction estimates for 0226-1024 and 1333+2840. We tabulate our measurements of the C IV BAL REW in total flux (W_{BAL}), red HREW of resonantly scattered polarized flux ($W_{rs,r}$), and REW of polarized scattered flux in the C IV BAL ($W_{s,t}$). The global covering factor estimated from Equation 5.2 is listed in column 7.

QSO must be caused by partial coverage of the electron scattering region.

In the partial continuum coverage model (Fig. 5.12), electron (or dust) scattering is responsible for the polarization in the continuum and in the BAL, and resonance scattering can be neglected. In this section, we are primarily discussing rays 1 and 2 in Figure 5.11. The polarization rise in the troughs is due to obscuration of the direct unpolarized continuum by the BAL clouds. The polarized scattered rays are on average obscured less than the direct rays. Some scattered rays may miss the BALR entirely if the scattering region has a larger angular diameter than the BALR.

We can estimate the velocity-averaged local BALR coverage of the scattering region by taking the ratio of the C IV BAL REW in polarized and total flux. The local covering factor measured in this manner spans the range $f_l = 0.24 - 1.4$, with 1246-0542 on the low end and 1333+2840 on the high end. Covering factors greater than 1 indicate contamination by BEL in the total flux spectrum or negative resonantly scattered flux in the polarized flux spectrum. If the partial coverage is in two dimensions, the corresponding ratio of BALR and scattering region angular sizes for this range is $\theta_{BAL}/\theta_{es} = 0.5 - 1.0$. This is a crude approximation, since the ratio of polarized and total REW will also depend on the geometry and optical depth of the scattering region, as we show below.

If the angular size of the scattering region were much smaller than the angular size of a BAL cloud ($\theta_{es} << \theta_{BAL}$), then scattered light and direct continuum would be equally absorbed; if it were much bigger, then the BAL would not appear in the polarized flux spectrum. The large range in f_l strongly suggests that the BAL clouds and scattering region have a similar angular extent. By clouds, we mean regions of the BAL flow which contribute to the optical depth in a given sub-trough velocity range $v \pm \Delta v$, not necessarily spatially

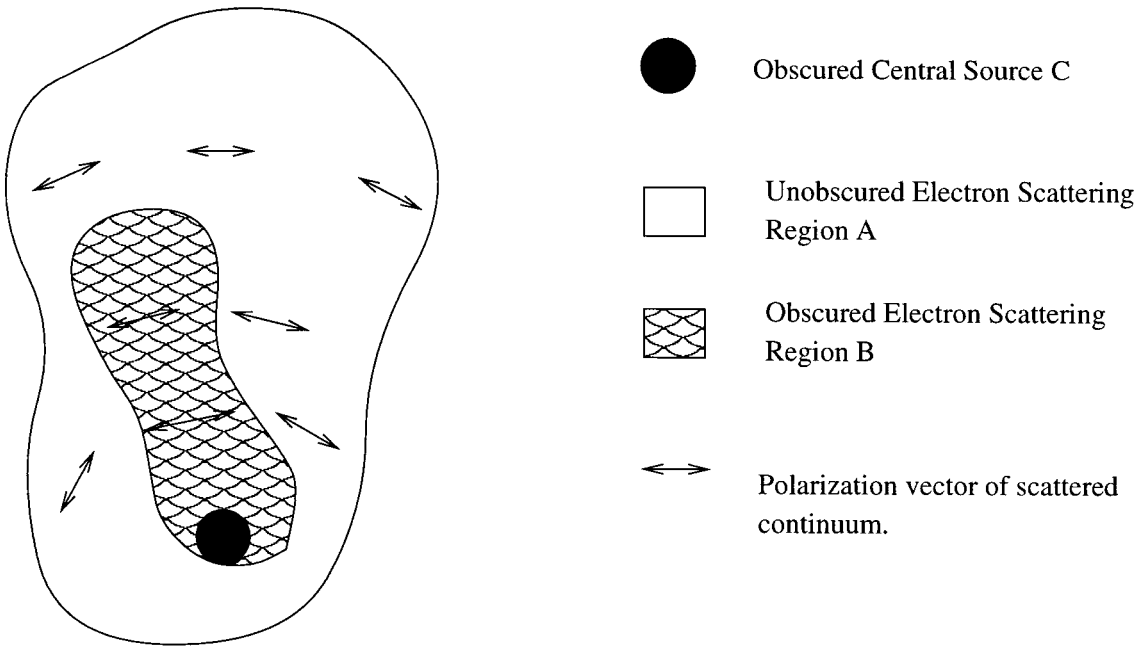

Figure 5.12: Partial continuum coverage model. We are viewing the BAL QSO in the plane of the sky. The central continuum comes from the point source C. The continuum is scattered by electrons in the region A+B and the polarization vectors are perpendicular to the radius from C. The dark region B represents a projected Sobolev surface where the continuum is obscured by the BALR in the velocity range $v \pm \Delta v$.

discrete clumps. In a diverging flow, there will naturally be an angular coherence length θ_{BAL}, outside of which the projected velocity has dropped by more than $\Delta v = v \sin \theta_{BAL}$.

In the general case, the BALR coverage is some function of velocity $f_l(v)$. This coverage is determined by the intersection of the Sobolev surfaces with the cylinder of sight to the scattering region. In the Sobolev approximation, resonance scattering occurs at a single surface then the photons escape without further scatterings. The Sobolev surfaces are the loci of constant projected velocity along the line of sight, and depend in detail on the geometry and velocity law of the outflow.

Figure 5.12 shows a sketch of the continuum coverage by a hypothetical Sobolev surface. In this model, the central continuum source C emits unpolarized UV-optical radiation, which is scattered by a cloud of electrons (A+B) in the inner regions of the QSO. The intervening BAL clouds and their projected Sobolev surfaces B completely cover the central source C and a portion of the electron scattering region. The remaining portion (A) of the electron scattering region is unobscured. The local covering fraction is therefore $f_l = B/(A + B)$. Nothing further is assumed about the 3-D configuration of the electron scattering cloud or

BAL clouds. Adding up the polarized flux and dividing by the total flux gives equations for the normalized Stokes parameters (F, Q, U) as a function of BALR optical depth (τ), which contain 4 free parameters (a, b, c, d):

$$F = \frac{F_{obs}}{F_{obs}(\tau = 0)} = \frac{1 + ce^{-\tau}}{1 + c} \tag{5.5}$$

$$Q = \frac{a + be^{-\tau}}{1 + ce^{-\tau}} \tag{5.6}$$

$$U = \frac{d(1 - e^{-\tau})}{1 + ce^{-\tau}} \tag{5.7}$$

$$PA = \frac{1}{2} \arctan \frac{d(1 - e^{-\tau})}{a + be^{-\tau}} \tag{5.8}$$

$$(a, d) = (Q_A, U_A) \tag{5.9}$$

$$b = \frac{\epsilon_B Q_B}{\epsilon_A} \tag{5.10}$$

$$c = \frac{1 + \epsilon_B}{\epsilon_A} \tag{5.11}$$

where (Q_A,U_A) and (Q_B,U_B) are the Stokes parameters of the integrated scattered flux from regions A and B in Figure 5.12, for $\tau = 0$. The electron scattering efficiencies are ϵ_A and ϵ_B. Note that we set $U_{A+B} = 0$ since we choose the zero point of our PA coordinate on the sky to match the continuum PA.

This is a purely empirical model. A calculation of the Sobolev surfaces for various outflow models is outside the scope of this thesis. The model parameters (a,b,c,d) depend on the geometry of the scattering region and Sobolev surfaces and the electron scattering efficiencies. The area-averaged electron scattering efficiencies are given by

$$\epsilon_A = f_A \tau_A \tag{5.12}$$

$$\epsilon_B = f_B \tau_B \tag{5.13}$$

in the case of optically thin scattering. The area-averaged global covering fractions of the electron scattering region are f_A and f_B, and the corresponding electron scattering optical depths are τ_A and τ_B. Note that ϵ_A and ϵ_B can range from 0.0-1.0, so $1 \leq c < \infty$.

It is instructive to consider two limiting cases of our model. The limiting case ($\epsilon_A << 1$

and $b, c >> 1$) corresponds to complete coverage of the electron scattering region, and $Q = b/c = \epsilon_B Q_B/(1+\epsilon_B)$ is constant for all τ. If this is true at all velocities, then the polarization is equal to the continuum polarization across the entire trough. The low velocity absorption systems in 0226-1024 and 1524+5147 provide a very nice demonstration of this, and have $(Q,U) = (Q_c, U_c)$.

In the other extreme, the BAL covers very little of the electron scattering region and only absorbs the central continuum ($\epsilon_A = 1$, $\epsilon_B = 0$, $c = 1$). For this geometry, the polarization in the BAL ($Q = Q_A/(1+ce^{-\tau})$) approaches the polarization of the electron scattered light as $\tau \rightarrow \infty$. The residual flux in the trough is entirely scattered light and the dilution from the central source is negligible. This is likely the case in objects such as 0105-265 which have saturated troughs with $P_t >> P_c$.

Note that BAL PA rotations are a natural consequence of the partial coverage model when the projected symmetry axes of the electron scattering region and BAL cloud are not aligned ($d \neq 0$). This would be true if there is any global deviation from axisymmetry in the BAL flow or scattering region. The BAL PA rotations may be a clue that there is a warp in the accretion disk. On the other hand, it could be a purely local phenomenon due to random structure or non-radial motion in the BAL clouds intersecting our line of sight.

The parameter b is constrained by the continuum polarization, $Q_c = (a+b)/(1+c)$. We can further constrain the parameters if we assume that the trough is saturated ($\tau \rightarrow \infty$) where the polarization reaches its maximum (Q_t, U_t). In this case, $(a,d) = (Q_A, U_A) = (Q_t, U_t)$. That leaves c as the only free parameter. As we discussed above, c is related to the local covering factor f_l (c is small for low coverage, large for complete coverage).

BAL QSO 1246-0542 shows an interesting velocity dependence in its C IV BAL coverage, as we discussed in Section 5.7. The main sub-trough (2) is shifted by -2000 km/s in polarized flux relative to total flux. The polarization is greater in the low-speed portion of the trough than the high-speed portion of the trough (Figure 5.13). The $Q'(F)$ curve shows an hysteresis at the trough depth where the polarization peaks. (Note how the points progress in a counter-clockwise direction around this loop with increasing $|v|$.) This effect is seen in a number of other objects in our sample, and indicates a transition from from low to high fractional coverage of the electron scattering region. There is a cluster of data points in the velocity range -15,500 to -16,500 km/s (8 bins), which have a residual trough flux of $F = 0.19 - 0.20$ and $Q' = 5.4 - 7.1\%$. This indicates that the BAL is saturated at a flux

level of 20% in this velocity range, and virtually all of the residual flux is from the electron scattering region.

We can parameterize the local covering fraction as a function of velocity by comparing the polarization with our partial continuum coverage model. The transformation between model parameter c and $f_l(v)$ depends on the particular density distribution and shape of the scattering region, and on the shapes of the Sobolev surfaces, so it is velocity dependent.

We calculated model $Q(F)$ and $U(F)$ curves (Equations 5.5-5.11) using the following constraints for 1246-0542: $Q_c = 1.4\%$ and $(Q_t, U_t) = (7\%, 1\%)$. Note that we used our unbinned data, which has better velocity resolution (600 km/s) and slightly higher peak polarization than the binned data. Figure 5.13 shows a comparison of the model to the data in two portions of the 1246-0542 C IV BAL. The polarization in the BAL rises as central source C is absorbed (decreasing residual flux F). It is remarkable that the polarization trend in the rapidly falling and rising portions of the trough matches the model quite well. This shows that the partial coverage model is a good description of BAL polarization behavior.

The high and low speed portions of the BAL are fit by $Q(F)$ curves with different model parameters (Table 5.5). The parameter c is a factor of 2.1 greater at high speed ($|v| > 16,000$ km/s) than at low speed ($|v| < 16,000$ km/s). This indicates that the local covering factor $f_l(v)$ generally increases with velocity. It is difficult to tell how the coverage progresses in the deepest portion of the BAL because it is saturated. There is also a systematic positive excursion from the trend in the range $F = 0.6 - 0.8$ (—v—=18,500-23,300 km/s) which may indicate that the covering fraction falls again at the highest velocities.

The simplest way to explain the velocity dependence of f_l in 1246-0542 is with an expanding and accelerating outflow which covers a polar electron scattering region (Fig. 5.14). Note that there must be a non-radial component to the flow because the BAL is detached from the BEL. We suggest that this component is in the polar direction, away from the accretion disk. The polar velocity component may be due to magnetic stresses (Emmering et al., 1992), or a gas pressure gradient away from the disk. Arav (1996) suggests a similar model where there are separate BAL flow tubes for each sub-trough. In that case, maximum coverage of the polarized continuum source can occur at an intermediate velocity in each sub-trough.

model	a	b	c	d
1	0.07	-0.01	3.3	-0.01
2	0.07	0.04	6.9	-0.01

Table 5.5: Model fits to 1246-0542 polarization. Models 1 and 2 are representative of the polarization behavior in the low ($|v| < 16,000$ km/s) and high-speed ($|v| > 16,000$ km/s) sections of the C IV BAL. Model parameters (a, b, c, d) from Equations 5.5-5.11 are described in the text. The larger c parameter in model 2 indicates a larger local covering fraction f_l at high speeds.

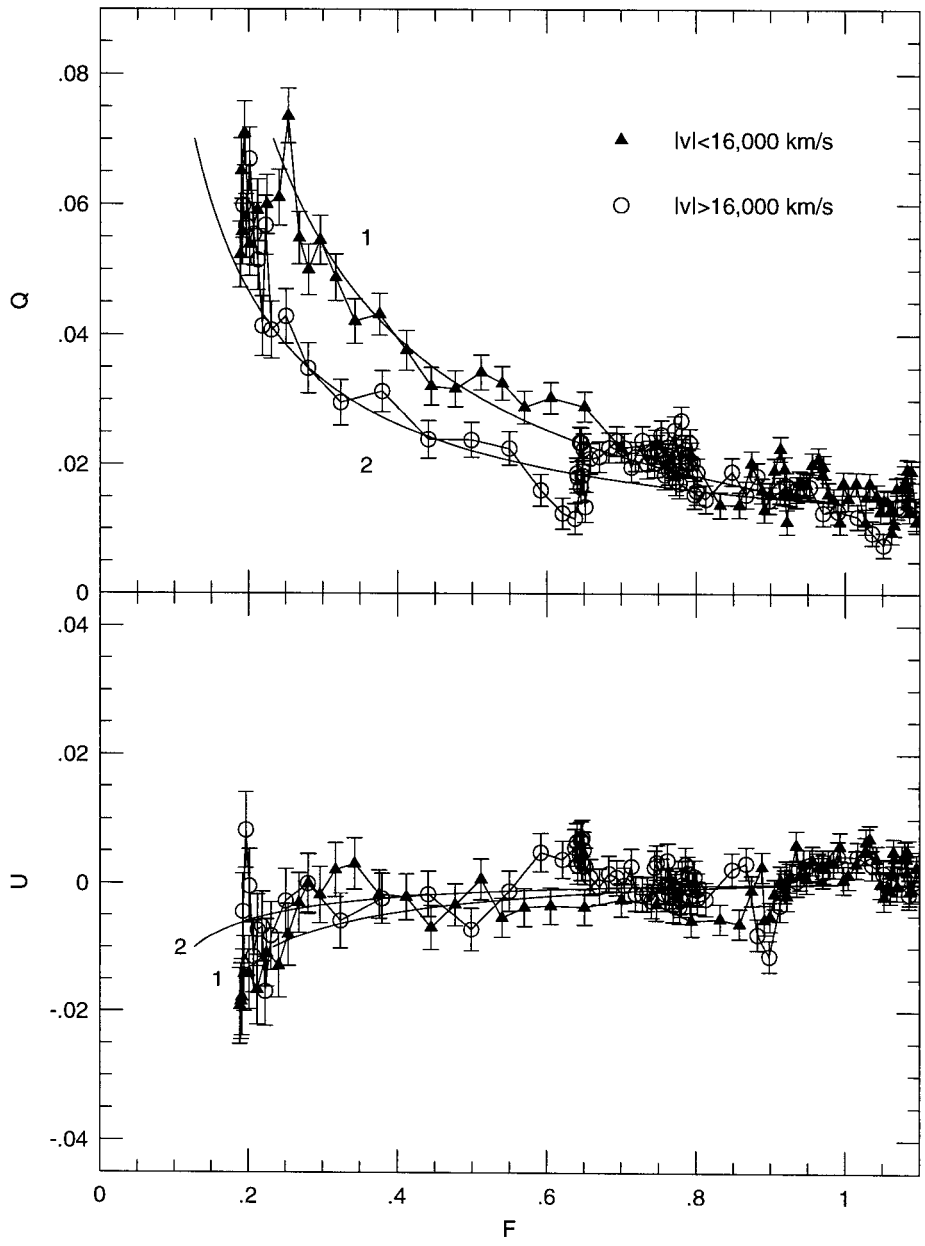

Figure 5.13: 1246-0542 polarization model fits. This figure plots the polarization (Q', U') in the C IV BAL of 1246-0542 vs. residual trough flux F, for -28,000< v < 0 km/s. Adjacent velocity bins are connected by lines. Trough depth increases to the left. We have plotted two curves (1 and 2) from the partial coverage model which best match the polarization in the low and high-speed sections of the BAL. The parameters for these curves are given in Table 5.5. The polarization is greater in the low-speed section of the BAL at any given trough depth. Also note that the deviation of U' from 0 indicates a PA rotation in the deepest part of the BAL.

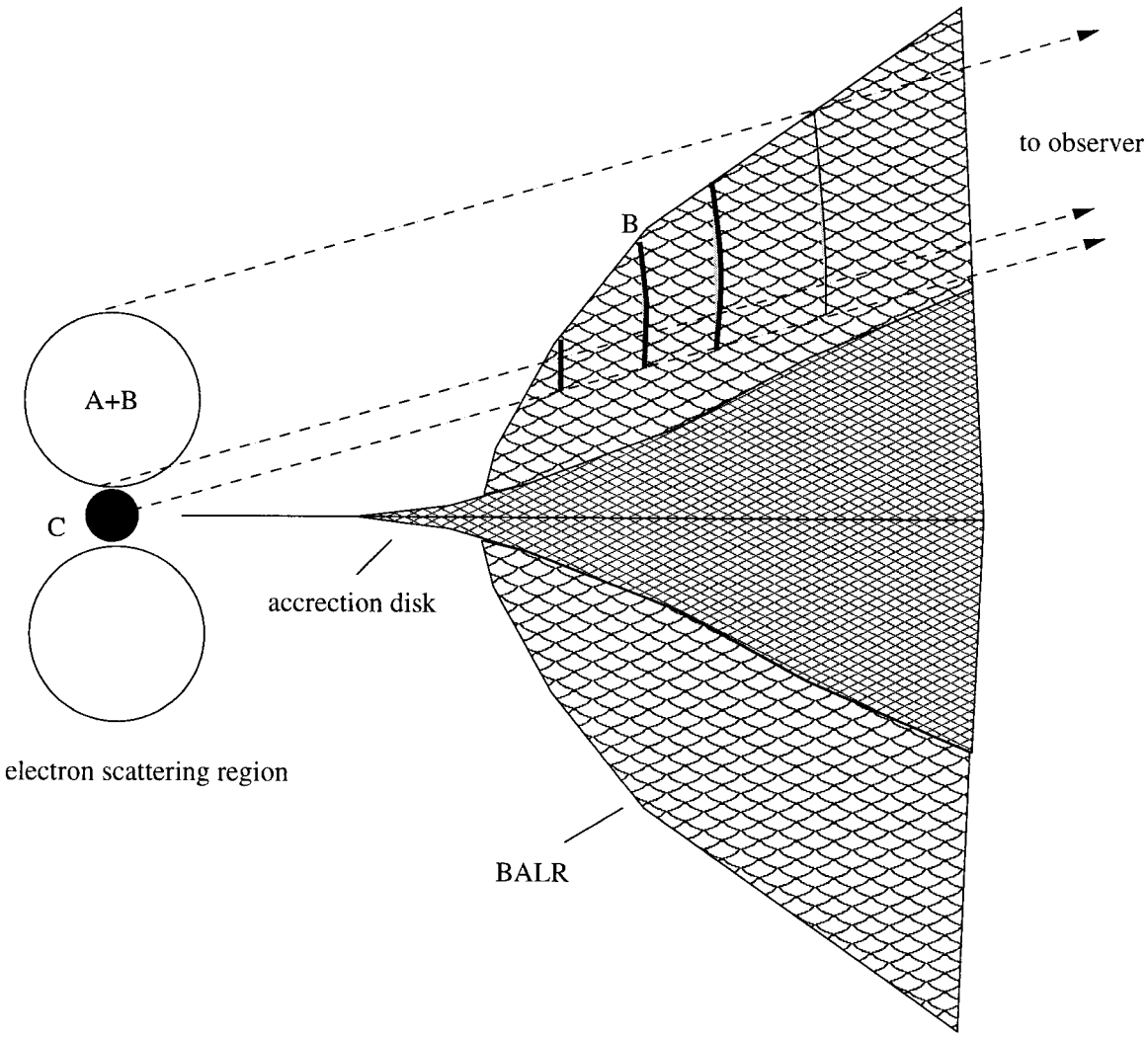

Figure 5.14: A non-radial, outwardly accelerating BAL outflow is ablated from the accretion disk. Partial coverage of the electron scattering region A+B by the Sobolev surfaces B increases with outflow velocity. The central continuum source is C, and the observer is located to the right. See Figure 5.12 for the observers point of view.

5.15 BAL Optical Depth

This thesis has emphasized the importance of partial coverage of the continuum and line sources by the BALR. Partial coverage introduces a host of potential difficulties in determining the optical depth of the BAL due to filling in by extended sources. A significant portion of the total flux in the bottom of a trough is electron scattered continuum light. The minimum fraction of scattered light in the BAL is given by the maximum trough polarization, which can be 10% or larger. Troughs that appear to have an optical depth of 2-3 may actually be saturated, making measurements of the true optical depth impossible. However, some portions of the trough may be truly optically thin, making it possible to separate the scattered and direct contributions to the flux. Typically there is less excess polarization in the high speed tail of the BAL trough, indicating that the contribution of scattered flux is less important. At high velocities there is also less contamination by the BEL.

Determination of the true optical depths in the troughs is important for determining the ionization and metal abundances in the BALR. Previous measurements have yielded extremely high abundances (10-100 times solar), but these have not taken into account saturation and scattered light. It is likely that the abundances derived from the BAL troughs are in error because they underestimate column densities in optically thick troughs and consequently underestimate the total hydrogen column N_H and ionization parameter.

While the BAL troughs show less saturation in polarized flux, it is probably not prudent to estimate ionization and abundances from the optical depths in polarized flux. For one, the scattered flux is integrated over lines of sight which pass through a mix of optically thick and optically thin clouds. Another problem is that contributions from resonantly scattered flux can contaminate the BAL. However, spectropolarimetry can be useful as a tool for determining what portions of the BAL are saturated and what portions are unsaturated and safe to use in abundance determinations. In addition, broad band polarimetry can be used to select objects with very low polarization ($P < 0.5\%$), for which it is likely there is less contamination from scattered light in the BAL.

5.16 Conclusions

The broad emission lines in BAL QSO have very low polarization. A few objects have BEL polarized at a detectable level, and at a PA different from the continuum. The C IV, Si IV, and Lyα/N V BEL are polarized differently from the C III] BEL, which suggests that they are resonantly scattered in the BALR. This is reinforced by their polarization perpendicular to the continuum, and a 1000 km/s redshift of the C IV BEL in polarized flux. The C III] BEL in 0019+0107 and 2225-0534 may be polarized by resonance scattering in the BELR.

We have found evidence of resonantly scattered continuum flux in the polarized flux spectra of BAL QSO 0226-1024 and 1333+2840. The small REW of the resonance scattering feature in 0226-1024 and the low upper limits in several objects are consistent with a low BALR global covering fraction ($f < 0.30$). However, the estimated covering fraction for 1333+2840 is near unity. This estimate may be compromised by anisotropic scattering and an equatorial viewing angle, which is suggested by the high polarization.

The resonance scattering feature extends past 12,000 km/s on the red side of the C IV BEL in 0226-1024 and 1333+2840. These extremely high velocities verify that it originates in the BALR. Resonance scattering in the red wing of C IV is more consistent with an equatorial outflow than a polar outflow if there is an opaque equatorial accretion disk. The resonantly scattered continuum photons in 1333+2840 are polarized perpendicular to the continuum PA, indicating that the BALR and electron scattering regions are separate and oriented orthogonally.

In most BAL QSO, the trough polarization is dominated by partial coverage of the electron scattering region, and the resonantly scattered flux is below our detection level. The partial coverage of the electron scattering region ranges from $f_l = 24-100\%$, indicating that the scattering region and the BAL clouds have similar angular sizes. There is strong evidence for velocity-dependent BALR coverage of the electron scattering region in our polarization spectra. In particular, our analysis of 1246-0542 indicates that the local covering factor increases with outflow velocity. This is consistent with a non-radial, expanding flow which arises in an accretion disk and is accelerated outward by radiation pressure. In addition, PA rotations in the BAL of several objects are consistent with the partial continuum coverage model. These rotations indicate a misalignment of the symmetry axes of the scattering region and intervening BAL clouds.

The narrow BAL sub-troughs at low velocity in 0226-1024 and 1524+5147 belong to a different class of absorption systems, which completely cover the electron scattering region, but only partially cover the BELR. This suggests that they may originate near the base of the outflow, and are closely associated with the BELR. They may be BEL clouds above the plane of the accretion disk seen in absorption against the continuum sources.

Chapter 6 Summary and Outlook

6.1 Results

- BAL QSO appear to be normal QSO viewed from a more equatorial direction, through a large column of highly ionized gas. They have higher average continuum polarization than non-BAL QSO because they are viewed at low latitudes. The polar BAL outflow model is ruled out. BAL QSO show a large intrinsic range in polarization ($0 - 6\%$) which is probably due to to a large range in electron scattering optical depths. The continuum polarization distribution of BAL QSO matches the polarization distribution of non-BAL QSO if the unification hypothesis is true and BAL QSO are viewed over a narrow inclination range. The lack of correlation between line equivalent widths and continuum polarization is also consistent with this model.

- The wavelength dependence of the continuum polarization is very weak, consistent with scattering from electrons and a pinch of dust. Dilution of the polarization by Fe II emission lines can account for some, but not all of the wavelength dependence. Absorption of the direct continuum by dust may also serve to bluen the polarization spectrum. There are only weak indications of neutral hydrogen opacity features, so the scattering medium must be highly ionized.

- The BEL in most BAL QSO are polarized at a very low level, indicating that the electron scattering region is smaller than the BELR. The C III] BEL is polarized in only two objects, possibly by resonance scattering in the BELR. The perpendicular polarization of the C IV BEL relative to the continuum suggests that it is resonantly scattered in the BALR.

- Resonantly scattered continuum is detected at high velocities (0-24,000 km/s) in two BAL QSO. We see continuum and BEL photons resonantly scattered from the far side of the BAL outflow. This is consistent with an equatorial outflow model. The low flux of resonantly scattered continuum suggests a global covering fraction $f < 30\%$ in several objects. Our large estimate for the covering fraction in 1333+2840 may be

due to anisotropic scattering effects in the BALR.

- High polarization and PA rotations are general features of the BAL. These are caused by partial coverage of the electron scattering region by the BAL clouds. The partial coverage phenomenon is consistent with a polar location for the scattering electrons. The velocity dependence of the partial coverage confirms that the BAL flow has a non-radial component and that it is accelerating and expanding outward. This appears to be a general result in the sub-troughs of a number of objects, though we focused on 1246-0542. Some relatively narrow BAL at low velocity completely cover the continuum sources, but not the BELR. This suggests that they are located near or in the BELR. It is also an independent confirmation that the BELR is larger than the electron scattering region.

6.2 Future Directions

Now that we have detected resonantly scattered emission from BAL QSO, the challenge is to better constrain the global BALR covering fractions. This will require a detection of the resonantly scattered component in total flux as well as in polarized flux. Additional progress may be made by spending many hours observing a single object. Our 4 hour observation of 0226-1024 indicates that it will be possible to determine a velocity profile for the resonantly scattered emission with several nights of observations. With this profile and high S/N observations of the BEL, it may be possible to decompose the direct and resonantly scattered portions of the flux in the C IV BEL. It will be necessary to correct for contamination by adjacent BEL at a level lower than 2 Å REW for this to be successful. With a good measurement of the total resonantly scattered flux, the main remaining uncertainty in the global covering fraction will be variation in the REW of the BAL with viewing direction. Another benefit of a higher S/N spectropolarimetric measurement of the resonance scattering profile is that it could be used to further constrain the geometry and dynamics of the BAL outflow.

The next challenge is to use the BAL polarization curves to test detailed dynamical models of the BAL outflow. To decipher these curves, we will need to go beyond our empirical model and use a specific model for the geometry of the scattering region and BALR. The geometry and dynamics are presumably coupled through the physics of ablation

from an accretion disk. The goal is to come up with a model with the smallest number of free parameters which predicts the coverage of the electron scattering region as a function of velocity.

Partial coverage of the electron scattering region is a bane for QSO ionization equilibrium and abundance determinations from the UV BAL optical depths. However, we have shown that spectropolarimetry may be used as a tool to determine which troughs and sub-troughs most completely cover the continuum. In particular, the low velocity, relatively narrow BAL and the high-velocity tails of the BAL have the greatest local covering fraction. Moreover, the BELR covering fraction of the low velocity systems can be determined from the unpolarized flux spectra of the BEL. Once suitable unsaturated absorption systems have been chosen, it will be possible to make improved estimates of their ionization and abundances by measuring their optical depths in a large number of UV BAL. Additional improvements to the ionization determinations will come with the measurement of total column densities from X-ray absorption and better constraints on the ionizing UV through X-ray spectral energy distribution.

Another potential area of progress is the search for and possible discovery of type 2 QSO. This will be a difficult task because the central source is expected to be obscured at most wavelengths. The search may best be carried out with a large area hard X-ray survey. If these objects are finally found, it will be possible to determine the beaming angle of the UV continuum from observations of the extended emission line regions, as we can now do with high-redshift radio galaxies. Imaging polarimetry and spectropolarimetry of the extended ionization cones will further help to constrain the geometry of the molecular torus and by inference, the inclination angle of the BAL outflow. We can also hope to find signatures of the 0.1c BAL outflow impinging on the interstellar medium of the host galaxy and learn what a BAL outflow looks like on kpc scales.

Finally, the holy grail is to determine why BAL QSO are almost exclusively radio-quiet, or probably more to the point, why radio-loud QSO do not show BAL absorption. The answer lies close to the central engine, where the radio jets are produced. One possibility is that radiation from the jets over-ionizes the BAL flow. Another attractive possibility is that the collimation of the radio jet can only occur if there is close alignment of the black hole spin axis with the accretion disk axis. Otherwise, the outflow originates at larger radii in the form of a radiatively driven BAL flow. Studies such as ours of QSO structure

on sub-parsec scales are the first steps towards determining the fundamental mechanisms which drive AGN outflows.

Bibliography

Antonucci, R. 1993, ARA&A, 31, 473

Antonucci, R., Geller, R., Goodrich, R. W., & Miller, J. S. 1996, ApJ, 472, 502

Antonucci, R. R. J. 1984, ApJ, 278, 499

Antonucci, R. R. J. & Miller, J. S. 1985, ApJ, 297, 621

Arav, N. 1996, ApJ, 465, 617

Arav, N. 1997. In Mass Ejection from Active Galactic Nuclei, eds. N. Arav, I. Shlosman, & R. J. Weymann, vol. 128 of ASP Conference Series, 208

Arav, N., Li, Z.-. Y., & Begelman, M. C. 1994, ApJ, 432, 62

Barlow, T. A. 1993. Time Variability of Broad Absorption-Line QSOs. Ph.D. thesis, UCSD

Barlow, T. A. 1994. private communication

Barlow, T. A., Junkkarinen, V. T., & Burbidge, E. M. 1989, ApJ, 347, 674

Barlow, T. A., Junkkarinen, V. T., Burbidge, E. M., Weymann, R. J., et al. 1992, ApJ, 397, 81

Barlow, T. A. & Sargent, W. L. W. 1997, AJ, 113, 1

Becker, R. H., Gregg, M. D., Hook, I. M., McMahon, R. G., et al. 1997, ApJ, 479, L93

Beland, S., Boulade, O., & Davidge, T. 1988. Tech. Rep. 19, CFHT. 16

Blaes, O. & Agol, E. 1996, ApJ, 469, L41

Blandford, R. D. & Znajek, R. L. 1977, MNRAS, 179, 433

Boroson, T. & Green, R. 1992, ApJS, 80, 109

Boroson, T. A. & Meyers, K. A. 1992, ApJ, 397, 442

Brotherton, M. S., Tran, H. D., van Breugel, W., Dey, A., & Antonucci, R. 1997, in prep.

Brown, J. C. & McLean, I. S. 1977, A&A

Burbidge, G. R., Crowne, A. H., & Smith, H. E. 1977, ApJS, 33, 113

Burstein & Heiles 1984, ApJS, 54, 33

Canalizo, G. & Stockton, A. 1997, ApJL, 480, 5

Chandrasekhar, S. 1960. Radiative Transfer. New York: Dover

Clarke, D., Stewart, B. G., Schwarz, H. E., & Brooks, A. 1983, A&A, 126, 260

Cohen, M. H., Ogle, P. M., Tran, H. D., Vermeulen, R. C., & Miller, J. S. 1995, ApJ, 448, L77

Cohen, M. H., Tran, H. D., Ogle, P. M., & Goodrich, R. W. 1998. Polarimetry and Unification of Low-Redshift Radio Galaxies. in prep.

Cohen, M. H., Vermeulen, R. C., Ogle, P. M., Tran, H. D., & Goodrich, R. W. 1997, ApJ, 484, 193

Dar, A. 1997, in prep.

Dey, A., Cimatti, A., Van Breugel, W., Antonucci, R., & Spinrad, H. 1996, ApJ, 465, 157

Emmering, R. T., Blandford, R. D., & Shlosman, I. 1992, ApJ, 385, 460

Foltz, C. B., Weymann, R. J., Morris, S. L., & Turnshek, D. A. 1987, ApJ, 317, 450

Francis, P. J., Hewett, P. C., Foltz, C. B., & Chaffee, F. H. 1991, ApJ, 373, 465

Francis, P. J., Hooper, E. J., & Impey, C. D. 1993, AJ, 106, 417

Glenn, J., Schmidt, G., & Foltz, C. 1994, ApJ, 434, L47

Goodrich, R. W. 1986, ApJ, 311, 882

Goodrich, R. W. 1991, PASP, 107, 1314

Goodrich, R. W. 1997, ApJ, 474, 606

Goodrich, R. W., Cohen, M. H., & Putney, A. 1995, PASP, 107, 179

Goodrich, R. W. & Miller, J. S. 1988, ApJ, 331, 332

Goodrich, R. W. & Miller, J. S. 1994, ApJ, 434, 82

Goodrich, R. W. & Miller, J. S. 1995, ApJ, 448, L73

Goodrich, R. W., Miller, J. S., Martel, A., Cohen, M. H., et al. 1996, ApJ, 456, L9

Green, P. G. 1997a. In Mass Ejection from Active Galactic Nuclei, vol. 128 of ASP Conference Series, 167

Green, P. J. 1997b, BAAS, 29, 1373

Green, P. J. & Mathur, S. 1996, ApJ, 462, 637

Green, P. J., Schartel, N., Anderson, S. F., Hewett, P. C., et al. 1995, ApJ, 450, 51

Hamman, F. 1998, ApJ. in press

Hamman, F., Korista, K. T., & Morris, S. L. 1993, ApJ, 415, 541

Hayes, D. S. 1970, ApJ, 159, 165

Hazard, C., McMahon, R. G., Webb, J. K., & Morton, D. C. 1987, ApJ, 323, 263

Hines, D. C., Schmidt, G. D., Smith, P. S., Cutri, R. M., & Low, F. J. 1995, ApJ, 450

Hines, D. C. & Wills, B. J. 1995, ApJ, 448, L69

Hsu, J.-C. & Breger, M. 1982, ApJ, 262, 732

Hughes, D. H., Dunlop, J. S., & Rawlings, S. 1997, MNRAS, 289, 766

Impey, C. D., Malkan, M. A., Webb, W., & Petry, C. E. 1995, ApJ, 440, 80

Jackson, N., Tadhunter, C., & Sparks, B. 1998, MNRAS. in press

Jackson, N., Tadhunter, C., Sparks, W. B., Miley, G., & Machetto, F. 1996, A&A, 307, L29

Johnstone, D., Hollenbach, D., Stoerzer, H., Bally, J., et al. 1996, BAAS, 189, 49.12

Kaspi, S., Smith, P. S., Maoz, D., Netzer, H., & Jannuzi, B. T. 1996, ApJ, 471, L75

Kellermann, K. I., Sramek, R., Schmidt, M., Green, R. F., & Shaffer, D. B. 1994, AJ, 108, 1162

Kellermann, K. I., Sramek, R., Schmidt, M., Shaffer, D. B., & Green, R. 1989, AJ, 98, 1195

Koratkar, A., Antonucci, R. R. J., Goodrich, R. W., Bushouse, H., & Kinney, A. L. 1995, ApJ, 450, 501

Korista, K. T. & Arav, N. 1997. In Mass Ejection from Active Galactic Nuclei, vol. 128 of ASP Conference Series, 201

Korista, K. T. & Ferland, G. 1997, ApJ. in press

Korista, K. T., Weymann, R. J., Morris, S. L., Kopko, Jr., M., et al. 1992, ApJ, 401, 529

Krolik, J. H. & Voit, G. M. 1998, ApJ. in press

Laor, A. & Draine, B. T. 1993, ApJ, 402, 441

Laor, A., Fiore, F., Elvis, M., Wilkes, B. J., & Mc Dowell, J. C. 1997, ApJ, 477, 93

Laor, A., Netzer, H., & Piran, T. 1990, MNRAS, 242, 560

Lee, H.-. W. 1994, MNRAS, 268, 49

Lee, H.-. W. & Blandford, R. D. 1997, MNRAS, 288, 19

Lightman, A. P. & Shapiro, S. L. 1975, ApJ, 198, L73

Magain, P., Surdej, J., Swings, J. P., Borgeest, U., et al. 1988, Nature, 334, 325

Manzini, A. & di Serego Alighieri, S. 1996, A&A

Martel, A. R. 1996. Spectropolarimetry of High-Polarization Seyfert 1 Galaxies. Ph.D. thesis, University of California, Santa Cruz

Masci, F. J. 1997. Obscuration of Quasars by Dust and the Reddening Mechanism in Parkes-Quasars. Ph.D. thesis, The University of Melbourne

Mathur, S. 1994, ApJ, 434, 493

Mathur, S., Elvis, M., & Singh, K. P. 1995, ApJ, 455, L9

Matthewson & Ford 1970, Mem. RAS, 74, 139

Miller, J. S. & Goodrich, R. W. 1990, ApJ, 355, 456

Miller, J. S., Goodrich, R. W., & Matthews, W. G. 1991, ApJ, 378, 47

Murray, N., Chiang, J., Grossman, S. A., & Voit, G. M. 1995, ApJ, 452, 498

Mushotzky, R. F. 1997. In Mass Ejection from Active Galactic Nuclei, eds. N. Arav, I. Shlosman, & R. J. Weymann, vol. 128 of ASP Conference Series, 141

Naghizadeh-Khouei, J. & Clarke, D. 1993, A&A, 274, 968

Ogle, P. M. 1997. In Mass Ejection from Active Galactic Nuclei, eds. N. Arav, I. Shlosman, & R. J. Weymann, vol. 128 of ASP Conference Series, 78

Ogle, P. M., Cohen, M. H., Miller, J. S., Tran, H. D., et al. 1997, ApJ, 482, L37

Oke, J. B. 1990, AJ, 99, 1621

Oke, J. B., Cohen, J. G., Carr, J., Cromer, J., et al. 1995, PASP, 107, 375

Oke, J. B. & Gunn, J. E. 1982, PASP, 94, 586

Osterbrock, D. E. 1989. Astrophysics of Gaseous Nebulae and Active Galactic Nuclei. University Science Books

Peterson, B. M. 1993, PASP, 105, 247

Pettini, M. & Boksenberg, A. 1985, ApJ, 294, L73

Pettini, M., King, D. L., Smith, L. J., & Hunstead, R. W. 1997, ApJ, 478, 536

Pogge, R. W. 1988, ApJ, 328, 519

Press, W. H., Teukolsky, S. A., Vettering, W. T., & Flannery, B. P. 1992. Numerical Recipes. Cambridge University Press

Putney, A. & Cohen, M. H. 1996. Second Order Light Effects in LRIS. Tech. rep., California Institute of Technology

Rudy, R. J. & Schmidt, G. D. 1988, ApJ, 331, 325

Schmidt, G. D., Elston, R., & Lupie, O. L. 1992, AJ, 104, 1563

Schmidt, G. D., Hines, D. C., & Smith, P. S. 1997. In Mass Ejection from Active Galactic Nuclei, eds. N. Arav, I. Shlosman, & R. J. Weymann, vol. 128 of ASP Conference Series, 305

Scoville, N. & Norman, C. 1995, ApJ, 451, 510

Serkowski, K., Mathewson, D. S., & Ford, V. 1975, ApJ, 196, 261

Shields, G. A. 1996, ApJ, 461, L9

Simmons, J. F. L. & Stewart, B. G. 1985, A&A, 172, L11

Sowinski, L. G., Schmidt, G. D., & Hines, D. C. 1997. In Mass Ejection from Active Galactic Nuclei, eds. N. Arav, I. Shlosman, & R. J. Weymann, vol. 128 of ASP Conference Series, 305

Sprayberry & Foltz 1992, ApJ, 390, 39

Stocke, J. T., Morris, S. L., Weymann, R. J., & Foltz, C. B. 1992, ApJ, 396, 487

Stockman, H. S., Angel, J. R. P., & Hier, R. G. 1981, ApJ, 243, 404

Stockman, H. S., Moore, R. L., & Angel, J. R. P. 1984, ApJ, 279, 485

Stockton, A., Canilizo, G., & Close, L. M. 1998, ApJ. In press

Sun, W.-H. & Malkan, M. 1989, ApJ, 346

Tran, H. D. 1995, ApJ, 440, 565

Tran, H. D., Cohen, M. H., Ogle, P. M., & Goodrich, R. W. 1998, ApJ, 499

Turnshek, D., Foltz, C., Grillmair, C. J., & Weymann, R. J. 1988, ApJ, 325, 651

Turnshek, D. A. 1997. In Mass Ejection from Active Galactic Nuclei, eds. N. Arav, I. Shlosman, & R. J. Weymann, vol. 128 of ASP Conference Series, 193

Urry, M. C. & Padovani, P. 1995, PASP, 107, 803

Wampler, E. J., Chugai, N. N., & Petitjean, P. 1995, ApJ, 443, 586

Webb, W., Malkan, M., Schmidt, G., & Impey, C. 1993, ApJ, 419, 494

Weymann, R. J., Morris, S. L., Foltz, C. B., & Hewett, P. C. 1991, ApJ, 373, 23

Weymann, R. J., Turnshek, D. A., & Christiansen, W. A. 1985. Astrophysics of Active Galaxies and Quasi-Stellar Objects. University Science Books: Mill Valley, CA

Wills, B. J., Netzer, H., & Wills, D. 1985, ApJ, 288

Wilson, A. S., Braatz, J., Heckman, T. M., Krolik, J. H., & Miley, G. K. 1993, ApJ, 419, L61

Wilson, A. S. & Colbert, E. J. M. 1995, ApJ, 438, 62

Wood, K., Bjorkman, J. E., Whitney, B. A., & Code, A. D. 1996, ApJ, 461, 828